Title
Dark Matter Searches with Gamma Rays from the Galactic Center Halo and Cosmic-Ray Antimatter

Author
Ryan, James Lee

Publication Date
2022

UNIVERSITY OF CALIFORNIA
Los Angeles

Dark Matter Searches with Gamma Rays from the Galactic Center Halo and Cosmic-Ray Antimatter

A dissertation submitted in partial satisfaction of the
requirements for the degree Doctor of Philosophy
in Astronomy and Astrophysics

by

James Lee Ryan

2022

ABSTRACT OF THE DISSERTATION

Dark Matter Searches with Gamma Rays from the Galactic Center Halo and Cosmic-Ray Antimatter

by

James Lee Ryan
Doctor of Philosophy in Astronomy and Astrophysics
University of California, Los Angeles, 2022
Professor Rene A. Ong, Chair

It is unknown what constitutes dark matter. The properties of dark matter particles may be observed indirectly if dark matter annihilates or decays into Standard Model particles that are then detected. Work is presented on two such experiments, performed with GAPS and VERITAS. GAPS is a forthcoming balloon-borne cosmic-ray antimatter detector whose unprecedented sensitivity to the fluxes of antiprotons, antideuterons, and antihelium makes possible the detection of a variety of exotic sources of these particles. We outline development of the GAPS TOF system, and demonstrate its ability to achieve desired resolutions in time, position, and energy. VERITAS is an imaging atmospheric Cherenkov telescope array that has been observing gamma rays from the Galactic Center region for over 10 years. We develop a template-based background estimation method to look for excess gamma rays in the Galactic Center halo. No significant excess is found, and limits on the thermally-averaged annihilation cross section are derived with dependence on the annihilation channel, reaching $\langle \sigma_{\mathrm{ann}} v \rangle < 1.38 \times 10^{-25}$ cm^3 s^{-1} for a 6 TeV dark matter particle that annihilates into $\tau^+\tau^-$.

The dissertation of James Lee Ryan is approved.

Jay Hauser

Alvine Kamaha

James Larkin

Rene A. Ong, Chair

University of California, Los Angeles

2022

To my parents

TABLE OF CONTENTS

LIST OF FIGURES

LIST OF TABLES

ACKNOWLEDGEMENTS

Thanks are due firstly to my advisor Rene Ong for his invaluable ideas and support over the years. I am also indebted to the people in the GAPS and VERITAS collaborations, whose efforts have enabled or augmented this work. In particular, I am thankful for the tremendous support and insight offered by Takeru Hayashi, especially on computer-related topics, and for productive discussions with Jeff Zweerink, Ralph Bird, Sean Quinn, Matt Buchovecky, Erik Everson, Isaac Mognet, Philip von Doetinchem, Achim Stoessl, and Sydney Feldman. I am grateful for the guidance offered by Jodi Christiansen and David Williams, as well as numerous faculty members in the UCLA Physics and Astronomy department. I have benefitted immensely from interactions with my fellow grad students, including my officemate Peter Williams, whose original thinking has irreparably shaped my own. I also recognize Aneta Siemiginowska, Josh Grindlay, and Melissa Franklin for starting me on the path of astronomy and particle physics. Lastly, I thank my friends and family, who have supported me most of all.

VITA

2015 A.B., Physics and Astrophysics, Harvard University

2017 M.A., Astronomy, University of California, Los Angeles

PUBLICATIONS

Munini, R., et al. The antinucleus annihilation reconstruction algorithm of the GAPS experiment. Astroparticle Physics, 133:102640, 2021

Adams, C. B., et al. An Archival Search for Neutron-star Mergers in Gravitational Waves and Very-high-energy Gamma Rays. ApJ, 918(2):66, 2021

Benbow, W., et al. A Search for TeV Gamma-Ray Emission from Pulsar Tails by VERITAS. ApJ, 916(2):117, 2021

Saffold, N., et al. Cosmic antihelium-3 nuclei sensitivity of the GAPS experiment. Astroparticle Physics, 130: 102580, 2021

Adams, C. B., et al. VERITAS Observations of the Galactic Center Region at Multi-TeV Gamma-Ray Energies. ApJ, 913(2): 115, 2021

EHT MWL Science Working Group, et al., Broadband Multi-wavelength Properties of M87 during the 2017 Event Horizon Telescope Campaign. ApJL, 911(1):L11, 2021

von Doetinchem, P., et al. Cosmic-ray antinuclei as messengers of new physics: status and outlook for the new decade. JCAP, 2020(8):035, 2020

Abeysekara, A. U., et al. Demonstration of stellar intensity interferometry with the four VERITAS telescopes. Nature Astronomy, 4: 1164-1169, 2020

Archer, A., et al. VERITAS Discovery of VHE Emission from the Radio Galaxy 3C 264: A Multiwavelength Study. ApJ, 896(1):41, 2020

Ryan, J. L., Siemiginowska, A., Sobolewska, M. A., and Grindlay, J. Characteristic Variability Timescales in the Gamma-Ray Power Spectra of Blazars. ApJ, 885(1):12, 2019

1 Introduction

1.1 Dark Matter

The question of what constitutes dark matter continues to drive experiments and theories on the frontiers of physics and astrophysics. Some of the earliest observations suggesting the existence of dark matter came from observations of the kinematics of galaxy clusters (Zwicky, 1933, 1937) and stars (Roberts, 1966; Rubin & Ford, 1970; Rubin et al., 1980), while the idea of non-luminous matter may be traced back further (Bertone & Hooper, 2018). The velocity dispersion of galaxies in clusters is higher than expected given the mass of luminous matter in galaxies, under the assumption of virialization. Similarly, the "rotation curves" of galaxies, graphs of the circular velocities of stars versus their distance from their galaxy's center, are observed to flatten at radii beyond where most of the galaxy's visible matter ends—inconsistent with the velocity $\propto 1/\sqrt{\text{radius}}$ relation expected from Newtonian dynamics, unless a significant amount of matter exists beyond the visible edge of galaxies. Additional evidence for dark matter has come from a variety of observations, including stellar velocities perpendicular to the Galactic plane (Oort, 1932; Bahcall et al., 1992) the Cosmic Microwave Background (CMB; Hinshaw et al., 2013; Planck Collaboration et al., 2020), large scale structure (Tegmark et al., 2004), and gravitational lensing (Massey et al., 2010). Lensing observations of merging galaxy clusters, such as the Bullet Cluster, reveal an offset between the bulk of the mass and baryonic matter, providing an important example where the baryonic and dark matter are spatially separated (Clowe et al., 2004, 2006; Bradač et al., 2008). Today, our best model of the Universe contains a "cold" dark matter component that accounts for ∼84% of its mass—more than five times the baryonic component. However, despite several decades of experimental effort, the nature of dark matter remains unknown.

Early observations of dark matter were not interpreted as evidence of new physics, as it was thought that the unobserved mass would be in the form of faint stars, solid bodies, and gases (e.g. Oort, 1932; Zwicky, 1937). The problem concerning the nature of dark matter arises as conventional physical explanations are ruled out. Gas in galaxies and clusters is not detected in sufficient amounts to explain dark matter (e.g. Woolf, 1967; Meekins et al., 1971; Wilson & Mauersberger, 1994), while low mass stars and brown dwarfs can be ruled out by considerations of the stellar initial mass function (Graff & Freese, 1996; Chabrier et al., 1996). Microlensing surveys further reveal that compact objects, including low mass stars, brown dwarfs, black holes, and neutron stars (termed massive compact halo objects, or MACHOs), cannot exceed 8% of our Galaxy's halo mass (Alcock et al., 2000; Tisserand et al., 2007). More generally, baryonic matter has been constrained to make up only a fraction of the matter density of the universe by observations of elemental abundances and the CMB (Reeves et al., 1973; Fukugita et al., 1998; Planck Collaboration et al., 2020). Neutrinos were a promising dark matter candidate, being stable and electrically neutral, but are excluded by considerations of the phase-space density in galaxies (Tremaine & Gunn, 1979) and observations of large scale structure (White et al., 1983). One explanation for dark matter that remains is a new particle beyond the Standard Model (SM) of particle physics. Other proposals, including primordial black holes (MacGibbon, 1987; Carr et al., 2016; Carr & Kühnel, 2020) and modified theories of gravity (Milgrom, 1983), are not considered in this work.

A dark matter particle that can account for the unsubstantiated mass at all scales where it is observed is subject to several constraints. The particle mass, $m_{\rm DM}$, must be > 70 eV[1] for a fermion or $> 10^{-22}$ eV for a boson, from quantum and cosmological considerations, respectively (Particle Data Group et al., 2020), and $< 5M_\odot$ based on observations of tidal disruptions of binary stars with wide separations in dark matter halos (Monroy-Rodríguez & Allen, 2014). It must be electrically neutral, or have an effective charge $\lesssim 10^{-14}$ that of the electron for $m_{\rm DM}$ ~1 GeV (Kadota et al., 2016), achieved either through being "millicharged" or through a mediator, such as a dark photon, which kinetically mixes with the SM photon. It must have a self-interaction cross section $< 0.47\ {\rm cm}^2/{\rm g} \times m_{\rm DM}$, constrained by observations

---

[1] Masses will often be given in units of energy, related to mass by $E = mc^2$.

of merging galaxy clusters (Harvey et al., 2015; Tulin & Yu, 2018). Lastly, it must be stable on timescales $\gtrsim 10^{19}$ s based on CMB and large scale structure constraints (Audren et al., 2014).

Properties of dark matter's spatial and velocity distributions have also been measured. Recent determinations of the local dark matter density find values $\sim$0.3–0.6 GeV cm^{-3} (Read, 2014; de Salas & Widmark, 2021). Cosmological modeling of the CMB and baryon acoustic oscillation measurements gives an average density of dark matter in the Universe $\Omega_{\mathrm{DM}} \equiv \rho_{\mathrm{DM}}/\rho_{\mathrm{crit}} \approx 0.265$, or $\rho_{\mathrm{DM}} = 1.26 \times 10^{-6}$ GeV cm^{-3} for $\rho_{\mathrm{crit}} = 4.79 \times 10^{-6}$ GeV cm^{-3} (Planck Collaboration et al., 2020). These models also constrain any dark matter species to be non-relativistic, or "cold," if they decouple after the Universe's quantum chromodynamic phase transition. Relativistic, or "hot" dark matter, is additionally disfavored by numerical simulations of structure formation (e.g. White et al., 1983). Structure formation simulations also suggest that dark matter halos follow a fairly "universal" profile (Navarro et al., 1996; Gao et al., 2008; Navarro et al., 2010; Ludlow et al., 2016), whose parameterizations include the Navarro-Frenk-White (NFW; Navarro et al., 1996, 1997) and Einasto (Einasto, 1965) profiles, among others (Bertone et al., 2005; Cirelli et al., 2011). The velocity distribution of dark matter may be assumed to follow a Maxwell-Boltzmann distribution based on considerations of halo formation (Freese et al., 1988), though simulations suggest potentially significant departures from a pure Maxwellian distribution (Vogelsberger et al., 2009; Kuhlen et al., 2012).

Additional constraints arise when considering the mechanism by which dark matter is produced. Production must have occurred in the early Universe (before Recombination), based on models of the CMB and structure formation, and several possible mechanisms have been identified (Cirelli, 2012; Particle Data Group et al., 2020). If dark matter particles were in thermal equilibrium with the Universe, their number density will "freeze out" when the rate of number-changing particle interactions falls below the expansion rate of the Universe. Other production mechanisms include "freeze in" scenarios where dark matter never reaches thermal equilibrium and is instead produced over time, asymmetry between dark matter and its antiparticle abundances, and decays from a heavier particle (that may have frozen out earlier).

A variety of theoretical particles have been proposed that may constitute dark matter (Feng, 2010; Particle Data Group et al., 2020). Among the vast theoretical landscape, those theories that have additional motivations independent of the dark matter problem tend to be prioritized by experimental searches. A well-motivated class of candidate dark matter particle is the weakly interacting massive particle (WIMP; Steigman & Turner, 1985; Jungman et al., 1996; Bertone et al., 2005; Roszkowski et al., 2018). A WIMP may be any non-baryonic massive particle that interacts through weak-scale or sub-weak forces, but most commonly refers to particles that interact through the weak nuclear force of the Standard Model and have masses around 1 GeV to 100 TeV (e.g. Roszkowski et al., 2018; Leane et al., 2018; Bottaro et al., 2022). The lower and upper mass limits come from cosmological constraints (Lee & Weinberg, 1977; Leane et al., 2018) and unitarity arguments (Griest et al., 1990; Smirnov & Beacom, 2019), respectively. WIMPs are present in many theories beyond the Standard Model, including supersymmetry, which addresses the "gauge hierarchy problem," and universal extra dimensions (UED), which has other motivations (Cheng et al., 2002; Servant & Tait, 2003; Bertone et al., 2005). Within supersymmetry, the lightest supersymmetric particle (LSP) is often the best dark matter candidate, and is a WIMP when the LSP is a sneutrino or neutralino. It has been argued that the neutralino is the most likely LSP in the minimal supersymmetric standard model (Ellis et al., 1984; Jungman et al., 1996). Non-WIMP candidates also exist (Baer et al., 2015; Arcadi et al., 2018), with axions being a particularly well-motivated alternative, as they address the "strong CP problem" (Peccei & Quinn, 1977a,b; Peccei, 2008; Kim & Carosi, 2010). Other potential LSPs, such as the axino and gravitino, are also non-WIMP dark matter candidates.

WIMP dark matter has another appealing feature in that it freezes out with a relic abundance close to $\Omega_{\rm DM}$ for masses around 100 GeV and an annihilation cross section typical of weak interactions—a coincidence that has been referred to as the "WIMP miracle" (e.g. Feng & Kumar, 2008). A thermal relic particle's abundance in the present can be found by calculating its equilibrium number density, then evolving it forward in time (done in detail in e.g. Kolb & Turner, 1990; Gondolo & Gelmini, 1991; Griest & Seckel, 1991; Steigman et al., 2012). The evolution of the number density of dark matter n is governed by a Boltzmann equation of the form (for self-annihilating particles; Gondolo & Gelmini, 1991)

$$\frac{dn}{dt} + 3Hn = -\langle\sigma_{\mathrm{ann}}v\rangle(n^2 - n_{\mathrm{eq}}^2) \tag{1}$$

where $\langle\sigma_{\mathrm{ann}}v\rangle$ is the thermally-averaged total annihilation cross section times velocity, $n_{\mathrm{eq}}(t)$ is the equilibrium value, $H \equiv (da/dt)a^{-1}$ is the Hubble parameter, and a is the scale factor of the Universe. Freeze-out occurs when the annihilation rate $\langle\sigma_{\mathrm{ann}}v\rangle n$ falls below H and the dark matter decouples from the other particle species, typically at a temperature $\sim (m_{\mathrm{DM}}/20)c^2k_B^{-1}$ for a WIMP (Jungman et al., 1996). Solving the equation to find the present value of n yields (Jungman et al., 1996)

$$\Omega_{\mathrm{DM}}h^2 \approx \frac{3\times10^{-27}\ \mathrm{cm}^3\ \mathrm{s}^{-1}}{\langle\sigma_{\mathrm{ann}}v\rangle} \tag{2}$$

where h is the Hubble constant H_0 in units of 100 km s^{-1} Mpc^{-1}. The WIMP annihilation cross section may be estimated $\langle\sigma_{\mathrm{ann}}v\rangle \approx \alpha_W^2 m_{\mathrm{DM}}^{-2}\hbar^2c^{-1}$ (Jungman et al., 1996), or $\langle\sigma_{\mathrm{ann}}v\rangle \approx g_W^4 m_{\mathrm{DM}}^{-2}\hbar^2c^{-1}$ (Feng & Kumar, 2008), where the weak fine structure constant $\alpha_W = 4\pi g_W^2 \approx 0.03$ (Griffiths, 2008) and typical weak-scale mass $m_{\mathrm{DM}} \approx 100$ GeV yield a cross section within a few orders of magnitude of the canonical "thermal cross section" value of 3×10^{-26} cm^3 s^{-1} (Steigman et al., 2012), which gives the correct relic density and guides many experimental searches.

1.2 Methods of Dark Matter Detection

Methods of detecting dark matter may be conceptualized into four methods: astrophysical probes, collider searches, direct detection, and indirect detection (Arrenberg et al., 2013). These approaches are complementary, in that they are sensitive to different dark matter properties and backgrounds, and in many cases detection in more than one channel may be necessary to establish a newly-discovered particle as dark matter.

Astrophysical probes refer primarily to observations of phenomena sensitive to dark matter's gravitational interactions. This includes all evidence for dark matter thus far, as well as measurements of dark matter structure via gravitational lensing, stellar kinematics, or other observational signatures. Such measurements can constrain dark matter's particle properties in some cases, when combined with numerical simulations (Boddy et al., 2022).

Collider searches aim to find evidence of dark matter production at particle colliders, typically in the form of missing momentum (Kahlhoefer, 2017). Such searches are sensitive to dark matter particles with masses below the center-of-mass energies reachable by colliders ($\lesssim$ 1 TeV at present), and rely on the specific couplings between dark matter and SM particles. Results are often presented in terms of simplified models or effective field theories in order to be applicable to general classes of theories, and also allowing elastic and inelastic cross sections to be calculated for comparison with direct and indirect searches (Goodman et al., 2010; Kahlhoefer, 2017; Arcadi et al., 2018).

Direct detection refers to observing the interaction of dark matter particles with SM particles in a detector, as first proposed by Goodman & Witten (1985). If dark matter and a SM particle have a non-zero inelastic cross-section, the effects of a recoil may be detected though the subsequent production of light, charge, or heat (Roszkowski et al., 2018). While WIMP dark matter is not expected to interact with electrons, scattering off nucleons is possible. The expected differential recoil rate $d\Gamma/dE$ is given by (Schumann, 2019)

$$\frac{d\Gamma}{dE} = \frac{\rho_\odot M}{m_N m_{\mathrm{DM}}} \int_{v_{\mathrm{min}}}^{v_{\mathrm{esc}}} dv\; v f(v) \frac{d\sigma_{\mathrm{inel}}}{dE} \tag{3}$$

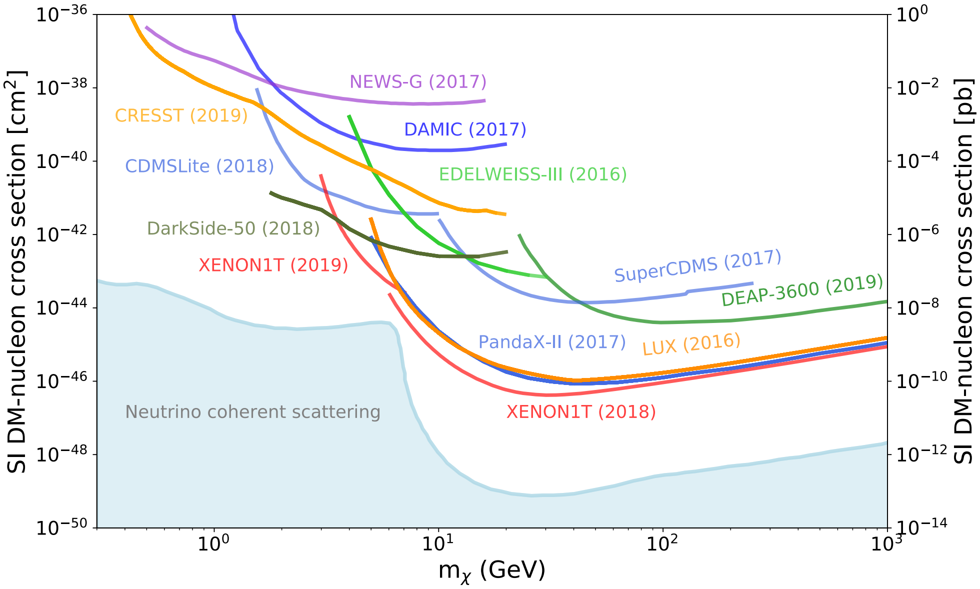

Figure 1: Direct detection limits (90% confidence) on the spin-independent dark matter-nucleon elastic cross section as a function of dark matter mass from various experiments. The light blue region indicates the boundary of the neutrino floor (see text). Figure from Particle Data Group et al. (2020).

where E is the nuclear recoil energy, $\rho_\odot$ is the local dark matter density, M is the detector mass, m_N is the mass of the target nucleus, v is the incoming dark matter particle velocity, $f(v)$ is the local dark matter velocity distribution, and $\sigma_{\rm inel}$ is the inelastic scattering cross section, which generally depends on v and E. Direct detection experiments thus require knowledge of dark matter's spatial distribution and kinematics in order to relate Γ to $\sigma_{\rm inel}$. The high sensitivity of direct detection experiments also means that great care must be taken to account for backgrounds, such as those from cosmic rays and radioactivity. Among the most problematic is the cosmic neutrino background, especially from neutrinos produced in the sun by beta decays of boron-8, whose coherent scattering off nuclei can mimic WIMP signals (Monroe & Fisher, 2007; Vergados & Ejiri, 2008; Strigari, 2009). The neutrino flux is in some cases an irreducible background that represents a hard limit for direct detection experiments' sensitivities (Billard et al., 2014), leading to it being called the "neutrino floor." On the other hand, the neutrino background might be better described as a "neutrino fog," due to the uncertainty in the value of the neutrino flux, and the fact that the signals from dark matter and neutrinos are potentially distinguishable (e.g. O'Hare, 2021). Some recent limits on the spin-independent WIMP-nucleon elastic cross section are shown in Figure 1. Liquid argon and xenon detectors have produced the strongest constraints for $m_{\rm DM} \gtrsim$ a few GeV, while cryogenic crystal detectors become more sensitive at lower masses (e.g. Roszkowski et al., 2018). Liquid xenon detectors have also placed the tightest constraints on the spin-dependent WIMP-neutron cross section, while bubble chambers and neutrino telescopes are the most sensitive to the spin-dependent WIMP-proton cross section.

Lastly, the method of indirect detection aims to detect standard model particles produced by dark matter annihilations or decays. As indirect detection is the search method pursued in this work, it will be described in greater detail in the next section.

1.3 Indirect Detection

Many theories allow dark matter to annihilate or decay into SM particles. The possibility of detecting the end-state SM particles resulting from such processes forms the basis of indirect detection. Among the earliest proposals considered the annihilation of heavy neutrino dark matter into gamma rays (Gunn et al., 1978; Stecker, 1978). Subsequent work has investigated a variety of models, targets, and end states (Gaskins, 2016). Searches for the effects of dark matter annihilations and decays on compact objects such as neutron stars (Goldman & Nussinov, 1989) and other astrophysical observables may also be included under the umbrella of indirect detection (Leane et al., 2021).

Various features of indirect detection make it complementary to the other dark matter search methods (Bergström et al., 2011; Bertone et al., 2012; Arrenberg et al., 2013). For instance, indirect methods can be sensitive to dark matter candidates whose masses are outside the kinematic reach of collider experiments. Reliance on the annihilation cross section (with a convenient benchmark value in the thermal cross section) also allows for sensitivity to dark matter models with small SM elastic cross sections that may consequently evade direct detection. Additionally, indirect detection aims to observe dark matter in astrophysical contexts, whereas demonstrating that a new particle created in a collider comprises the dark matter may be less straightforward. On the other hand, many theories permit the possibility of dark matter detection in multiple channels, and it is possible that such a battery of detections will be necessary to unambiguously determine dark matter's particle properties. Furthermore, the sources of confusion for indirect detection, such as astrophysical backgrounds, instrumental systematics, and uncertainties in the dark matter distribution, are different than for direct and collider searches.

The signal strength for indirect detection is quantified in the flux of the end-state particles. In the case of annihilating dark matter and electrically neutral end states (e.g. photons and neutrinos), the differential flux of produced SM particles $d\Phi/dE$ (with dimensions of area^{-1} time^{-1} energy^{-1}) is given by (e.g. Gaskins, 2016)

$$\frac{d\Phi}{dE} = \frac{1}{4\pi}\frac{\langle\sigma_{\rm ann}v\rangle}{2m_{\rm DM}^2}\frac{dN}{dE}\int d\Omega \int_{\rm los} ds\ \rho_{\rm DM}^2 \tag{4}$$

where E is the particle's energy, $\langle\sigma_{\rm ann}v\rangle$ is the annihilation cross section averaged over the dark matter velocity distribution, $m_{\rm DM}$ is the dark matter particle mass, dN/dE is the differential energy spectrum of particles produced per annihilation, $\rho_{\rm DM}$ is the dark matter density, and the integrals are carried out over observed solid angle Ω and spatial coordinate s along the line of sight. Written this way, the equation can be separated into a particle physics component, consisting of $m_{\rm DM}$, and dN/dE, and an astrophysical component. The latter component may be abbreviated as the J-factor[2] (Bergström et al., 1998)

$$J = \int_{\rm los} ds\ \rho_{\rm DM}^2 \tag{5}$$

---

[2] The J-factor is sometimes alternately defined to include the integral over Ω, or to have additional multiplicative factors that make it dimensionless.

The flux from dark matter decays is defined similarly with (e.g. Gaskins, 2016)

$$\frac{d\Phi}{dE} = \frac{1}{4\pi}\frac{1}{m_{\rm DM}\tau}\frac{dN}{dE}\int d\Omega \int_{\rm los} ds\ \rho_{\rm DM} \tag{6}$$

where τ is the dark matter particle lifetime, and the analogously defined D-factor (e.g. Evans et al., 2016) is

$$D = \int_{\rm los} ds\ \rho_{\rm DM} \tag{7}$$

For charged end states, the particles do not propagate in straight lines due to intervening electric and magnetic fields, complicating the flux calculation. The production rate of particles in the dark matter halo is given by a source term q, which for annihilations is (e.g. Donato et al., 2008; Cirelli et al., 2011)

$$q = \frac{1}{2}\langle\sigma_{\rm ann}v\rangle\frac{dN}{dE}\left(\frac{\rho_{\rm DM}}{m_{\rm DM}}\right)^2 \tag{8}$$

and which can be related to the flux through diffusion equations, describing the propagation of charged particles from their origin to the location of a detector. Propagation will be discussed in Section 1.4.

Annihilation cross sections and differential spectra can be calculated for specific theories, once $m_{\rm DM}$ and other parameters are chosen. The total spectrum of produced SM particles depends not just on annihilations or decays directly into the SM particle, but also on channels that subsequently produce the SM particle of interest. For example, dark matter annihilations into τ leptons, gauge bosons, or quarks lead to a broad spectrum of photons being produced through the creation and subsequent decays of neutral pions (Slatyer, 2021). The spectrum can thus be written as a sum

$$\frac{dN}{dE} = \sum_f B_f\frac{dN_f}{dE} \tag{9}$$

where B_f is the annihilation branching fraction into channel f, and dN_f/dE is the spectrum of SM particles of interest produced in channel f. The annihilation spectra are complicated to calculate and so they are typically derived from high-energy particle Monte Carlo simulations (e.g. Cirelli et al., 2011; Bringmann et al., 2018) The branching fractions depend on the annihilation cross sections into each channel. The velocity-weighted cross section is often expanded in powers of v^2 for convenience (Srednicki et al., 1988; Gondolo & Gelmini, 1991)

$$\sigma_{\text{ann}} v = a + bv^2 + O(v^4) \tag{10}$$

where a corresponds to the s-wave (total orbital angular momentum $L = 0$) contribution and b corresponds to the p-wave ($L = 1$) contribution (Jungman et al., 1996; Kumar & Marfatia, 2013; Slatyer, 2021). Expressions for a and b have been derived, for example, for the neutralino, whose mass eigenstates are normalized linear combinations of the neutral wino, bino, and two neutral higgsinos (Griest et al., 1990; Jungman et al., 1996). For the annihilation of non-relativistic dark matter, calculations may usually consider only the a term without great loss of accuracy. If s-wave annihilation is suppressed and the p-wave term dominates, however, the present-day annihilation cross section will be much smaller than the thermal cross section, due to dark matter cooling after freeze-out. Alternatively, the cross section could be enhanced at low velocities if dark matter particles experience some long-range attractive force, in what is called the Sommerfeld enhancement (Sommerfeld, 1931; Hisano et al., 2004; Hisano et al., 2005; Arkani-Hamed et al., 2009; Cassel, 2010). Additional enhancement of the low-velocity cross section can occur through bound-state formation (von Harling & Petraki, 2014; Bottaro et al., 2022).

Having determined the particle physics component, the rest of the flux calculation will depend on the dark matter distribution. For charged end states, the flux is sensitive to the local dark matter density, but it has weaker dependance on our Galaxy's exact dark matter profile—for example, different profiles modify the antiproton flux by ∼30% (Donato et al., 2004; Korsmeier et al., 2018). For uncharged end states, experiments may focus on lines of sight with high J-factors (or D-factors), thereby increasing signal strength. Preserved directionality also allows signal morphology to aid interpretation. High J-factors are found towards the Galactic Center (GC; discussed in Section 1.5), nearby dwarf spheroidal galaxies (dSphs), and nearby external galaxies (Evans et al., 2004; Gaskins, 2016). For neutrinos, additional promising targets include the Sun and Earth (Jungman et al., 1996; Bertone et al., 2005), though in practice such searches usually constrain the inelastic dark matter-nucleon cross section, as in direct detection (e.g. IceCube Collaboration et al., 2017). Diffuse, isotropic searches are also possible, where the relevant line of sight integral includes many dark matter halos out to high redshift (Bergström et al., 2001; Abdo et al., 2010). Flux predictions for both charged and uncharged end states are thus subject to uncertainties in halo profiles (Benito et al., 2019), including the potential of additional substructure (Moore et al., 1999; Diemand et al., 2007; Kamionkowski et al., 2010; Pieri et al., 2011). Substructure in the form of clumps would also has the effect of boosting end-state particle fluxes (Bengtsson et al., 1990).

Indirect detection experiments will optimally focus on end-state particles that have both theoretical motivations and small SM backgrounds. To this end, common end states considered are gamma rays, high-energy neutrinos, and antimatter. In practice, ”model-independent” constraints on $\langle\sigma_{\mathrm{ann}}v\rangle$ are often derived over a range of m_{DM} in individual annihilation channels. Constraints from various experiments using different end states, in the annihilation to $\tau^+\tau^-$ channel, are shown in Figure 2. The most stringent limits for lower masses come from high-energy gamma-ray observations of dSphs, while observations around the GC are also competitive for certain dark matter profiles (Gómez-Vargas et al., 2013). At higher masses, above ∼1 TeV, very-high-energy gamma-ray observations of the GC have produced the best limits.

Gamma-ray indirect searches benefit from the abundant production of gamma rays in many dark matter annihilation channels, as well as the existence of sensitive gamma-ray instruments and dark matter-dense targets. Annihilations to τ leptons, gauge bosons,

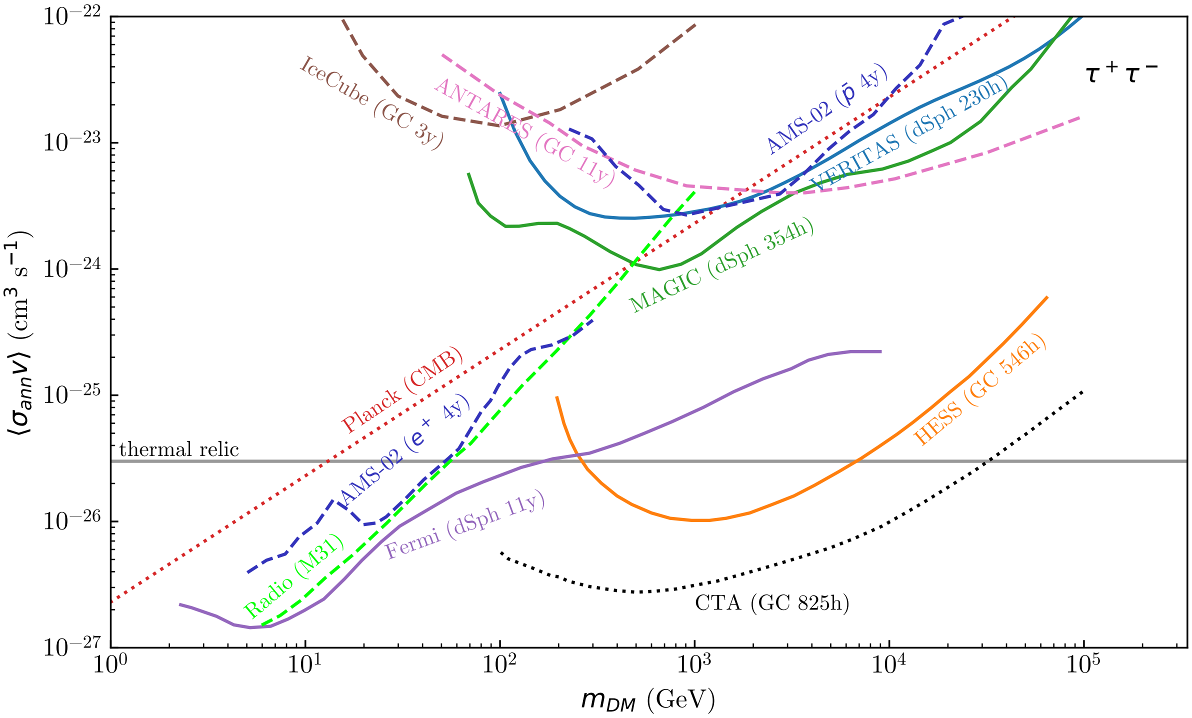

Figure 2: Indirect detection limits (95% confidence) on the thermally-averaged annihilation cross section as a function of dark matter mass, assuming complete annihilation into $\tau^+\tau^-$, from various experiments. Limits are derived from observations of gamma rays by *Fermi*-LAT (Hoof et al., 2020), H.E.S.S. (Abdallah et al., 2016), MAGIC (Acciari et al., 2022), and VERITAS (Archambault et al., 2017), neutrinos by IceCube (Aartsen et al., 2017) and ANTARES (Albert et al., 2020), positrons and antiprotons by AMS-02 (Bergström et al., 2013; Cuoco et al., 2018), the CMB by Planck (Planck Collaboration et al., 2020), and radio emission from M31 with multiple surveys (Egorov & Pierpaoli, 2013). Experiments, targets, and dataset lengths are labeled. The thermal relic cross section (gray) and the expected limits from CTA's GC dataset (black dotted line; Acharyya et al., 2021) are also shown. While thermal relics with $m_{\rm DM} \lesssim 2$ TeV are ruled out in this channel, GeV masses are not ruled out in general (Leane et al., 2018).

and quarks result in hadronization, leading to a broad spectrum of gamma rays produced mainly through neutral pion decays. Additionally, any charged particle can produce photons during propagation, either through inverse Compton scattering, synchrotron radiation, or bremsstrahlung. The gamma-ray spectra in these channels tend to be broad and featureless, however, and modeling the astrophysical backgrounds can be challenging. This can be mitigated somewhat by choosing targets with low predicted astrophysical gamma-ray fluxes, such as dSphs. Annihilation directly to photons, either through $\gamma\gamma$, γZ, or γH end states, is also allowed (though WIMPs couple to photons only through loop diagrams) and would produce a gamma-ray line signal quite distinct from astrophysical background spectra (Bergström et al., 1998; Bringmann & Weniger, 2012). At present, the Large Area Telescope aboard the space-based *Fermi* Gamma-ray Space Telescope (*Fermi*-LAT; Atwood et al., 2009) is the most sensitive observatory of gamma rays with energies $\lesssim$ 100s of GeV, the ground-based imaging atmospheric Cherenkov telescopes (IACTs) VERITAS, H.E.S.S., and MAGIC are most sensitive between ∼50 GeV and ∼50 TeV (Weekes et al., 2002; Hinton & HESS Collaboration, 2004; Aleksić et al., 2016), and HAWC and LHAASO are sensitive at even higher energies (Abeysekara et al., 2013; di Sciascio & LHAASO Collaboration, 2016). Future experiments, such as the Cherenkov Telescope Array (CTA), are expected to significantly improve the sensitivity for dark matter masses between 100 GeV and 50 TeV (Cherenkov Telescope Array Consortium et al., 2019; Acharyya et al., 2021).

Antiprotons are also produced in dark matter annihilation channels where hadronization occurs (Silk & Srednicki, 1984; Stecker et al., 1985), offering a signal complementary to gamma rays. These antiprotons can be measured as a component of the cosmic rays, though directional information of their origin is lost during propagation through the Galaxy. In some channels, antiprotons have led to stronger limits than those set by gamma-ray observations, as shown in Figure 3, which shows $\langle\sigma_{\rm ann}v\rangle$ limits in the $b\bar{b}$ channel. The antiproton spectrum from dark matter is diffuse, with a cutoff around $m_{\rm DM}$ for annihilations or $m_{\rm DM}/2$ for decays. Unfortunately, a comparable astrophysical antiproton background exists, produced predominantly through inelastic collisions between cosmic rays and interstellar gas (Gaisser, 1990). Uncertainties in propagation and other effects can make the dark matter and astrophysical components of the cosmic-ray antiproton spectrum difficult to distinguish. Heavier antinuclei, such as antideuterons, offer orders of magnitude greater separation between signal and background, but have weaker signals (Donato et al., 2000). Recent measurements of the antiproton spectrum have come from BESS-Polar II, PAMELA, and AMS-02 (Abe et al., 2012; Adriani et al., 2013; Aguilar et al., 2016). The future GAPS experiment will measure the low-energy antiproton spectrum with greater precision, and will search for antideuterons with significantly improved sensitivity (Aramaki et al., 2014, 2016a).

Though not explored in this work, other end states of interest include positrons, neutrinos, and radio waves. Positrons are particularly important for searches considering annihilation to e^+e^- and $\mu^+\mu^-$, while also being produced abundantly in hadronic channels, mainly through π^+ decays (Bergström et al., 2013; Mazziotta et al., 2018). Measurements of neutrino fluxes provide complementary limits in many channels, and are necessary to probe the $\nu\bar{\nu}$ channel (Beacom et al., 2007; El Aisati et al., 2017; Blennow et al., 2019). Radio emission from various targets can produce limits comparable to those from gamma rays in most channels, though such limits are subject to uncertainties in magnetic fields and cosmic-ray diffusion (Egorov & Pierpaoli, 2013; Storm et al., 2013; Chan et al., 2019). Another important constraint on $\langle\sigma_{\mathrm{ann}}v\rangle$ comes from measurements of CMB anisotropies, which are sensitive to energy injection by dark matter annihilations (Planck Collaboration et al., 2020).

Several indirect detection experiments have already revealed excesses that may have dark matter origins (Leane et al., 2022). *Fermi*-LAT has revealed an excess from the GC peaking at a few GeV (Goodenough & Hooper, 2009; Hooper & Goodenough, 2011; Ajello et al., 2016; Ackermann et al., 2017). In addition to a dark matter interpretation, this "GC excess" may be explained by a combination of point sources (Abazajian, 2011; Abazajian & Kaplinghat, 2012; Bartels et al., 2016; Lee et al., 2016; Macias et al., 2018) and cosmic rays (Hooper & Linden, 2011; Carlson & Profumo, 2014; Petrović et al., 2014; Cholis et al., 2015; Gaggero et al., 2015). The cosmic-ray antiproton spectrum also may exhibit an excess ~10 GeV (Cuoco et al., 2017; Cui et al., 2017). Interestingly, dark matter interpretations for the possible antiproton excess exist that are compatible with both the antiproton and GC excesses (Cuoco et al., 2019; Cholis et al., 2019). However, uncertainties in the background antiproton spectrum combined with uncertainties in the error covariances of the data make the existence of the possible antiproton excess difficult to evaluate (Boudaud et al., 2020;

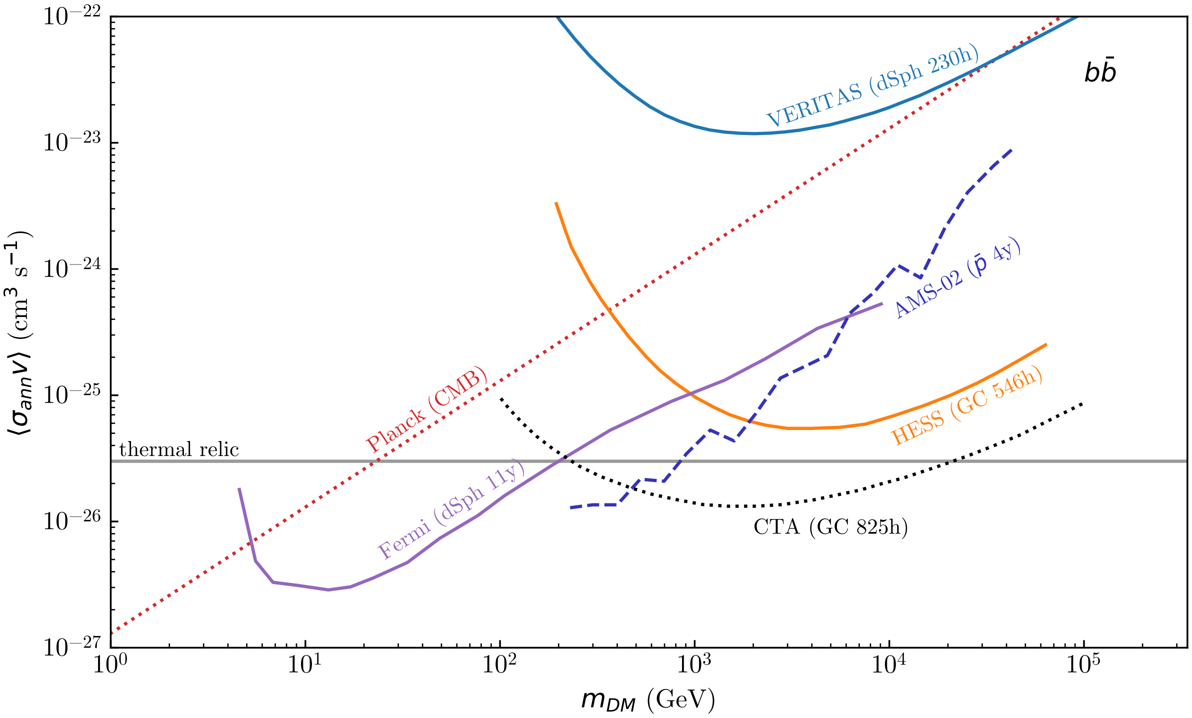

Figure 3: Indirect detection limits (95% confidence) on the thermally-averaged annihilation cross section as a function of dark matter mass, assuming complete annihilation into $b\bar{b}$. Limits are derived from observations of gamma rays by *Fermi*-LAT (Hoof et al., 2020), H.E.S.S. (Abdallah et al., 2016), and VERITAS Archambault et al. (2017), antiprotons by AMS-02 (Cuoco et al., 2018), and the CMB by Planck (Planck Collaboration et al., 2020). Experiments, targets, and dataset lengths are labeled. The thermal relic cross section (gray) and the expected limits from CTA's GC dataset (black dotted line; Acharyya et al., 2021) are also shown. The antiproton limits (black solid line) in this channel are stronger than in the $\tau^+\tau^-$ channel shown in Figure 2.

Heisig et al., 2020). A positron excess in the form of a hardening above ∼10 GeV has been measured by PAMELA (Adriani et al., 2009, 2013), *Fermi*-LAT (Ackermann et al., 2012), and AMS-02 (Aguilar et al., 2013, 2019). While a dark matter interpretation is possible, reacceleration of the positrons produced in cosmic-ray spallations in supernova remnants (Blasi, 2009; Mertsch & Sarkar, 2014) and production of electron-positron pairs by pulsars (Yüksel et al., 2009; Hooper et al., 2017) present alternative explanations. Anomalous X-ray lines have also been detected at 3.5 keV by XMM-Newton (Bulbul et al., 2014; Boyarsky et al., 2014) and 511 keV by several instruments (Leventhal et al., 1978; Purcell et al.,

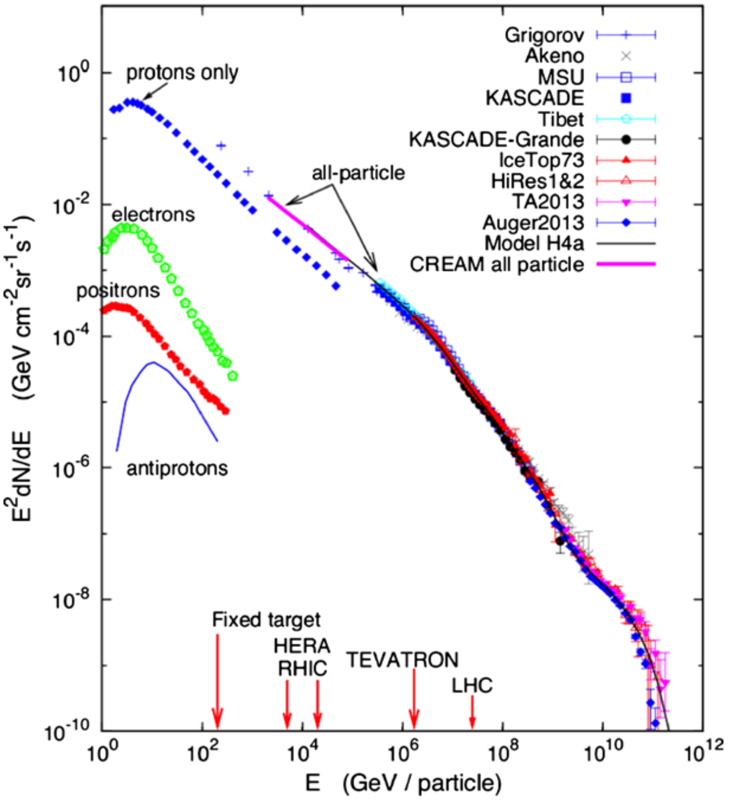

Figure 4: Cosmic ray fluxes at the top of the atmosphere for protons, antiprotons, electrons, positrons, and the all-particle spectrum, measured by various experiments. Fluxes have been scaled by energy squared to highlight spectral features. Figure from Blasi (2013).

1997; Jean et al., 2003; Knödlseder et al., 2005), with potential dark matter interpretations (e.g. Finkbeiner & Weiner, 2016). Increasingly sensitive indirect detection experiments may elucidate these excesses, while also exploring new parameter space.

1.4 Cosmic Rays

Cosmic rays (CRs) are charged particles characterized by high energies that arrive nearly isotropically at Earth. Since their discovery by Hess (1912), CRs have been the subject of much observational and theoretical work, and a general paradigm of CRs has emerged (Blasi, 2013). However, questions of the CR sources, acceleration, and propagation remain.

CRs are mostly protons, and they also include heavier nuclei, antinuclei, electrons, and positrons. Fluxes of different CR species at the top of the Earth's atmosphere are shown in Figure 4. The "all-particle" combined flux of CR nuclei extends from $\sim$0.1 GeV to 10^{12} GeV, and it is well-described by a power law $\propto E^{-2.7}$ between a few GeV and $\sim 10^5$ TeV (Particle Data Group et al., 2020). The all-particle spectrum exhibits several deviations from a pure power law outside this range, including flattening below $\sim$10 GeV, a softening at the "knee" $\sim 10^{6.5}$ GeV, a hardening at the "ankle" $\sim 10^{10}$ GeV, and a cutoff at $\sim 4 \times 10^{10}$ GeV (e.g. Kachelrieß & Semikoz, 2019; Particle Data Group et al., 2020; Becker Tjus & Merten, 2020). The flattening at low energies can be attributed to solar modulation (Gleeson & Axford, 1968). The physical origin of the knee is less certain, and may reflect the maximal energy reached by a population of Galactic CR accelerators or be due to propagation effects (Hörandel, 2004; Kachelrieß & Semikoz, 2019)—many of these models result in a rigidity-dependent series of knees, or "Peters cycle" (Peters, 1961). The ankle may indicate a transition where the CR flux from extragalactic sources (e.g. gamma-ray bursts, active galactic nuclei, galaxy clusters; Becker Tjus & Merten, 2020) begins to exceed the Galactic component. This cutoff is consistent with the predicted GZK cutoff (Greisen, 1966; Zatsepin & Kuz'min, 1966), above which the proton flux attenuates due to interactions with the CMB producing pions, but may also represent a maximum energy to which CRs are accelerated.

The relative elemental abundances of CR nuclei are shown in Figure 5, along with solar abundances derived from observations of our Sun, samples from nearby rocky astronomical bodies, and interstellar gas (Simpson, 1983). For most elements, the CR abundances trace the solar values, though elements like lithium, beryllium, and boron are found to be far more abundant in the cosmic rays. These discrepancies reflect differences in the origins of those species. "Primary" cosmic rays are those accelerated to cosmic ray energies at their sources, and make up the bulk of CRs for elements produced in stellar nucleosynthesis. A population of "secondary" cosmic rays is produced in spallation processes between primaries and gas in the interstellar medium (ISM), where collisions cause the nuclei to fragment into lighter ones. The peak of the antiproton spectrum around 2 GeV and sharp falloff at lower energies suggest that the antiprotons are predominantly secondary, based on the kinematics

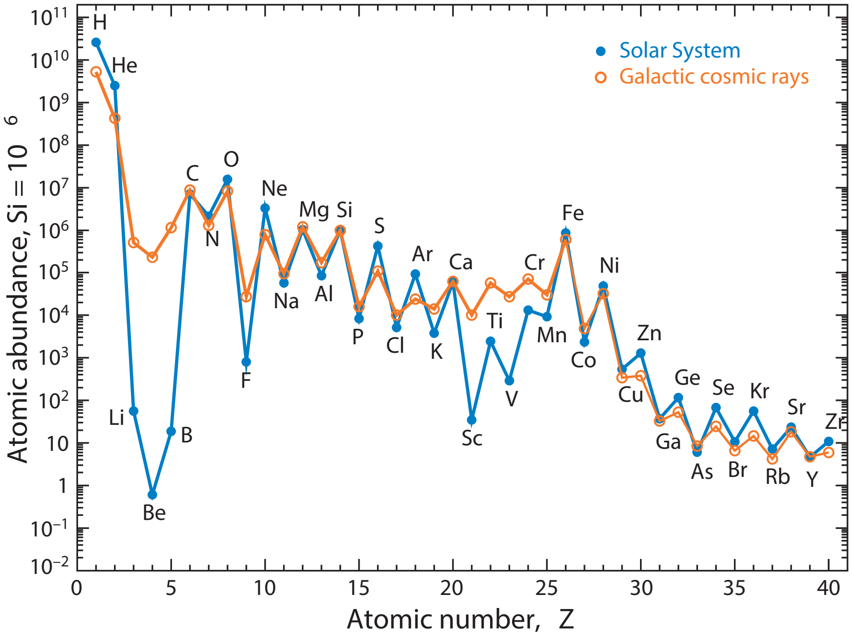

Figure 5: Cosmic ray elemental abundances (orange) compared with solar abundances (blue). Abundances are relative, normalized such that the silicon abundance is 10^6. Figure from Tatischeff & Gabici (2018).

of antiproton production (Gabici et al., 2019). Positrons are also expected to be mostly secondaries, produced through charged pion decays, though the positron excess complicates this picture (Serpico, 2012).

The primary CRs are believed to be produced predominantly in supernova remnant (SNR) shocks within our Galaxy (Blasi, 2013; Gabici et al., 2019). A supernova origin was first put forward based on the energetics matching those of CRs, supposing extragalactic supernova (Baade & Zwicky, 1934), and later, Galactic ones were hypothesized (Hayakawa et al., 1958; Ginzburg, 1953, 1956). Subsequently, evidence for this theory has come from detection of gamma rays from SNRs, consistent with a signal from pions produced by CR protons (Blasi, 2013). The CRs are accelerated through diffusive shock acceleration (DSA), which can produce a power-law CR spectrum with the observed spectral index (Krymskii, 1977; Axford et al., 1977; Bell, 1978a,b; Blandford & Ostriker, 1978). Unlike second-order Fermi acceleration, which considers reflections off of clouds of plasma (Fermi, 1949) or hydromagnetic waves (Fermi, 1954), DSA is first-order in velocity (of the plasma), and can accelerate CRs up to ∼100 TeV (Gaisser, 1990). Many features that challenge this "SNR paradigm" are known to exist, however, and alternative sites of CR acceleration have been proposed, including the GC, pulsar wind nebulae (PWNe), X-ray binaries, and stellar winds (Gabici et al., 2019). In particular, SNR observations have not revealed acceleration of CRs to PeV energies and theoretical challenges for SNRs exist in reaching energies above ∼10 TeV (Lagage & Cesarsky, 1983), even when considering mechanisms such as Bell's instability (Bell, 2004; Gabici et al., 2016; Becker Tjus & Merten, 2020; Cristofari, 2021).

Stable neutral particles produced in association with accelerated CRs, such as gamma rays and neutrinos, offer a way of observing CRs accelerating at their sources (e.g. Gaisser, 1990; Longair, 2011). In hadronic scenarios, gamma rays are produced through neutral pion decays, while charged pion decay products include neutrinos. In leptonic scenarios, electrons and positrons emit photons through synchrotron radiation, bremsstrahlung, and inverse Compton scattering. For inverse Compton scattering, common scenarios for the source photons are synchrotron self-Compton, where the photons are synchrotron radiation produced by the same electron/positron population, and external Compton, where the photons come from elsewhere.

After accelerating at their sources, CRs propagate through the Galaxy. Propagation significantly affects the CR flux at Earth, and it can be separated into three distinct regimes: Galactic propagation, solar modulation, and atmospheric propagation. During Galactic propagation, CRs are subject to random scattering by small magnetic field inhomogeneities in the ISM, resulting in diffusion, and destruction via spallation or decay is also possible (Longair, 2011). Based on secondary-to-primary ratios (e.g. B/C), and isotopic fractions of radioactive isotopes (e.g. Be^{10}/Be), the escape time of CRs is found to be ∼10 Myr, spending only ∼1 Myr in the Galactic disk, and the rest of the time in the lower-density Galactic halo (Gabici et al., 2019).

Galactic propagation of CRs can be described by the equation (Strong et al., 2007)

$$\frac{\partial \psi}{\partial t} = q + \vec{\nabla} \cdot (D_{xx} \vec{\nabla} \psi - \vec{V} \psi) + \frac{\partial}{\partial p} p^2 D_{pp} \frac{\partial}{\partial p} \frac{1}{p^2} \psi - \frac{\partial}{\partial p} \left(\frac{dp}{dt} \psi - \frac{p}{3} (\vec{\nabla} \cdot \vec{V}) \psi \right) - \frac{1}{\tau_f} \psi - \frac{1}{\tau_r} \psi \quad (11)$$

ψ is some CR species' number density per unit momentum p; it is a function of p, time t, and location in the Galaxy. The source term q describes the number of CRs being created per unit time, volume, and momentum. D_{xx} and D_{pp} are the spatial and momentum diffusion coefficients, and the terms they appear in correspond to spatial and momentum diffusion. $\vec{V}$ is the convection velocity, including contributions from Alfvén waves and outflows, with $\vec{\nabla} \cdot \vec{V} \psi$ describing convection. Changes in energy, e.g. to ionization losses, are included in the dp/dt term, while $\frac{\partial}{\partial p}(\frac{p}{3} \vec{\nabla} \cdot \vec{V} \psi)$ corresponds to adiabatic processes resulting from changes in the convection speed with location. τ_f and τ_r are the timescales for fragmentation and radioactive decay, respectively, and hence they appear in the relevant sink terms. The flux Φ (with dimensions of area^{-2} time^{-1}) is related to ψ by

$$\frac{d^2 \Phi}{dp d\Omega} = \frac{v}{4\pi} \psi \quad (12)$$

where Ω is solid angle and v is the particle velocity. Galactic propagation calculations will describe the local interstellar spectra of CRs. Local interstellar spectra have been measured beyond the heliopause by the Voyager probes (Stone et al., 2013; Krimigis et al., 2013; Stone et al., 2019; Krimigis et al., 2019).

The calculation of CR fluxes at the top of the Earth's atmosphere requires taking into account the effects of the Sun, often called "solar modulation." The clearest evidence that such an effect exists is the observation of periodic changes in the top-of-atmosphere CR spectra correlated with the 11-year solar cycle. Broadly speaking, CRs are decelerated by the outgoing, magnetized solar wind and are subject to additional scattering by the wind's magnetic irregularities (Longair, 2011; Potgieter, 2013). This effect is described by the Parker equation (Parker, 1965), which can be written (Boschini et al., 2018)

$$\frac{\partial f}{\partial t} = -\vec{\nabla} \cdot (f\vec{V}) + \nabla \cdot (K^S \cdot \vec{\nabla} f) + \frac{1}{3p^2}\vec{\nabla} \cdot \vec{V}_{\mathrm{sw}} \frac{\partial}{\partial p}(p^3 f) \tag{13}$$

The CR distribution function f is a function of time, position, and momentum. The first term on the right describes convection, with $\vec{V} = \vec{V}_{\mathrm{sw}} + \vec{V}_{\mathrm{drift}}$ representing the sum of the solar wind velocity $\vec{V}_{\mathrm{sw}}$ and drift velocity $\vec{V}_{\mathrm{drift}}$ induced by the heliosphere magnetic field. The second term represents diffusion, with K^S being the symmetric part of the diffusion tensor. The third term represents adiabatic CR energy changes. As previously mentioned, solar modulation is felt most strongly by CRs with masses $\lesssim 10$ GeV, while being negligible at the highest energies.

Lastly, propagation through the atmosphere to a detector must be considered for non-space-based experiments, to convert between top-of-atmosphere and top-of-instrument fluxes. The geomagnetic field, parameterized by a geomagnetic cutoff rigidity, attenuates CRs (Smart & Shea, 2005). At small atmospheric depths of a few g/cm^2, CRs experience energy losses and attenuation through nuclear interactions, which may produce an additional background of CRs that must be subtracted (Papini et al., 1996; Duperray et al., 2005). CRs may be numerically backtraced to estimate such effects (Desorgher et al., 2006; von Doetinchem, 2009; Aramaki et al., 2016b).

High energy CRs will also produce cascades of particles known as "air showers" detectable at the Earth's surface (Greisen, 1960; Gaisser, 1990; Longair, 2011). A cosmic ray colliding with another nucleus in the atmosphere will create lower-energy nucleons and pions, which will repeat the process until energies drop below ~1 GeV. Neutral pions quickly (1.78×10^{-16} s) decay into two gamma rays, which also initiate electromagnetic cascades. Charged pions can decay into muons, which are detected at the Earth's surface at a rate of ~1 cm^{-2} min^{-1} (Particle Data Group et al., 2020). Through repeated interactions, the bulk of the shower energy ends up in photons, electrons, and positrons.

1.5 The Galactic Center

The Milky Way's dark matter halo density is expected to peak at the Galactic Center (GC), the dynamical center of the Milky Way. Consequently, observations of this region have resulted in some of the strongest dark matter constraints to date (e.g. Abdallah et al., 2016). The GC is also the location towards which the eponymous GC excess is observed. However, the many sources of high-energy particles near the GC complicate dark matter searches and interpretations of the gamma-ray emission in particular. The inner few degrees (hundreds of parsecs) around the GC will be considered here.

The average J-factor within a degree of the GC is predicted to be $\sim 10^{22} - 10^{25}$ GeV^2 cm^{-5} (Cirelli et al., 2011; van Eldik, 2015; Abdallah et al., 2016; Acharyya et al., 2021). In comparison, the largest J-factors for dwarf spheroidal galaxies are $\sim 10^{19}$ GeV^2 cm^{-5} (e.g. Geringer-Sameth et al., 2015; Archambault et al., 2017). J-factor calculations are subject to uncertainties in the dark matter halo density profile, such as whether the profile is cusped or cored at small radii.

The GC also hosts numerous sources of high-energy particles, many of which are visible at radio wavelengths, as shown in Figure 6 Most prominent is the radio source Sagittarius A* (Sgr A*), spatially coincident with the supermassive ($\sim 10^6 M_\odot$; Ghez et al., 2008; Genzel et al., 2010; Boehle et al., 2016) black hole located at a distance from Earth of ∼8 kpc (Boehle et al., 2016; Gravity Collaboration et al., 2019). Other sources visible in the radio include SNRs, PWNe, radio filaments, HII regions, and massive star clusters.

Another important feature is the dense region of molecular gas within a Galactocentric radius ∼200 pc, called the "central molecular zone" (CMZ; Morris & Serabyn, 1996). The region is characterized by densities, temperatures, turbulent velocities, and cosmic-ray densities orders of magnitude higher (on average) than elsewhere in the Galactic disk (Henshaw et al., 2022). While studies of the CMZ often focus on star and planet formation or conditions near galactic nuclei (Mills, 2017; Bryant & Krabbe, 2021; Henshaw et al., 2022), the gas distribution and magnetic field also have important consequences for CR propagation

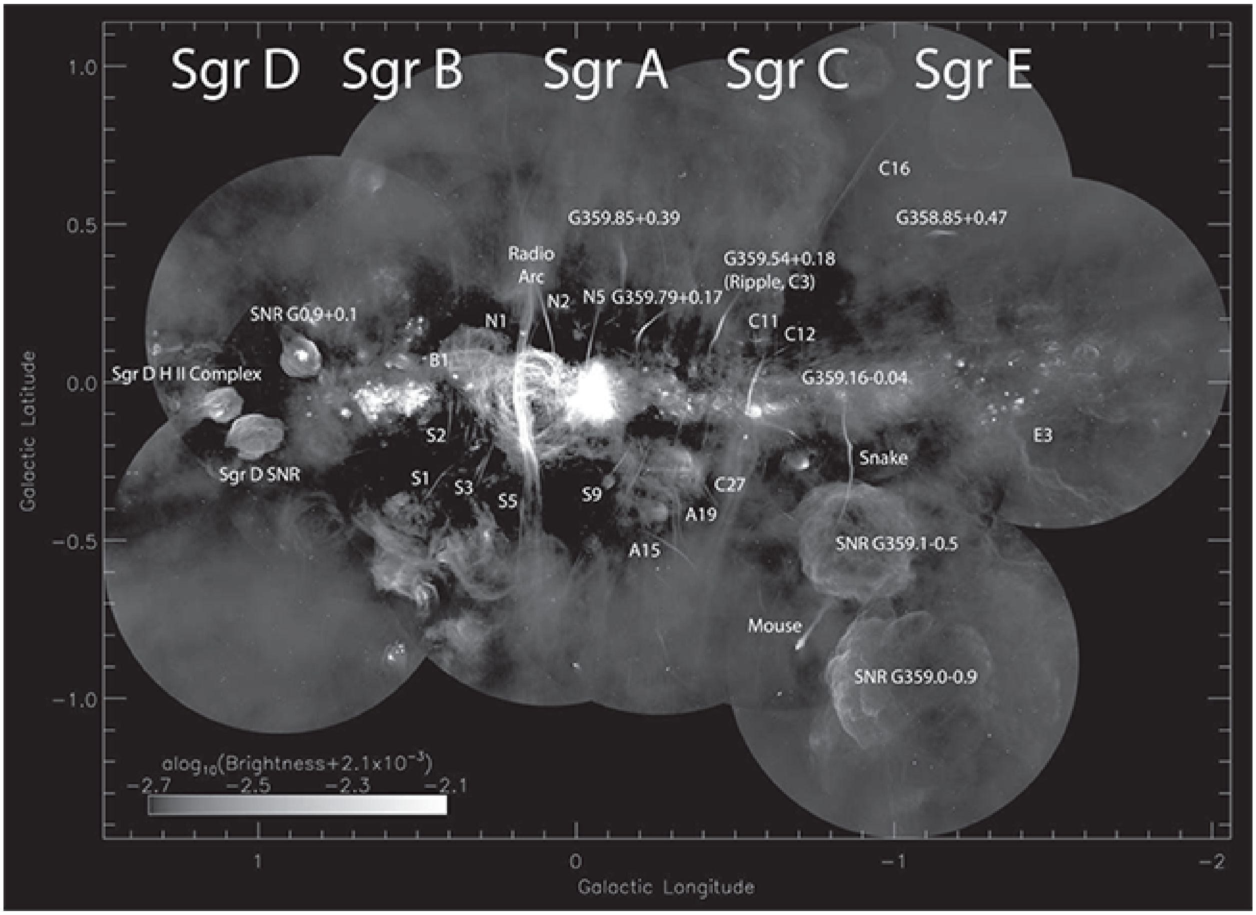

Figure 6: Flux map of the inner ∼3.5° × 2.5° around the Galactic Center measured by MeerKAT at 1.28 GHz. Resolution is 6.4″. A variety of sources with diverse morphologies can be observed. Figure from Yusef-Zadeh et al. (2022).

and, through CR interactions with the gas, gamma-ray emission (e.g. Crocker et al., 2011; Yusef-Zadeh et al., 2013; Gaggero et al., 2017; Guenduez et al., 2020). Observations at numerous different wavelengths trace the two-dimensional (2D) distribution of gas, with additional line-of-sight velocity information from emission line measurements (e.g. Oka et al., 1998; Dahmen et al., 1998; Tsuboi et al., 1999; Jones et al., 2012, 2013; Molinari et al., 2011; Langer et al., 2017; Krieger et al., 2017). Such observations reveal asymmetry about the GC, with about three quarters of the gas at positive Galactic longitudes (Bally et al., 1988; Morris & Serabyn, 1996), and a total molecular gas mass of a few times $10^7\ M_\odot$ (e.g. Dahmen et al., 1998; Tsuboi et al., 1999; Ferrière et al., 2007). Neutral atomic hydrogen HI and ionized hydrogen H^+ are also present in the CMZ, with total masses ∼10% and

$\sim$5% that of H_2, respectively (Ferrière et al., 2007). Major components of three-dimensional (3D) descriptions of the CMZ (e.g. Morris & Serabyn, 1996; Guenduez et al., 2020; Henshaw et al., 2022) include an outer ring-like structure at Galactocentric radius $\sim$200 pc (possibly an "expanding molecular ring" or dust lanes; Kaifu et al., 1972; Scoville, 1972; Binney et al., 1991; Oka & Geballe, 2020; Henshaw et al., 2022), an inner ring-like structure at $\sim$100 pc containing many of the densest molecular clouds (Molinari et al., 2011; Kruijssen et al., 2015), and the "circumnuclear disk" in the inner $\lesssim 7$ pc (Becklin et al., 1982; Genzel & Townes, 1987). However, the 3D CMZ geometry remains uncertain—in addition to lacking a simple way to derive distances along our line-of-sight, complications arise when inferring the total mass (mainly in H_2) from individual wavelength observations.

Interactions of CRs with interstellar gas and radiation fields are responsible for the bulk of the $\sim$GeV gamma-ray emission around the GC (Ong, 1998; Murgia, 2020). Figure 7 shows the bright, diffuse gamma-ray emission observed from the Galactic plane, as well as emission from point sources which include SNRs, PWNe, star-forming regions, X-ray binaries, and radio filaments (van Eldik, 2015). The residual map in the right panel of Figure 7 reveals additional emission, which Ackermann et al. (2017) attribute to inverse Compton scattering of leptonic CRs and low-energy photons, Loop I (Large et al., 1962; Casandjian & Grenier, 2009), the "*Fermi* bubbles" (Su et al., 2010; Ackermann et al., 2014), and other extended sources, including the GC excess.

The GC excess is the component of gamma-ray emission from the GC that remains after modeling all known astrophysical sources. The excess peaks around 1–3 GeV, and has a spatial extent $\sim$10–15° (Murgia, 2020). As mentioned in Section 1.3, possible explanations include annihilating dark matter, a new population of point sources (usually millisecond pulsars), and both transient and steady-state CR scenarios. Greater accuracy in the modeling of the astrophysical emission, as well as the related tasks of characterizing the spatial and spectral morphology of the GC excess, are necessary to firmly establish a physical origin (e.g. Leane et al., 2022).

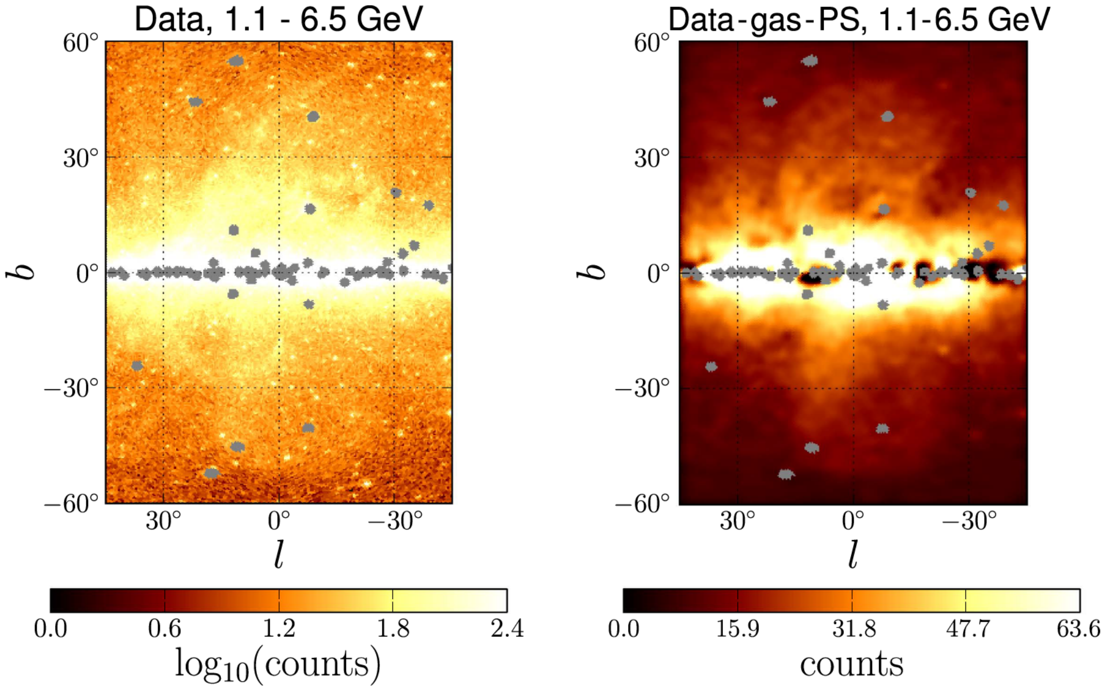

Figure 7: Gamma-ray flux map centered on the GC by *Fermi*-LAT (left), and residuals after subtracting gas-correlated components and point sources (right). Pixel size is 0.46°. Gray regions are 1° radius masks around the 200 brightest *Fermi*-LAT sources. Figure adapted from Ackermann et al. (2017).

TeV observations also provide an important avenue toward understanding the high-energy processes and potential dark matter signal in the GC. The TeV emission, first detected from the direction of Sgr A* by IACTs (Tsuchiya et al., 2004; Kosack et al., 2004; Aharonian et al., 2004), also includes point sources and diffuse emission extending several degrees along the Galactic plane. Similar to GeV energies, TeV emission might be expected from point source accelerators of CRs (including unresolved populations), interactions of diffuse CRs, the *Fermi* bubbles, and dark matter (e.g. Acharyya et al., 2021). Dark matter analyses of the GC TeV emission have placed some of the most stringent limits on the thermally-averaged annihilation cross section for masses above ∼1 TeV (Abdalla et al., 2022). TeV observations may also have implications for the millisecond pulsar hypothesis if the pulsars have TeV halos (Hooper & Linden, 2018; Guépin et al., 2018; Hooper & Linden, 2022). At the same time, TeV emission from the GC informs our picture of CRs in the region through spectra resulting from CR acceleration at their sources, as well as diffuse emission constraints on models of the ambient CR density and energy spectrum. Reflecting its continuing scientific potential, the GC has been made a key science project for CTA (Cherenkov Telescope Array Consortium et al., 2019).

2 Dark Matter Signals for Indirect Searches

This work covers two indirect searches for dark matter: measurement of cosmic-ray antimatter by GAPS (Section 3), and measurement of gamma rays from the GC with VERITAS (Sections 4 and 5). In order to infer properties of dark matter from flux measurements, the particle fluxes expected from dark matter annihilations or decays must be determined. While such fluxes may be calculated for specific dark matter models (e.g. Bertone et al., 2005, and references therein), we take a model-independent approach where primary channels of dark matter annihilation or decay are examined individually with the corresponding branching fraction taken to be unity. Fluxes will be calculated for antiprotons, antideuterons, and gamma rays. This work will only consider the case of annihilation.

2.1 The Milky Way's Dark Matter Density Profile

While the local dark matter density has been observationally constrained to be ∼0.3–0.6 GeV cm^{-3} (Read, 2014; de Salas & Widmark, 2021), the density profile of the Milky Way's dark matter halo is less well-constrained—particularly the inner few kpc, where both cored and cusped profiles are allowed (e.g. Pato et al., 2015; Iocco & Benito, 2017; Benito et al., 2019; Sofue, 2020). We consider several benchmark models, with the aim of bracketing these uncertainties.

The first model we consider is the NFW profile, given by (Navarro et al., 1996, 1997)

$$\rho(r) = \frac{\rho_0}{(r/r_s)(1+r/r_s)^2} \tag{14}$$

where $\rho(r)$ is the dark matter density at radius r, ρ_0 is a density normalization factor and r_s is a characteristic radius where the density profile steepens from r^{-1} to r^{-3}. The second model is the Einasto profile, given by (Einasto, 1965)

$$\rho(r) = \rho_0 e^{-(2/\alpha)([r/r_s]^{\alpha}-1)} \tag{15}$$

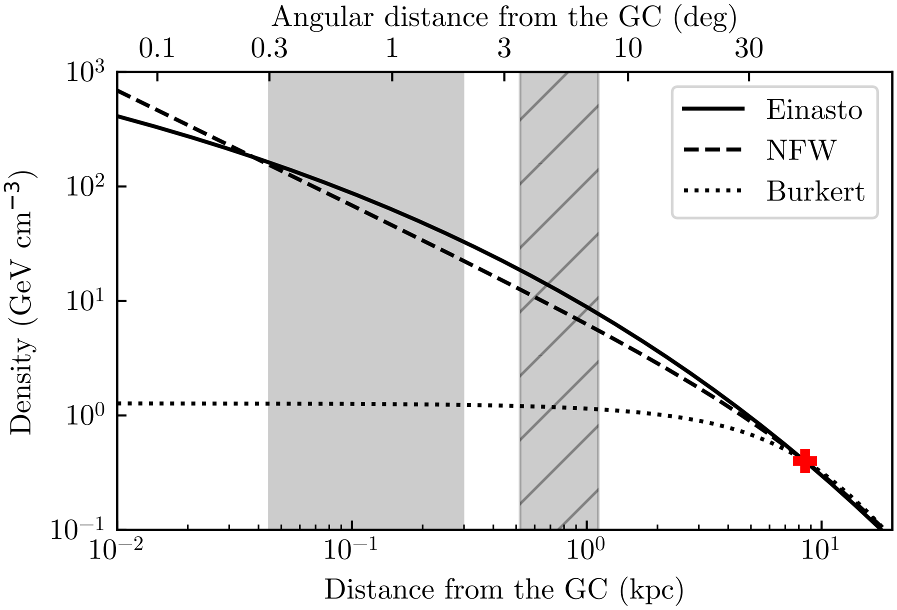

Figure 8: Dark matter density profiles versus distance from the GC, for Einasto (solid line), NFW (dashed line) and Burkert (dotted line) profiles. Shaded regions indicate the ±2° around the Sgr A* (gray, solid) and Sgr A* Off (gray, hatched) pointings discussed in Section 4, omitting the innermost 0.3°. The local dark matter density, to which the profiles are normalized, is indicated by the red cross.

where the additional parameter α influences the profile shape, yielding a cuspy profile for $\alpha < 1$, and a cored profile otherwise. Lastly, the Burkert profile is given by (Burkert, 1995)

$$\rho(r) = \frac{\rho_0 r_s^3}{(r + r_s)(r^2 + r_s^2)} \tag{16}$$

and gives a cored profile with approximately constant density at $r < r_s$.

The NFW and Einasto profiles are motivated by dark matter halo simulations, with the Einasto profile slightly preferred (e.g. Gao et al., 2008; Navarro et al., 2010; Wang et al., 2020), while cored profiles like the Burkert profile are motivated by observations of dwarf galaxies. For the Milky Way, cored and cuspy profiles are both allowed by observations (e.g. Nesti & Salucci, 2013; Bovy & Rix, 2013; Pato et al., 2015; Sofue, 2020).

We adopt parameters close to those used by previous GC gamma-ray dark matter studies (Abramowski et al., 2011; Abdallah et al., 2016; Acharyya et al., 2021; Abdalla et al., 2022) to facilitate comparison, rather than use other potentially more accurate values available in the literature. For the NFW and Einasto profiles, we use $r_s = 20$ kpc (also near to the values of e.g. Pieri et al., 2011; Cirelli et al., 2011) and $\alpha = 0.17$, while for the Burkert profile $r_s = 10$ kpc. The normalizations ρ_0 are chosen such that the local dark matter density is $\rho_\odot = 0.4$ GeV cm^{-3} at a distance of 8.5 kpc from the GC. The profiles, all radially symmetric about the GC, are plotted versus r in Figure 8.

2.2 Cosmic-ray Antinuclei

A variety of physical processes are involved in the determination of cosmic-ray antinuclei fluxes originating from dark matter annihilations (primary) and spallation (secondary). Some of these processes are illustrated in Figure 9 for the case of primary antideuterons. We derive simple estimates of the local interstellar and top-of-atmosphere fluxes for antiprotons and antideuterons, in order to motivate the GAPS experiment, described in Section 3.

2.2.1 Source Terms

We begin with the calculation of the source terms q (Equation 8) that later enter into the propagation equation (Equation 11). A source term describes the production rate of particles with energy E per volume element at some location in the dark matter halo.

For antiprotons, the average number of antiprotons produced per annihilation $dN_{\bar{p}}/dE$ for different annihilation channels is tabulated in Cirelli et al. (2011). These values are derived from Monte Carlo simulations of high-energy particles and they average over the effects of hadronization. For antideuterons, both an antiproton and an antineutron must be produced and subsequently undergo coalescence, forming an antideuteron. While the coalescence mechanism is not well-understood (von Doetinchem et al., 2020), a simple scheme is to assume that any two nucleons whose relative momentum difference is less than some value p_0 coalesce (Schwarzschild & Zupančič, 1963). Under the further assumption that antineutrons and antiprotons have equal production rates and are produced independently

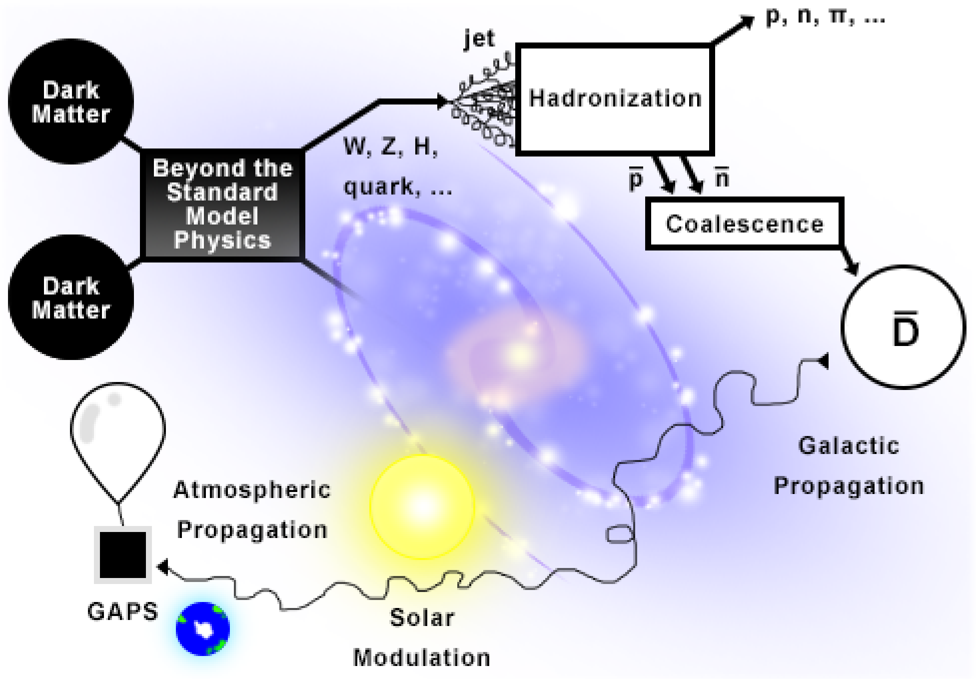

Figure 9: Cartoon illustrating the physical processes involved in determining the flux of primary antideuterons seen by GAPS. After dark matter annihilates (or decays) into SM particles, antideuterons may be produced through hadronization into an antiproton and antineutron and their subsequent coalescence. Antideuterons must then propagate through the Galaxy, heliosphere, and upper atmosphere of Earth before reaching GAPS.

of one another, the differential antideuteron production per annihilation is given by (e.g. Donato et al., 2000; Fornengo et al., 2013)

$$\frac{dN_{\bar{d}}}{dE}(E) = \frac{4}{3}\frac{p_0^3}{8p_{\bar{d}}}\frac{m_{\bar{d}}}{m_{\bar{p}}m_{\bar{n}}}\left(\frac{dN_{\bar{p}}}{dE}(E/2)\right)^2 \tag{17}$$

where $p_{\bar{d}}$ is the antideuteron momentum, and $m_{\bar{d}}$, $m_{\bar{p}}$, and $m_{\bar{n}}$ are the masses of the antideuteron, antiproton, and antineutron, respectively. We use a coalescence momentum of $p_0 = 200$ MeV, reflecting recent measurements (e.g. Acharya et al., 2018) though neglecting possible kinematic dependence. Source terms for antiprotons and antideuterons in the $b\bar{b}$ annihilation channel, for a dark matter particle with the thermal annihilation cross section and mass $m_{\mathrm{DM}} = 50$ GeV, and with $\rho_{\mathrm{DM}} = \rho_\odot$ are shown in Figure 10.

We also estimate source terms for secondary antinuclei for comparison to the primary

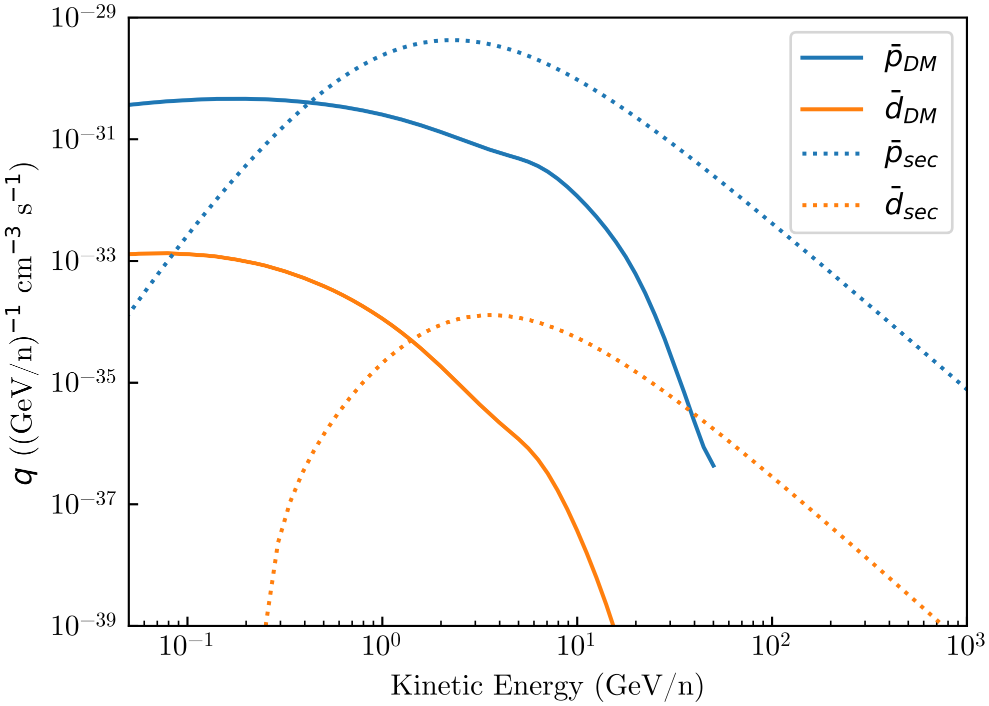

Figure 10: Local source terms from primary antiprotons (solid blue line) and antideuterons (solid orange line), for a dark matter particle with $m_{\mathrm{DM}} = 50$ GeV, annihilating into $b\bar{b}$ with the thermal relic cross section. Other parameters are as stated in the text. Secondary antiprotons (dotted blue line) and antideuterons (dotted orange line) from proton-proton spallations are also shown.

terms, following (Chardonnet et al., 1997). Considering only the contributions of protons in the cosmic rays and ISM, the source term is given by

$$q = 4\pi n_{\mathrm{ISM}} \int_{E_{\mathrm{th}}}^{\infty} dE \frac{d\Phi_{\mathrm{CR}}}{dE} \frac{d\sigma}{dE} \tag{18}$$

where n_{ISM} is the number density of protons in the ISM, the integral is performed over the CR energy, E_{th} is the energy threshold for secondary production, $d\Phi_{\mathrm{CR}}/dE$ is the interstellar CR differential flux, and $d\sigma/dE$ is the differential cross section for secondary production, with dependence on both the antinucleus and CR energies.

The minimum energy required to produce an antiproton is $E_{\mathrm{th}} = 7m_p$, which can be quickly shown using the invariance of the four-momentum inner product.[3] For an incoming cosmic-ray proton with energy $E_{\rm CR}$ and momentum $p_{\rm CR}$ in the ISM frame,

$$\left(\frac{E_{\rm CR}+m_pc^2}{c}\right)^2 - p_{\rm CR}^2 = \left(\frac{E_{\rm CM}}{c}\right)^2 \tag{19}$$

where $E_{\rm CM}$ is the total energy in the center-of-momentum frame. Since baryon number is conserved, the antiproton must be accompanied by three protons, so the minimum total energy in the center-of-momentum frame is $E_{\rm CM} = 4m_pc^2$. Substituting and solving gives $E_{\rm th} = 7m_p$ for antiproton production, while similar calculations give $17m_p$ for an antideuteron and $31m_p$ for antihelium-3.

We use the CR proton spectrum parametrization (Bottino et al., 1998; Donato et al., 2000)

$$\frac{d\Phi_{\rm CR}}{dE} = 1.595\beta(E/{\rm GeV})^{-2.76} \tag{20}$$

where β is the particle velocity divided by the speed of light c. This simple form agrees with more recent determinations (e.g. Boschini et al., 2020; Kachelrieß et al., 2020) to within ~20% over most of the energy range relevant for antiproton and antideuteron production.

We derive $d\sigma/dE$ from the Lorentz-invariant differential cross section $Ed^3\sigma/dp^3$ with

$$\frac{d\sigma}{dE} = 2\pi pc^2 \int_0^{\theta_{\rm max}} d\theta \sin\theta E\frac{d^3\sigma}{dp^3} \tag{21}$$

where p is the antiparticle momentum, θ is the angle between the antiparticle and incident CR momenta in the lab frame, and $\theta_{\rm max}$ is the maximal kinematically-allowed value of θ. The necessary kinematic variables for this calculation have been derived elsewhere (e.g. di Mauro et al., 2014; Donato et al., 2017). For antiprotons produced by proton-proton collisions, we use $Ed^3\sigma_{\bar{p}}/dp^3$ as parameterized by Tan & Ng (1982). For antideuterons, we can approximate

---

[3] This is Example 3.4 in Griffiths (2008).

the Lorentz-invariant differential cross section with (e.g. Donato et al., 2008)

$$E\frac{d^3\sigma_{\bar{d}}}{dp^3}(p_{\bar{d}}) = \frac{1}{\sigma_{pp}}\frac{4\pi}{3}\frac{p_0^3}{c^2}\frac{m_{\bar{d}}}{m_{\bar{p}}m_{\bar{n}}}\left(E\frac{d^3\sigma_{\bar{p}}}{dp^3}(p_{\bar{d}}/2)\right)^2 \tag{22}$$

where $p_{\bar{d}}$ is the antideuteron momentum and σ_{pp} is the total proton-proton cross section. We use the COMPETE HPR$_1$R$_2$ model of σ_{pp} (Cudell et al., 2002) with parameters as given in Particle Data Group et al. (2020), which yields $\sigma_{pp} \approx 40$ mb for a 10 GeV incident proton.

2.2.2 Fluxes

We next solve the CR propagation equation to estimate local insterstellar fluxes, evaluated just outside of the heliosphere. We use the two-zone diffusion model (Donato et al., 2000, 2001; Maurin et al., 2001) with a simplified version of Equation 11 that considers only source terms, diffusion, convection, and spallation processes, ignoring effects such as convection and reacceleration (e.g. Webber et al., 1992)

$$\frac{\partial\psi}{\partial t} = q + D_{xx}\nabla^2\psi - V_{\mathrm{c}}\frac{\partial}{\partial z}\psi - \frac{1}{\tau_f}\psi \tag{23}$$

We use the MED parameters of Donato et al. (2004), where the diffusion coefficient is parameterized with

$$D_{xx} = K_0\beta(R/1\ \mathrm{GV})^{\delta} \tag{24}$$

The sink term is given by $\tau_f^{-1} = n_{\mathrm{ISM}}\sigma_{\bar{p}p,\mathrm{inel}}v$ for antiprotons and $\tau_f^{-1} = n_{\mathrm{ISM}}\sigma_{\bar{d}p,\mathrm{inel}}v$ for antideuterons. The inelastic proton-antiproton cross section is found using the values in Particle Data Group et al. (2020) with

$$\sigma_{\bar{p}p,\mathrm{inel}} = \sigma_{\bar{p}p,\mathrm{tot}} - \sigma_{\bar{p}p,\mathrm{el}} \tag{25}$$

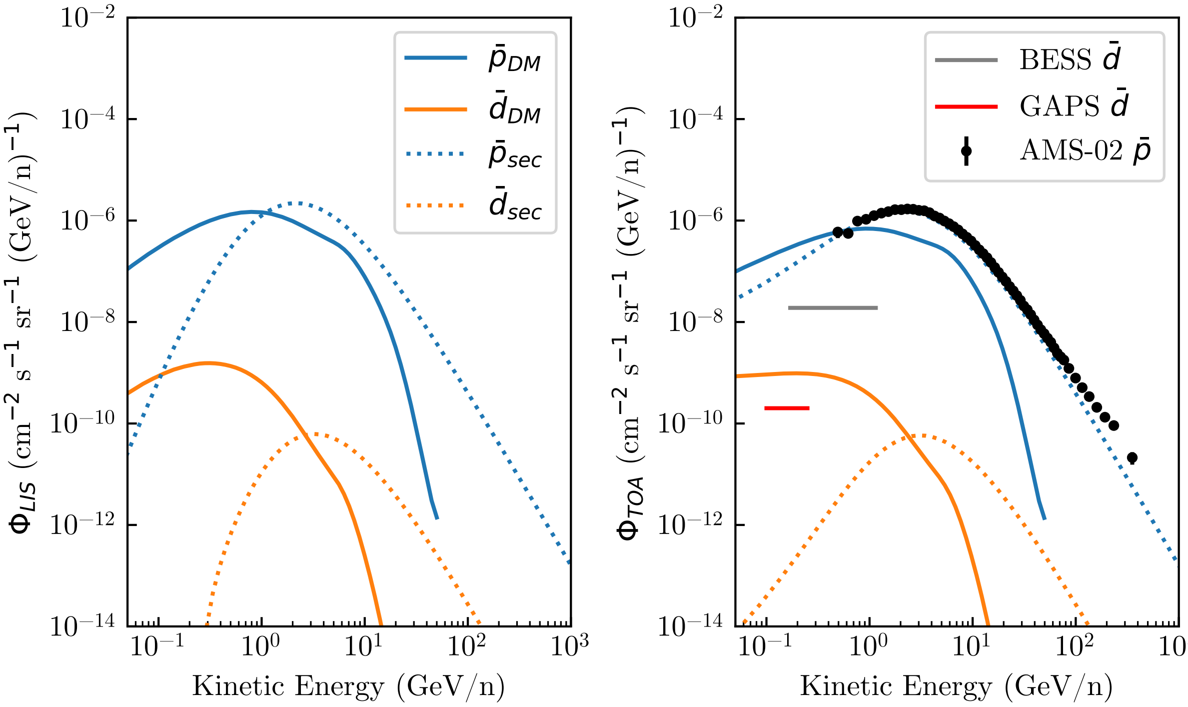

Figure 11: Local interstellar (left) and top-of-atmosphere (right) fluxes for primary antiprotons (solid blue line) and antideuterons (solid orange line), for a dark matter particle with $m_{\mathrm{DM}} = 50$ GeV, annihilating into $b\bar{b}$ with the thermal relic cross section. Other parameters are as stated in the text. Secondary antiprotons (dotted blue line) and antideuterons (dotted orange line) from proton-proton spallations are also shown. The secondary antiproton top-of-atmosphere flux resembles the AMS-02 measurements (black; Aguilar et al., 2016). Also indicated are the 95% confidence level upper limit by BESS (gray; Fuke et al., 2005) and estimated GAPS sensitivity (red; Aramaki et al., 2016a).

and approximating the inelastic antideuteron-proton cross section as (e.g. Korsmeier et al., 2018)

$$\sigma_{\bar{d}p,\mathrm{inel}} = \frac{\sigma_{\bar{p}p,\mathrm{inel}}}{\sigma_{\bar{p}p,\mathrm{tot}}} \sigma_{\bar{p}d,\mathrm{tot}} \tag{26}$$

The dark matter halo is assumed to follow an Einasto profile. We use the analytical Bessel function form of the diffusion equation's solution (e.g. Donato et al., 2001; Barrau et al., 2002; Korsmeier et al., 2018). Local insterstellar fluxes Φ_{LIS} are then calculated with Equation 12 and are shown in the left panel of Figure 11.

Finally, we find the fluxes at the top of Earth's atmosphere Φ_{TOA} by incorporating the effects of the solar wind and associated magnetic field. We use the force-field approximation to Equation 13 (Gleeson & Axford, 1968; Fisk, 1976; Perko, 1987)

$$\frac{\Phi_{\mathrm{TOA}}(E)}{E^2 - m^2} = \frac{\Phi_{\mathrm{LIS}}(E + \frac{Ze}{A}\phi)}{(E + \frac{Ze}{A}\phi)^2 - m^2} \tag{27}$$

where E is the total particle energy at the top of the atmosphere, Z is the atomic number, A the atomic mass, e is the elementary charge, and ϕ is the solar modulation potential describing energy loss. Typical values of ϕ fall between ∼300–1000 MV, depending on solar activity (e.g. Caballero-Lopez & Moraal, 2004; Usoskin et al., 2005). Top-of-atmosphere fluxes with $\phi = 500$ MV are shown in the right panel of Figure 11.

As first noted by Donato et al. (2000), the secondary antideuteron top-of-atmosphere flux falls off steeply below a few GeV/nucleon while other, more exotic sources of antideuterons may remain abundant. This is a consequence of the high threshold energy for antideuteron production via spallation, which reduces the number of low-energy antideuterons appearing in the source term. We note that while including effects such as energy losses, reacceleration, interstellar helium, and tertiary production can increase the background flux at low energies, more intricate models also find background antideuteron flux levels to remain at least an order of magnitude below many viable dark matter models at low energies (e.g. Donato et al., 2017; Korsmeier et al., 2018; Cholis et al., 2020). Low-energy antideuterons therefore provide a low-background window for rare event searches for new physics.

2.3 Gamma Rays from the Galactic Center Halo

The gamma-ray flux resulting from dark matter annihilation can be calculated with Equation 4, once $\langle\sigma_{\mathrm{ann}}v\rangle$, m_{DM}, dN/dE, and the J-factor are known. For cuspy dark matter profiles, the lines of sight yielding the highest J-factors point towards the GC, making the region surrounding the GC a promising target for indirect dark matter searches.

We calculate J-factors for different dark matter density profiles according to Equation

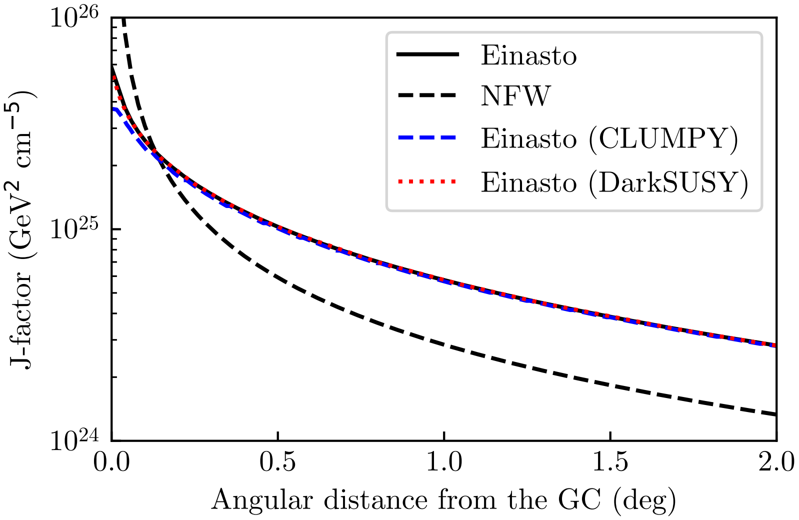

Figure 12: J-factors versus angular distance from the GC, from the Einasto (solid black line) and the NFW (dashed black line) profiles. J-factors for the Einasto profile calculated with numerical codes `CLUMPY` (blue dashed line) and `DarkSUSY` (red dotted line) are also shown. The values calculated with `DarkSUSY` closely match our calculation, while those calculated with `CLUMPY` are ∼10% lower at smaller angular distances.

5 using the values described in Section 2.1, and we plot them versus angular distance from the GC in Figure 12. The J-factors for the Burkert profile are orders of magnitude lower than for the Einasto and NFW profiles in the inner 2° around the GC and are not shown in the figure. Line-of-sight integrals are performed numerically, using 10^5 points equally spaced logarithmically between 10^{-4} and 10^4 kpc. For a line of sight with a given angular distance from the GC, the physical distance from the GC used to calculate the dark matter density is found at each distance along the line of sight using the law of cosines. The average J-factor within each pixel is then calculated under the simplifying assumptions that the sky is locally flat, and the average J-factor in a pixel equals the J-factor at the pixel center. As a cross-check, J-factors for the Einasto profile are also calculated with the numerical codes `CLUMPY` (Charbonnier et al., 2012; Bonnivard et al., 2016; Hütten et al., 2019) version 18.06 and `DarkSUSY` (Gondolo et al., 2004; Bringmann et al., 2018) version 6.3.1, which employ independent integration schemes and handle projection of pixels onto the sky with `HEALPix` (Górski et al., 2005), with resolution parameter $N_{\text{side}} = 4096$. Our J-factors agree with these

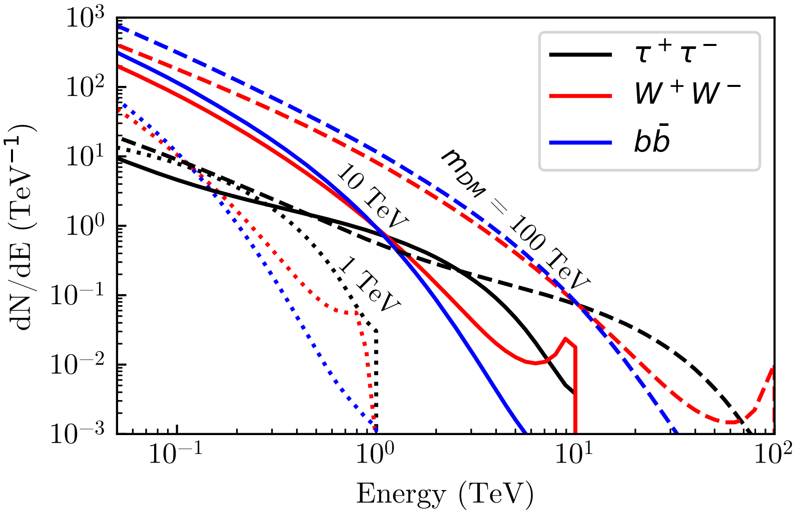

Figure 13: Gamma-ray spectra from single dark matter annihilations from Cirelli et al. (2011). Spectra are shown for annihilation into $\tau^+\tau^-$ (black), W^+W^- (red), and $b\bar{b}$ (blue), assuming $m_{\rm DM} = 1$ TeV (dotted lines), $m_{\rm DM} = 10$ TeV (solid lines), and $m_{\rm DM} = 100$ TeV (dashed line).

codes to $\lesssim$1% accuracy at angular distances >0.3°, so we proceed using our calculations in the analysis. At smaller angular distances, we note that the J-factors we calculate with `CLUMPY` are ∼10% lower than the values from `DarkSUSY` and our calculation, similar to what is observed by Acharyya et al. (2021).

The gamma-ray spectrum dN/dE may be determined for a given $m_{\rm DM}$ and annihilation channel. We use the spectra from Cirelli et al. (2011), who calculate the prompt gamma-ray emission for all annihilation channels for masses between 5 GeV and 100 TeV. Several spectra are shown in Figure 13. These calculations are used in Section 5, where $\langle\sigma_{\rm ann}v\rangle$ is left as a free parameter to be measured.

3 Preparations for the GAPS Experiment

This section will outline work on the forthcoming General AntiParticle Spectrometer (GAPS) experiment, focusing on its time-of-flight (TOF) system. GAPS will search for as yet undetected primary cosmic-ray antimatter that would be a sign of new physics, such as dark matter. After giving an overview of the GAPS mission, aspects of the TOF design, analysis, and testing will be covered.

3.1 GAPS

The GAPS experiment is a NASA Antarctic long-duration balloon mission with unprecedented sensitivity to low-energy (< 0.25 GeV/nucleon) cosmic-ray antinuclei (Aramaki et al., 2016a). An early iteration of the GAPS concept was proposed by Mori et al. (2002), motivated in part by the antideuteron dark matter signal hypothesized by Donato et al. (2000). The decision to use a solid target rather than gas was made early on, after successful testing with the antiproton beam at KEK, the High Energy Accelerator Research Organization in Japan (Hailey et al., 2006). A prototype mission (pGAPS) was flown from Japan in 2012 for several hours, demonstrating the validity of the various GAPS subsystem designs (Mognet et al., 2014; von Doetinchem et al., 2014; Fuke et al., 2014). To achieve its science goals, GAPS aims to undertake at least three $\sim$35-day flights from Antarctica.

As discussed in Section 2.2, cosmic-ray antinuclei, and low-energy antideuterons in particular, provide well-motivated avenues for indirect dark matter detection in an unexplored parameter space. Additional scientific prospects for cosmic antinuclei measurements were reviewed by von Doetinchem et al. (2020) and include sensitivity to potential alternative primary sources of antiparticles such as evaporating primordial black holes (Barrau et al., 2002, 2003) and astrophysical objects composed of antimatter (e.g. Steigman, 1976; Chardonnet et al., 1997). GAPS' sensitivity to low-energy antiprotons will also allow it to inform interpretations of the AMS-02 antiproton excess and cosmic-ray propagation (Rogers et al.,

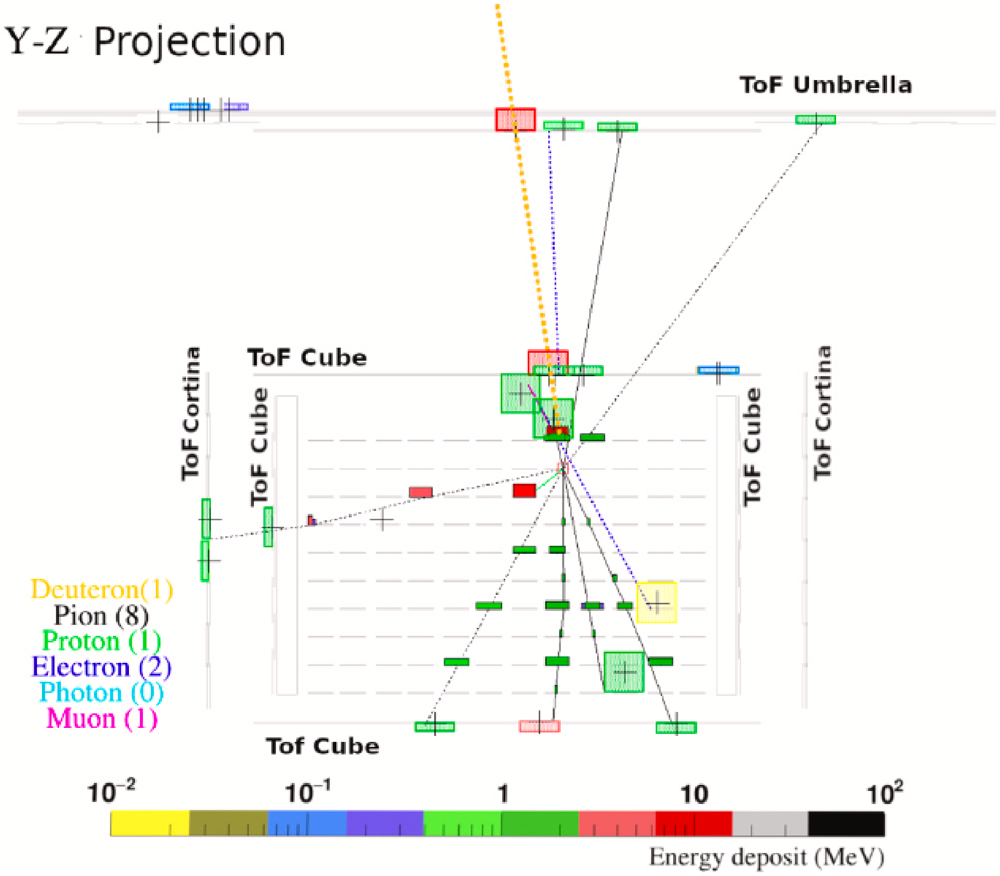

Figure 14: Visualization of a simulated antideuteron event, illustrating the GAPS detection scheme. An incoming antideuteron passes through the two layers of the TOF before stopping in the tracker, forming an exotic atom. In the formation of the exotic atom, X-rays are emitted with characteristic energies and are measured by the tracker. The exotic atom quickly decays, producing a characteristic number of protons and pions, among other particles. Figure from Munini et al. (2021).

2022). GAPS' sensitivity to low-energy antihelium will also have implications for some cosmic-ray antimatter models (Saffold et al., 2021a), particularly those motivated by the possible antihelium detections by AMS-02 (Ting, 2016).

Typically, instruments that have measured cosmic-ray antiprotons, such as BESS (Abe et al., 2008), AMS (Aguilar et al., 2016), and their successors rely on a strong magnetic field to distinguish matter from antimatter. In contrast, GAPS exploits the formation of an exotic atom that can occur when antimatter and matter interact. Slow antiparticles have a high probability of being captured by atomic nuclei, replacing an electron and forming an exotic

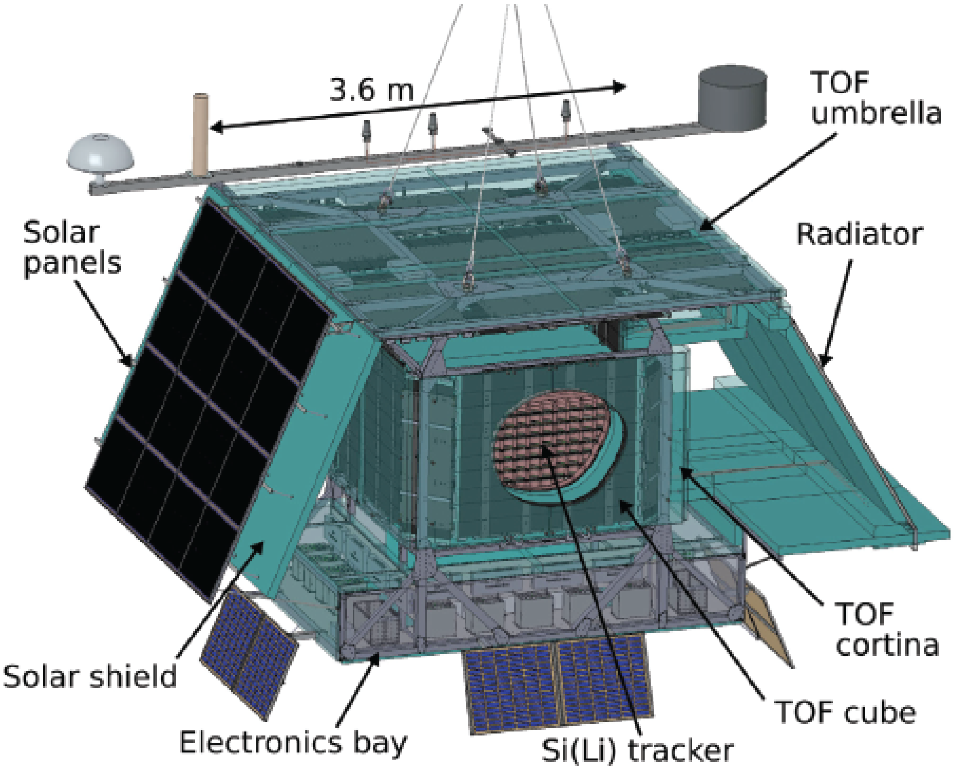

Figure 15: Schematic of GAPS, with several major components labeled. Parts of the TOF cortina and cube are cut out and the cortina opacity is reduced to reveal the tracker. Figure from Munini et al. (2021).

atom. The newly-formed atom is in a highly-excited state, which de-excites through emission of Auger electrons and X-rays with characteristic frequencies, determined by the species of nucleus and antiparticle. The antiparticle and nucleus ultimately annihilate, emitting pions and protons in characteristic amounts. A simulated antideuteron event is shown in Figure 14, illustrating typical decay products. The X-rays and pion/proton multiplicity can be used to reliably identify the antiparticle species. GAPS thus detects cosmic-ray antiparticles with a method complementary to previous experiments, subject to different systematics.

A schematic of the GAPS instrument is shown in Figure 15. GAPS consists of two detector components and some auxiliary systems. A silicon tracker cube serves as target material for incoming antiparticles, tracks particle trajectories, and detects X-rays. The tracker is surrounded by two layers of thin scintillators that measure the time-of-flight (TOF) of through-going particles. The tracker and TOF system are both read out by custom electronics. The tracker detectors and electronics are cooled by a thermal system consisting of an oscillating heat pipe (OHP) and radiator.

The tracker contains 1440 lithium-drifted silicon (Si(Li)) detectors that occupy an approximately 1.6 m × 1.6 m × 1.0 m volume. The Si(Li) detectors have an energy resolution $\lesssim 4$ keV between 20–100 keV. They operate at temperatures between $-50°$ C and $-30°$ C. Development and performance of the Si(Li) tracker and OHP have been described elsewhere (Fuke et al., 2017; Okazaki et al., 2018; Perez et al., 2018; Kozai et al., 2019; Rogers et al., 2019; Saffold et al., 2021b). The TOF system is described in detail in the next section.

3.1.1 Time-of-Flight

The TOF is composed of two layers of plastic scintillator paddles that measure times, positions, and energy depositions of incoming and outgoing particles. From the difference in times and positions measured in each layer one can calculate the particle velocity, which is used in the event reconstruction. Energy depositions have dependence on particle charge and they thus aid in charge discrimination. GAPS requires a timing resolution < 400 ps and a charge resolution < 0.25 times the elementary charge.

The bulk of the TOF is composed of polyvinyltoluene (PVT) scintillator paddles, which function as the active detector volume for incoming and outgoing particles. The paddles are fairly long, with lengths between 108.2 and 180 cm, and have constant thickness and width of 0.635 cm and 16 cm, respectively. The TOF contains 160 paddles, with 60 in the inner layer and 100 in the outer layer. The inner TOF paddles are arranged in an approximately 1.6 m × 1.6 m × 1.1 m "cube" surrounding the Si(Li) tracker. The outer TOF consists of a 3.6 m × 3.6 m "umbrella," parallel to the top of the cube at a separation of ∼0.9 m, and a 1.6 m-high "cortina," which skirts around the sides of the cube at a separation of ∼30 cm. Most paddles are arranged in carbon fiber panels, which provide structural support. The panels attach to an aluminum gondola frame that will be suspended from the balloon. A schematic of the TOF is shown in Figure 16.

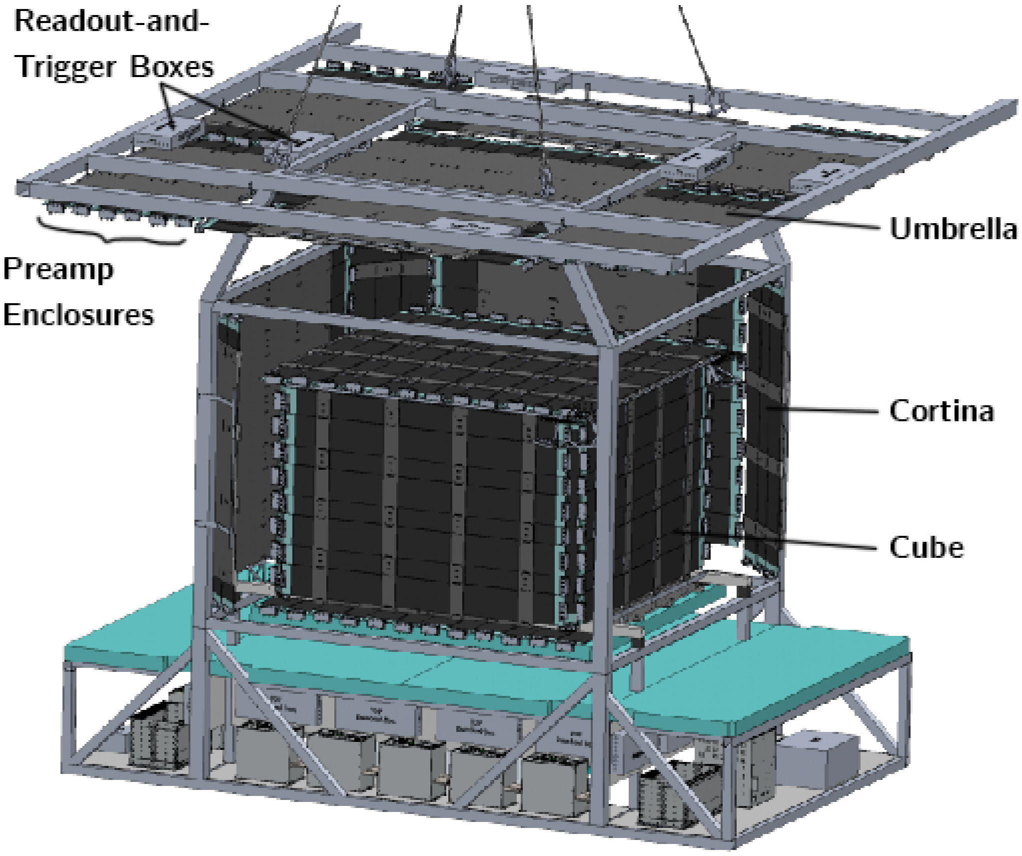

Figure 16: Schematic of the GAPS TOF and gondola, with most other subsystems omitted. Part of the cortina is removed to reveal the cube. Elements including preamp enclosures, readout-and-trigger boxes, and carbon fiber panels are also visible.

The plastic scintillator material is Eljen Technology's EJ-200[4], chosen for its fast rise time (0.9 ns) and long light attenuation length (380 cm). Charged particles passing through a scintillator paddle deposit energy via ionization and excitation of the scintillator molecules which, through fluorescence or phosphorescence (Birks, 1964), emit photons that propagate through the scintillator and may be detected by photomultiplier tubes (PMTs) or silicon photomultipliers (SiPMs). Photons propagating through the scintillator are subject to total internal reflection at the boundary between the scintillator and air for angles greater than 39.3°, measured from the normal. Reflection is aided by the smooth EJ-200 faces, which are either diamond-milled or cast. The scintillator is wrapped with aluminum foil, which

---

[4] All material names with the EJ prefix are from Eljen Technology. Material data are found on their website: `https://eljentechnology.com`.

Figure 17: Photograph of a single constructed 1.8 m paddle. Relative sizes of the scintillator and preamp enclosure can be seen. Black plastic covers the entire assembly. We define the long (horizontal) axis as the x axis.

has a chance to reflect any photons escaping the scintillator. The paddles are then wrapped with opaque black plastic, making each paddle light-tight. A coil of quarter-inch black plastic tubing is inserted so that the paddle is not air-tight—thus being able to handle large changes in pressure—but remains light-tight. A photograph of a single constructed 1.8 m paddle is shown in Figure 17.

Each paddle end is coupled to six SiPMs, which detect the scintillation light. SiPMs were chosen over PMTs after extensive testing. The SiPMs demonstrated better timing resolution, added redundancy to the design (six SiPMs per end versus a single PMT), and resulted in lower weight, lower power, and no high voltage requirement. Hamamatsu Photonics' S13360-6050VE SiPMs are used, having high photon detection efficiency[5] over the wavelengths expected from the scintillator, as shown in Figure 18. The photon detection efficiency is mostly determined by the product of the geometrical fill factor, quantum efficiency, and probability of Geiger discharge (Otte et al., 2017; Ghassemi et al., 2018). In early lab tests, scintillator and SiPMs were coupled with EJ-550 silicone grease. The optical coupling for flight is different, instead involving EJ-560 silicone rubber optical interfaces (or "cookies"), bonded to the scintillator and SiPMs with EJ-500 optical cement. The flight coupling allows for small displacements due to thermal contraction, while avoiding the outgassing from grease. The specific materials are chosen to have similar indices of refraction (listed in table 1) in order to reduce reflections. The transmission probability P_{transmit} for a photon normally incident to a boundary between materials of refractive indices n_1 and n_2 is given by (e.g.

---

[5] Data for the S13360-6050VE is found on the Hamamatsu Photonics website: `https://www.hamamatsu.com/content/dam/hamamatsu-photonics/sites/documents/99_SALES_LIBRARY/ssd/s13360-2050ve_etc_kapd1053e.pdf`

Material	n
Scintillator (EJ-200)	1.58
Optical cement (EJ-500)	1.57
Optical grease (EJ-550)	1.46
Cookie (EJ-560)	1.43
SiPM resin window	1.55

Table 1: Indices of refraction n of materials along the TOF paddle optical path.

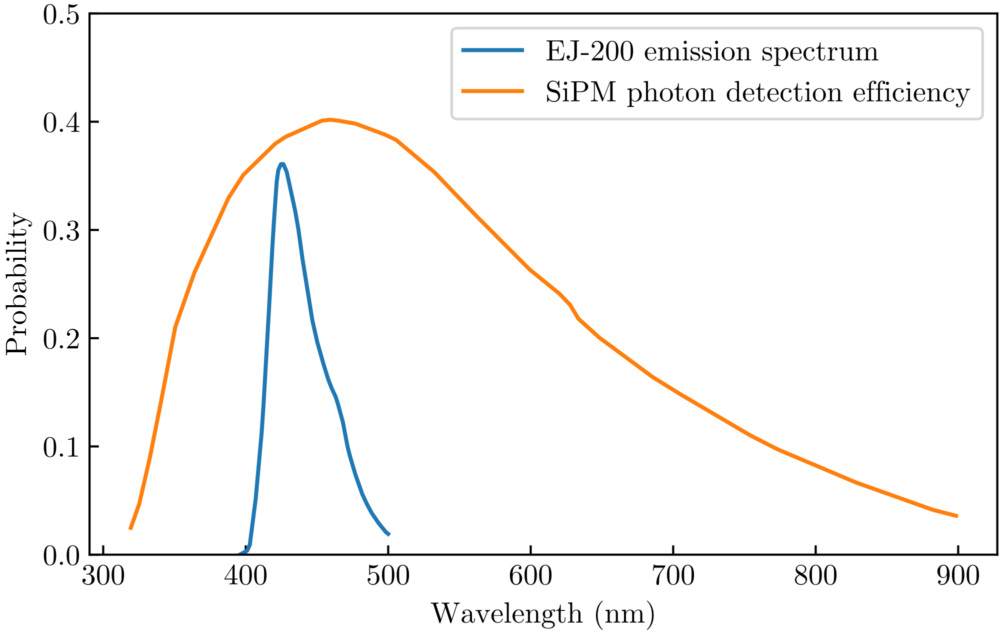

Figure 18: Scintillator emission spectrum (arbitrary normalization), and SiPM photon detection efficiency as a function of wavelength, from the EJ-200 and S13360-6050VE data sheets, respectively.

Jackson, 1998)

$$P_{\text{transmit}} = 1 - \left(\frac{n_1 - n_2}{n_1 + n_2}\right)^2 \tag{28}$$

Transmission probabilities from the scintillator into a SiPM's resin window are ∼0.998 and ∼0.996 for the grease and flight couplings, respectively.

A preamplifier (preamp) board powers the SiPMs, sums and shapes the SiPM signals, and provides low-gain and high-gain outputs for trigger formation and readout, respectively. The board has four stages: summation of the six SiPM signals, a transimpedance amplifier, pole-zero cancellation, and a current feedback amplifier. Pole-zero cancellation has been shown to shorten the fall time of the SiPM response (Gola et al., 2013; Cattaneo et al., 2014; Otte et al., 2015; Acerbi & Gundacker, 2019). The board also contains a temperature sensor, which allows us to account for the temperature-dependent SiPM performance. A version 4.2 preamp board, with SiPMs attached, is shown in Figure 19. The preamps are housed in aluminum enclosures that attach to the scintillator, aiding positioning of the SiPMs. The SiPMs are biased above their breakdown voltage, so that a single photoelectron can initiate an avalanche of charge carriers, resulting in large gains (e.g. Renker & Lorenz, 2009). The difference in bias and breakdown voltage is called overvoltage. The TOF SiPMs have breakdown voltages of 51.6 ± 0.18 V, measured individually to within 0.01 V. They are operated with bias voltages around 58.0 V, or 6.4 V overvoltage, yielding gains of 3.6×10^6 at room temperature. This gain value is chosen so that minimum ionizing particles produce pulses with voltage peaks ∼30 mV, allowing pulses up to ∼30 times larger to remain in our 1.0 V readout range.

The high-gain outputs from the preamps are digitized and recorded by a readout board. Voltages as a function of time, or "traces," are recorded since they contain a wealth of information. Traces are digitized by a DRS4 chip (domino ring sampler 4; Ritt et al., 2010) and an analog-to-digital converter. Each DRS4 has nine channels with 1024 sampling capacitors, where eight channels record preamp outputs, and the ninth channel records a global reference sine wave. While the DRS4 can operate at sampling rates between 700 MHz and 6 GHz, we choose a rate of 2 GHz to attain our desired timing resolution, while also providing a window of ∼100s of nanoseconds to record outgoing particles. Under certain conditions, picosecond time resolution is possible (Stricker-Shaver et al., 2014). The DRS4 dynamic range is 1.0 V, with an adjustable read offset. We operate the DRS4 such that is can read voltages between −50 mV and +950 mV, above which saturation occurs. Details concerning TOF readout board operation are given in Section 3.5.

The low-gain outputs from the preamps feed into local trigger boards. A local trigger

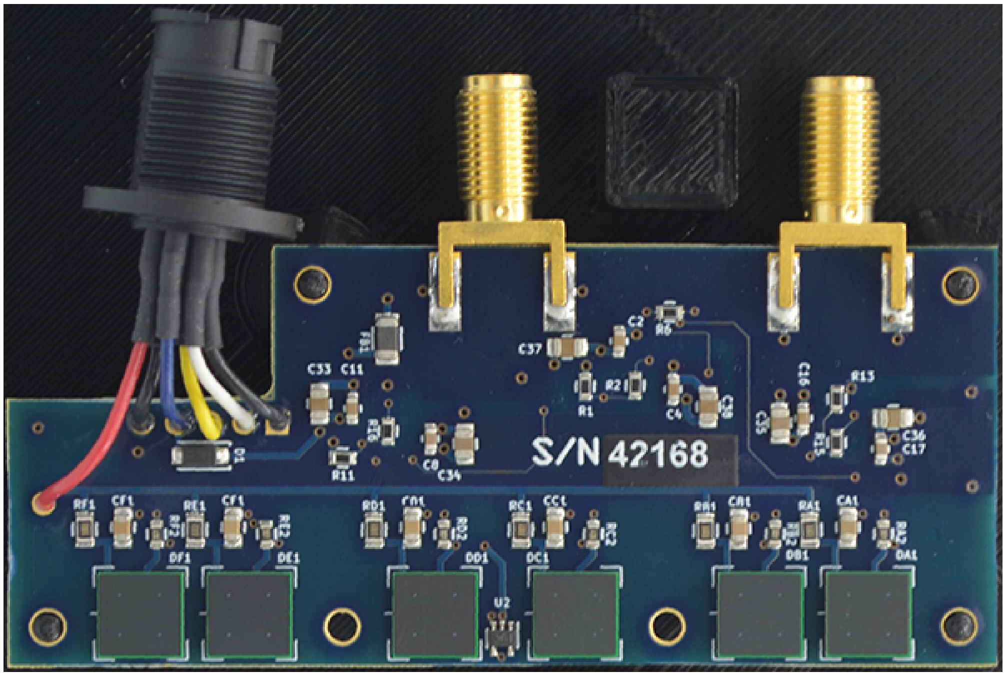

Figure 19: Photograph of a TOF preamp board (version 4.2). The connector on the left includes power and temperature sensor lines. The middle and right connectors are low and high-gain outputs, respectively. The six SiPMs are at the bottom.

board combines data from eight paddles and sends signals to the master trigger board. The master trigger board processes the outputs from the 20 local trigger boards and forms the trigger decision, which initiates readout.

Data are stored on the TOF computer, which also handles remote communications, through the flight computer. In addition to receiving commands during flight, it is anticipated that GAPS will transmit down promising events. Multiple Ethernet switches facilitate communication between the flight computer, TOF computer, master trigger board, and readout boards.

Power boards power the preamps, readout boards, and local trigger boards. The power board is designed to provide adjustable voltages to the preamps and it also meets the preamp and readout board power-on sequence requirements. Sets of one power board, two readout boards, and one local trigger board are housed in aluminum readout-and-trigger boxes, or "RATs." The power for the TOF computer, Ethernet switches, master trigger board, and

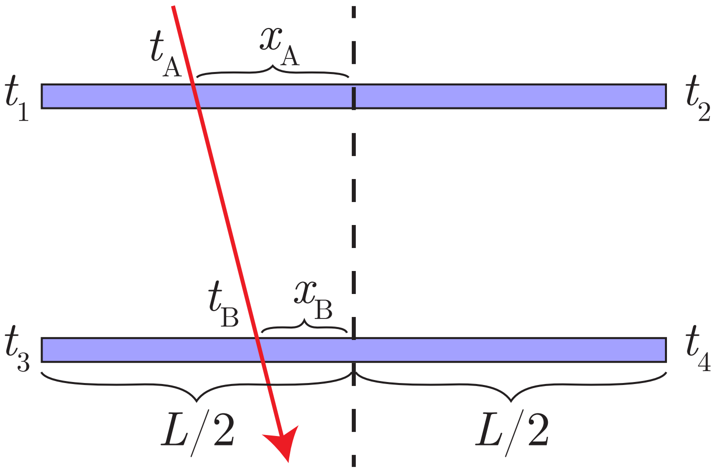

Figure 20: 2D TOF schematic of two paddles with length L, with labels for times and positions related to a particle trajectory (red). The vertical dashed line represents the paddle center, from which distances are measured.

the power boards themselves come from the main GAPS battery.

3.2 Measurement of Time and Position

3.2.1 Derivations

We seek to determine the TOF resolution σ_{TOF}, which characterizes the uncertainty in the measurement of a particle's time of flight between the two TOF layers. We derive this quantity from measurements of the difference in pulse arrival times at each end of a paddle for particles passing through a known paddle position. These time differences should be approximately normally-distributed around a constant value, with a width giving the time difference resolution $\sigma_{t_1-t_2}$. The relation between σ_{TOF} and the quantity we measure, σ_{t1-t2}, may be derived as follows.

Consider a particle track through two paddles of length L, as shown in Figure 20, where we make simplifying assumptions of parallel paddles and equal positions along the paddle width dimension. Let the particle hit the top paddle at time t_{A} a distance x_{A} from the paddle center towards end 1 (left, in Figure 20), and define t_{B} and x_{B} similarly for the bottom paddle. Also, let the photon arrival time be t_1 at end 1 of the top paddle, t_2 at the other end, and let t_3 and t_4 be similarly defined for the bottom panel. Fluctuations in photon arrival times are ignored here, but will be discussed in Section 3.3. Using c_s to represent an effective light propagation speed in the scintillator, we can write

$$\begin{aligned} t_1 + t_2 &= (t_\mathrm{A} + (L/2 - x_\mathrm{A})/c_s) + (t_\mathrm{A} + (L/2 + x_\mathrm{A})/c_s) && (29) \\ &= 2t_\mathrm{A} + L/c_s && (30) \end{aligned}$$

The time of flight may then be written in terms of the photon arrival times

$$\begin{aligned} t_\mathrm{TOF} &\equiv t_\mathrm{B} - t_\mathrm{A} && (31) \\ &= \frac{t_3 + t_4 - L/c_s}{2} - \frac{t_1 + t_2 - L/c_s}{2} && (32) \\ &= \frac{(t_3 + t_4) - (t_1 + t_2)}{2} && (33) \end{aligned}$$

Assuming $\sigma_{t_1} = \sigma_{t_2} = \sigma_{t_3} = \sigma_{t_4}$, we find $\sigma_\mathrm{TOF} = \sigma_{t_1}$, or

$$\sigma_\mathrm{TOF} = \sigma_{t1-t2}/\sqrt{2} \tag{34}$$

We also find that the position may be written in terms of the photon arrival times as

$$x_\mathrm{A} = \frac{c_s(t_2 - t_1)}{2} \tag{35}$$

And thus, position resolution may be found with

$$\sigma_x = \frac{c_s \sigma_{t1-t2}}{2} \tag{36}$$

3.2.2 Experimental Setup and Data Taking

Measurements of timing and position resolutions for a 1.8 m scintillator paddle were carried out using atmospheric muons in December 2019. The testing setup used version 4.2 preamps with six SiPMs, with bias voltage 58.6 V. The SiPMs were coupled to the scintillator with optical grease. The 1.8 m paddle was placed in a dark box, since the paddle ends were not light-tight for these tests. Two 5 cm-wide "defining paddles"—pieces of scintillator coupled to PMTs via light guides and optical cement—were placed across the 1.8 m paddle at different positions and were used to form the trigger. Coincidence of the defining paddles, indicating that a muon has passed through the defining paddles, triggers readout of the 1.8 m paddle. The defining paddle lengths slightly exceeded the 1.8 m paddle width, so some triggers did not coincide with muons passing through the 1.8 m paddle. For this reason, 1.3×10^4 events were taken, to ensure that at least 10^4 events contained muon hits. Data were taken with the defining paddles placed in 10 cm increments from the paddle center to 80 cm from the center and an additional data run was taken at 85 cm from the center, for a total of ten different positions.

Since the TOF readout boards were under development at the time, readout was performed using a DRS4 evaluation board.[6] Voltage and timing calibrations of the DRS4 were done with the evaluation board software and on-board calibration sources. We also used the evaluation board software algorithm to remove two-cell-wide spikes of ∼14.8 mV amplitude.

After calibration, traces still exhibit a constant, non-zero offset, or pedestal. Pedestals are calculated for individual traces using the mean of cells 20-220 (∼10–110 ns), and subtracted from the entire trace. The first few cells are excluded since we observed significantly higher noise in them. Figure 21 shows a 2D histogram of the means and root-mean-square (RMS) values of the pedestal region for muons passing through the paddle center. The distribution is skewed to higher pedestals and RMS values, relative to a 2D Gaussian, due mainly to the presence of dark counts and the tails of previous pulses in the pedestal region. The mean pedestal RMS of 0.54 mV is a measurement of the noise in the cell voltages. A Gaussian fit to the pedestal distribution (between −4.0 and −2.5 mV, 0.05 mV-wide bins) yields a mean of −3.26 mV and standard deviation of 0.13 mV, though the fit is poor (χ^2/d.o.f. = 160.8/23)

---

[6] Described on the PSI website: `https://www.psi.ch/en/drs/evaluation-board`

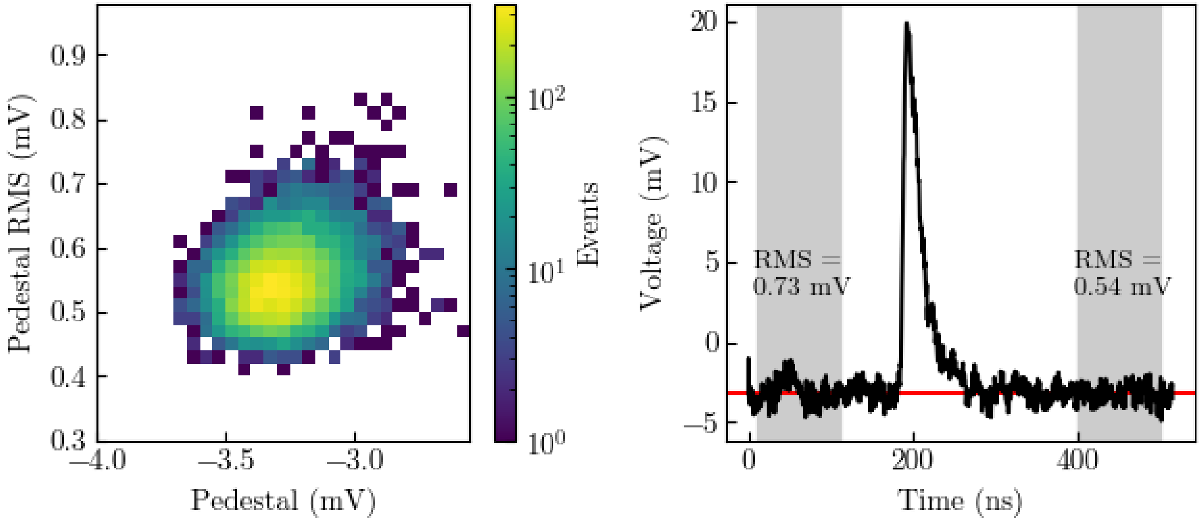

Figure 21: *Left*: 2D histogram of pedestal and pedestal RMS values for muons passing through the center of a 1.8 m paddle. The distribution is skewed to higher pedestals and RMS values, relative to a 2D Gaussian. *Right*: A single trace (black) with an unusually high pedestal RMS of 0.73 mV, likely due to multiple dark counts in the pedestal region (gray shaded region on left). For comparison, the 400-500 ns region (gray shaded region on right) has a typical pedestal RMS value of 0.54 mV. The pedestal is also shown (red).

due to the skewness. The statistical fluctuations in the pedestal due to noise alone may be approximated as pedestal RMS/(number of cells used in the pedestal calculation)$^{1/2}$ = 0.04 mV, suggesting that the true pedestal value is not constant with time.

A 2D histogram of pedestal-subtracted traces for muons passing through the paddle center is shown in Figure 22. The broad distribution of pulse heights results from the Landau-distributed energy depositions of muons passing through the scintillator; discussed further in Sections 3.3 and 3.4. The median trace (shown in black) has a peak voltage of 37.6 mV, while the peak voltage distribution itself peaks around 32 mV. Jitter in the leading edge of the trace distribution can be seen, though only a small fraction of this is due to timing resolution, which we now measure.

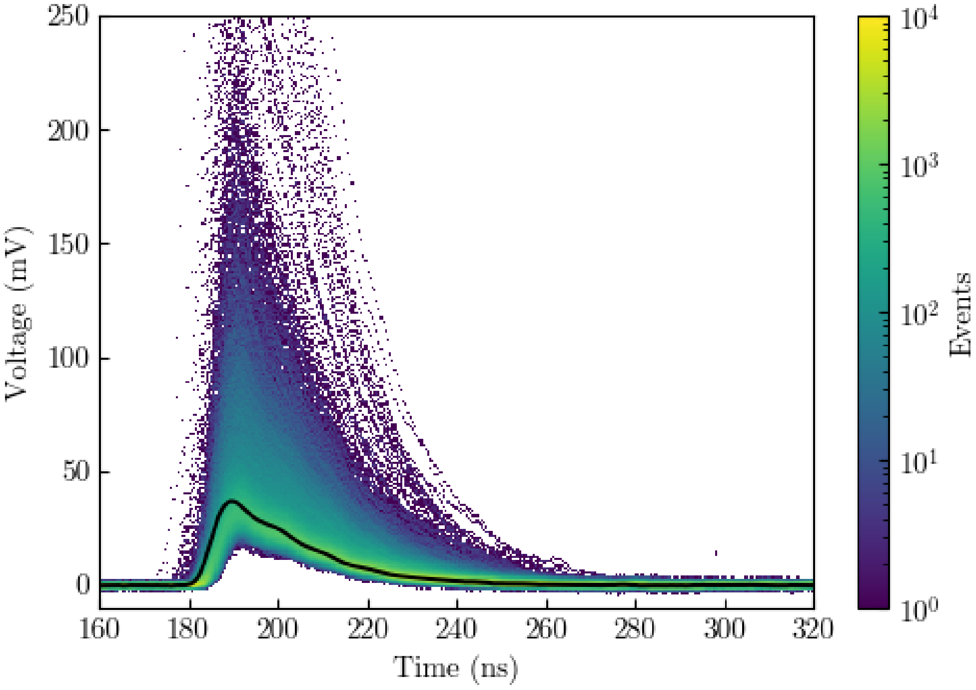

Figure 22: 2D histogram of traces for muons passing through the center of a 1.8 m paddle. The median trace (black line) has a peak voltage of 37.6 mV, slightly higher than the mode of the peak voltage distribution of 32 mV. The DRS4 evaluation board and version 2.4 preamps are used, with bias voltage 58.6 V.

3.2.3 Pulse Timing Methods

Times are derived from pulses using constant threshold (CT) and constant fraction (CF) methods (Knoll, 2010). CT methods are subject to “amplitude walk” when pulses vary in height (i.e. threshold crossings happen earlier for larger pulses), which must be corrected for to achieve optimal timing resolutions. In contrast, CF methods are less affected by amplitude walk. In contrast to an electronic CF discriminator, we use a software algorithm where we estimate the peak voltage using the mean of the maximum voltage and the two adjacent cells and then find the time on the leading edge of the pulse corresponding to the CF times the peak voltage, linearly interpolating between cells if necessary. We note that these timing methods actually measure the photon arrival time plus an offset. However, these offsets cancel in our time resolution calculations which involve $t_2 - t_1$.

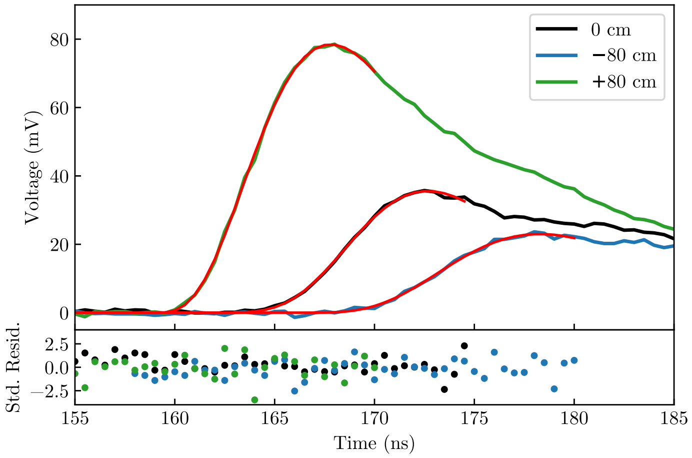

Figure 23: Pulse fits to typical traces for muons passing through three different positions (top), and standardized residuals of the fits (bottom). Traces are shown for $x = 0$ cm (black), -80 cm (blue), and $+80$ cm (green). Equation 37 provides good fits (red) to the leading edge of each pulse.

A method involving fitting the leading edge of the pulse is also explored, using a functional form of a power law times an exponential

$$V(t) = \begin{cases} p_0 \left(\frac{t-p_1}{p_2}\right)^{p_3} e^{-(t-p_1)/p_2} \times (e/p_3)^{p_3} & ; \quad t \geq t_0 \\ 0 & ; \quad t < t_0 \end{cases} \tag{37}$$

where p_0 is the peak voltage, p_1 shifts the pulse in time, p_2 is a width parameter, and p_3 is the power law index. The last term normalizes the pulse so that its maximum value is p_0, at time $p_1 + p_2 p_3$. We fit only the 40 bins before a trace's peak and 5 bins after, to cover the peak, leading edge (∼10 ns), and part of the pedestal. While the pulse shape varies depending on the position of the muon hitting the paddle, we find that Equation 37 can provides a good fit to the leading edge of all the various pulse shapes in our data set. The time at a constant fraction of the fitted pulse can then be found, which will be abbreviated the "pulse CF" method.

3.2.4 TOF Resolution Results

Histograms of time differences are shown in Figure 24. Times are binned into 20 ps bins, and the histograms are fit with Gaussians, approximating the uncertainties in each bin as the square root of the number of events in the bin (the Gaussian approximation for Poisson random variables). The best resolution is obtained with the pulse CF method, though the CF method performs similarly. The fit to the pulse CF distribution yields $\sigma_{t1-t2} = 0.376$ ns, corresponding to $\sigma_{\mathrm{TOF}} = 0.266$ ns. Different binnings give resolutions within 0.01 ns of the above value. The distributions contain excess events in the tails, induced mainly by bad pedestal estimates and multi-particle events (i.e. traces containing multiple pulses).

CF methods often perform best for fractions between 0.1 and 0.2 (Knoll, 2010). Time difference resolutions are measured with different CF values and are plotted in Figure 25. The best resolution is achieved with CF = 0.2065, yielding $\sigma_{t1-t2} = 0.387$. However, since systematic uncertainties (e.g. from choice of binning) in σ_{t1-t2} are around 0.01 ns, improvements within ±0.05 of 0.2 have low significance. We decide to use CF = 0.2 for our measurements.

Histograms of time differences for muons at different positions are shown in Figure 26. The distribution means shift approximately linearly with distance from the paddle center x, while the widths remain similar. However, time resolution might be expected to degrade further away from paddle center since the distance to the farther end of the paddle increases, possibly resulting in broader photon arrival times and fewer incident photons. The x-dependence of time difference resolution is shown in Figure 27. While σ_{t1-t2} generally increases with x, it does not exceed 0.433 ns. The resolutions at $x = 70$ cm and 85 cm show relative improvements—the origin of this feature is unclear.

Time resolution should also worsen at low peak voltages, since noise in the pulse leading edge and peak voltage estimate become more significant. We bin traces by smaller peak voltage (of the traces at the two paddle ends) in bins of 2 mV, and derive the time difference resolution for each bin. Due to the small number of events in most peak voltage bins, and the

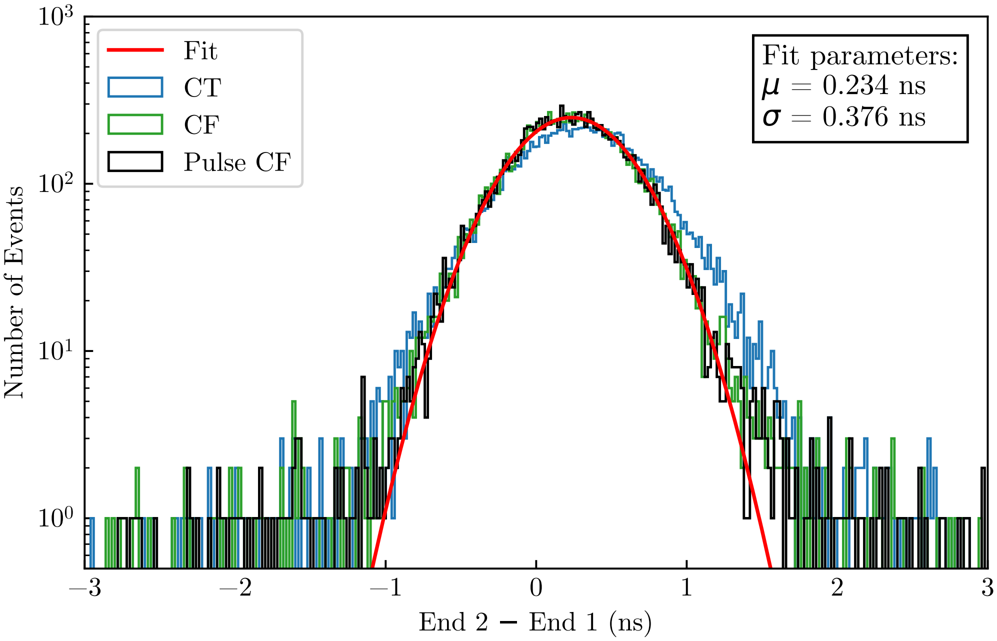

Figure 24: Histograms of difference in measured times at the two ends of a 1.8 m paddle, for muons passing through the paddle center. Histograms are shown for three different timing methods. A time difference resolution of $\sigma_{t1-t2} = 0.376$ ns is found with the pulse CF, corresponding to $\sigma_{\text{TOF}} = 0.266$ ns. The CT and CF method give $\sigma_{t1-t2} = 0.444$ ns and $\sigma_{t1-t2} = 0.382$ ns, respectively. The distributions have excess events in the tails, mainly from misestimated pedestals and multi-particle events. The distributions are not centered at zero due to differences in cable lengths between the preamps and readout board.

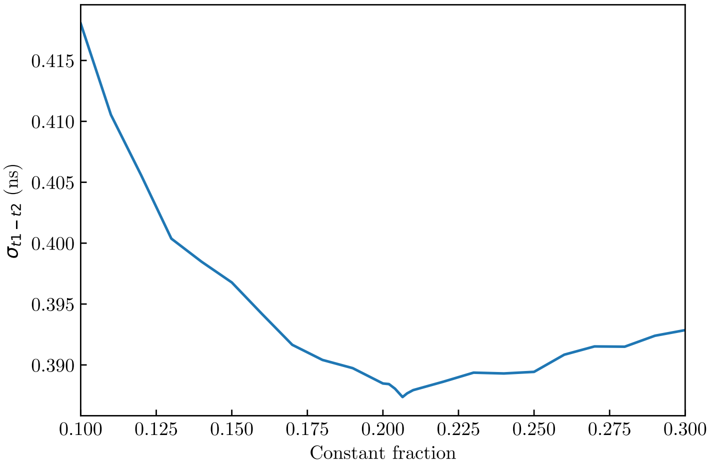

Figure 25: Time difference resolution σ_{t1-t2} versus CF value, for muons passing through the paddle center. The minimum occurs at CF = 0.2065, yielding $\sigma_{t1-t2} = 0.387$ ns.

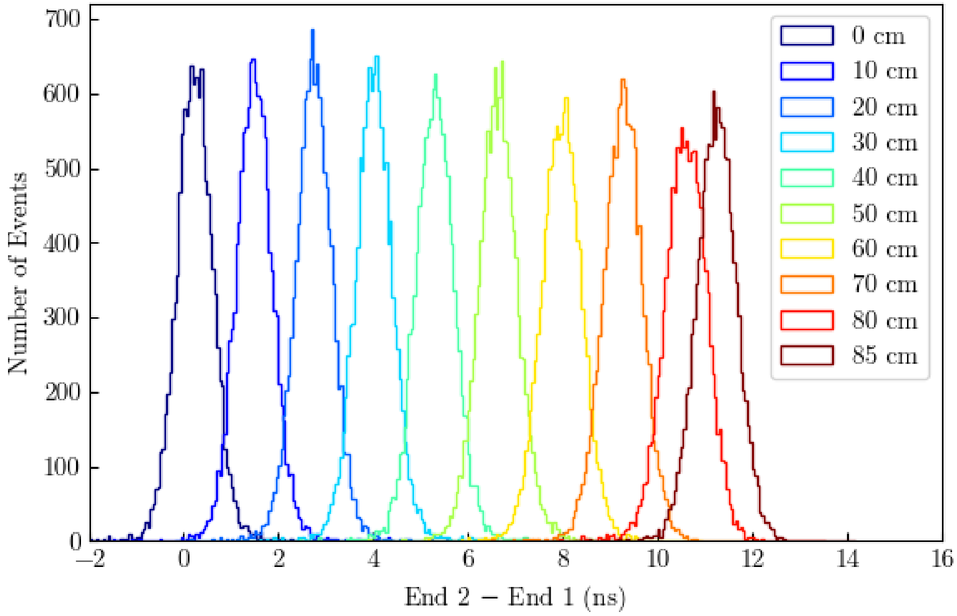

Figure 26: Histograms of time differences for muons passing through different positions along the paddle. Times are calculated with the pulse CF method.

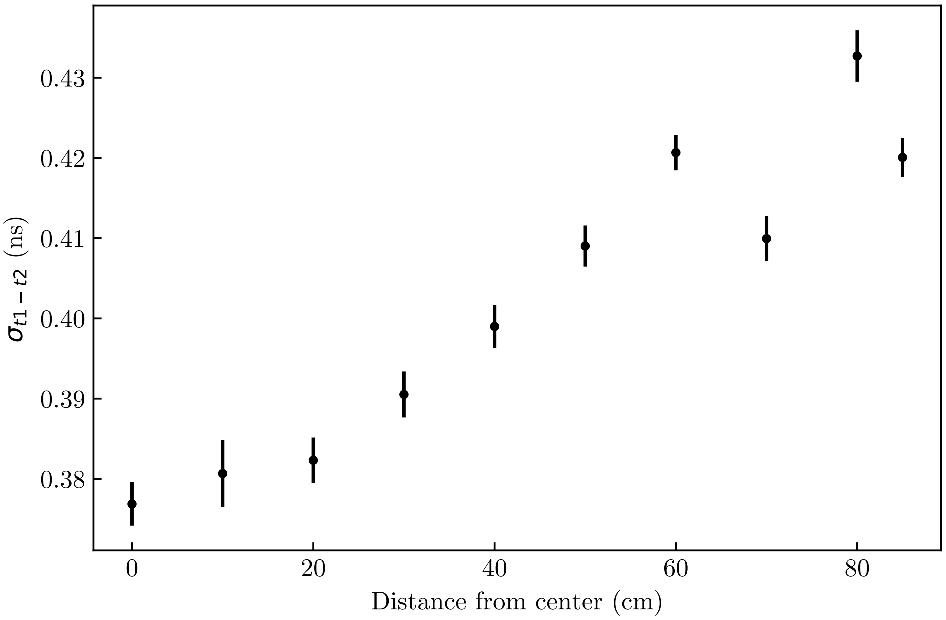

Figure 27: Time difference resolution σ_{t1-t2} versus distance from the paddle center. Error bars represent 1σ uncertainties on the fit parameter.

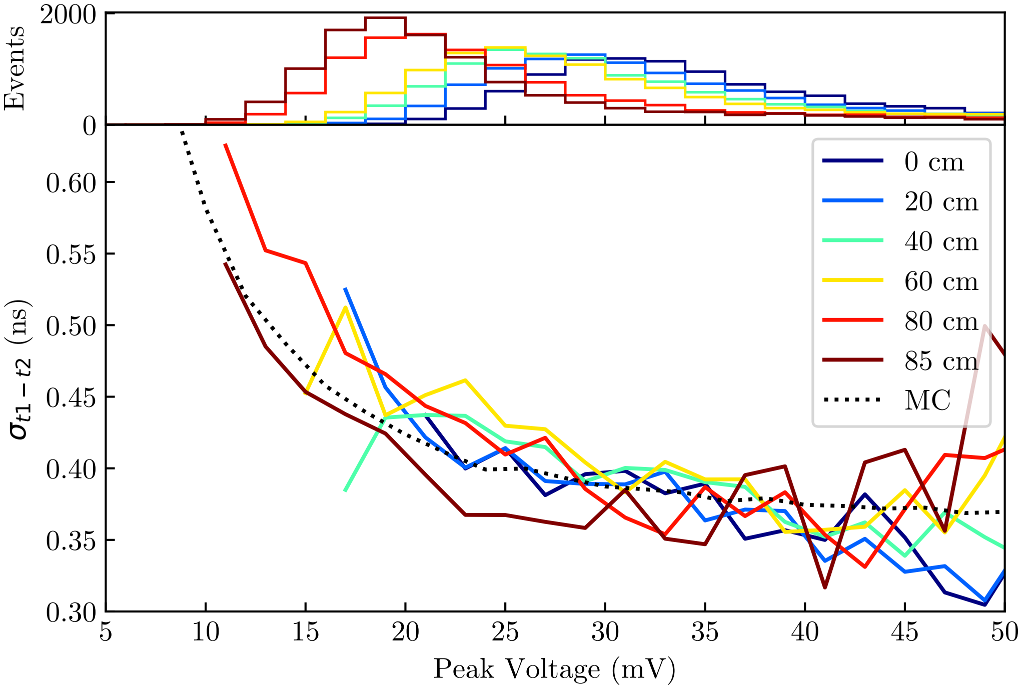

Figure 28: Time difference resolutions σ_{t1-t2} versus peak voltage for muons at different positions (bottom) in bins of 2 mV, and histogram of peak voltages (top) with the same binning. The peak voltage of the smaller of the two pulses is used. Since most bins do not have enough events for a Gaussian fit using fine bins, we approximate the resolution as half the width of the central 68% interval of time differences in each voltage bin. Resolutions are especially unreliable in voltage bins with few events. Despite these caveats, it is apparent that resolution worsens at lower peak voltages. Time difference resolutions derived from Monte Carlo simulations are also shown (dotted black line).

presence of tail events, we estimate the resolution as half the central 68% of the distribution (i.e. the 84th percentile minus the 16th, divided by two). Traces are binned by 2 mV and resolutions are derived for each bin. We repeat these calculations for several different muon positions, and plot the results in Figure 28. It can be seen that while resolution worsens at lower peak voltages, the required time resolution is maintained down to the lowest anticipated peak voltages. The resolutions at different x within a single peak voltage bin are fairly consistent, suggesting that the x-dependent peak voltage distributions are a major contributor to the observed x-dependence of the time resolution. Below ∼14 mV and above ∼44 mV, the small number of events in each bin make the time resolutions unreliable.

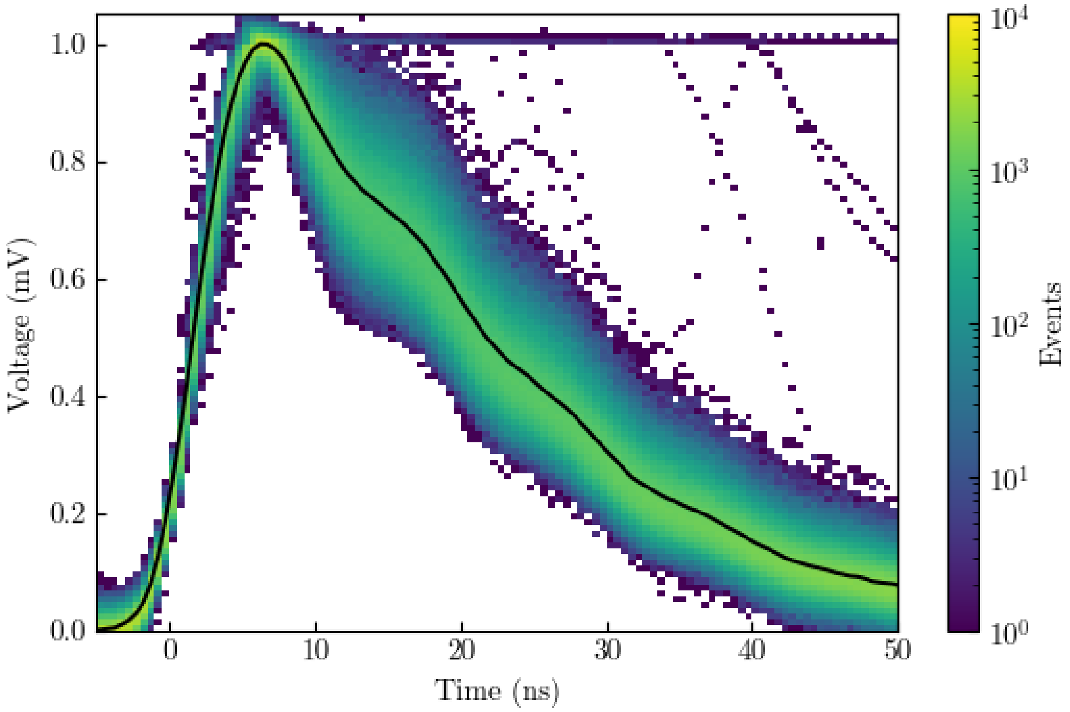

Figure 29: 2D histogram of scaled traces at one paddle end for muon data at $x = 0$ cm. The traces are normalized to their peak voltages (the mean of the maximum voltage and the two adjacent cells) and their pulse CF times are subtracted from their time arrays. The scaled, time-shifted traces show little variation in their leading edges, though the trace shape following the peak exhibits greater variance. Saturated pulses, some of which are visible, are exceptions.

The expected contribution of voltage noise to the timing uncertainty can be estimated with a toy Monte Carlo simulation. Traces in our data at a given x position all resemble the median trace in their leading edge, up to a multiplicative factor, as shown in Figure 29. Thus, traces at a given peak voltage may be simulated as the median trace times a scale factor, plus white noise. We first generate 10^4 realizations of the median traces for the two paddle ends at $x = 0$ cm (peak voltage = 37.6 mV), with Gaussian white noise added (with standard deviation = 0.54 mV, the pedestal RMS). From these simulated traces, a time difference resolution of 0.122 ns is derived using the pulse CF. The contribution to the timing uncertainty measured at one paddle end from sources other than voltage noise can be estimated as $\sigma_{t1,\text{other}} = \sqrt{\sigma_{\text{TOF}}^2 - (0.122\text{ ns})^2)/2} = 0.252$ ns. We then generate 10^4

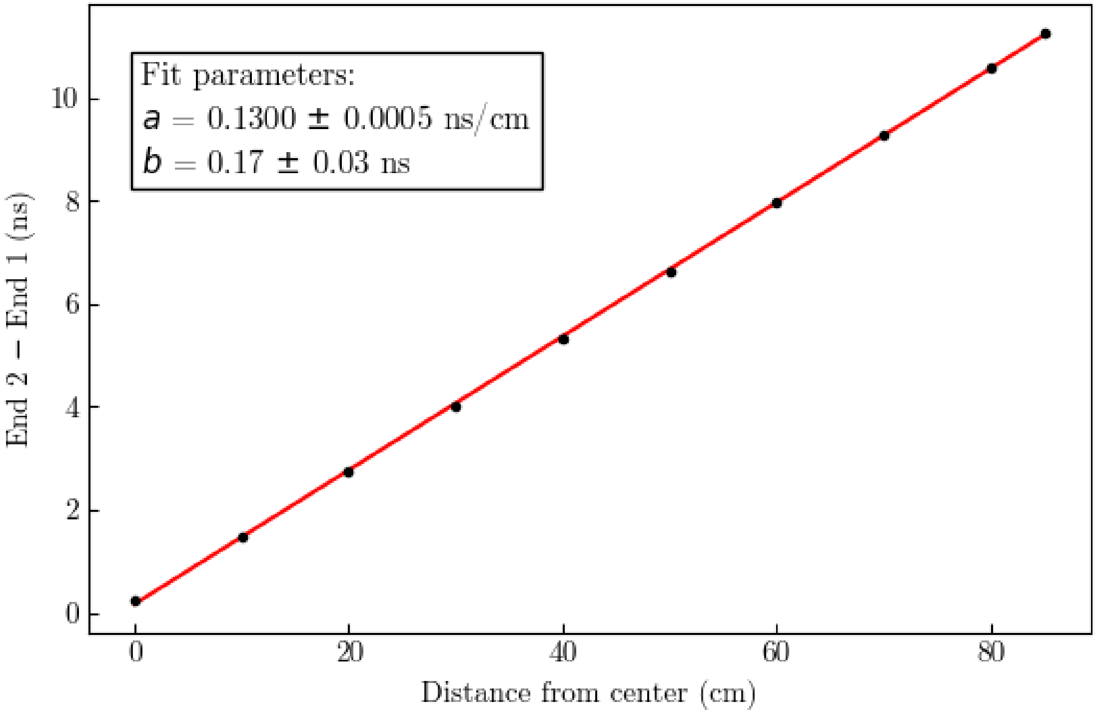

Figure 30: Mean time difference versus muon distance from the paddle center (black points). Error bars representing the 1σ uncertainties in the means from the Gaussian fits are too small to be visible. A straight line of the form $ax + b$ is fit, yielding $a = 0.1300 \pm 0.0005$ ns/cm and $b = 0.19 \pm 0.03$ ns.

realizations of the median $x = 0$ cm trace pair scaled to the central peak voltage of each peak voltage bin, adding white noise, and now also adding jitter to the times measured at each end, normally distributed with standard deviation $\sigma_{t1,\text{other}}$. The result of this simulation is shown in Figure 28 along with the data. While the simulation is fairly consistent with the data, it generally predicts lower σ_{t1-t2} values, suggesting that there may be additional sources of timing uncertainty at lower peak voltages. We can also conclude that, by itself, noise is not expected to degrade our timing resolution below the requirement.

The value of c_s is also derived in order to determine x when it is unknown. The means of the time difference distributions in Figure 26 are plotted against x in Figure 30. A linear fit of the form $t_2 - t_1 = ax + b$ yields $a = 0.1300 \pm 0.0005$ ns/cm and $b = 0.19 \pm 0.03$ ns. The nonzero value of b was determined to come from cable length differences. From equation

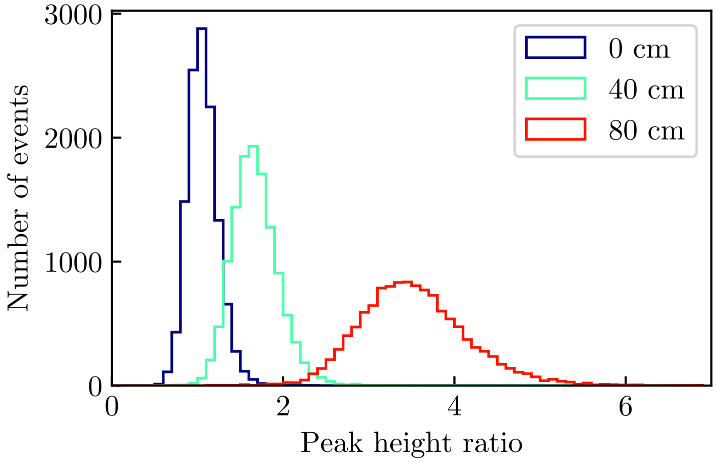

Figure 31: Histograms of peak voltage ratios versus position, for $x = 0$ cm (dark blue), 40 cm (turquoise), and 80 cm (red). The RMS of the ratio distribution at $x = 0$ cm is $\sim$16%, corresponding to $\sim$11 cm uncertainty.

35, we then have $c_s = 15.4$ cm/ns. This is slower than the speed of light in the scintillator (with $n = 1.58$) of 19.0 cm/ns, due to geometrical and other effects. From equation 36 and $\sigma_{t1-t2} = 0.376$ ns, we have $\sigma_x = 2.90$ cm.

The ratio of peak voltages also carries some information about an incident particle's position, as it is on average unity for particles passing through the paddle center and changes with position, as shown in Figure 31. While the ratio is nonlinear with x, we find that $x \approx 70$ cm $\times$ (peak height ratio $- 1$) near $x = 0$ cm. The RMS of the ratio distribution is $\sim$16%, suggesting that positions near the center can be recovered from the ratio of peak voltages with $\sim$11 cm uncertainty. This is much worse than the position derived from timing difference, but could be used as a consistency check.

In summary, we have measured for particles going through the center of a 1.8 m paddle:

- the uncertainty in the time of flight, $\sigma_{\mathrm{TOF}} = 0.266$ ns
- the corresponding uncertainty in position, $\sigma_x = 2.90$ cm
- the relation between x and CF times, $x = \frac{1}{2}(t_2 - t_1)15.4$ cm/ns

The uncertainties in time and position increase for smaller pulses, though this effect will be unimportant for slow-moving $Z = -1$ and $Z = -2$ particles, which produce larger pulses than relativistic muons. We also investigated several timing methods, finding that CF or pulse CF methods give the best time resolution for a CF value of around 0.20.

3.3 Simulations

Precise calculations of the instrument response of GAPS to incoming particles require numerical simulations due to the complexity of the GAPS instrument and the variety of physical processes and trajectories available to particles passing through it. Simulations exist for the various GAPS subsystems as well as the entire instrument, with varying levels of detail reflecting the different foci of each simulation. Here, we describe the simulation of a single TOF paddle.

The simulations are developed with the `GEANT4` framework (Agostinelli et al., 2003; Allison et al., 2006, 2016) version 10.7 and written primarily in `C++` and `ROOT` (Brun & Rademakers, 1997; Antcheva et al., 2009) version 6.24. Scintillation detectors have been successfully modeled with `GEANT4` previously (e.g. Hartwig & Gumplinger, 2014; Ogawara & Ishikawa, 2016). Within `GEANT4`, we use the physics list `FTFP_BERT_HP` with `G4OpticalPhysics` added to govern particle interactions.

The TOF simulations consider a 1.8 m scintillator paddle, with 16 cm width and 0.635 cm height. The largest paddle is considered since smaller paddles may be expected to have better performance. The material properties are defined to match those of EJ-200. Its density is 1.023 g cm^{-3} and it is composed of carbon and hydrogen atoms with mass fractions 91.6% and 8.4%, respectively. Of optical properties, the index of refraction is set to 1.58 and the bulk photon attenuation length, the distance over which the average number of propagating photons drops by a factor of e, is 380 cm, though departures from this monochromatic approximation may be significant (Senchyshyn et al., 2006). The scintillation emission spectrum is as shown in Figure 18, peaking at 425 nm. The scintillation yield is 64% of that expected for pure anthracene, or ∼10000 photons per MeV deposited in the scintillator. The fluorescence time spectrum is described as a fast leading edge and exponential decay (Knoll, 2010), with decay time 2.1 ns, while slower components are ignored. We approximate the relation between light yield dL/dx and energy loss dE/dx with Birks' formula

$$\frac{dL}{dx} \propto \frac{dE/dx}{1 + kB(dE/dx)} \tag{38}$$

where x is path length and $kB = 0.126$ mm MeV^{-1} (using the two-parameter fit value to NE-102 by Craun & Smith, 1970).

The paddles are surrounded by 0.5 mm-thick aluminum wrapping, separated from the paddle by an air barrier of 0.25 mm. The aluminum is given a reflectivity of 80% (e.g. Janecek & Moses, 2008).

Six SiPMs are placed at the paddle ends at the positions determined by our preamp design. The SiPM material properties are defined to match those of the S13360-6050VE. The SiPM detector volume is modeled as a 6 mm × 6 mm silicon rectangular prism behind a 0.1 mm epoxy resin window. The photon detection efficiency, shown in Figure 18, is implemented in `GEANT4` by setting the `EFFICIENCY` parameter of the dielectric-metal surface between the window and silicon. The two optical couplings described in Section 3.1.1 are implemented. The grease coupling is implemented as a 0.2 mm-thick layer of optical grease between the SiPMs and scintillator. The flight coupling is implemented as a 1 mm-thick cookie with 0.2 mm of optical cement on both sides. The coupling materials' properties match their data sheet values.

A visualization of a simulated muon event is shown in Figure 32. For each event, the incident particle momentum, position, and energy deposition are recorded, along with the photon arrival times measured by the SiPMs at each end. Care is taken to only record photons detected by the SiPMs, and not those absorbed at the resin-SiPM boundary (Dietz-Laursonn, 2016).

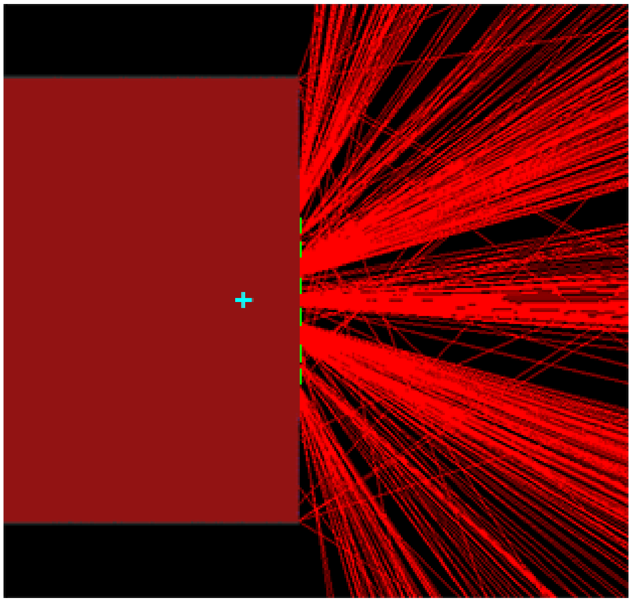

Figure 32: Visualization of the TOF paddle simulation, showing the top-down view of one paddle end. The muon hit position is shown (cyan cross). Tracks of photons (red) fill the paddle volume. The aluminum wrapping is rendered as a semi-transparent gray. Some photons are absorbed by the six SiPMs (green) at the paddle end, while others escape since the simulated paddle is not wrapped in blackout material.

3.3.1 Simulation of Atmospheric Muons

For comparison with our data, we simulate atmospheric muons impinging on the TOF paddle with vertical tracks at different positions x along the paddle's long axis measured from the center. The muon momenta are randomly drawn from the probability distribution shown in Figure 33, which is defined between momenta of 210 MeV/c and 54 GeV/c. This distribution is close to other parameterizations of the vertical muon intensity spectrum at sea level (e.g. Gaisser, 1990; Guan et al., 2015; Shukla & Sankrith, 2016), but is flatter at low momenta to account for our detector being underground. The effect of the precise distribution of muon momenta is expected to be small, since the simulated muons are all nearly minimum-ionizing particles, i.e. muons with kinetic energy close to that which minimizes the Bethe-Bloch equation (Longair, 2011; Particle Data Group et al., 2020). 10^4 muons at $x = 0$ cm and $x = 80$ cm are simulated. Since photons are measured at both ends, a simulation at x also models the behavior at $-x$.

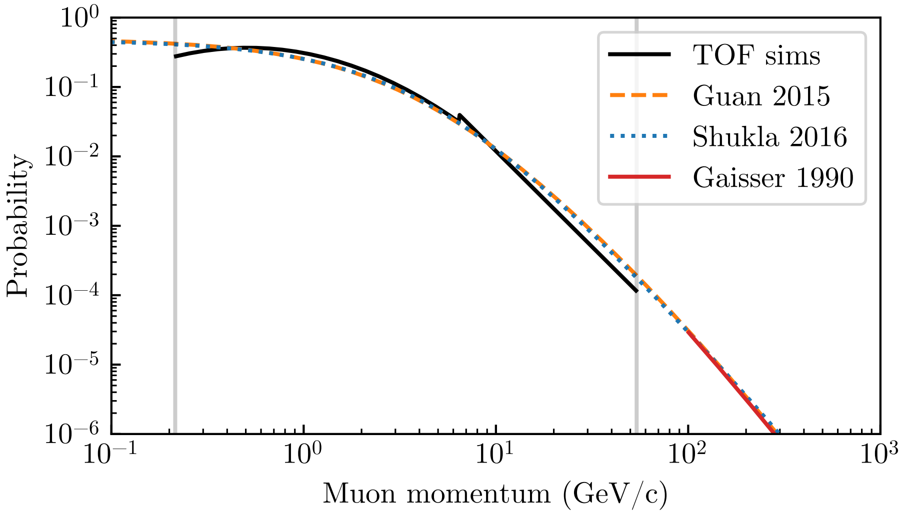

Figure 33: Muon spectrum used in the TOF paddle simulation (black), along with other parameterizations found in the literature (Gaisser, 1990; Guan et al., 2015; Shukla & Sankrith, 2016).

The energy depositions at $x = 0$ follow a Landau distribution, as shown in Figure 34—the distribution at $x = 80$ is nearly identical. The Landau distribution, with location and scale parameters μ and w, can be expressed (Landau, 1944; Kölbig & Schorr, 1984)

$$f_{\text{Landau}}(E; \mu, w) = \frac{1}{\pi w} \int_0^\infty du\, e^{u(E-\mu)/w} u^{-u} \sin(\pi u) \tag{39}$$

We compute the Landau distribution using the formulae of Kölbig & Schorr (1984). The most probable energy loss Δ_p for a particle traveling through a distance x of a material is (Bichsel, 1988; Particle Data Group et al., 2020)

$$\Delta_p = \xi \left[\ln\left(\frac{2m_e c^2 \beta^2 \gamma^2}{I} \right) + \ln\left(\frac{\xi}{I} \right) + j - \beta^2 - \delta(\beta\gamma) \right] \tag{40}$$

where m_e is the electron mass, c is the speed of light, β is the incident particle velocity over c, $\gamma = (1 - \beta^2)^{-1/2}$, I is the mean excitation energy of the material, $j = 0.2$, and δ is the density effect correction. The coefficient is $\xi = (K/2)\langle Z/A \rangle z^2(\rho x/\beta^2)$, where $K \approx 0.307$ MeV cm^2 mol^{-1}, $\langle Z/A \rangle$ is the average ratio of atomic number to atomic mass of the

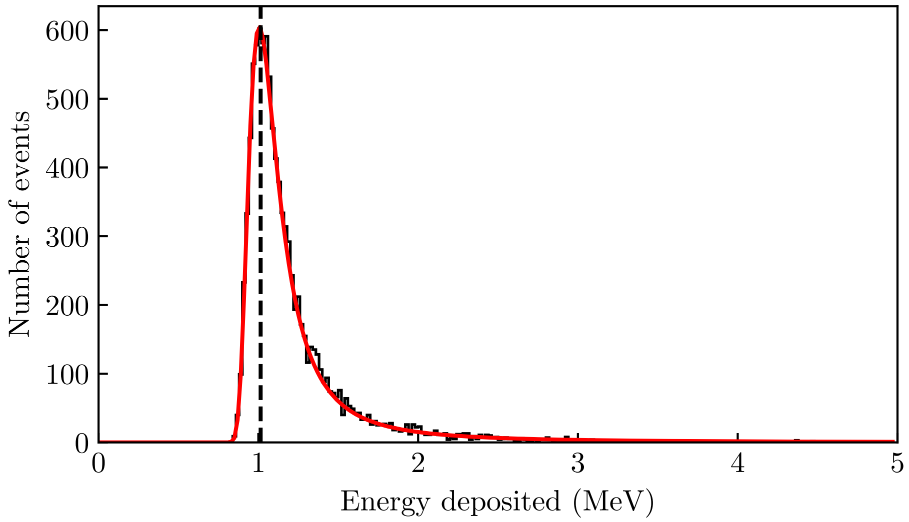

Figure 34: Distribution of 10^4 simulated energy depositions for muons with vertical tracks passing through $x = 0$ cm (solid black line). The energy depositions are binned in 0.02 MeV bins. The best-fit Landau distribution (red) has $\mu = 1.019$ MeV and $w = 0.060$ MeV (see Equation 39). The theoretical most-probable energy deposition for a minimum-ionizing muon through our scintillator is $\Delta_p = 1.014$ MeV (dashed black line).

material, ρ is the material density, and z is the incident particle charge. Using the values for muons in PVT (Groom et al., 2001), $\Delta_p = 1.014$ MeV for minimum ionizing muons (kinetic energy = 325 MeV) in EJ-200. The simulated energy deposition distribution, in bins of width 0.02 MeV, is best fit by a Landau distribution with $\mu = 1.019$ MeV and $w = 0.060$ MeV. The full width at half maximum of the fit is 0.239 MeV, close to $4\xi = 0.230$, as expected (Particle Data Group et al., 2020). The simulated energy depositions are thus consistent with theoretical predictions for minimum-ionizing muons.

Distributions of photon arrival times are shown in Figure 35, for $x = 0$ cm and $x = \pm 80$ cm. Times are measured relative to the first photon detection. The $x = 80$ cm distribution exhibits a fast rise time and a decay time constant close to the value we defined (2.1 ns). When the muon hit is further away from the SiPMs, the photon arrival time distribution broadens due to geometrical effects. Populations of photons that first reflect off the far end of the paddle can also be observed. Given our empirically-derived effective light propagation speed $c_s = 15.4$ cm/ns, reflections should arrive 1.3 ns, 11.7 ns, and 22.1 ns after the initial

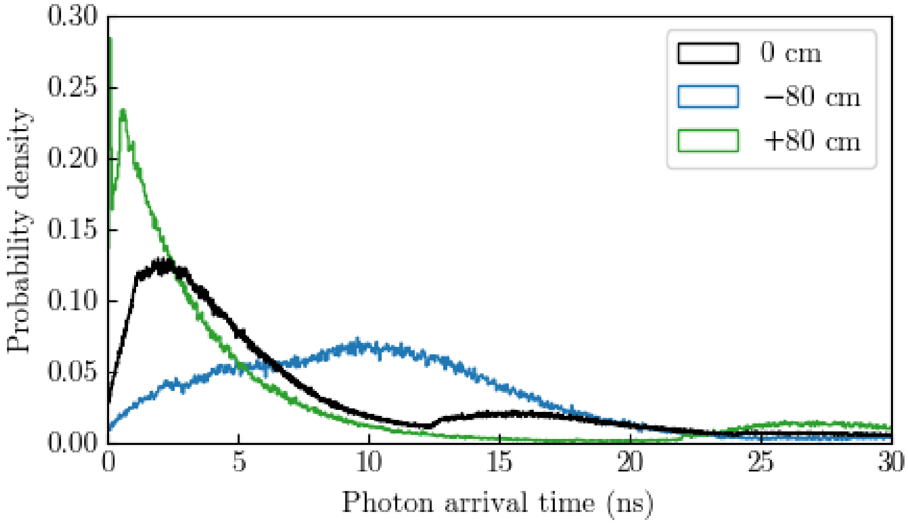

Figure 35: Distribution of simulated photon arrival times for 10^4 muon events with vertical tracks passing through $x = 0$ cm (black), -80 cm (blue), and $+80$ cm (green). The times are binned in 0.01 ns bins, and the distribution is normalized such that it represents a probability density.

photons at $x = -80$ cm, 0 cm, and 80 cm, respectively—the 0 cm and 80 cm reflections are visible.

The number of photons detected by the SiPMs in the first few nanoseconds should be approximately proportional to the peak voltage. We can therefore compare the x-dependence of the number of photons detected with the peak voltages measured in our data. We simulate 10^3 muons at $x = 0$ cm, 40 cm, and 80 cm, and we find the median number of photons detected within the first 5 ns and 10 ns after the initial photon arrives. The median number of photons versus x are plotted with the median peak voltages of our data in Figure 36. Each set of values is normalized to equal one at $x = 0$ cm. Medians are used rather than means to reduce the effects of Landau fluctuations and saturation (for the peak voltage measurements).

The variation in number of photons with x does not show good agreement with the peak voltage data, particularly at the edges, and it strongly depends on the timing window of photons being counted. One parameter that influences x-dependence is the "reflectivity" R

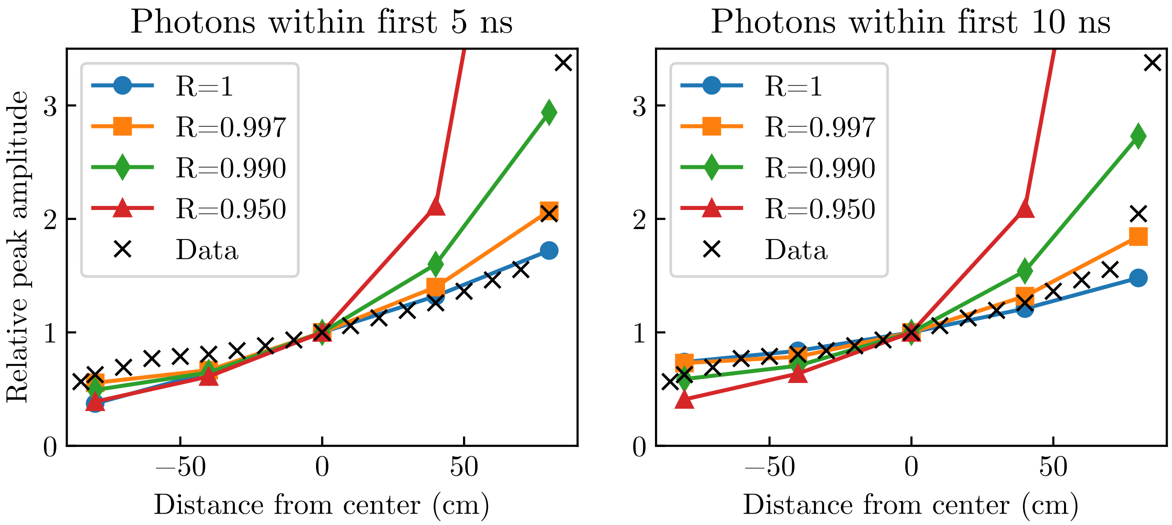

Figure 36: Relative peak amplitude versus x, estimated from the number of photons detected in the first 5 ns (left) and 10 ns (right), normalized to equal one at $x = 0$ cm. Results for simulations with reflectivity set to 100% (blue circles), 99.7% (orange squares), 99% (green diamonds) and 95% (red triangles) are shown, as well as normalized median peak amplitudes from our data (black xs).

at the scintillator-air boundary, which introduces a probability of $(1 - R)$ of being absorbed at the boundary, while transmission and reflection probabilities are calculated normally otherwise (e.g. due to dirt on the surface; Dietz-Laursonn, 2016). We simulate an additional 10^3 muons at $x = 0$ cm, 40 cm, and 80 cm for R values of 100%, 99.7%, 99%, and 95%. It is possible that this parameter may be responsible for the discrepant peak voltages we measure towards the paddle edges, particularly at $x = 80$ cm and $x = 85$ cm. However, fine-tuning of the simulation to the data requires a more realistic estimate of the simulated traces and peak voltages.

3.3.2 Simulation of Nuclei

To investigate the TOF response to particles other than atmospheric muons, we simulate slower and heavier particles including protons, helium-4 nuclei, and carbon-12 nuclei. Since energy losses described by the Bethe equation include a factor z^2/β^2, higher energy depositions E_{dep} can be expected versus minimum-ionizing muons. To avoid simulating particles

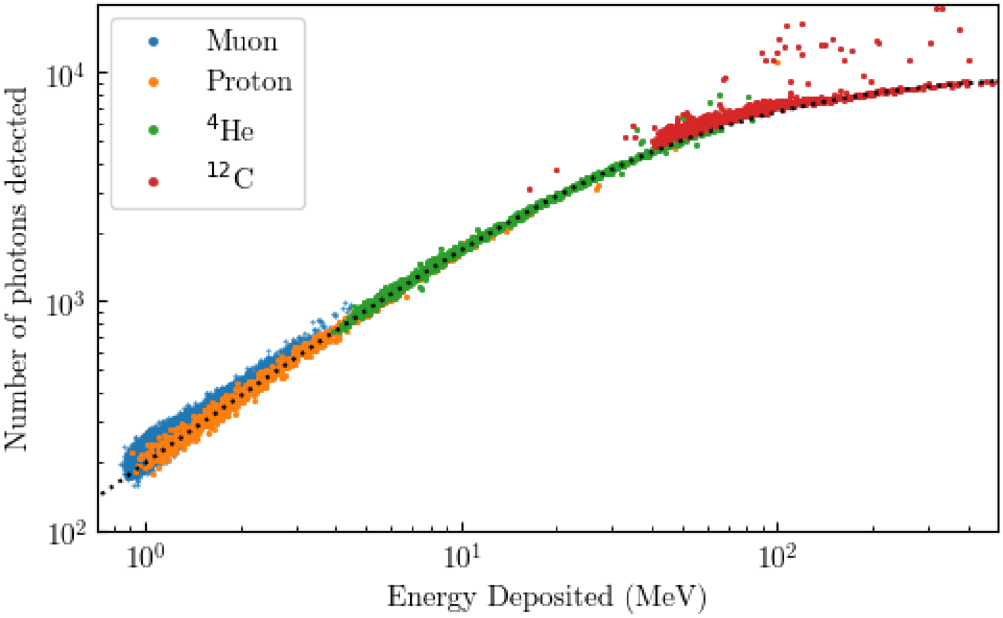

Figure 37: Simulated number of detected photons at one end of the paddle versus $E_{\rm dep}$, for 10^4 muons (blue), protons (orange), helium-4 nuclei (green) and carbon-12 nuclei (red). The expected behavior due to Birks' formula, number of photons $\propto E_{\rm dep}/(1+E_{\rm dep}/(50.4\ {\rm MeV}))$ is shown (dotted black line).

getting trapped in the scintillator while also getting a wide $E_{\rm dep}$ distribution, values of β were drawn uniformly between 0.3 and 1.0. For each particle species, 10^4 particles with various β are fired vertically through the center of the paddle.

A plot of the number of photons detected at one end of the paddle versus $E_{\rm dep}$ is shown in Figure 37. As expected, the slower, higher-z particles have higher $E_{\rm dep}$ than muons, typically. The number of detected photons is approximately linear with $E_{\rm dep}$ at small $E_{\rm dep}$ values, before leveling off at higher values, due to the Birks' constant we include in the simulation. The number of photons produced as a function of $E_{\rm dep}$ shows little dependence on particles species.

Distributions of photon arrival times are shown in Figure 38, for the different particle species. As before, times are measured relative to the first photon detection. No significant difference is observed in the distributions for the different particles.

We also investigate the effect of the angle of incidence of the incoming particle on the

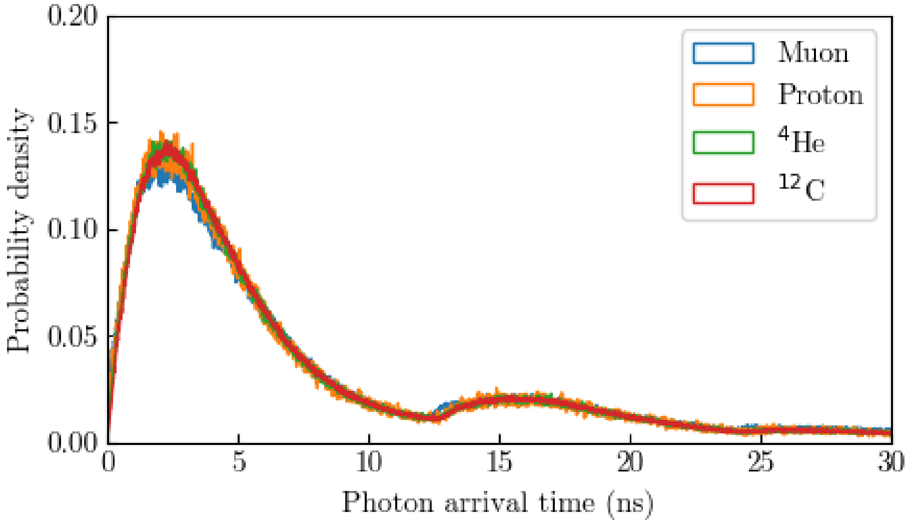

Figure 38: Distributions of simulated photon arrival times for 10^4 muons (blue), protons (orange), helium-4 nuclei (green) and carbon-12 nuclei (red). All particles are fired along vertical tracks passing through $x = 0$ cm. The times are binned in 0.01 ns bins, and the distributions are normalized such that they represent probability densities.

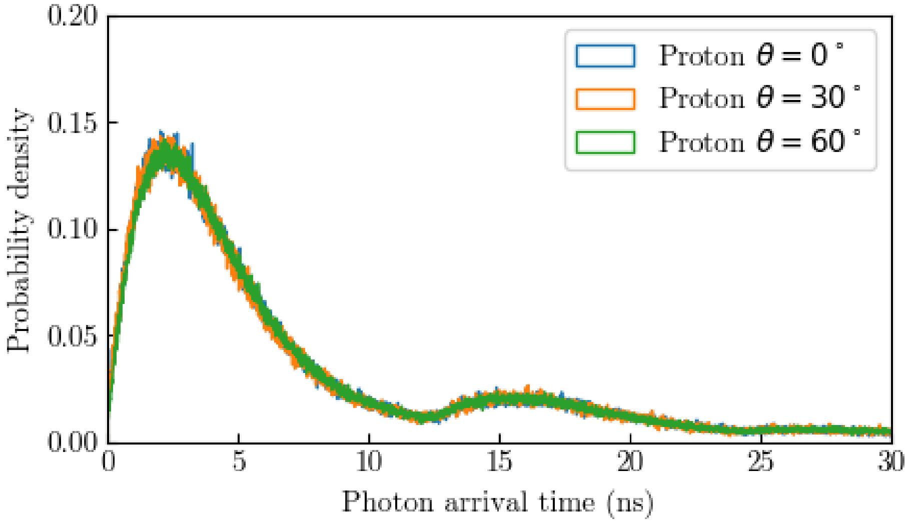

Figure 39: Distributions of simulated photon arrival times for 10^4 muons (blue), protons (orange), helium-4 nuclei (green) and carbon-12 nuclei (red). All particles are fired along vertical tracks passing through $x = 0$ cm. The times are binned in 0.01 ns bins, and the distributions are normalized such that they represent probability densities.

photon arrival time distribution. We simulate 10^4 protons impinging on the top of the paddle at its center with momentum vectors angled 30° and 60° from the vertical, with the horizontal component of the momenta in the $-x$ direction. Distributions of photon arrival times are shown in Figure 39, for protons fired at different angles. No significant difference is observed in the distributions for the different angles.

These simulations indicate that trace shape is determined almost entirely by x and E_{dep}, with little dependence on particle species, β, or angle of incidence (after E_{dep} is determined).

3.3.3 Trace Generation

For accurate comparison between simulations and data, the simulation of traces is necessary. The trace is determined by the response of the SiPMs, preamp, and readout board to the signal generated by photons detected by the SiPMs. Two methods of trace generation are explored. In the first, we use trace templates derived from our data. In the second, we model the trace as the sum of single-photoelectron (SPE) pulses occurring at the simulated photon arrival times—the SiPM response can generally be described to good approximation by a superposition of SPE pulses (Ghassemi et al., 2018). We will refer to these as the template method and the SPE method.

In the template method, traces are generated for given x and E_{dep} as follows:

1. Trace templates derived from our data are interpolated in x onto a grid of times with 0.5 ns spacing.
2. Each trace is scaled to a V_{peak} drawn from an empirically-derived distribution dependent on x and E_{dep}.
3. Gaussian-distributed white noise is added to each trace.
4. Traces are truncated at 950 mV, the top of the DRS4 voltage range.

This approach is motivated by the finding in Section 3.2 that traces at a given x position

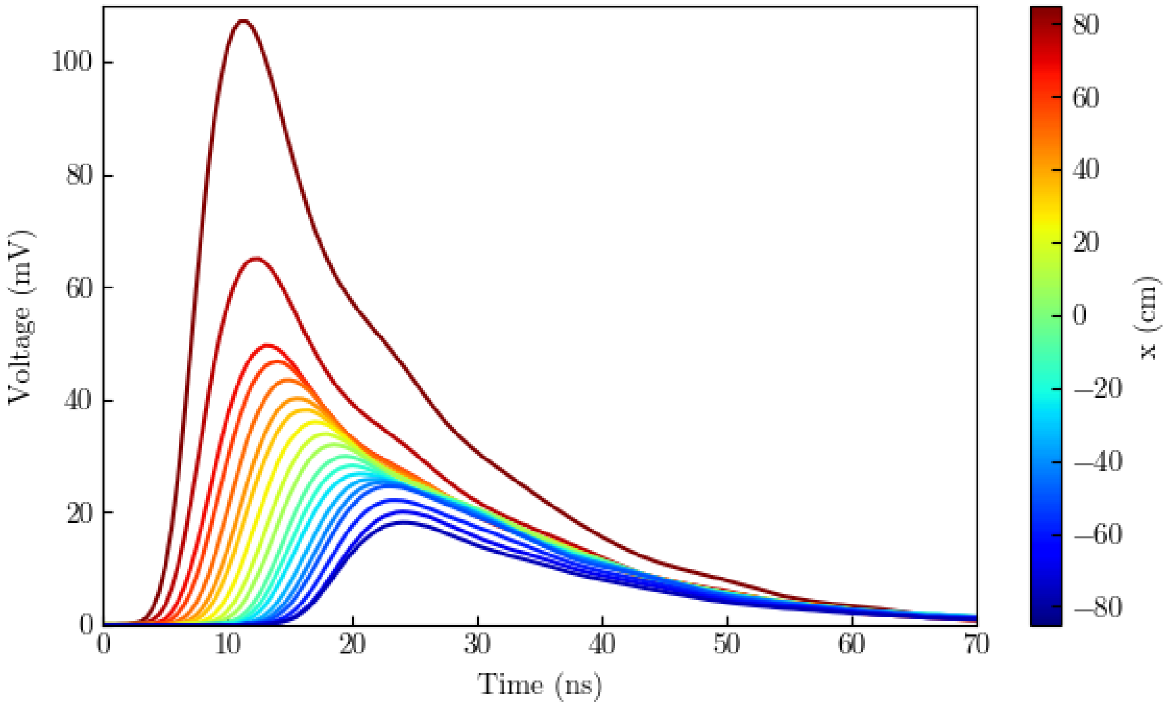

Figure 40: Trace templates, derived from our data as the median traces seen at 19 different values of the incident particle position along the paddle (x). The x-dependence of shape, peak amplitude, and timing are included in the templates.

all have the same approximate shape, scaled to different peak voltages V_{peak} and shifted in time.

Trace templates are derived by taking the median of the traces from muon data taken at ten different x positions. The templates are shown in Figure 40. The x-dependence of the templates can be observed: for particles impinging on the scintillator further away from the SiPMs, the traces become smaller and broader, and arrive later in time. Templates may be linearly interpolated for any x between −85 cm and +85 cm.

The V_{peak} distribution can be derived by making several assumptions. First, if the most-likely peak voltage $\overline{V}_{\text{peak}}$ scales linearly with number of detected photons, then from Birks' formula, $\overline{V}_{\text{peak}}$ can be written as

$$\overline{V}_{\text{peak}}(x, E_{\text{dep}}) = f(x)\frac{E_{\text{dep}}}{1 + E_{\text{dep}}/(50.4\ \text{MeV})} \tag{41}$$

x (cm)	$f(x)$ (mV/MeV)	x (cm)	$f(x)$ (mV/MeV)
		0	32.0
−85	18.2	10	33.9
−80	20.1	20	36.0
−70	22.1	30	38.1
−60	24.6	40	40.2
−50	25.3	50	43.5
−40	25.8	60	46.8
−30	26.8	70	49.6
−20	28.3	80	65.0
−10	29.9	85	107.2

Table 2: Most-likely peak voltages per 1 MeV of energy deposited at different x positions.

for vertical tracks, where $f(x)$ is the ratio of the most-likely V_{peak} to E_{dep} at low energy, and is x-dependent. If the most-likely energy deposition for vertical muons corresponds to the mode of the measured V_{peak} distributions, then $f(0) = 32.0$ mV/MeV. Values of $f(x)$ measured at other values of x are tabulated in table 2. Scatter around $\overline{V}_{\mathrm{peak}}$ is expected from Poisson fluctuations and other effects. Our simulations showed fluctuations in the number of photons detected for a given E_{dep} that were approximately Gaussian with standard deviations ~10% of the mean number of photons, so we make the assumption that V_{peak} will be Gaussian-distributed with standard deviation $\sigma_{V_{\mathrm{peak}}} \propto \overline{V}_{\mathrm{peak}}$. We derive $\sigma_{V_{\mathrm{peak}}}$ by comparing the expected V_{peak} distribution for Landau-distributed muon energy depositions with our measured V_{peak} distribution at $x = 0$ cm. The expected V_{peak} distribution is found by drawing 10^6 samples from a Landau distribution, converting the energy to a voltage with equation 41, then adding Gaussian noise. With $\sigma_{V_{\mathrm{peak}}} = 0.14\overline{V}_{\mathrm{peak}}$ the data can be reproduced for $V_{\mathrm{peak}} \lesssim 50$ mV, as shown in Figure 41. The expected V_{peak} distribution without Gaussian noise added is also shown. At higher V_{peak} values, the data are in excess of the predicted values. The excess region contains ~10% of the data. We find that neither noise with a E_{dep}-dependent Gaussian distribution nor more asymmetric distributions (such as the exponential distribution) can reproduce the excess, which resembles a bump more than the broadening of a single Landau distribution. This excess may be due to events that

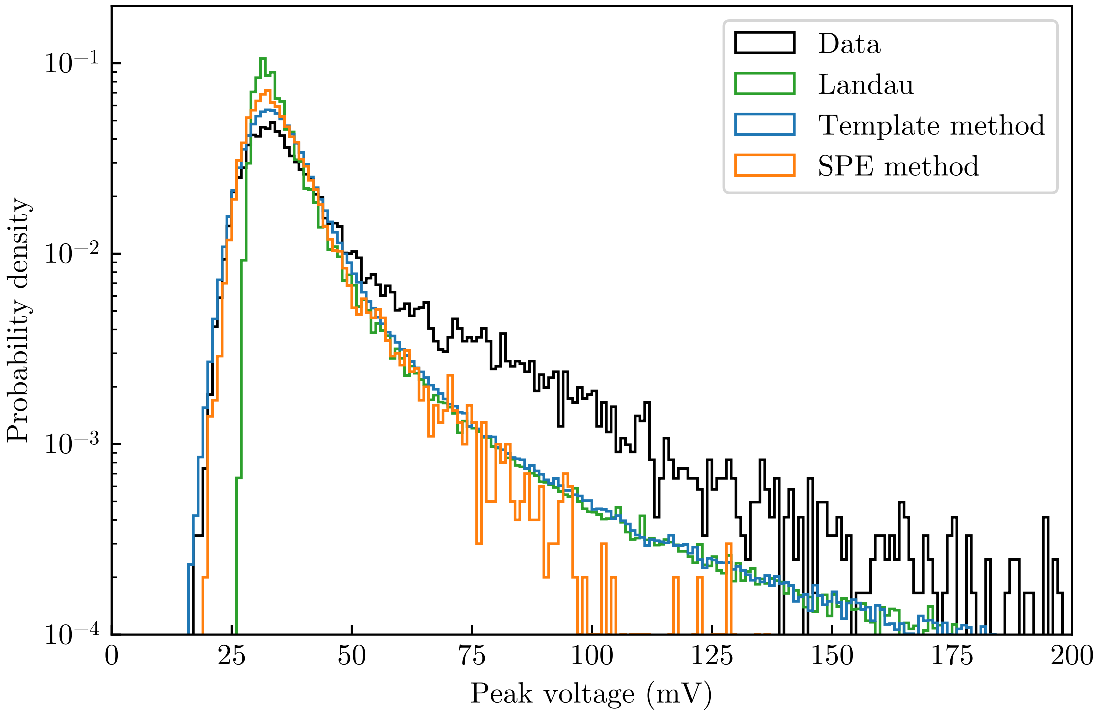

Figure 41: Peak voltage distributions for vertical muons at $x = 0$ cm from data (black) and generated with the template method from 10^6 Landau-distributed E_{dep} (blue) and the SPE method (orange). Landau-distributed energies times 32 mV/MeV are also shown. The distributions derived with the template and SPE methods match the data below ~50 mV, but underpredict the data at higher V_{peak} values. The excess events in the data may be due to non-minimum-ionizing events.

are not minimum-ionizing, such as slower protons or simultaneous muon hits.

The noise in V_{peak} at fixed E_{dep} may be correlated between paddle ends. From the V_{peak} differences between paddle ends in our vertical muon data taken at $x = 0$ cm, we estimate that the uncorrelated noise in the two V_{peak} values is $\sigma_{V_{\mathrm{peak}},\mathrm{uncorr}} = 0.11\overline{V}_{\mathrm{peak}}$, implying a correlated noise component of $\sigma_{V_{\mathrm{peak}},\mathrm{corr}} = 0.09\overline{V}_{\mathrm{peak}}$.

In the final steps, white noise is added to each trace value, then values greater than 950 mV are set to 950 mV. The white noise is Gaussian-distributed with standard deviation 0.54 mV, the mean pedestal RMS value measured in Section 3.2.2.

The second method of generating traces, the SPE method, aims to more realistically model the relevant optical physics and electronics, thereby testing the assumptions of the template method. In the SPE method, traces are generated as follows:

1. An array of photon arrival times is found from simulations for each trace.
2. For each photon, a SPE is shifted in time and interpolated onto a grid of times with 0.5 ns spacing, multiplied by an integer drawn from the crosstalk distribution, and added to the trace.
3. Gaussian-distributed white noise with standard deviation 0.54 mV is added to each trace.
4. Traces are truncated at 950 mV, the top of the DRS4 voltage range.

We neglect the effects of dark counts and afterpulsing, which should have little influence on the leading edges of the traces.

The SPE pulse shape from a SiPM can be described by two falling exponentials with the slower time constant related to the SiPM cell recovery time (Corsi et al., 2006; Klanner, 2019), before our preamp circuit's pulse shaping. While the SiPM SPE response might be determined by simulating the electronics (e.g. Niggemann et al., 2015), we aim to measure the SPE shape, since our fast readout of traces allows it. However, as a consequence of our version 4 (v4) preamp board's dynamic range, SPEs are difficult to detect above the noise, complicating the measurement. In contrast, the earlier version 2 (v2) preamp board clearly resolves SPEs, with peak voltages ∼2 mV, compared to a noise RMS of ∼0.5 mV. The v2 preamp can therefore be used to determine the amount of SPEs that result from a light-emitting diode (LED), and subsequently, measurements of the LED with a v4 preamp many times can be averaged to find the SPE trace, scaled to the expected amount of SPEs.

Measurements were taken on August 6 2019 with an LED pulser and SiPM on a preamp board, placed in a dark box. Version 4.1 preamps were used, though the version 4.2 preamps are expected to behave identically. A simple circuit triggered the LED pulser and SiPM readout, with a short delay. Using the v2 preamp, we determined that an LED voltage of

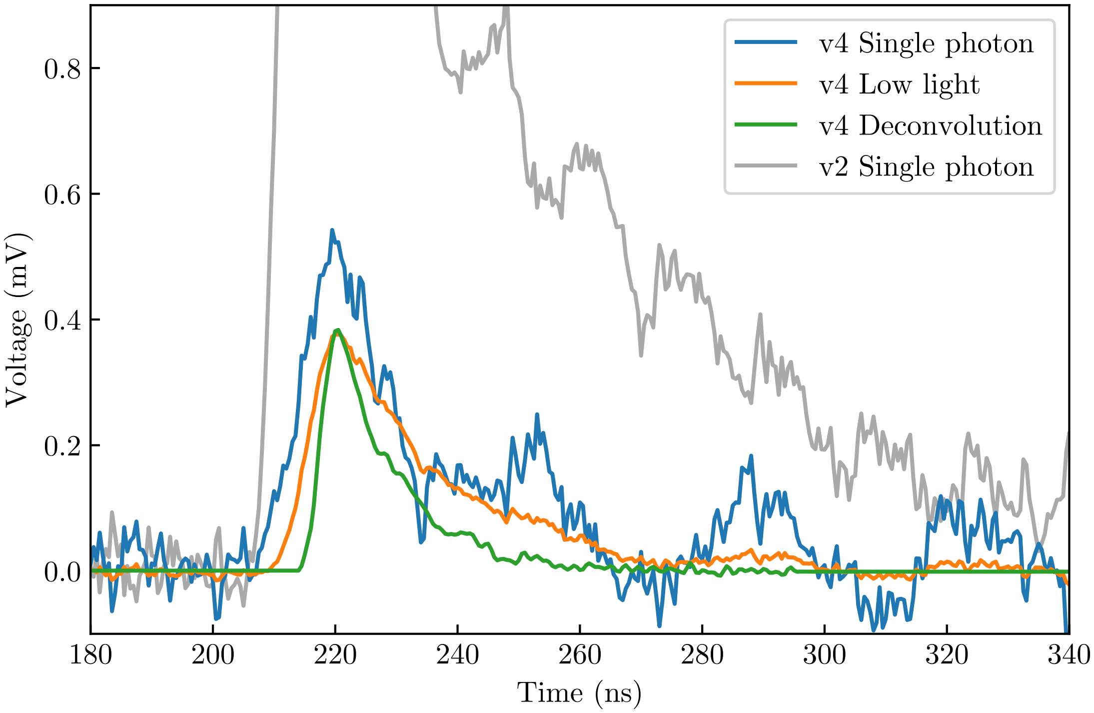

Figure 42: SPE traces of the v4 preamp derived from single-photon data (blue), low-light data (orange), and the deconvolution of the mean vertical muon trace at $x = 0$ cm with the corresponding simulated photon arrival time distribution, with 100% reflectivity (green). The deconvolution is narrower than the measured SPE traces, but becomes broader at lower reflectivity since the time distribution narrows. The clearly-resolved v2 preamp SPE trace derived from single-photon data, which peaks ∼2 mV, is also shown (gray).

5.35 mV produces on average one SPE, and a voltage of 5.60 mV produces on average 6.22 SPEs. We then took 10^3 events with a v4 preamp at these single-photon and low-light levels. The average traces (with the low-light SPE divided by 6.22) are shown in Figure 42. The SPE peak voltage is ∼0.4 mV, implying that the typical number of photons contributing to the leading edge of minimum-ionizing particle traces at $x = 0$ in a 1.8 m paddle (peak voltage ∼32 mV) is ∼80.

The SPE pulse was also estimated semi-empirically from vertical muon data and simulated photon arrival times. The median trace for muons with vertical tracks passing through $x = 0$ cm was deconvolved with the photon arrival distribution for $x = 0$ cm vertical muon simulations with 100% reflectivity. The trace and time distributions were first interpolated onto 0.2 ns grids, then smoothed with Gaussians with 0.5 ns standard deviation to remove the large oscillations that otherwise appear in the deconvolution. The resulting SPE is shown in Figure 42, scaled to the height of the low-light SPE. This SPE pulse, by definition, returns the empirical muon trace when convolved with the simulated photon arrival time distribution. The deconvolved SPE pulse is narrower than the measured ones, either due to timing jitter in the v4 SPE measurements or inaccuracies in the simulation. For example, simulations with lower reflectivity at the scintillator-air boundary have narrower time distributions, which would broaden the deconvolved SPE.

Crosstalk is a phenomena wherein single photons initiating avalanches in the SiPM pixels have a chance to induce avalanches in neighboring pixels, which may also initiate subsequent avalanches. The S13360 (prompt) crosstalk probability, the probability that > 0 avalanches will be produced after an initial avalanche, is $p_{\mathrm{CT}} \approx 0.1$ for our overvoltage of 7 V, at 25°C (Ghassemi et al., 2018). We estimate the resulting probability mass function of the total number of crosstalk pixels $P(n)$ with a Monte Carlo simulation. We assume that for each pixel that fires, each of four adjacent pixels has a probability p_{adj} of firing, if it has not done so already, though this is a simplification (e.g. Rosado & Hidalgo, 2015). This probability is related to the other by $(1-p_{\mathrm{adj}})^4 = 1-p_{\mathrm{CT}}$ (Niggemann et al., 2015), giving $p_{\mathrm{adj}} = 0.026$. We simulate cells firing due to crosstalk a maximum of 5 times on an 11×11 grid whose central pixel has fired, representing a portion of the SiPM. The result of 10^7 crosstalk simulations is shown in Figure 43. $P(n)$ closely follows

$$P(n) = (1 - p_{\mathrm{CT}})(p_{\mathrm{CT}})^n \tag{42}$$

We tabulate the $P(n)$ values derived from the Monte Carlo simulations in table 3.

We generate traces for the 10^4 vertical muon simulations at $x = 0$ cm with the SPE-based method. The median and central 68% of the trace distributions are shown in Figure 44 for the low-light SPE and deconvolved SPE shapes. A fraction of the number of simulated photons

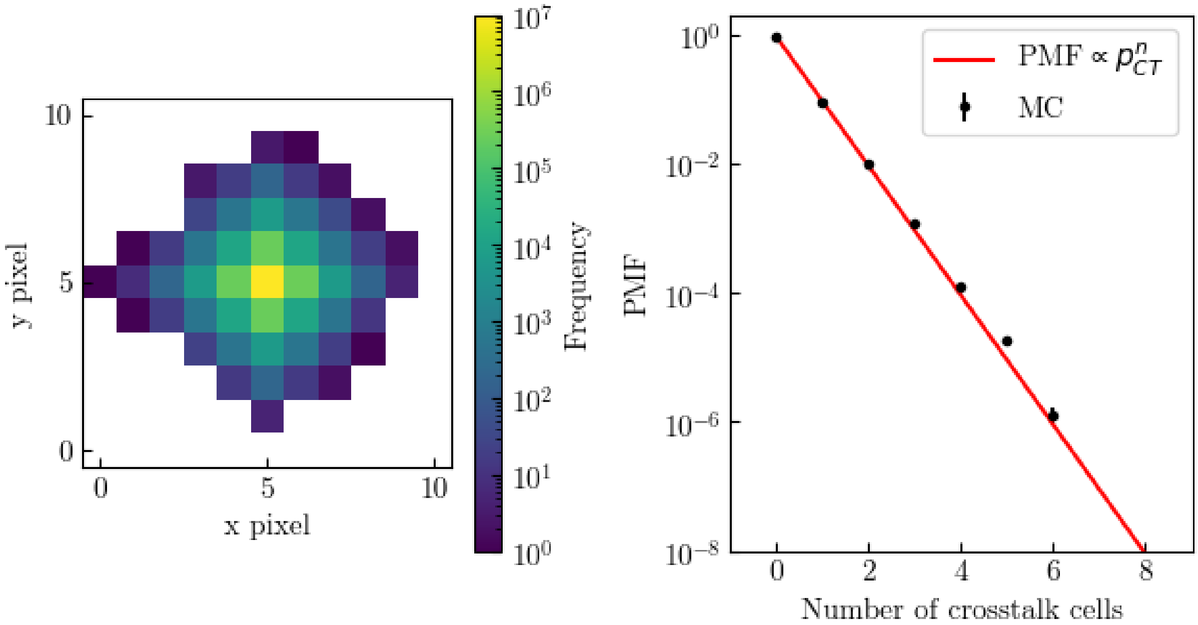

Figure 43: Results of 10^7 crosstalk simulations, showing spatial distribution of all cell firings (left) and the probability mass function of the number of the crosstalk cells (right). The Monte Carlo probabilities (black) are nearly log-linear with number of crosstalk cells, and are closely-approximated by equation 42 (red). The error bars represent estimates of Poisson uncertainty. Only the error on the last data point is large enough to be visible.

is used such that the median V_{peak} of the data is recovered—the physical cause of this could be lower reflectivity, mismodeled optical coupling, or lower photon detection efficiency. The median and central 68% of traces from our data and generated with the template method are also shown. The median traces generated with the template method and the SPE method using the deconvolved SPE match the median data trace by construction, while the low-light SPE produces traces that are wider than the data. The SPE method also induces jitter in the trace timing resulting from optical processes. The CF times measured at one paddle end have a spread of 0.19 ns, accounting for about half the uncertainty contributing to $\sigma_{\text{TOF}} = 0.266$ ns.

The SPE method leads to V_{peak} distributions consistent with the template method, as shown in Figure 41. Also like the template method, the SPE method underpredicts the V_{peak} distribution at high V_{peak}, relative to the data. The uncorrelated noise in between V_{peak}

Number of cells	Probability
1	0.9000102
2	0.0887907
3	0.0098719
4	0.0011788
5	0.0001285
6	0.0000186
7	0.0000013

Table 3: Probabilities for total number of SiPM cells that fire due to a single incident photon, for a crosstalk probability of 0.1. Probabilities are derived from 10^7 simulations.

between paddle ends is found to be $\sigma_{V_{\rm peak},{\rm uncorr}} = 0.10\overline{V}_{\rm peak}$, close to the value seen in our data.

The x-dependence of the medians of the $V_{\rm peak}$ distributions for the SPE method, applied to simulations with different reflectivities, is shown in Figure 45. While the template method matches the data, the SPE method does not, for any reflectivity value. Furthermore, the SPE method traces using the deconvolved SPE shape derived from $x = 0$ cm data deviate slightly from the trace shape at different x values, as shown in Figure 46.

We conclude that the template method reproduces traces with the properties observed in our data. Two exceptions are the fat tail of the peak voltage distribution in the data, which we assume comes from slow particle and multi-particle events and the part of the trace following the peak which shows more variance in the data, and is not captured by using a single template for each x value. The SPE method requires more tuning of the simulation to match the data. At present, a single set of simulation parameters and SPE shape does not simultaneously reproduce the trace distributions measured at multiple different x values.

3.4 Measurement of Energy Deposition

We next develop a method to estimate $E_{\rm dep}$ from the traces measured at both paddle ends. $E_{\rm dep}$ carries information about the incident particle and can thus assist event reconstruction, though Landau fluctuations can be significant. Two trace properties, the peak voltage $V_{\rm peak}$ and integrated charge $Q_{\rm int}$ are sensitive to $E_{\rm dep}$, with $V_{\rm peak}$ sensitive to the photons

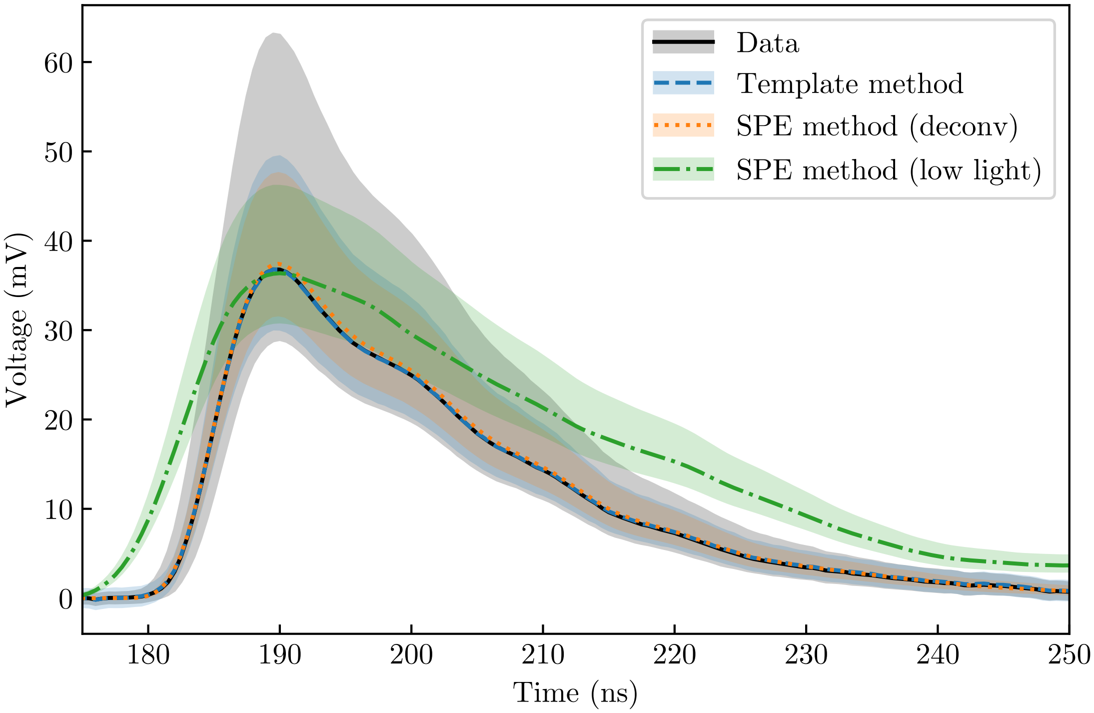

Figure 44: Simulated traces for vertical muons at $x = 0$ cm. 10^4 traces are generated with the template method (blue dashed line), SPE method with the deconvolved SPE (orange dotted line), and SPE method with the low-light SPE (green dash-dotted line). Data are also shown (black). Lines and shaded region represent the medians and central 68% of the trace distributions.

contributing to the initial few nanoseconds of the pulse and Q_{int} potentially being sensitive to all the scintillation light detected. Distributions of these quantities measured from muon data at $x = 0$ cm, with three different integration windows for Q_{int}, are shown in Figure 47, normalized to their most-likely values. We find that the distributions have similar widths, suggesting that they are all equally good tracers of E_{dep}. We therefore focus only on V_{peak} in this work.

An estimate of E_{dep} can be obtained from the V_{peak} measured at one end by inverting equation 41, yielding

$$E_{\text{dep}}(x, V_{\text{peak}}) \approx \frac{V_{\text{peak}}}{f(x) - V_{\text{peak}}/(50.4\ \text{MeV})} \tag{43}$$

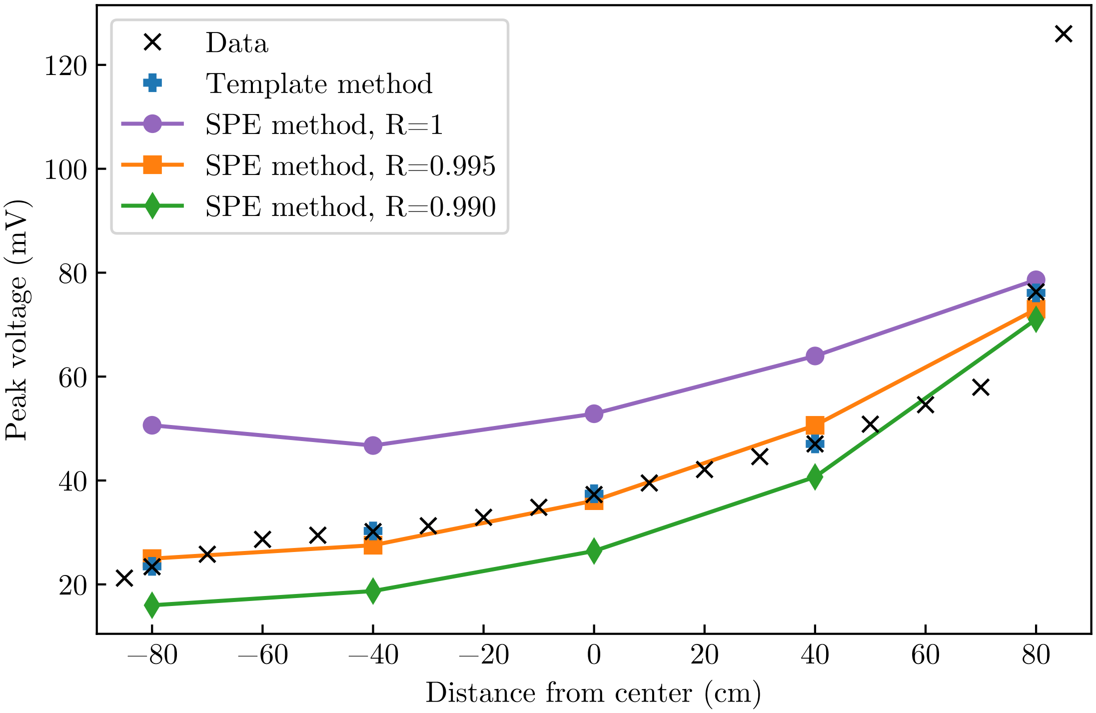

Figure 45: Peak voltages versus position along the paddle, x, from data (black), the template method (blue crosses), and the SPE method for simulations with reflectivity set to 100% (purple circles), 99.5% (orange squares), and 99% (green diamonds). The template method reproduces the x-dependence, while the SPE method does not.

However, uncertainties are not accounted for by this equation.

We instead estimate E_{dep} using the likelihood function for the two peak voltages, V_1 and V_2, and the measured time difference Δt. The likelihood is given by

$$\begin{aligned} L(\Delta t, V_1, V_2|x, E_{\text{dep}}) &= P(\Delta t|V_1, V_2, x, E_{\text{dep}})P(V_1|V_2, x, E_{\text{dep}})P(V_2|x, E_{\text{dep}}) \quad (44) \\ &= P(\Delta t|V_1, V_2, x, E_{\text{dep}})P(V_1|x, E_{\text{dep}})P(V_2|x, E_{\text{dep}}) \quad (45) \end{aligned}$$

where we have assumed V_1 and V_2 are independent for a given x and E_{dep}. We found these probabilities to be approximately Gaussian in the preceding sections. The Δt distribution has a mean of $x/(c_s/2)$ and standard deviation $\sigma_{\Delta t}$, equivalent to σ_{t1-t2}, measured in Section 3.2. Also in Section 3.2, $\sigma_{\Delta t}$ was found to exhibit dependence on V_1 and V_2 at low peak voltages, while any dependence on x was too small to be observed. The peak voltages

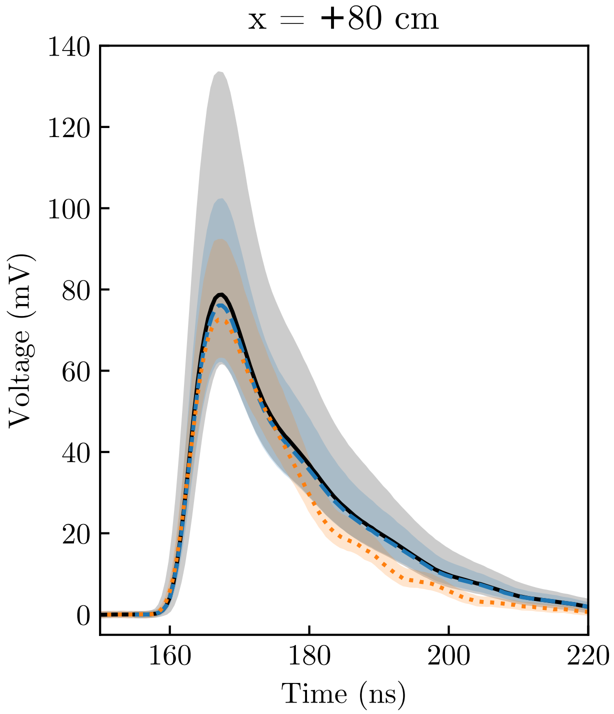

Figure 46: Simulated traces for vertical muons at $x = 80$ cm (left) and $x = -80$ cm (right). 10^4 traces are generated with the template method (blue dashed line) and SPE method with the deconvolved SPE (orange dotted line). Data are also shown (black). Lines and shaded region represent the medians and central 68% of the trace distributions.

are distributed as Gaussians with means $\overline{V}_{\text{peak}}(x, E_{\text{dep}})$ given by equation 41 and standard deviations $\sim\alpha\overline{V}_{\text{peak}}(x, E_{\text{dep}})$, with $\alpha = 0.15$. A consequence of the standard deviation's E_{dep} dependence is that the $P(V_1|x, E_{\text{dep}})$ is not maximized at $V_1 = \overline{V}_{\text{peak}}(x, E_{\text{dep}})$, but at $V_1 = \frac{-1+\sqrt{1+4\alpha^2}}{2\alpha^2}\overline{V}_{\text{peak}}(x, E_{\text{dep}})$.

As an example, the likelihood function is shown for $V_1 = V_2 = 32$ mV, $\Delta t = 0$ ns in Figure 48. Confidence intervals on E_{dep} or x may be found with the profile likelihood method (e.g. Rolke et al., 2005; Cowan et al., 2011; Particle Data Group et al., 2020), based on the difference in log likelihood values with the maximum likelihood, $\Delta \ln L = \ln L_{\max} - \ln L(\Delta t, V_1, V_2)$. If we are only interested in E_{dep}, the 1σ confidence interval is found where $2\Delta \ln L = 1$, giving $E_{\text{dep}} = 1.00^{+0.11}_{-0.09}$ MeV. If we instead jointly estimate E_{dep} and x, the 1σ confidence intervals are found where $2\Delta \ln L = 2.3$, giving $E_{\text{dep}} = 1.00^{+0.18}_{-0.13}$

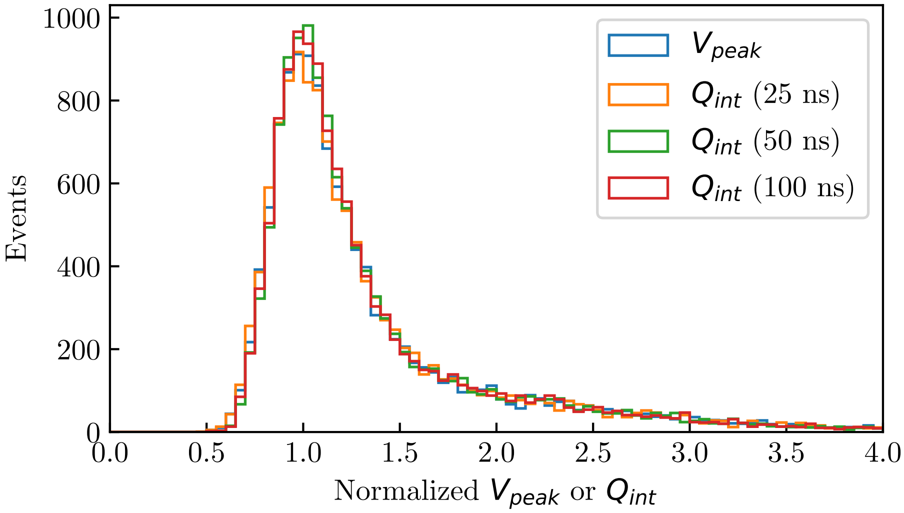

Figure 47: Peak voltage (blue) and integrated charge distributions, normalized to their most probable value, such that they peak at 1.0. Integrated charges are calculated by integrating over 25 ns (orange), 50 ns (green), and 100 ns (red) windows. The distributions all have similar widths.

MeV and $x = 0.0 \pm 4.3$ cm.

3.4.1 Lookup Table

The likelihood in the previous section is derived under multiple simplifying assumptions. More detailed likelihoods can be derived from simulations, aided by lookup tables (LTs). After obtaining many simulations with the same physical parameters (e.g. x, E_{dep}), distributions of V_1, V_2, and Δt can be measured, and the relative frequency of any (Δt,V_1, V_2) bin will correspond to its likelihood. Effects such as saturation, edge effects, or those due to position along the other paddle axis (perpendicular to x and the vertical) can be accounted for with LTs.

Saturation occurs when voltages exceed $V_{\text{max}} = 950$ mV prior to digitization by the DRS4, which truncates voltages to V_{max}. For saturated pulses, the consistent peak shape guarantees that the time over threshold t_{ot}, the time between the first and last trace bin with voltages equal to V_{max}, will be related to V_{peak}, and therefore also E_{dep}. In practice, separate

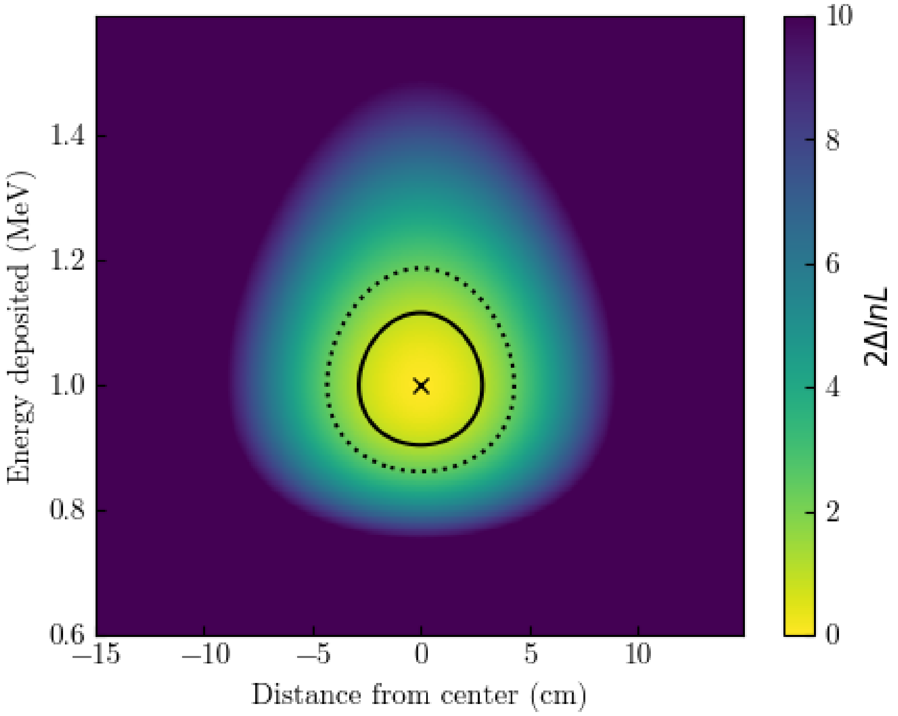

Figure 48: Likelihood as a function of E_{dep} and x, for $V_1 = V_2 = 32$ mV and $\Delta t = 0$ ns. The 1σ confidence regions for the estimation of a single parameter (solid black line) and joint estimation of two parameters (dotted black line) are shown. 1σ confidence intervals of $E_{\text{dep}} = 1.00^{+0.11}_{-0.09}$ MeV for single parameter estimation and $E_{\text{dep}} = 1.00^{+0.18}_{-0.13}$ MeV and $x = 0.0 \pm 4.3$ cm for joint parameter estimation are found.

LTs can be created for t_{ot} and the probabilities from the t_{ot} and V_{peak} LTs can be multiplied, since $P(t_{\text{ot}}, V_{\text{peak}}) = P(t_{\text{ot}}|V_{\text{peak}})P(V_{\text{peak}})$. The t_{ot} LT can be ignored for $V_{\text{peak}} < V_{\text{max}}$, since $P(t_{\text{ot}} = 0|V_{\text{peak}} < V_{\text{max}}) = 1$.

We create a set of LTs with x from 0 to 15 cm in steps of 1 cm and E_{dep} from 0.5 MeV to 2 MeV in steps of 0.05 MeV. For computational considerations, 10^5 traces are simulated for each LT, and V_1, V_2, and Δt are assumed to be independent—more simulations would be necessary to get sufficient statistics for the joint likelihood. An example likelihood function is shown in Figure 49 for the same set of V_1, V_2, and Δt as before (with $t_{\text{ot},1} = t_{\text{ot},2} = 0$ added). The LT approach performs similarly to the analytical approach in the previous section.

We also create a set of LTs spanning higher E_{dep} to test our ability to handle saturated pulses. These LTs have x from 0 to 15 cm in steps of 1 cm and E_{dep} from 0.5 MeV to 100

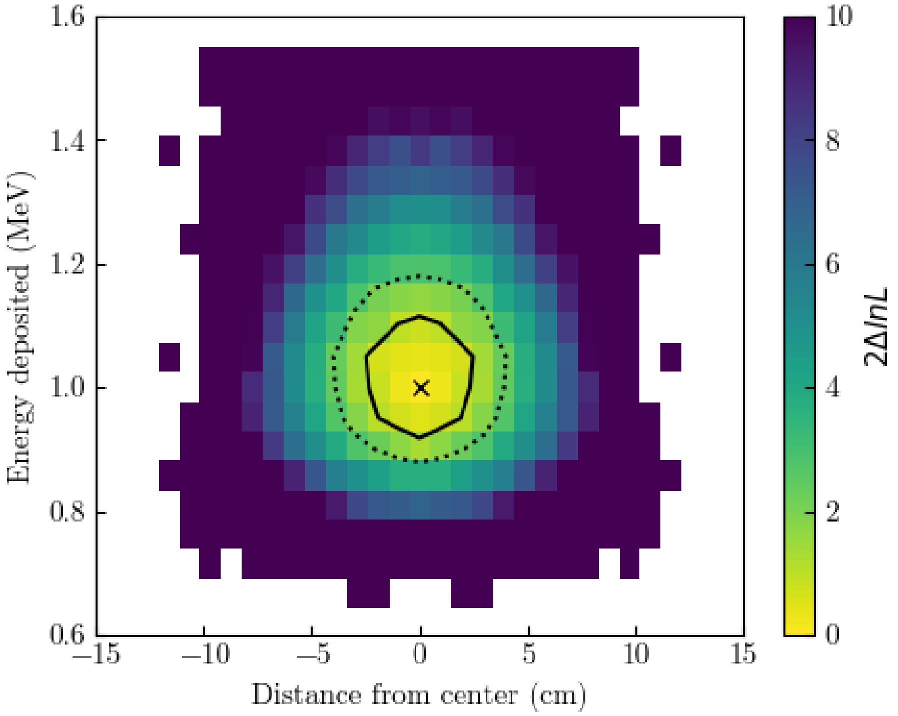

Figure 49: LT-derived likelihood as a function of E_{dep} and Δt, for $V_1 = V_2 = 32$ mV and $\Delta t = 0$ ns. Symbols as in Figure 48. Each pixel corresponds to a separate LT with 10^5 simulations. Blank pixels represent likelihoods of zero, indicating that the LTs contain no simulations with the given trace properties.

MeV in coarser steps of 0.5 MeV. As before, 10^5 traces are simulated for each LT. We then simulate 10^3 traces with the template method at $x = 0$ cm with E_{dep} uniformly distributed between 0.5 MeV and 100 MeV. Using the LTs, the maximum-likelihood E_{dep} is found for each pair of traces. The reconstructed E_{dep} values versus their true values are plotted in Figure 50. We find that E_{dep} for saturated pulses is reconstructed reasonably well using t_{ot}. Reconstruction loses sensitivity above ∼50 MeV, due to Birks' formula.

We note that LTs may also be implemented to store posterior probability distributions for E_{dep}, rather than likelihoods. Such an implementation requires a prior probability distribution to first be assumed for E_{dep}. Posterior LTs are not explored in this work.

While we have demonstrated the validity of LTs for E_{dep} reconstruction, it remains to be seen if this approach is feasible for the full TOF. It is possible different scintillator paddles will

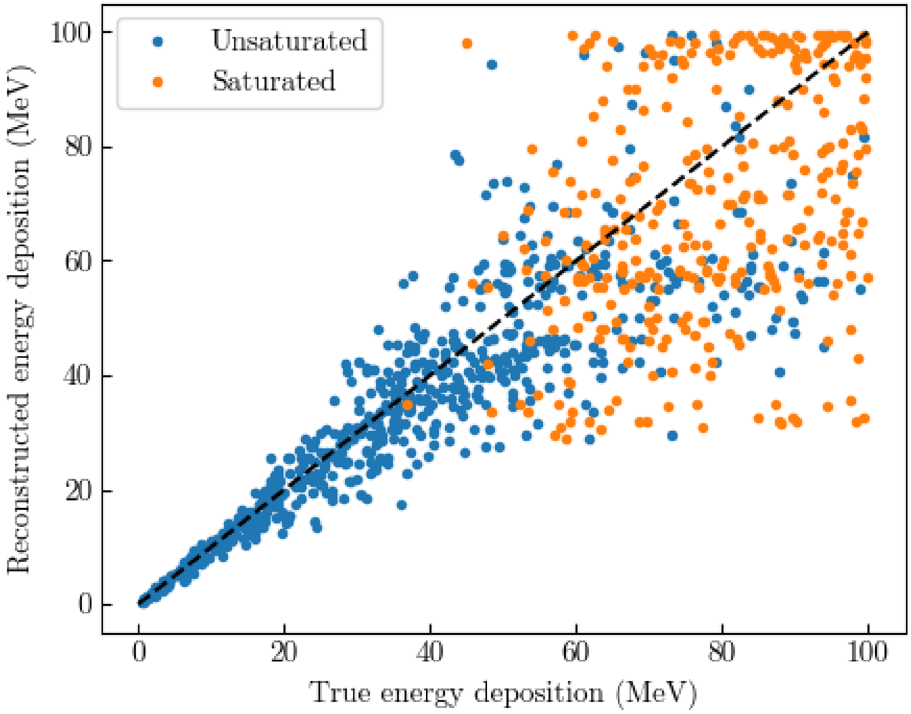

Figure 50: 10^3 reconstructed E_{dep} values versus their true values, for particles at $x = 0$ cm. Reconstructed E_{dep} values are the maximum-likelihood estimates, using LTs. Simulated events with (orange) and without (blue) saturated traces are indicated. Reconstruction loses sensitivity above ∼50 MeV, due to Birks' formula.

require unique LTs, spanning different temperatures. Dependence on additional parameters and increased resolution in the LT parameters would also increase the computational burden.

3.4.2 Charge Resolution

We explore charge reconstruction based on our ability to reconstruct E_{dep}. While charge reconstruction may follow a likelihood-based analysis similar to E_{dep}, we investigate the typical charge resolution using simulations of $z = 1$ and $z = 2$ particles at fixed β, recalling from the Bethe-Bloch equation that $E_{\text{dep}} \propto z^2$, before Landau fluctuations. In general, the charge resolution will depend on the incident particle properties and track geometry, however.

10^4 protons and helium-4 nuclei are simulated at $x = 0$ with vertical tracks. The particles

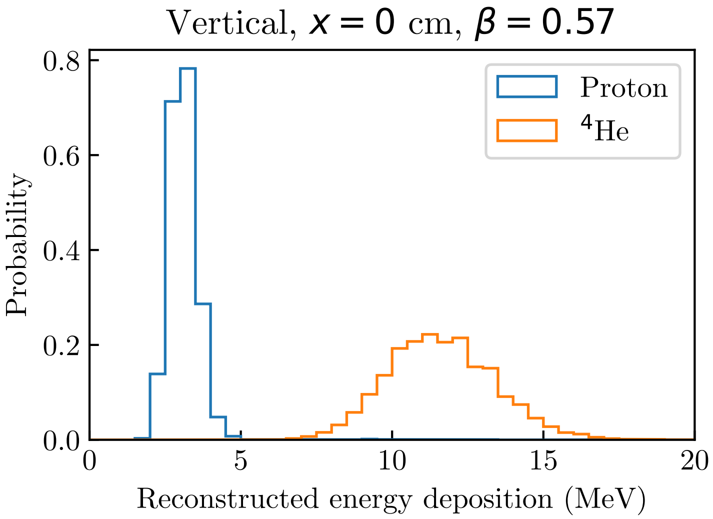

Figure 51: Distributions of reconstructed energy depositions for $\beta = 0.57$ protons and helium nuclei with vertical tracks at $x = 0$ cm. Charge resolutions of $\sim$8% and $\sim$17% of the electron charge can be inferred from the widths of the central 68% of the distributions for protons and helium nuclei, respectively.

are all given $\beta = 0.57$, corresponding to kinetic energies of $\sim$0.2 GeV per nucleon. Traces are generated with the template method, and the maximum-likelihood E_{dep} is found with LTs. The reconstructed E_{dep} distributions are shown in Figure 51. We find that the median and central 68% of the distributions are approximately 3.0 ± 0.5 MeV for the protons and 11.5 ± 2.0 MeV for the helium nuclei. This corresponds to a relation $E_{\text{dep}}/\text{MeV} \approx 3.0z^2$, implying a charge resolution $\sim$8% of the elementary charge for protons and $\sim$17% of the elementary charge for helium nuclei.

3.5 Readout Board and Flight Software

A readout board (RB) was custom-made for the GAPS TOF. Similar to the DRS4 evaluation board, the TOF RB connects external signals to the DRS4 inputs and digitizes the DRS4 outputs with a 14-bit analog-to-digital converter (ADC), the AD9245 from Analog Devices. A phase-locked loop synchronizes the DRS4 sampling rate with an external reference clock, which is expected to reduce timing jitter to $\sim$10s of ps (Ritt et al., 2010). Inputs are received

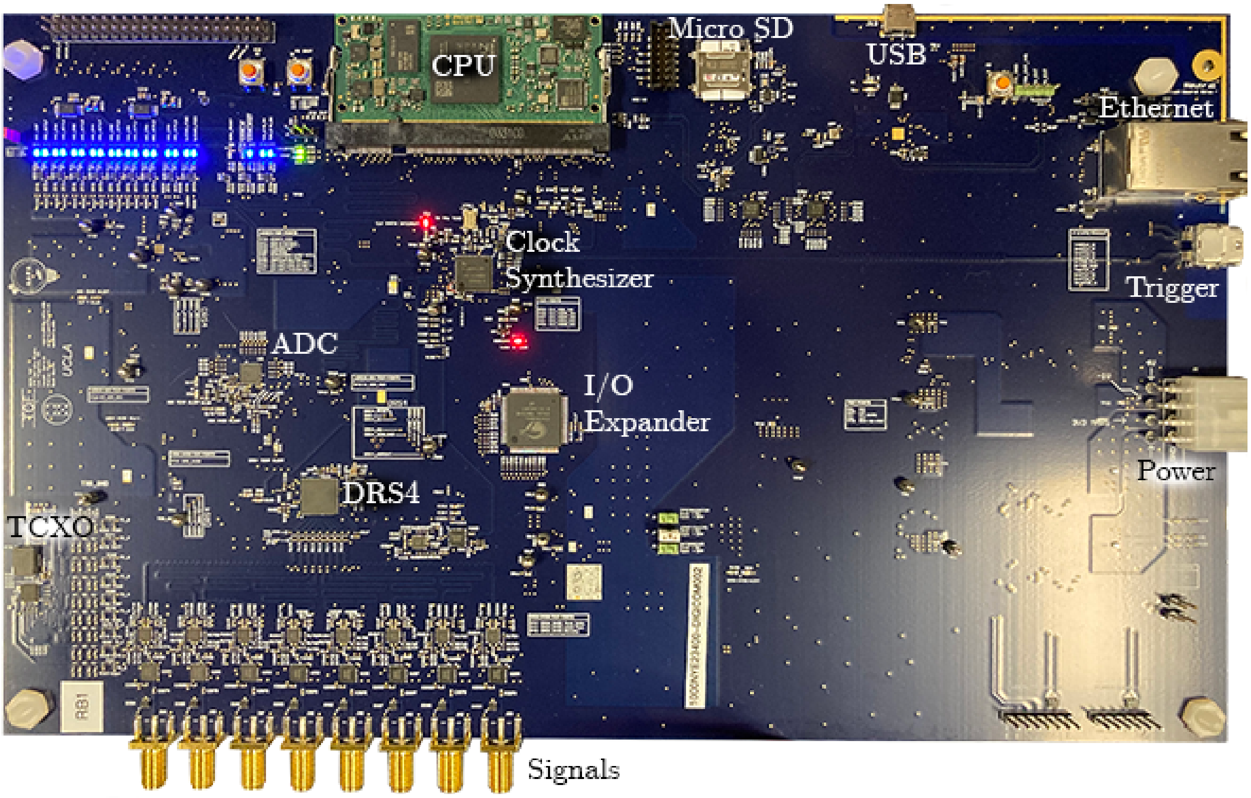

Figure 52: TOF readout board (version 2.4), with Mars ZX2 and Micro SD card installed. Some major components and I/O lines are labeled.

from the preamp boards via SMA connectors, and they pass through analog front ends before reaching the DRS4. The RB also has the capability to connext onboard voltage and timing calibration sources to the DRS4 inputs. In addition, the RB is equipped with a computer that receives the ADC output. Communication with the RB computer is facilitated through a gigabit Ethernet line. A trigger input line carries signals from the master trigger board and global clock. Additional GPIO, JTAG, and micro USB inputs/outputs are included for debugging purposes. The version 2.4 RB is shown in Figure 52, with major components labeled.

Testing of the version 2.4 RB with paddles began in September 2021. A custom Linux kernel was generated and installed on a micro SD card for controlling the Mars ZX2 computer. Prior to the completion of the TOF power board, the RB was powered with a bench power supply.

Software and firmware were developed to achieve the desired RB functionality. Three modes of operation were defined: voltage calibration, timing calibration, and external data-taking. In voltage-calibration mode, low-noise differential voltages are connected to the DRS4 inputs. In timing-calibration mode, a sine wave with known frequency from a temperature compensated crystal oscillator (TCXO) is copied and distributed to the DRS4 inputs. In external data-taking mode, the eight SMA lines are connected to the first eight DRS4 inputs, while a sine wave from an external clock is sent to the ninth.

Readout can be initiated by an external trigger signal or with software. Data are read out serially through the ADC, in the form of packets that include metadata. In addition to the ADC data, packets include head and tail bits, an event number, a timestamp, and the "stop cell" read out from the DRS4's stop shift register, as well as other information. The stop cell indicates which of the 1024 physical DRS4 cells corresponds to the first cell read out and saved in the data packet.

Data packets are written into memory on the RB computer before being sent to the TOF computer. To minimize dead time, a two-buffer scheme was implemented on the RB computer where data can be written to the second buffer while data in the first is being sent. Communication is implemented with ZeroMQ (Hintjens, 2013).

3.5.1 Voltage Calibration

Voltage calibration of the DRS4 is necessary to reduce noise and convert ADC values to voltages. The calibration source on the RB is the AD5675 from Analog Devices, a 16-bit digital-to-analog converter with a 0 to 2.048 V range. The voltages connected to the DRS4 IN+ and IN− inputs can be controlled through software. The read offset is also adjustable, and is set to 1.1 V to obtain a differential input range of −50 mV and +950 mV with the DRS4.

As described in the DRS4 data sheet[7], voltages are subject to "fixed-pattern offsets,"

---

[7] The DRS4 data sheet is available on the PSI website: `http://drs.web.psi.ch/datasheets`

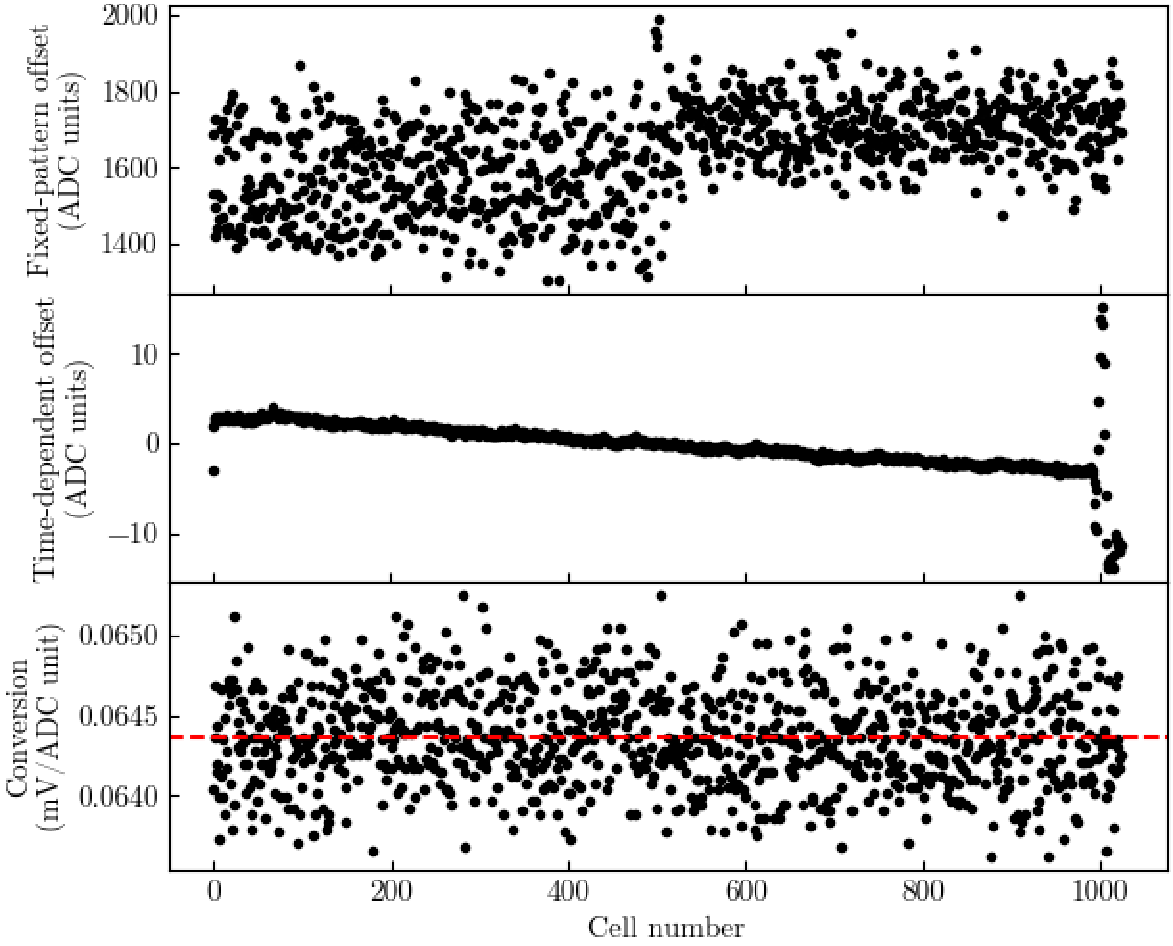

Figure 53: Voltage calibrations for a single DRS4 channel. Fixed-pattern offsets (top), time-dependent offsets (middle), and conversion factors from ADC units to voltages (bottom) are shown. The first 512 and last 512 cells have different fixed-pattern offset characteristics. The first two and last ∼30 cells have unusual time-dependent offsets. The mean conversion factor (dashed red line) is 0.0644 mV/ADC unit, slightly higher than expected.

which are constant for each cell. To measure these offsets, we take data in voltage-calibration mode with an input voltage of 0.0 V, with IN+ = IN− = 0.8 V. We take 5×10^3 samples of all 1024 cells in the nine channels, triggering readout with software. For each channel, the mean ADC value for each cell i is found by averaging the voltages in cell ($i +$ stop cell) modulo 1024. The first 5 cells after the stop cell of each trace are excluded since we observed significantly higher noise in these voltages. The resulting nine mean traces represent the fixed-pattern offsets of a given DRS4. An example for one channel is shown in the top panel of Figure 53. These offset traces are shifted by the stop cell and subtracted from each DRS4 trace. We observe the RMS noise (in ADC units) to decrease from approximately 124 to 5 after subtracting the fixed-pattern offsets.

Time-dependent offsets are also measured, following Stricker-Shaver et al. (2014). For each channel, the mean ADC value after fixed-pattern offset correction is found for each cell, relative to the stop cell. An example for one channel is shown in the center panel of Figure 53. These time-dependent offset traces are subtracted from each DRS4 trace, without any shifting. These offsets are typically only a few ADC units. The offsets are slightly large in the last ∼30 cells, but still do not exceed ∼15 ADC units.

Conversions between ADC units and voltages are measured for each cell. The expected values should be around 1 V/2^{14} ADC units, or ∼0.0610 mV/ADC unit. We measure the conversion by finding the fixed-pattern offsets at a second input voltage, then dividing the voltage difference by the ADC unit difference. An example for one channel is shown in the bottom panel of Figure 53. For the second input voltage, we send the DAC values of 25600 and 38400, corresponding to 0.8 V and 1.2 V, but measure 1.032 V and 1.217 V at IN− and IN+, giving a voltage difference of 185 mV. These conversions, shifted by the stop cell, are multiplied with each DRS4 trace after the offset corrections. The conversion factors are typically around 0.0644 mV/ADC unit, slightly higher than the expected value.

An additional step necessary for accurate voltage measurement is the removal of the DRS4's characteristic two-cell-wide spikes of ∼14.8 mV amplitude. We implement a spike-removal algorithm similar to that in the DRS4 evaluation board software. The algorithm handles single spikes and two adjacent spikes that are four cells wide. Spikes are considered real only if a spike is found at the same cell number in at least two channels. Voltages in cells affected by spikes are replaced by linear interpolations between the voltages in the cells on either side of the spike.

We apply the voltage calibrations and remove spikes from the 0 mV voltage calibration data. The resulting traces are consistent with white noise, as shown in Figure 54. After the means of each trace are subtracted (i.e. pedestal subtraction), the voltages for all cells

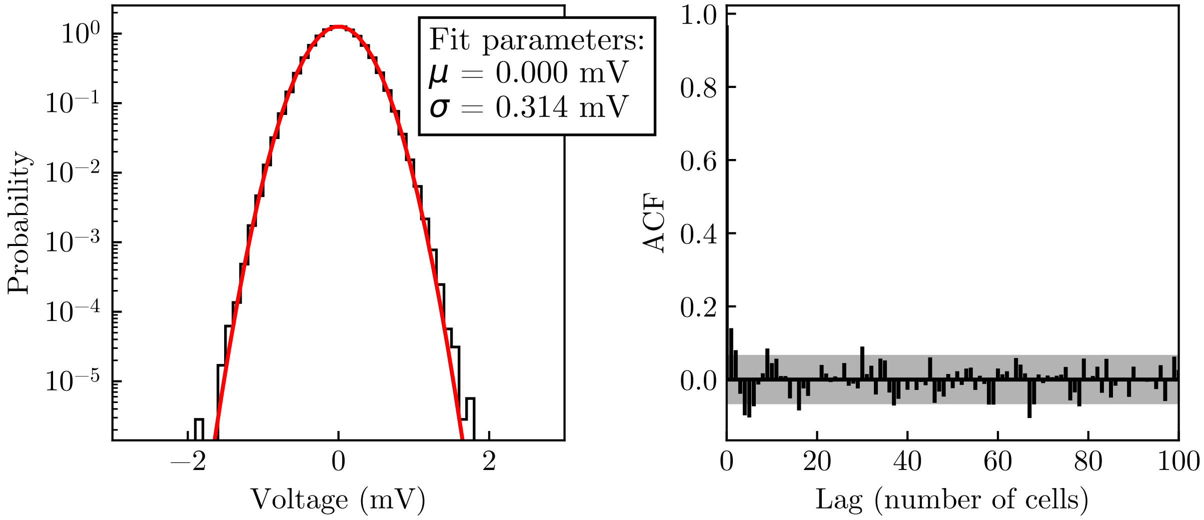

Figure 54: Voltage calibrated trace voltage distribution (left) and autocorrelation function of a single trace (right). Only cells 5 to 990 are used, since the voltages in the bins outside this range show high variance. After traces are mean-subtracted, the voltages are normally distributed with a standard deviation of 0.314 mV. A Gaussian fit is shown, assuming Poisson errors for each bin (red). No autocorrelations fall far outside the 95% confidence interval (gray shaded region), suggesting that the errors are uncorrelated. Only lags up to 100 are shown.

between 5 and 990 for a single channel are normally distributed with a standard deviation of 0.314 mV. The pedestal values are nearly constant over the course of the run, with an RMS of only 0.007 mV. Correlation between cells can also be quantified with the autocorrelation function. Autocorrelations of uncorrelated, normally-distributed random variables with unit variance at nonzero lags are asymptotically normally distributed with mean zero and variance 1/number of cells in trace (Anderson, 1942). Most traces show no evidence of correlated noise, based on their autocorrelation functions.

Voltage calibrations have been carried out for eight version 2.4 RBs, operating at room temperature. Calibration values are stored as text files and are applied as data packets are unpacked and saved as ROOT files. Each RB requires its own voltage calibration. Furthermore, voltage calibration is temperature dependent, so calibrations must be repeated at multiple different temperatures covering our expected temperature range. If the voltage calibration values vary smoothly with temperature, interpolation should be considered.

3.5.2 Timing Calibration

Timing calibration of the DRS4 is necessary to account for the "fixed pattern aperture jitter" between cell readout times, described in the DRS4 data sheet. While cells are read out at approximately the sampling rate of 2 GHz, the effective sampling intervals between cells exhibit small, constant deviations from 0.5 ns. Timing calibration consists of measuring these time intervals for each cell. While the time intervals for a given cell number are similar between channels, better timing resolution can be achieved by calibrating each channel independently. We perform timing calibrations using a 25 MHz, 382 mV peak-to-peak amplitude sine wave from the onboard TXCO, and we follow the methodology of Stricker-Shaver et al. (2014).

We take 5×10^3 samples in timing-calibration mode, triggering readout with software at a rate of ~50 Hz with random delays added so that the sine wave is sampled at different phases. A "local" timing calibration is performed first, using the portions of the sine wave near the zero-crossing. Since a sine wave is close to linear around its zero-crossings, the voltage difference between cell i and the one following it ΔV_i will be proportional to the (unknown) effective sampling interval Δt_i. After measuring N_i values of ΔV_i, we can estimate Δt_i with

$$\Delta t_i = \frac{1}{f_{\mathrm{samp}}} \frac{\overline{\Delta V}_i}{\frac{1}{1024}\sum_{i=1}^{1024} \overline{\Delta V}_i} \tag{46}$$

where f_{samp} is the average sampling speed of the DRS4 cells (2 GHz), and $\overline{\Delta V}_i = \frac{1}{N_i}\sum_{j=1}^{N_i}(\Delta V_i)_j$ is the mean ΔV_i measured. Rising and falling edges of the sine wave must be treated separately, since $\overline{\Delta V}_i \approx 0$ otherwise. We note that if the slope of the sine wave near zero-crossings s is known, then $\Delta t_i = \overline{\Delta V}_i / s$ can also be used since any small, constant multiplicative factor affecting all Δt_i is corrected for in the next timing calibration step.

We make several choices in our specific implementation of the local timing calibration. As in the voltage calibration, we only use measurements in cells between 5 and 990 for the local timing calibration. No pedestal subtraction is performed since the pedestals seen in

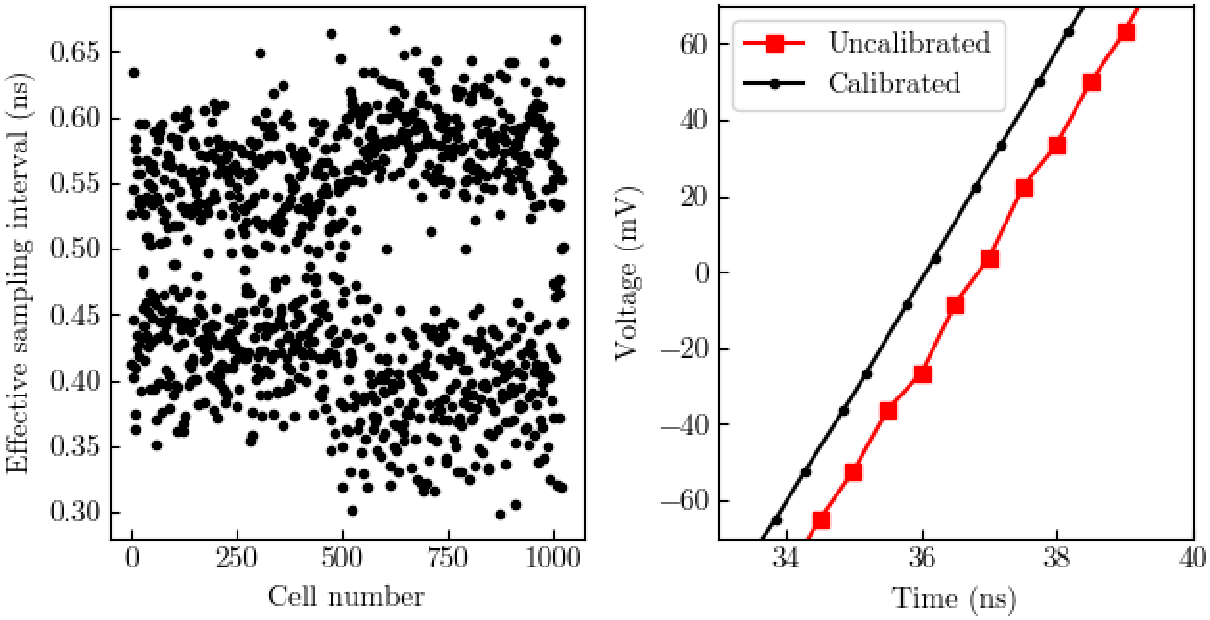

Figure 55: Effective sampling intervals Δt_i for a single readout board channel (left) and part of a sine wave before (red) and after (black) timing calibration (right). The first and last 512 cells have different fixed-pattern aperture jitter characteristics. The values of Δt_i also alternate between shorter and longer than $1/f_{\text{samp}}$. There is a visible decrease in jitter in the sine wave after calibration.

the voltage calibration data were within ±0.2 mV of zero. Furthermore, the sine wave data lacks a pedestal region, complicating pedestal estimation—fitting the data with sine waves gives pedestal values within ±1 mV of zero, with typical 1σ uncertainties of 0.2 mV from the fit. We use the part of the sine wave within ±60 mV, yielding $N_i \approx 446$ measurements of ΔV_i on rising edges, and an equal amount on the falling edges. Typically, $|\Delta V_i| \approx 15$ mV, in agreement with the analytically-determined $s = \pm 30$ mV/ns, and an RMS of ∼0.5 mV is observed in the measurements. We exclude $|\Delta V_i| > 30$ mV, as we found that a few of these outliers were present in channel one, causing calibration to fail. Finally, we measure Δt_i using rising and falling edges of the sine wave separately and then we average the results, as in Stricker-Shaver et al. (2014), though we find that combining the rising and falling edge measurements and using $|\Delta V_i|$ produces a similar result.

The local timing calibration given by equation 46 is only approximate, due to statistical

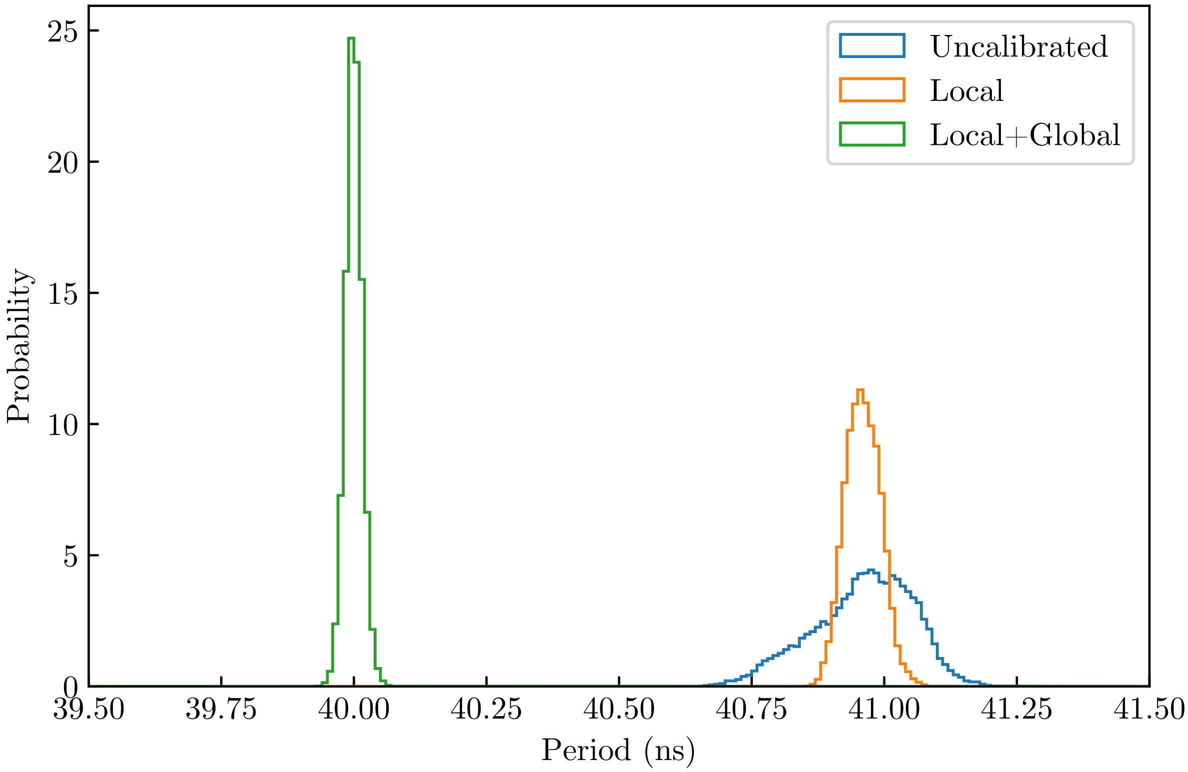

Figure 56: Distributions of the periods measured using the rising edges of the sine waves, after no timing calibration (blue), local timing calibration (orange), and local and global timing calibration (green). The full local and global timing calibration produces the narrowest distribution, with an RMS of 16 ps. Our initial estimate of f_{samp} is slightly off, which is corrected for by the global calibration, but causes the uncalibrated and local calibrations to be centered around a higher value than $\tau_{\text{cal}} = 40$ ns.

fluctuations as well as the physical behavior of the DRS4 (Stricker-Shaver et al., 2014). A "global" timing calibration is thus performed, using the precisely-known period τ_{cal} of the sine waves. For each full period in a sine wave, we can measure the period τ_{meas} using the Δt_i from the local timing calibration, then multiply each contributing Δt_i by a correction factor

$$k_{\text{corr}} = \frac{\tau_{\text{cal}}}{\tau_{\text{meas}}} \tag{47}$$

In detail, τ_{meas} is given by

$$\tau_{\text{meas}} = \left(\sum_{i=p+1}^{q} \Delta t_i \right) + \Delta t_p \left| \frac{V_{p+1}}{\Delta V_p} \right| + \Delta t_{q+1} \left| \frac{V_q}{\Delta V_q} \right| \tag{48}$$

where V_i is the voltage in cell i, and cell numbers p and q are the cells before the zero-crossings at either end of the sine wave. In practice, and following the implementation in the DRS4 evaluation board software, we get better results by incorporating a damping factor k_{damp}

$$k_{\text{corr,damped}} = k_{\text{damp}}(k_{\text{corr}} - 1) + 1 \tag{49}$$

where we use $k_{\text{damp}} = 0.1$. For every measured period, the Δt_i are multiplied by a different measured $k_{\text{corr,damped}}$ for all i between p and q, inclusive. We calculate sets of Δt_i using periods derived from rising and falling edges of the sine wave separately then average the results. We note that without first doing the local timing calibration, our global timing calibration performs poorly.

The Δt_i distribution for a single readout board channel found after local and global timing calibrations is shown in Figure 55. The Δt_i values alternate between values shorter and longer than $1/f_{\text{samp}}$, and have different characteristics between the first and last 512 cells. The mean Δt_i is 0.4883 ns for all channels, suggesting an actual $f_{\text{samp}} \approx 2.048$ GHz. The effect of the timing calibration on jitter observed in the sine wave is also shown in Figure 55.

Distributions of the periods measured using the rising edges of the sine waves are shown in Figure 56. Periods are measured using uncalibrated $\Delta t_i = 0.5$ ns, the Δt_i obtained with the local timing calibration, and the Δt_i obtained with the local and timing global calibration. As a consequence of the mean $\Delta t_i = 0.4883$ ns rather than 0.5 ns, the uncalibrated and local calibration distributions are centered around a higher value than $\tau_{\text{cal}} = 40$ ns. The RMS values of the distributions derived from no calibration, local calibration, and local+global calibration are 94 ps, 33 ps, and 16 ps, respectively. As each period is the sum of $\sim$80 Δt_i

values, the RMS values are $\sim$9 times the uncertainty in a single Δt_i values.

3.6 Future Directions

We have demonstrated the timing, spatial, and charge resolution capabilities of the GAPS TOF. Future work will include expanding and standardizing the TOF software pipeline, such that it correctly interfaces with the tracker. Other improvements include using the DRS4 channel nine data to increase global timing accuracy, and fine-tuning of the simulations.

We have also characterized many major aspects of the TOF instrument response to charged particles. An important next step is to calibrate every TOF paddle, with their unique scintillators, SiPMs, preamps, and RBs. Calibrations and characterization of pulses will also be done at temperatures and pressures expected during flight. The SiPM response in particular is temperature dependent (e.g. Ghassemi et al., 2018), though this will be partially mitigated through gain compensation.

Construction of the TOF continues, in preparation for GAPS' first Antarctic flight. In fall 2021, a functional prototype was assembled at MIT, integrating for the first time components of the TOF, tracker, and thermal system.

4 VERITAS Data and Methodology

The remainder of this work focuses on an indirect search for dark matter with gamma rays from the GC. This section will introduce VERITAS, the data, and the methodology developed for this analysis.

4.1 VERITAS

The Very Energetic Radiation Imaging Telescope Array System (VERITAS; Weekes et al., 1997, 2002) is an IACT array consisting of four 12 m diameter telescopes, located at the Fred Lawrence Whipple Observatory in Amado, Arizona at 31° 40′ 30″ N, 110° 57′ 07″ W, 1268 m above sea level. Each telescope consists of 345 mirror facets in a Davies-Cotton optical system (Davies & Cotton, 1957), with a 499-PMT camera positioned at the reflector focal point, read out by flash-ADCs at a rate of 500 MS/s. The first telescope began operating in February 2005 (Holder et al., 2006), and all four telescopes were operational by 2007 (Krennrich et al., 2007). The array was reconfigured to improve performance in 2009 (Perkins et al., 2009), and significant upgrades to the cameras and electronics occurred between 2011 and 2012 (Kieda, 2013). A recent photograph of VERITAS is shown in Figure 57.

While its exact performance depends on observing conditions, VERITAS can detect gamma rays with energies from 100 GeV up to >30 TeV, with angular resolution ~0.1°

Figure 57: Photograph of the VERITAS array at the Fred Lawrence Whipple Observatory.

for 1 TeV gamma rays. The sensitivity of VERITAS allows for significant detections of point sources with fluxes ∼1% that of the Crab Nebula in 25 hr of observations (Adams et al., 2022).

IACTs detect gamma rays indirectly, through the imaging of the Cherenkov light that accompanies cascades of particles, or "extensive air showers," initiated by gamma rays in the atmosphere (e.g. Weekes, 1996; Ong, 1998). Gamma rays do not reach the Earth's surface, but rather produce an electron-positron pair in the upper atmosphere, which emit subsequent high-energy photons through bremsstrahlung, repeating the processes of pair production and bremsstrahlung until the particle energies drop below a certain threshold (e.g. Longair, 2011). Charged particles moving faster than the speed of light in the atmosphere will also emit a cone of optical Cherenkov radiation (Čerenkov, 1937; Rybicki & Lightman, 1985; Longair, 2011). The Cherenkov light is predominantly blue or ultraviolet and arrives at the ground in short (∼5 ns) pulses, allowing the Cherenkov light to exceed the night sky background light in an optimized wavelength range and time integration window. The primary gamma ray's energy and direction may be inferred from the amount of Cherenkov light produced and the direction it is received from. Due to the size of the Cherenkov light cone on the ground, IACTs may detect gamma rays passing through a large area on the sky, resulting in an effective detector area orders of magnitude larger than the telescope mirrors' area. At the same time, IACTs must suppress a significant background of extensive air showers induced by cosmic rays. Cherenkov light from cosmic-ray air showers was theorized by Blackett (1947) and first detected by Galbraith & Jelley (1953), while Weekes et al. (1989) accomplished the first detection of astrophysical gamma rays with an IACT.

VERITAS, like other IACT arrays such as H.E.S.S. (Hinton & HESS Collaboration, 2004) and MAGIC (Aleksić et al., 2012, 2016), improve upon previous single-telescope IACTs, such as the Whipple 10 m telescope (Weekes et al., 1989), by using the stereoscopic view of air showers to achieve better event reconstruction and background suppression (Weekes et al., 2002).

4.2 Observations

The observations used in this analysis were taken by VERITAS between 2010 April and 2022 June, and include 177.8 hr of on-source exposure time of the GC and an additional 50.8 hr of off-source exposure time of a nearby patch of sky. The GC observations are taken with the telescope pointing offset by 0.5° or 0.7° from Sgr A*, whose right ascension (RA) and declination (Dec) in equatorial coordinates (J2000) are (RA,Dec)=$(266.417°, -29.0078°)$. The off-source observations, which we refer to as Sgr A* Off, are taken with similar offsets towards (RA,Dec)=$(260.917°, -29.0078°)$, a region 5.5° away from Sgr A* with no known gamma-ray sources and few bright stars. These regions are shown in Figure 58. Observations of these regions occur between late March and early July. Additional data used for calibrations are taken with flashes from blue, light-emitting diodes or nitrogen lasers (Hanna, 2008; Hanna et al., 2010). All data are stored using the VERITAS bank format (Hays, 2008).

The data, comprised of 543 observation runs, are required to have all four telescopes participating and fair weather, as determined by the observers. Additionally, each run is manually inspected for anomalies in triggering rates, average traces, pointing offsets, sky temperatures, and other metrics using the VERITAS data quality monitoring image viewer. Short segments of runs showing anomalous behavior are cut from the analysis. The post-quality cut, deadtime-corrected exposure times total 154.3 hr of Sgr A* data and 44.0 hr of Sgr A* Off data.

The data span two of VERITAS' observing epochs, which we will refer to as V5 and V6. V5 data are observations taken after the 2009 array reconfiguration (Perkins et al., 2009) and before the summer 2012 hardware upgrade (Kieda, 2013), while V6 data are all subsequent observations. The V6 hardware allows lower level-1 discriminator thresholds to be used for triggering, increasing the detection rate for lower-energy events (Zitzer & VERITAS Collaboration, 2013). About 27% of the Sgr A* data and 30% of the Sgr A* Off data are from V5, while the remainder are from V6.

Whereas most VERITAS data are taken at small zenith angles (SZA), our data are taken

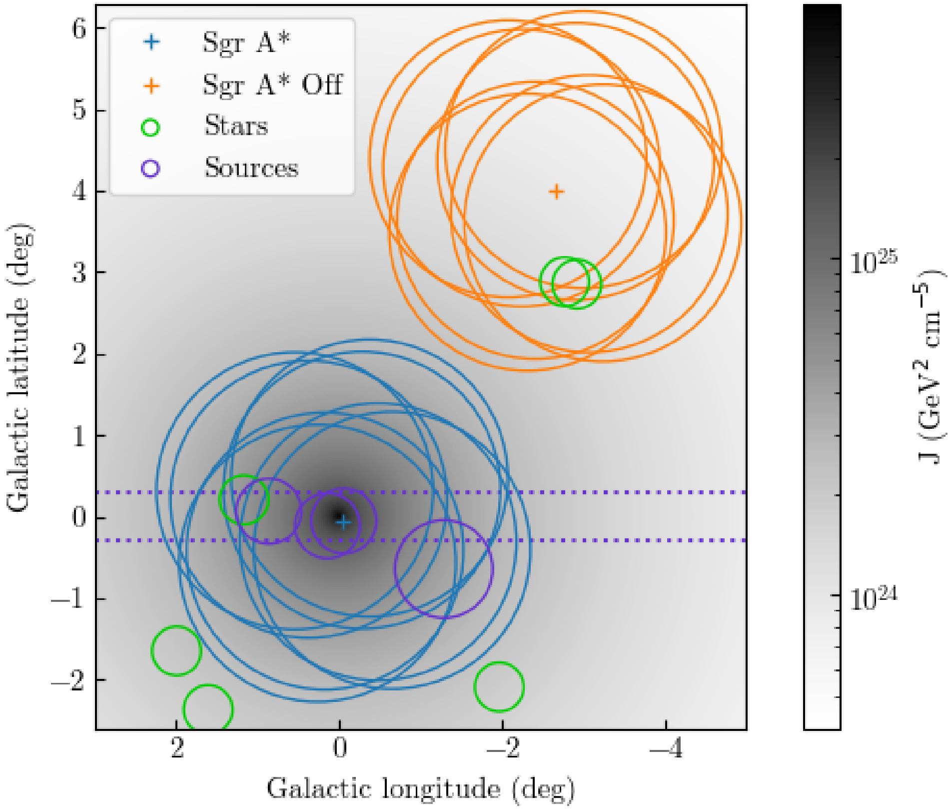

Figure 58: Observation regions superimposed on a map of J factors (Einasto profile), in Galactocentric coordinates. The 3.4° fields of view for all eight unique telescope pointings are shown for Sgr A* (blue) and Sgr A* Off (orange). Also shown are exclusion regions around bright stars (green), gamma-ray sources (purple), and the GC ridge (purple dotted lines).

only at large zenith angles (LZA), greater than 55° (equivalently, less than 35° above the horizon). Such observations are necessitated by the location of VERITAS, from which point Sgr A* does not transit above 30° in elevation. A practical distinction between SZA and LZA is that at zenith angles $\gtrsim 40°$, the standard VERITAS analysis techniques (described in Section 4.3) perform inaccurately (Aliu et al., 2012; Archer et al., 2014).

An advantage of observing at LZA is an increase in the effective detector area at higher energies (Sommers & Elbert, 1987; Konopelko et al., 1999). At LZA, the point of maximum shower development occurs further from the IACT array, increasing the size of the Cherenkov light cone at the telescope location. This results in showers with greater impact distance, the

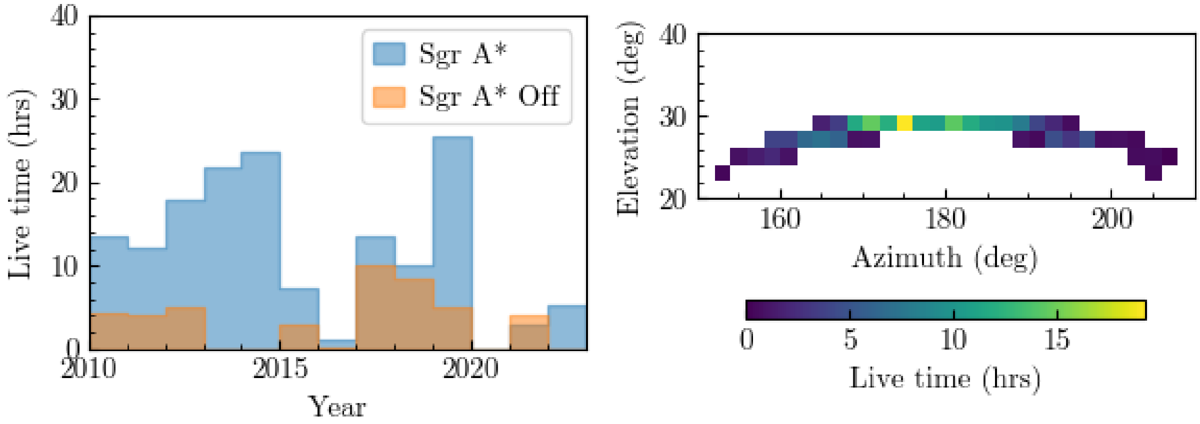

Figure 59: Histograms of live time binned by year (left) for observations of Sgr A* (blue), and Sgr A* Off (orange). A 2D histogram of total observation time binned in average elevation and azimuth angle is also shown (right), with 2° bins in both dimensions.

distance between the shower core and the center of the VERITAS array, to be detected. At the same time, however, the larger light pool, and to a lesser extent increased atmospheric absorption, results in fainter shower images at a given energy, increasing the energy threshold of detectable events. Typical effective areas as functions of energy for different zenith angles during the V5 and V6 epochs are shown in Figure 60.

4.3 Event Reconstruction

Reconstruction of gamma-ray events generally follows the methodology described by Daniel (2008a). For each event, images of the air shower taken by each telescope are calibrated and the image parameters are derived. Simulations are then employed to recover the gamma ray's energy and direction from the shower image parameters. VERITAS has two independent analysis packages—Eventdisplay (Maier & Holder, 2017) and VEGAS (Cogan, 2008)—of which VEGAS is used in this work.

In the first stages of the analysis, parameters related to the run conditions are found and trace information is calculated for each event. Flasher runs are used to find relative gain and timing corrections, after which pedestal subtraction and calculation of integrated charge

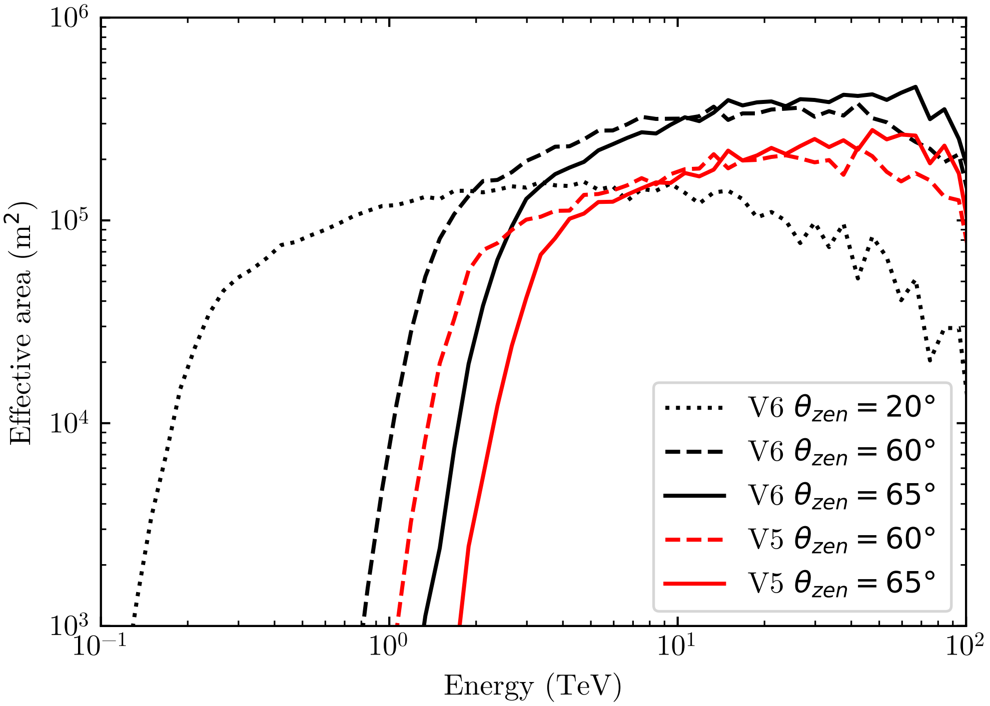

Figure 60: Effective area as a function of energy for V5 (red) and V6 (black) data, at different zenith angles. Effective areas are taken from lookup tables (Section 4.3.2) for gamma rays coming from directions 0.5° offset from the camera center and with a pedestal noise level typical of the GC data. The increasing energy threshold and effective area at higher energies at LZA can be seen.

occurs. Pedestals and their RMS values are calculated for each pixel from the numerous pedestal events accumulated during each run, recorded at a rate of 1 Hz. Integrated charges are the sums of the pedestal-subtracted trace values in a 7-bin (14 ns) window and are left in units of digital counts (d.c.). For V6 data, one photoelectron corresponds to ∼5 d.c. (Adams et al., 2022). Dead or noisy pixels are cut from the analysis, based on hardware records and measured pedestal RMS values. Each image then undergoes "cleaning," where pixels unrelated to the core image are cut from the analysis. An event prior to cleaning is shown in Figure 61.

Events are then subjected to several quality cuts, to reduce the number of poorly-reconstructed events that enter the analysis. Images are each required to have ≥5 contributing PMTs. The sum of integrated charges from the contributing PMTs, or *size*, must

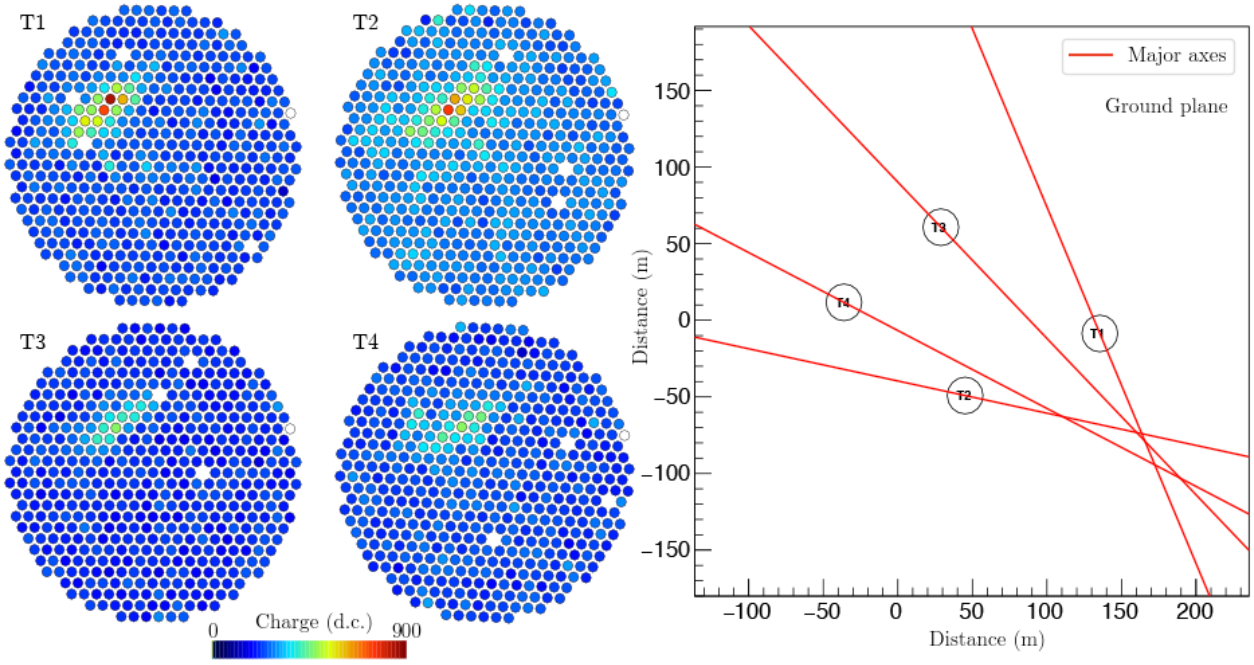

Figure 61: Shower images for a single gamma-ray event in each camera (left), where each circle represents a PMT and color indicates integrated charge. Dead pixels (white) are omitted. Also shown are the telescope locations and image major axes in the ground plane (right). The event is from an observation of Sgr A* taken in May 2015, at a zenith angle of 60°.

be >500 d.c. for V5 data and >650 d.c. for V6 data. The distance between the shower image centroid and the camera center must be <1.38°, to avoid image truncation at the camera edges. Images passing these cuts are required from at least two telescopes for SZA data, and at least three for LZA data. Table 4 shows typical numbers of events cut at this stage and at later stages of the analysis.

The images of events passing quality cuts undergo moment analysis, based on the method of Hillas (1985). First, the major axis of each ellipsoidal shower image is determined as the line which minimizes the sum of the pixels' perpendicular distances from the line, weighted by the integrated charges. The image length and width are then calculated, which are the RMS of the charge distribution along the major axis and perpendicular to the major axis, respectively.

For standard observations taken at SZA, a gamma ray's point of origin can be recon-

	V5 run (#51015)	V6 run (#86021)
Total non-pedestal events	159218	260831
Pass quality cuts	13027	16750
Pass gamma/hadron cuts	132	118
Pass energy threshold and θ cuts	87	61

Table 4: Number of events passing cuts at different stages of the analysis for typical V5 and V6 observations of Sgr A* Off. The exposure times are 20 minutes. Quality cuts are described in Section 4.3. Gamma/hadron cuts are described in Section 4.4.1. Events in the last row have energies above our 2 TeV energy threshold (described in Section 4.3.2) and have angular distances from the telescope pointing position $\theta < 1.7°$, where the acceptance is sufficiently high (described in Section 4.4.2)

.

structed with the *geometric* method (e.g. Aharonian et al., 1997; Hofmann et al., 1999; Krawczynski et al., 2006). In this method, the point minimizing the perpendicular distances to the images' major axes is found in the camera plane, giving the direction from which the primary gamma ray originated when projected onto the sky plane. Distances are weighted by the image sizes. The impact distance is determined in a similar way after first projecting the images onto the ground plane.

The primary gamma-ray energy is reconstructed using information from Monte Carlo simulations of gamma-ray showers (described in Section 4.3.1), through the use of lookup tables (described in Section 4.3.2). The energy lookup tables are indexed by image size, reconstructed impact distance, and reconstructed source position. Separate tables are made for different observation conditions, which include observation zenith angle, azimuth angle, pedestal noise level, atmosphere model, and telescope epoch.

Observations at LZA require a different methodology to reconstruct direction and energy (e.g. Aliu et al., 2012; Archer et al., 2014). The *geometric* method becomes unreliable due to decreased telescope separation in the plane perpendicular to the shower axis and larger impact distances resulting from the larger effective area, causing the images' major axes to become closer to parallel (e.g. Kosack et al., 2004; Senturk, 2011). The inaccuracy in the shower direction and impact distance causes energy reconstruction to worsen, in turn.

At LZA, direction reconstruction can be improved by using a variant of the *displacement* method (e.g. Akerlof et al., 1991; Buckley et al., 1998; Lessard et al., 2001; Senturk, 2011; Weiner, 2017). In this method the distance along the image major axis between the source position and image centroid, or the *disp* parameter, is estimated from individual image properties. Early versions of this method noted the relation between the *disp* parameter and a shower image's width-to-length ratio (Akerlof et al., 1991), while the VERITAS implementations use additional parameters. The first VERITAS *displacement* method used lookup tables to estimate the *disp* parameter as a function of image length, width, and size, with separate tables for different observation zenith angles, azimuth angles, and pedestal noise levels. This lookup table *displacement* method was used successfully in several LZA studies (e.g. Aliu et al., 2012; Archer et al., 2014, 2016). An improved *displacement* method was later developed (Weiner, 2017) using boosted decision trees (BDTs) trained on the same set of parameters used by the lookup tables, with the addition of two parameters describing the arrival time gradient across the image and the integrated charge lost due to image truncation at the camera edges. These additional parameters have been found to increase the accuracy of other decision tree-based *disp* estimators (e.g. Aleksić et al., 2010). The central interval containing 68% of the distribution of angular positions reconstructed with the BDT *displacement* method has a half-width of ∼0.12°.

A BDT-based algorithm was also developed to reconstruct energy at LZA (Buchovecky, 2019). The energy BDTs are trained on the same parameters as those used by the *disp* BDTs, excluding azimuth angle. For simulated events at a zenith angle of 65°, it is found that using the *disp* and energy BDTs eliminates the ∼20% energy bias present when using the standard methods, and reduces uncertainty in the reconstructed energy to ∼19% (Buchovecky, 2019).

4.3.1 Simulations

Event reconstruction relies on accurate Monte Carlo simulations of air showers initiated by gamma rays. Simulations for VERITAS are run in two steps: air showers are simulated with

`CORSIKA` (Heck et al., 1998) and then the telescope response is simulated with `GrISUDet`[8] Holder et al. (2006); Maier (2008). The simulations are stored in the standard VERITAS Bank Format so that may be processed with VEGAS. Processed simulations are used to create the VERITAS instrument response functions.

Showers are simulated with `CORSIKA` version 6.960. Hadronic interactions are computed with QGSJet II-03 (Ostapchenko, 2011) at energies above 100 GeV and UrQMD (Bleicher et al., 1999) at lower energies. Between 2–5 $\times$ 10^6 showers are simulated with energies spanning 30 GeV to 200 TeV at ten different zenith angles between 0° and 65°. Shower cores are randomly distributed over a circle of radius 750 m centered on the telescope array's center. Simulations are performed for two atmospheric models, corresponding roughly to "winter" (November–April) and "summer" (May–October) observing conditions, informed by radiosonde data (Daniel, 2008b).

The telescope response simulated by `GrISUDet` considers the propagation of Cherenkov shower photons through the instrument optics and the subsequent response of the electronics and trigger system. The modeled optics include the geometry of the mirrors, Winston cones, and PMTs, as well as reflectivity. The modeled electronics include PMT gains, quantum efficiencies, and the single photoelectron response with amplitude and timing jitter, digitized at 500 MS/s. The trigger decision for each shower is recorded. The same `CORSIKA` simulations are used for nine different pointing offsets between 0° and 2°. For each offset, ten different pedestal noise levels are added to the simulated traces, representing different sky brightnesses.

4.3.2 Instrument Response Functions

Event reconstruction relies on instrument response functions (IRFs) to map observables to quantities of interest, using the results of simulations. The relevant IRFs for the present analysis include lookup tables for energy, shower width, shower length, and effective area. At LZA, lookup tables are used along with BDTs for direction and energy reconstruction.

---

[8] `GrISUDet` is documented and hosted on its website: `http://www.physics.utah.edu/gammaray/GrISU/`

To create IRFs, the simulations are processed by VEGAS up to the image parametrization stage. The relevant image parameters and true Monte Carlo parameters are then used to fill lookup tables for energy, measured shower width, and measured shower length. Lookup tables are multidimensional arrays storing the mean values of the desired parameter, averaged over multiple simulated showers. For the energy, width, and length tables, impact distance is a dimension of the table, so different IRFs are needed when different direction reconstruction methods are used. Lookup tables are also made for the uncertainty in reconstructed energy.

BDTs for estimating *disp* and energy, along with their uncertainties, are also trained after the image parametrization stage (Weiner, 2017; Buchovecky, 2019). A BDT algorithm with gradient boosting is used, implemented in the Toolkit for MultiVariate data Analysis (TMVA; Hoecker et al., 2007; Speckmayer et al., 2010) with `ROOT`. The trained BDT weights are saved in XML files.

Lookup tables are used to determine effective area A, which, which may be defined such that

$$\bar{N} = \int dE d\Omega dt \frac{d^2\Phi}{dE d\Omega} A \tag{50}$$

where $\bar{N}$ is the average number of counts observed over some range of energy E, solid angle Ω, and time t, from a source with flux Φ. The effective area can be determined after subjecting the simulated data to quality cuts and gamma/hadron separation cuts (described in Section 4.4.1) with (e.g. Kertzman & Sembroski, 1994; Mohanty et al., 1998)

$$A = A_0 \left(\frac{\text{number of events passing cuts}}{\text{number of events simulated}} \right) \tag{51}$$

where A_0 is a sufficiently large area over which simulated shower cores fall—$\pi(750\text{ m})^2$ in our simulations. Effective area tables for SZA data are made using events reconstructed with the *geometric* method and energy lookup tables, while for LZA data, events are reconstructed with the BDT *disp* method and energy BDTs. In addition to dependence on the analysis cuts used, the effective area depends on physical parameters including gamma-ray energy, shower direction in the camera plane, zenith angle, azimuth angle, and night sky background level[9]. Separate tables exist for each combination of these parameters.

From the effective area versus energy curve, an effective energy threshold may be defined as the energy which maximizes $E^{-\gamma}A(E)$ for a source with a differential energy spectrum $\propto E^{-\gamma}$ (Weekes, 1976; Weekes et al., 2002). For VERITAS analyses, the Crab Nebula spectrum's $\gamma = -2.4$ is normally used (e.g. Archambault et al., 2017). Below this threshold, the effective area drops steeply. For SZA observations, the threshold is typically around 0.17 TeV for V5 data and 0.15 TeV for V6 data, while for our LZA data the threshold is around 2.4 TeV for V5 data and 1.9 TeV for V6 data.

Recently, IRFs have been made for SZA data that account for the telescopes' time-dependent gains and reflectivities (Adams et al., 2022). The product of the average gain and reflectivity, or throughput factor, relative to measurements taken in 2012 September is plotted over time in Figure 62. The throughput factor is represented as a constant over different IRF periods, which each have their own sets of IRFs. Throughput corrections have not yet been incorporated into LZA IRFs, so the effects on flux sensitivity are only approximated in our analysis.

4.4 Background Estimation

In addition to the air showers initiated by gamma rays, IACTs detect a large number of air showers initiated by cosmic rays. While a significant amount of discrimination between gamma-ray and cosmic-ray showers can be achieved, some cosmic-ray showers, especially those initiated by electrons or positrons, represent an irreducible background for current IACTs (e.g. Maier & Knapp, 2007). Numerous methods have been employed to model the remaining background (e.g. Rowell, 2003; Berge et al., 2007). We develop two additional background estimation methods for VERITAS that may be applied to observations of extended sources occupying most of the field of view.

---

[9] The night sky background level refers to the rate at which photons not originating from air showers are detected by PMTs. It is quantified as the mean current in all the telescopes' PMTs—generally a few μA.

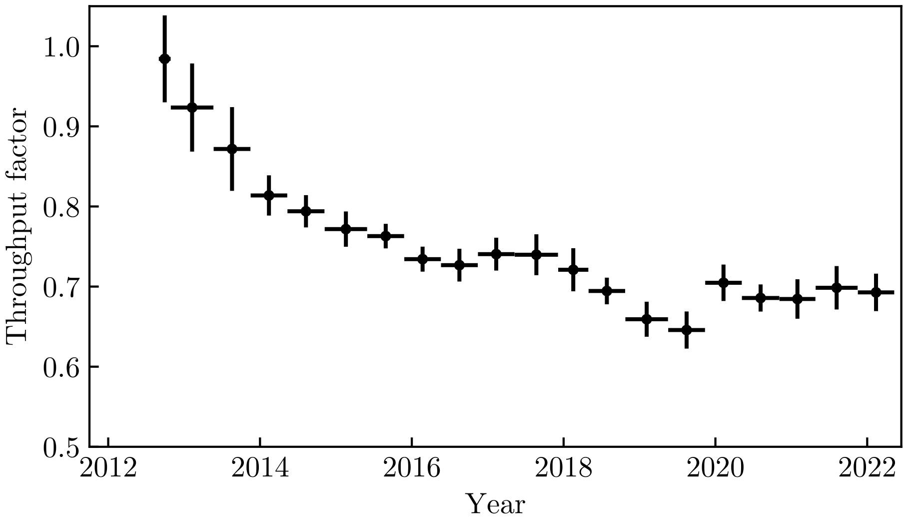

Figure 62: Throughput factors averaged over the four telescopes for different IRF periods. Periods are indicated by the horizontal error bars. Vertical error bars represent the RMS of the measurements within each period.

4.4.1 Gamma/Hadron Separation

The different physics involved in electromagnetic versus nucleonic cascades makes it possible to separate gamma-ray showers from cosmic-ray showers (Weekes, 1988). Nucleonic cascades, induced by hadronic cosmic rays, generally involve production of a number of pions, which eventually initiate electromagnetic cascades (e.g. Longair, 2011). The spatial properties of the Cherenkov light image therefore differ between the two types of showers and are commonly used as discriminators (Hillas, 1985). Other suggestions have included the use of shower height, number of muons, temporal information, and stereoscopic agreement (e.g. Grindlay, 1971; Hillas, 1996; Fegan, 1996; Krawczynski et al., 2006).

In the present analysis, we use box cuts on mean-scaled Hillas parameters width (MSW) and length (MSL), as well as height of shower maximum. The parameters p are scaled to their mean simulated values $\bar{p}_{\mathrm{sim}}$ found using lookup tables, such that the mean scaled

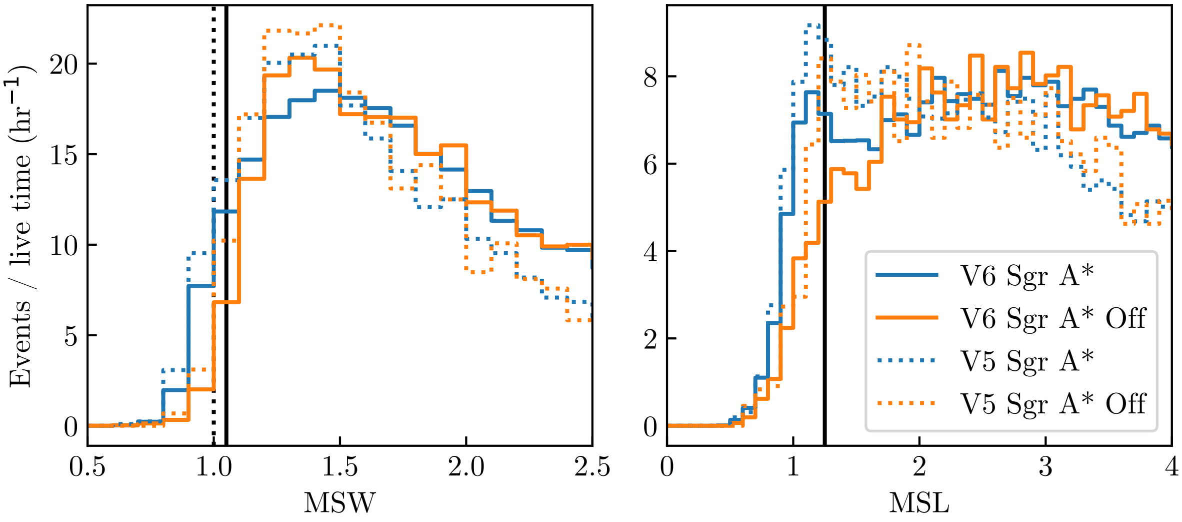

Figure 63: Distributions of MSW (left) and MSL (right) of events within 0.13° of Sgr A* (blue) and the Sgr A* Off position (orange). V5 (dotted lines) and V6 (solid lines) data are shown separately. Events have already passed size cuts and have reconstructed energies > 2 TeV. The cut values optimized for Crab Nebula observations taken at LZA are also indicated for V5 (vertical dotted black line) and V6 (vertical solid black lines) data. The number of events is divided by each data set's live time so that the Sgr A* and Sgr A* Off distributions may be compared.

parameter (MSP) is calculated with (Daniel, 2008a)

$$\mathrm{MSP} = \frac{1}{n_{\mathrm{tel}}} \sum_{i=1}^{n_{\mathrm{tel}}} \frac{p_i}{\bar{p}_{\mathrm{sim}}} \tag{52}$$

where the sum is over the images in the $n_{\mathrm{tel}} \leq 4$ telescopes. Scaling is employed before cuts due to the dependence of length and width on the shower geometry and observational parameters such as zenith angle (Konopelko, 1995; Daum et al., 1997).

Standard cuts for SZA are optimized using observations of several bright sources. The source significance is evaluated over a grid of maximum MSW, maximum MSL, and minimum height cuts, and the set of cuts that maximizes significance is chosen. A similar procedure is performed to find cuts for LZA, using observations of the Crab Nebula at zenith angles >60° (Buchovecky, 2019). These cuts are tabulated in Table 5. The height cut was found to be ineffective for gamma/hadron separation at LZA, and so is kept at its SZA value

Data type	MSW	MSL	height (km)
SZA V5,V6	<1.10	<1.30	>7
LZA V5	<1.00	<1.25	>7
LZA V6	<1.05	<1.25	>7

Table 5: Gamma/hadron separation cuts on MSW, MSL, and shower height, for different data types. The cuts place upper bounds on MSW and MSL, and a lower bound on height. The various parameters are described in the text.

(Buchovecky, 2019). Distributions of event MSW and MSL from Sgr A* and Sgr A* Off data are shown in Figure 63. Below the MSW and MSL cut values, excess events can be seen in the Sgr A* data versus the Sgr A* Off data.

We also define a set of cuts that aims to select CR-like events, rather than gamma rays. These cuts consist of the same MSL and height cuts as in in Table 5, but require $1.2 < \mathrm{MSW} < 2.2$.

4.4.2 On/Off Methods and Acceptance

A residual background of "gamma-like" events remain after gamma/hadron separation from showers not initiated by gamma rays. This background can be treated with an "on/off" method (e.g. Berge et al., 2007), where for each on-source measurement, containing both signal and background gamma-like events, an off-source measurement is taken, containing just background gamma-like events, and the signal may be evaluated by comparing the two datasets. The on-source and off-source measurements may come from separate observations, or separate regions of interest (ROI) inhabiting the same field of view, as in the ring and reflected region background methods (e.g. Berge et al., 2007).

In on/off analyses, it is necessary to estimate the ratio of background counts in the on-source region to the off-source region, α, such that the number of signal counts N_S is approximated by

$$N_\mathrm{S} = N_\mathrm{on} - \alpha N_\mathrm{off} \tag{53}$$

where N_on and N_off are the total counts in the on-source region and off-source region, re-

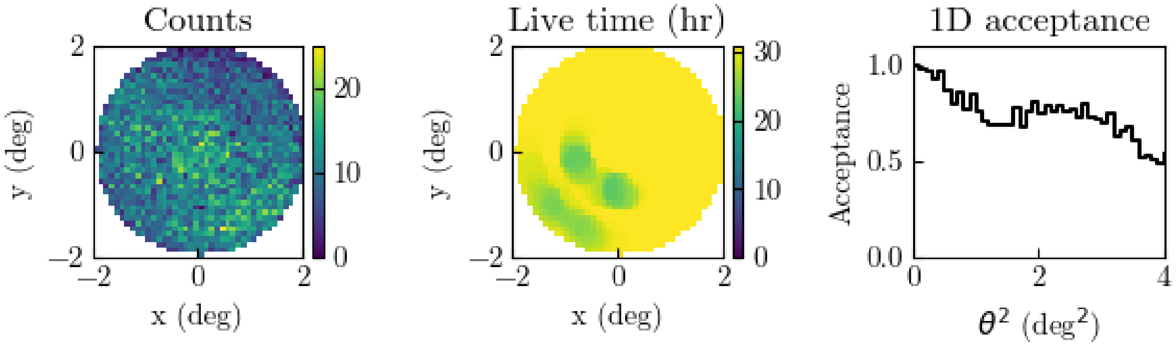

Figure 64: 2D histogram of counts of gamma-like events (left), 2D map of live times (middle), and the normalized 1D acceptance (right) for all 30.8 hr of V6 Sgr A* Off data. The 2D maps are in camera coordinates, with bins of 0.1° in both dimensions. The deviations in live time are due to exclusion regions around bright stars. Bins of constant $\Delta\theta^2 = 0.01$ deg^2 are used in the 1D acceptance plot to yield constant solid angle in each θ bin.

spectively. If the background event rate is constant in the two regions, then α is the ratio of the product of the exposure times and the regions' solid angles. However, the background event rate will in general vary over time and the field of view (among other parameters) due to the system's acceptance.

The acceptance is the probability that an event that triggers the telescope array passes all cuts (for quality and gamma/hadron separation). The acceptance may depend on the event's radial angular distance from the center of the telescope pointing position, the zenith and azimuth angles of the telescope pointing, the reconstructed event energy, the time at which the observation is taken, and the event's position on the celestial sphere (e.g. Berge et al., 2007; Da Vela et al., 2018). The acceptance may also differ for showers initiated by different particles (Berge et al., 2007; Fernandes et al., 2014; Prandini et al., 2015).

Under the assumption of a spatially isotropic background event rate, the acceptance can be derived empirically from observations of fields without astrophysical gamma-ray sources. Since bright stars in the field of view can affect the acceptance, we exclude circular regions of 0.3° radius around stars with apparent B band magnitudes 6 and brighter from acceptance calculations. We also exclude circular regions of radius 0.4° around known gamma-ray sources. This radius includes ~96% of the LZA point spread function (PSF; Buchovecky, 2019). To account for these exclusion regions, the total live time at each position in the camera's field of view must be tracked. The 1D acceptance as a function of angular distance from the camera center, θ, may be found by summing the counts in different θ bins, weighted by the reciprocal of the bins' average live times. Figure 64 shows plots of counts, live times, and the average 1D acceptance for all 30.8 hr of V6 Sgr A* Off data. While events are reconstructed out to $\theta = 2°$, we limit our analysis to the usual VERITAS field of $\theta \leq 1.7°$, beyond which the acceptance decreases to $\lesssim$50% of its peak value.

Background count rates also exhibit zenith dependence, resulting from changing acceptance and cosmic ray rates. At SZA, a linear gradient in rates has been observed of ~10% per degree, increasing towards zenith (e.g. Rowell, 2003; Zitzer & VERITAS Collaboration, 2017). However, in our LZA data we observe gradients of negative 20–30% per degree, decreasing towards zenith.

We will briefly describe the commonly-used reflected region method (RRM) and ring background method (RBM), in order to motivate the development of different background methods for our extended source analysis. Both methods are illustrated in Figure 65 The RRM uses a circular on-source region observed at some offset θ, and several identically-sized off-source regions placed symmetrically around the camera center with the same radial offset. The θ dependence of the acceptance can therefore be ignored, while the zenith dependence will average out, so that $\alpha = 1/(\text{number of reflected regions})$. The RBM also uses a circular on-source region, but uses as its off-source region a ring of some thickness centered on the source position. The average acceptances in the RBM on-source and off-source regions are not guaranteed to be equal, so the normalized 1D acceptance and zenith gradient are calculated for individual runs and used to compute α. The RBM can offer better statistics and more flexibility for source positions and morphologies than the RRM, so is often used for significance maps. However, energy dependence of the acceptance is not accounted for by the RBM, so the RRM is preferred for calculations of spectra.

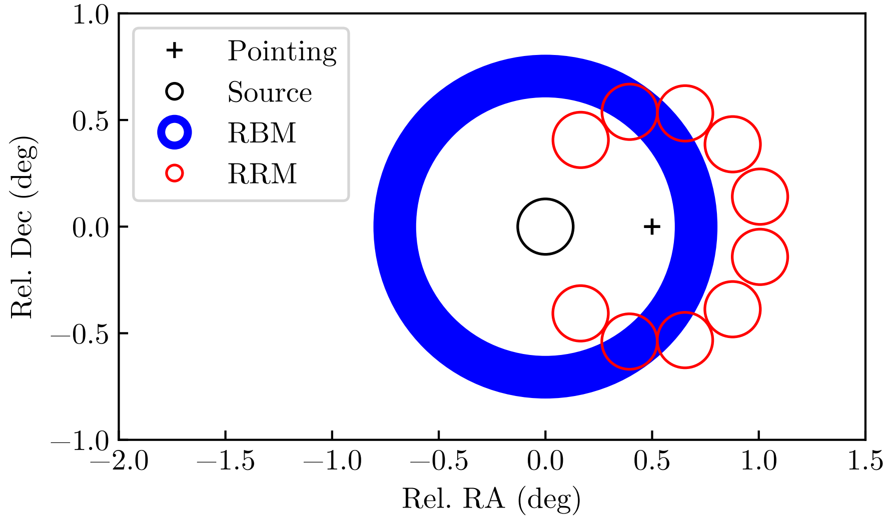

Figure 65: Illustration of the RBM and RRM. The region(s) from which background counts are drawn in the RBM (blue) and RRM (red) are indicated, along with the source region (black circle) and telescope pointing position (black cross).

The RBM and RRM thus require small on-source regions (relative to the field of view) and fields of view absent of bright stars and gamma-ray sources. These conditions are not fulfilled by our GC data, where the dark matter halo is extended over the entire field of view, in principle, and the inner few degrees contain multiple other gamma-ray sources. We therefore develop background estimation methods more suitable to our analysis.

4.4.3 Matched Runs Method

The first method we explore is the matched runs method (MRM; e.g. de la Calle Pérez et al., 2003; Abramowski et al., 2012; Flinders & VERITAS Collaboration, 2015; Abeysekara, 2019; Hona & VERITAS Collaboration, 2022), which pairs on-source runs with off-source runs observed under similar conditions in order to estimate the number of background counts. The MRM circumvents the usual drawback of taking off-source data at the expense of on-source data by instead using archival data for the background estimation. The MRM allows the entire field of view to be used as an on region, excepting exclusion regions.

To determine the suitability of matched runs we adopt the criteria of Abeysekara (2019),

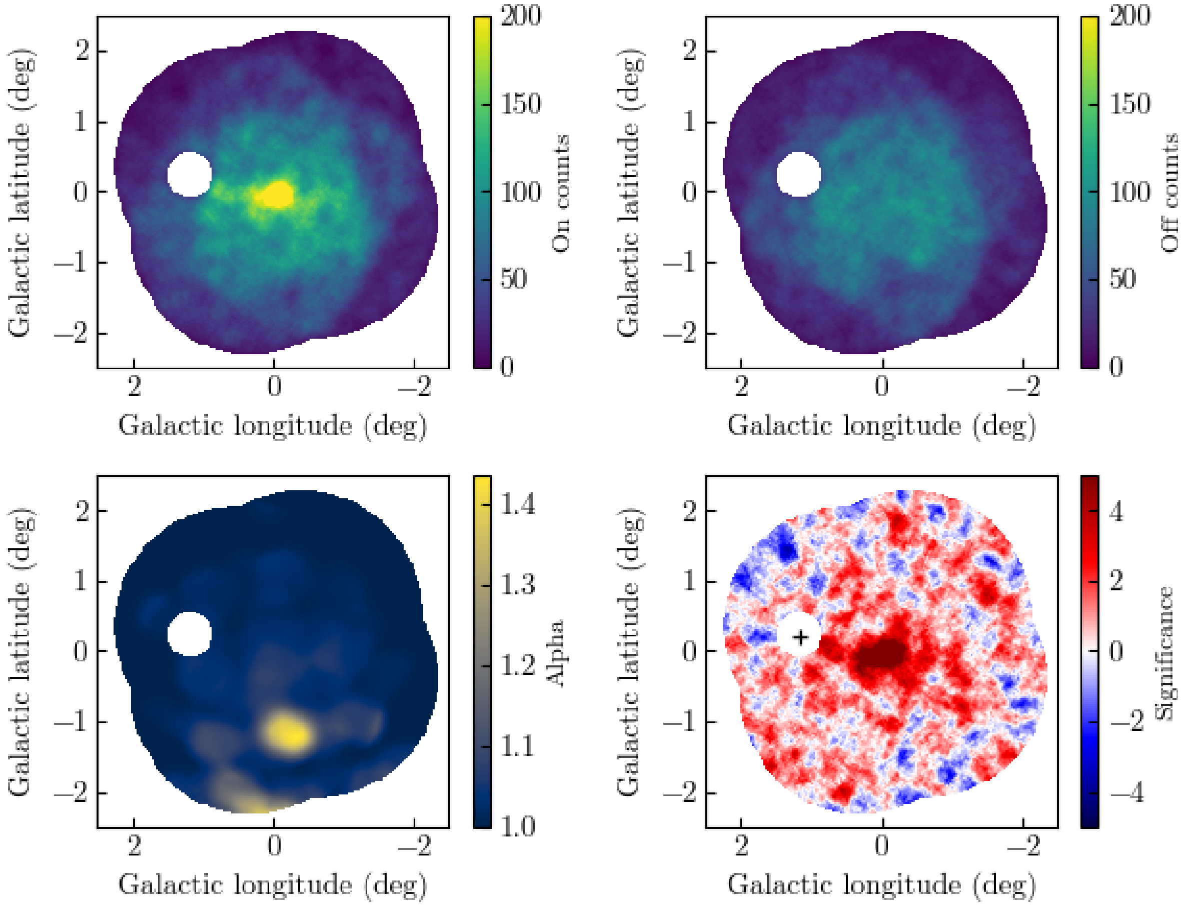

Figure 66: Application of the MRM to Sgr A* data. Maps are shown of correlated on counts (top left), off counts (top right), α (bottom left), and significance (bottom right). Emission from sources along the Galactic plane are visible in the on count and significance maps. The blank circle is the result of the exclusion region around X Sagittarii. The deviations in α from one are due to exclusion regions in the off-source runs.

requiring the difference in average azimuth and zenith angle of the on-source run and matched run to be $< 10^\circ$, the difference in observation date to be less than a year, and the difference in CR-like events in the full field of view to be small ($\lesssim 10\%$). Once matched, if runs differ in live time, the longer run is truncated to the length of the shorter run. To make the sky map of off counts, the sky coordinates of the off-source run events are rotated and translated such that the telescope pointing and camera axes align with those of the on-source run. Since the vertical camera axis is aligned with the zenith angle axis, the rotation aligning camera axes ensures that the zenith gradients in the acceptances align as well.

We use identical circular on and off regions of radius 0.13°. On and off counts are summed over their respective regions, while α is given by the ratio of the acceptance-weighted live time

$$\alpha = \frac{\int d\Omega \sum_i^{n_{\rm runs}} {\rm Acc}_{{\rm on},i}(\theta, z) t_{{\rm on},i}}{\int d\Omega \sum_i^{n_{\rm runs}} {\rm Acc}_{{\rm off},i}(\theta, z) t_{{\rm off},i}} \tag{54}$$

where the integrals are over the solid angle of the on and off regions, the sums are over the number of runs $n_{\rm runs}$, Acc is the normalized acceptance, with dependence on θ and zenith angle z, and t is live time. For each run, radial acceptances are fit with an 8th-order polynomial times a linear zenith-dependent term. Significances can then be calculated with the formula of Li & Ma (1983).

Application of the MRM for a subset of Sgr A* data is shown in Figure 66. The significance map indicates that the method is reliable, and the central source is detected with a significance of 14.5 sigma. Unfortunately, due to the atypical observing conditions of the GC data, we are only able to find suitable matched runs for 148 of the 422 Sgr A* observations, for a total live time of 44.6 hr. Observations of Sgr A* Off comprise 35.6 hr, while the remaining 9 hr come from observations of other targets.

We explored the possibility of expanding the range of suitable azimuth and zenith angles. However, differences in background rates not accounted for by the normalized acceptance curves prevent reliable background estimates from being made without knowledge of the absolute background rate, motivating the approach taken in the next method.

4.4.4 Template Background Method

We develop another background estimation method that models the background count rate under different observing conditions, allowing us to use large regions of interest for our dark matter analysis. This method uses templates of gamma-ray-like event rates, derived from observations of empty fields, and so we refer to it as the template background method (TBM). Previous IACT analyses have used this approach (Mayer, 2014; Devin, 2018; Vovk et al., 2018; Kelley-Hoskins, 2019; Knödlseder et al., 2019; Mohrmann et al., 2019; Acharyya et al., 2021), while similar approaches that use cosmic-ray-like events to construct templates have also been employed (Rowell, 2003; Aharonian et al., 2006; Berge et al., 2007; Fernandes et al., 2014). The advantage of this method over MRM is that templates derived from off-source data may be used to analyze a larger set of on-source data.

The templates are 3D maps in angular and energy coordinates. The maps consist of the differential count rate, R, derived in units of min^{-1} deg^{-2} TeV^{-1} and stored in camera coordinates. Templates cover a 3.4° diameter field of view with 0.025° angular bins, and 20 logarithmically-spaced energy bins between 1 TeV and 100 TeV. Above 10 TeV, due to the low number of counts, a single spatial template is used, scaled to the number of counts in each energy bin. Similarly, a single spatial template is used for energies below 2 TeV. Templates are derived from data by constructing 2D acceptance maps for each energy bin and smoothing them with a 2D Gaussian kernel with standard deviation 0.125°. The fine spatial binning is chosen so that exclusion regions can be accounted for properly. For our GC analysis, we derive templates using observations of Sgr A* Off. Templates can then be transformed into sky coordinates to calculate the expected number of background counts for on-source observations. Since the sky plane rotates with respect to the camera coordinates over the course of a run, templates are aligned to the average camera coordinates in the sky plane.

Differences between V5 and V6 data, including differing energy thresholds, gamma/hadron separation cuts, and evolving instrument throughput factors motivate the possibility that different observing epochs require different templates. We derive 1D background count rates (acceptances, before normalization) from Sgr A* Off data for different years as functions of θ and plot them in Figure 67. The mean rates are consistent with each other within observing epochs V5 and V6, suggesting that only two templates are needed (one for each epoch). However, we observe that the variance of the rates between runs significantly exceeds what might be expected from Poisson noise, suggesting that templates require run-by-run scaling factors.

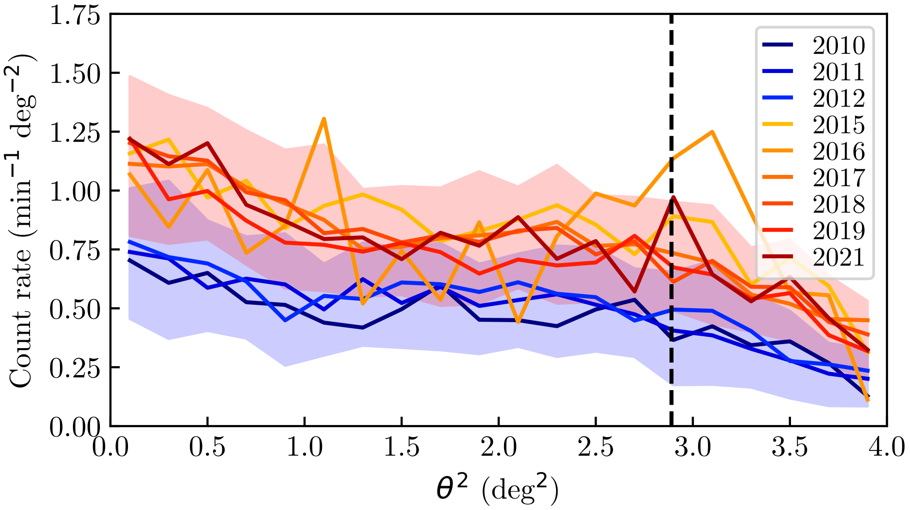

Figure 67: Background count rates averaged over rings of constant θ^2, by year. The 2016 data contains only a single run. The central intervals containing 68% of the run-by-run rates are shown for V5 (blue shaded region) and V6 (red shaded region). The edge of the template field of view is 1.7° (dashed vertical line).

Normalized templates derived from the V5 and V6 Sgr A* Off data set are shown in Figure 68. The camera's y axis aligns with the zenith axis, with the positive y direction corresponding to the negative zenith angle direction, and the x axis aligns with the azimuth axis. A gradient is visible along the zenith axis, naturally entering background estimates.

We evaluate the ability of the templates to model the backgrounds of individual runs through examining a goodness-of-fit statistic. The expected number of background counts $\mu_{\mathrm{B}}(x, y, E)$ in a bin centered at spatial coordinates x and y and energy E is given by

$$\mu_{\mathrm{B}}(x, y, E) = R(\vec{p}) t_{\mathrm{live}}(x, y) \Delta\Omega \Delta E(E) \tag{55}$$

where $\vec{p}$ are the parameters that the templates will depend on, t_{live} is an observation's live time, $\Delta\Omega$ is the spatial bin solid angle, and $\Delta E(E)$ is the energy bin width. The likelihood of observing binned counts $\vec{n}$ given the template parameters $\vec{p}$ is then the product of Poisson

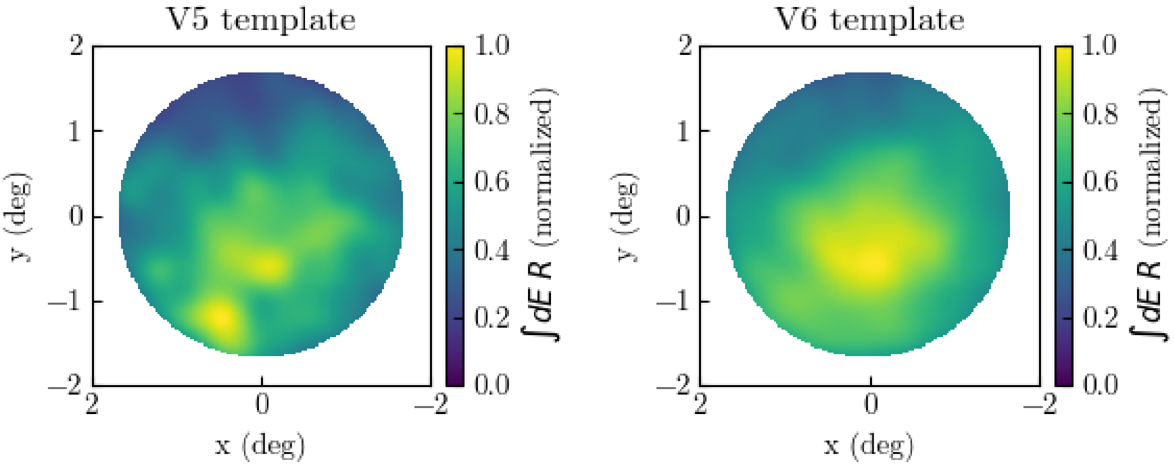

Figure 68: Normalized templates integrated over energy in camera coordinates for observing epochs V5 (left) and V6 (right). Due to the alignment of the camera axes with the azimuth and zenith axes, asymmetries in these parameters are visible.

probabilities

$$L(\vec{n}|\vec{p}) = \prod_{i,j,k} \frac{(\mu_{\mathrm{B}}(x_i, y_j, E_k))^{n_{ijk}}}{n_{ijk}!} e^{-\mu_{\mathrm{B}}(x_i,y_j,E_k)} \tag{56}$$

where i and j index over the spatial bins and k indexes over the energy bins. If we define the saturated model likelihood L_{sat} as (e.g. Baker & Cousins, 1984; Lindsey, 1998; Cousins, 2010)

$$L_{\mathrm{sat}}(\vec{n}) = \prod_{i,j,k} \frac{(n_{ijk})^{n_{ijk}}}{n_{ijk}!} e^{-n_{ijk}} \tag{57}$$

then the test statistic $-2\ln\lambda \equiv -2\ln(L(\vec{n}|\vec{p})/L_{\mathrm{sat}}(\vec{n}))$ asymptotically follows a χ^2 distribution with degrees of freedom equal to the number of bins minus the number of fit parameters, from which we may derive a p-value. However, for individual runs, many bins have few or zero counts, so the test statistic distribution differs from its asymptotic expectation. We can instead estimate the distribution for each run by running Monte Carlo simulations. We run 10^4 simulations for each run, drawing a random sample of counts for each from Poisson distributions with rates equal to the template predictions, then calculating $-2\ln\lambda$. The p-value can then be estimated as the fraction of simulated $-2\ln\lambda$ values greater (lower in likelihood) than what we measure. Using only the mean templates, we observe a large number of small p-values, indicating a poor fit to the data. We therefore introduce a normalization parameter N_0 that scales the mean templates R_0 such that $R = N_0 R_0$. We fit N_0 to each Sgr A* Off run by maximizing the likelihood function given by Equation 56. As a result, we observe p-values mostly ≥ 0.1. We conclude the two templates with a single normalization parameter provide an adequate fit to the Sgr A* Off data.

While N_0 is fit in the analysis of the Sgr A* Off data, we must avoid using the gamma-ray data to estimate the background in the Sgr A* data, as doing so would weaken our search for diffuse emission by potentially overestimating the background. Taking the fit value N_{fit} that maximizes the likelihood to be the true scaling parameter for each run, we aim to predict N_0 in a way that minimizes the RMS of the distribution of normalized residuals $(N_0 - N_{\text{fit}})/N_{\text{fit}}$. We first investigate the relation between the number of events selected by CR-like cuts and N_0, since both quantities are related to physical CR rates. Correlated variations of N_0 and CR-like event rate may be due to a given run's weather, night sky background, and other observing conditions. To properly account for exclusion regions and the acceptance for CR-like events, we derive V5 and V6 templates from the CR-like events in the Sgr A* Off data. Fitting these to the CR-like events in each run yields a CR normalization N_{CR}. Using a linear relation $N_0 = 0.26 N_{\text{CR}}$, we reduce the RMS of normalized residuals to 33%, versus 55% when using a single N_0 for all runs, as shown in Figure 69. We refine this relation by adding dependence on zenith angle θ_{zen} and year of observation t, such that

$$N_0 = \begin{cases} 0.14 N_{\text{CR}}(1 + 0.17(\theta_{\text{zen}} - 60)) & ; \quad t = 2010 \\ 0.16 N_{\text{CR}}(1 + 0.17(\theta_{\text{zen}} - 60)) & ; \quad t = 2011 \\ 0.18 N_{\text{CR}}(1 + 0.17(\theta_{\text{zen}} - 60)) & ; \quad t = 2012 \\ 0.27 N_{\text{CR}}(1 + 0.17(\theta_{\text{zen}} - 60)) & ; \quad \text{otherwise} \end{cases} \tag{58}$$

The normalized residuals achieved with this relation are also shown in Figure 69. This empirical formula for N_0 allows N_{fit} to be predicted with 14% uncertainty. This value is comparable to that of Mohrmann et al. (2019), who determine normalizations for their 3D

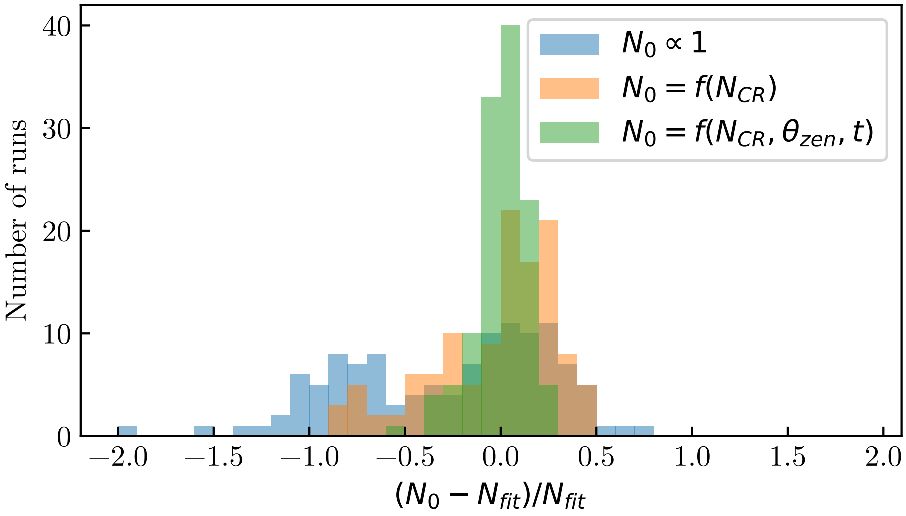

Figure 69: Histogram of template normalization residuals, assuming a constant N_0 (blue), dependence on N_{CR} (orange), and dependence on N_{CR}, zenith angle and date of observation (green). Residuals are calculated as the predicted N_0 minus the scaling that maximizes the likelihood N_{fit}, divided by N_{fit}. The narrowest N_0 residual distribution has an RMS of 14%.

background templates to within 12%, using the parameters θ_{zen}, t, and the "transparency coefficient."

One test of the validity of a background estimation method (and of the significance calculation) is that significances calculated at many trial positions over the field of view should be normally distributed, in the absence of gamma-ray sources (e.g. Berge et al., 2007). We calculate significances in circular regions of 0.13° radius centered at each pixel with nonzero live time. Details of the significance calculation will be discussed in Section 4.5. A 2D map and a 1D histogram of significances are shown in Figure 70. Maps of the on counts and mean background counts are also shown. The significances are approximately normally distributed, illustrating that the TBM provides an adequate description of the background over the entire field of view.

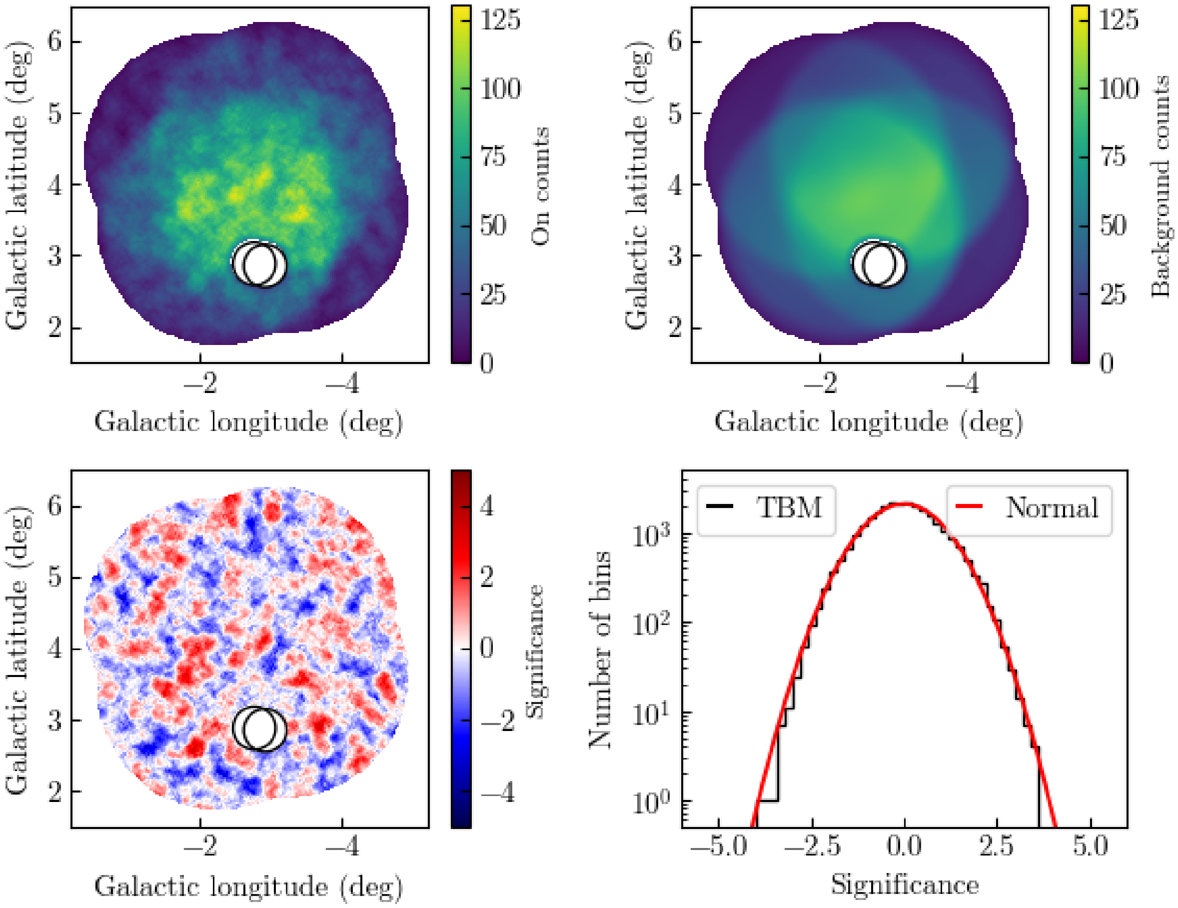

Figure 70: Application of the TBM to Sgr A* Off data. Maps are shown of correlated on counts (top left), mean background counts (top right), and significance (bottom left). Exclusion regions around bright stars d Ophiuchi and HIP85442 (black) are indicated. A histogram of significances is also shown (bottom right). The red curve is the normal distribution multiplied by the number of bins where significances are evaluated.

4.5 Significance

To evaluate whether or not a signal is present, we use the p-value, which in our case is the probability of observing the data under the assumption that the null hypothesis, that there is no signal, is true. The significance S (sometimes called the Z-value) communicates a p-value by giving the corresponding number of standard deviations for the normal distribution. A significance of 5σ is often used as the threshold for discoveries in high-energy physics (e.g. Lyons, 2013).

For on/off background estimation methods such as the RBM and MRM, the number of events in an on region, N_{on}, and off region, N_{off}, are measured, which are both observations of Poisson-distributed random variables. The expected number of on counts may be expressed as the signal counts, N_{S}, plus background counts, N_{B}, while the expected number of off counts is conventionally defined as N_{B}/α. Assuming that the off region contains no signal counts, N_{S} may then be estimated as $N_{\mathrm{on}} - \alpha N_{\mathrm{off}}$. Using the Gaussian approximation for Poisson uncertainties gives a significance

$$S \approx \frac{N_{\mathrm{on}} - \alpha N_{\mathrm{off}}}{\sqrt{N_{\mathrm{on}} + \alpha^2 N_{\mathrm{off}}}} \tag{59}$$

However, Monte Carlo simulations reveal Equation 59 to be a poor estimator of the significance, particularly for $\alpha \neq 1$ (Li & Ma, 1983; Cousins et al., 2008). Li & Ma (1983) derive the following, more accurate expression using likelihood ratios

$$S_{\mathrm{LiMa}} = \sqrt{2}\left\{N_{\mathrm{on}} \ln\left[\frac{1+\alpha}{\alpha}\left(\frac{N_{\mathrm{on}}}{N_{\mathrm{on}} + N_{\mathrm{off}}}\right)\right] + N_{\mathrm{off}} \ln\left[(1+\alpha)\left(\frac{N_{\mathrm{off}}}{N_{\mathrm{on}} + N_{\mathrm{off}}}\right)\right]\right\}^{1/2} \tag{60}$$

Their derivation proceeds from the likelihood L of observing N_{on} and N_{off} given N_{S} and N_{B}

$$L(N_{\mathrm{S}}, N_{\mathrm{B}}) = \frac{(N_{\mathrm{S}} + N_{\mathrm{B}})^{N_{\mathrm{on}}}}{N_{\mathrm{on}}!} e^{-(N_{\mathrm{S}}+N_{\mathrm{B}})} \frac{(N_{\mathrm{B}}/\alpha)^{N_{\mathrm{off}}}}{N_{\mathrm{off}}!} e^{-N_{\mathrm{B}}/\alpha} \tag{61}$$

The likelihood ratio λ of the maximum-likelihood model with fixed $N_{\mathrm{S}} = 0$ to the maximum likelihood is

$$\lambda = \frac{L(0, \hat{\hat{N}}_{\mathrm{B}})}{L(\hat{N}_{\mathrm{S}}, \hat{N}_{\mathrm{B}})} \tag{62}$$

where $\hat{\hat{N}}_{\mathrm{B}}$ maximizes $L(0, \hat{\hat{N}}_{\mathrm{B}})$, and $\hat{N}_{\mathrm{S}}$ and $\hat{N}_{\mathrm{B}}$ maximize L without the $N_{\mathrm{S}} = 0$ constraint.

L is maximized when $N_\mathrm{S} + N_\mathrm{B} = N_\mathrm{on}$ and $N_\mathrm{B}/\alpha = N_\mathrm{off}$, so

$$\hat{N_\mathrm{S}} = N_\mathrm{on} - \alpha N_\mathrm{off} \tag{63}$$

$$\hat{N_\mathrm{B}} = \alpha N_\mathrm{off} \tag{64}$$

$\hat{\hat{N_\mathrm{B}}}$ can be derived by noting that under the null hypothesis, N_on and N_off are both measurements of the background rate, so

$$N_\mathrm{on} + N_\mathrm{off} = \hat{\hat{N_\mathrm{B}}} + \hat{\hat{N_\mathrm{B}}}/\alpha \tag{65}$$

which may be rearranged to yield

$$\hat{\hat{N_\mathrm{B}}} = \frac{\alpha}{1+\alpha}(N_\mathrm{on} + N_\mathrm{off}) \tag{66}$$

Then, by Wilks' theorem (Wilks, 1938), $-2\ln\lambda$ will be asymptotically distributed as a χ^2 statistic with one degree of freedom if the null hypothesis is true. Since S^2 is also distributed as a χ^2 statistic with one degree of freedom for the normal distribution, we have

$$S_\mathrm{LiMa} = \sqrt{-2\ln\lambda} \tag{67}$$

which yields Equation 60 after substituting in the values of $\hat{\hat{N_\mathrm{B}}}$, $\hat{N_\mathrm{S}}$, and $\hat{N_\mathrm{B}}$.

In deriving Equation 60, uncertainty in α is assumed to be negligible. If α is instead drawn from a Gaussian distribution with mean μ_α and standard deviation σ_α, the likelihood becomes (Dickinson & Conrad, 2013; Spengler, 2015)

$$L(N_\mathrm{S}, N_\mathrm{B}, \alpha) = \frac{(N_\mathrm{S}+N_\mathrm{B})^{N_\mathrm{on}}}{N_\mathrm{on}!} e^{-(N_\mathrm{S}+N_\mathrm{B})} \frac{(N_\mathrm{B}/\alpha)^{N_\mathrm{off}}}{N_\mathrm{off}!} e^{-N_\mathrm{B}/\alpha} \frac{1}{\sqrt{2\pi\sigma_\alpha^2}} e^{-\frac{1}{2}(N_\mathrm{B}-\mu_\alpha)^2/\sigma_\alpha^2} \tag{68}$$

Spengler (2015) derive a modified significance from this likelihood

$$S_{\text{Modified}} = \text{sign}(N_{\text{on}} - \alpha N_{\text{off}}) \sqrt{S_{\text{LiMa}}^2 + \left(\frac{\alpha^* - \alpha}{\sigma_\alpha}\right)^2} \tag{69}$$

In the TBM case, we instead observe only N_{on}, while N_{B} is drawn from a Gaussian distribution with mean μ_{B} and standard deviation σ_{B}. The likelihood for this "Gaussian-mean background" problem is (Cousins et al., 2008)

$$L_{\text{G}}(N_{\text{S}}, N_{\text{B}}) = \frac{(N_{\text{S}} + N_{\text{B}})^{N_{\text{on}}}}{N_{\text{on}}!} e^{-(N_{\text{S}}+N_{\text{B}})} \frac{1}{\sqrt{2\pi\sigma_{\text{B}}^2}} e^{-\frac{1}{2}(N_{\text{B}}-\mu_{\text{B}})^2/\sigma_{\text{B}}^2} \tag{70}$$

To find the significance, we again must find $\hat{N}_{\text{S}}$, $\hat{N}_{\text{B}}$, and $\hat{\hat{N}}_{\text{B}}$. We can see that the Poisson and Gaussian parts of L_{G} can be maximized simultaneously with $N_{\text{S}} + N_{\text{B}} = N_{\text{on}}$ and $N_{\text{B}} = \mu_{\text{B}}$, so

$$\hat{N}_{\text{S}} = N_{\text{on}} - \mu_{\text{B}} \tag{71}$$

$$\hat{N}_{\text{B}} = \mu_{\text{B}} \tag{72}$$

$\hat{\hat{N}}_{\text{B}}$ may be found by solving $\frac{\partial}{\partial N_{\text{B}}} L_{\text{G}}(0, N_{\text{B}}) = 0$, yielding

$$\hat{\hat{N}}_{\text{B}} = \frac{1}{2}\left(\mu_{\text{B}} - \sigma_{\text{B}}^2 \pm \sqrt{(\mu_{\text{B}} - \sigma_{\text{B}}^2)^2 + 4N_{\text{on}}\sigma_{\text{B}}^2}\right) \tag{73}$$

where only the positive solution is physical. The significance can then be written

$$S_{\text{G}} = \text{sign}(N_{\text{on}} - \mu_{\text{B}}) \sqrt{-2N_{\text{on}}(1 + \ln(\hat{\hat{N}}_{\text{B}}/N_{\text{on}})) + 2\hat{\hat{N}}_{\text{B}} + (\hat{\hat{N}}_{\text{B}} - \mu_{\text{B}})^2/\sigma_{\text{B}}^2} \tag{74}$$

4.6 Upper Limits

In the case of a non-significant detection, an upper limit can be placed on N_{S}. We derive upper limits using the profile likelihood method (e.g. Rolke et al., 2005; Cowan et al., 2011;

Particle Data Group et al., 2020), which corresponds asymptotically to the limits of Feldman & Cousins (1998). The limit is based on the likelihood ratio λ given by

$$\lambda = \frac{L(N_{\mathrm{S}}, \hat{\hat{N}}_{\mathrm{B}})}{L(\hat{N}_{\mathrm{S}}, \hat{N}_{\mathrm{B}})} \tag{75}$$

where the hat notation has the same meaning as in Section 4.5. Contours of constant $-2\ln\lambda$ correspond to different confidence levels on combinations of parameters. For estimation of a single parameter N_{S}, from Wilks' theorem (Wilks, 1938) it can be found that $-2\ln\lambda = 1.0$ corresponds to a 68.3% confidence level, and $-2\ln\lambda = 3.84$ to 95% (Particle Data Group et al., 2020). We follow the method of Rolke et al. (2005), wherein N_{S} is increased until $-2\ln\lambda$ reaches a value corresponding to the desired confidence level, with $L(N_{\mathrm{S}}, \hat{\hat{N}}_{\mathrm{B}})$ maximized at each N_{S} when calculating $-2\ln\lambda$. For the likelihood given by Equation 74, $\hat{\hat{N}}_{\mathrm{B}}$ for a given N_{S} is

$$\hat{\hat{N}}_{\mathrm{B}} = \frac{1}{2}\left(-N_{\mathrm{S}} + \mu_{\mathrm{B}} - \sigma_{\mathrm{B}}^2 \pm \sqrt{(N_{\mathrm{S}} + \mu_{\mathrm{B}} - \sigma_{\mathrm{B}}^2)^2 + 4N_{\mathrm{on}}\sigma_{\mathrm{B}}^2}\right) \tag{76}$$

For more complicated likelihoods, optimizations are performed numerically with `SciPy` version 1.7.1 (Virtanen et al., 2020).

4.7 Differential Flux

While our significance and limit calculations use the number of detected counts, dark matter theories predict differential fluxes. Counts are related to the differential flux $d\Phi/dE$ (with dimensions of area^{-1} time^{-1} energy^{-1}) by the effective area A according to Equation 50, which we rewrite in a way that can apply to multiple observations as

$$N_{\mathrm{S}} = \int dt \int d\Omega \int_{E-\Delta E/2}^{E+\Delta E/2} dE' \frac{d^2\Phi}{dE'd\Omega} A I(t) \tag{77}$$

where N_{S} is the expected number of signal counts with energies within $E \pm \Delta E/2$, integrated over solid angle Ω and time t, and $I(t)$ is an indicator function that equals one when the instrument is live and the time has not been cut, and zero otherwise. In practice, this integral is simplified to

$$N_{\mathrm{S}} = t_{\mathrm{live}} \int_{E-\Delta E/2}^{E+\Delta E/2} dE' \frac{d\overline{\Phi}}{dE'} \overline{A} \tag{78}$$

where t_{live} is the live time contained in all observations, and the quantities $d\overline{\Phi}/dE$ and $\overline{A}$ are averaged over time and solid angle. $\overline{A}$ may be approximated by using the A_i found from lookup tables for each event. with an energy in the energy bin considered. Since the number of events, N_{ev}, is proportional to both time and A_i, we must weight each A_i by $1/A_i$ to avoid biasing $\overline{A}$ to higher values, yielding

$$\overline{A} = \frac{\sum_i^{N_{\mathrm{ev}}} A_i/A_i}{\sum_i^{N_{\mathrm{ev}}} 1/A_i} \tag{79}$$

or

$$1/\overline{A} = \frac{1}{N_{\mathrm{ev}}} \sum_i^{N_{\mathrm{ev}}} 1/A_i \tag{80}$$

This formula may be used to find the effective area at different energies, before integrating $\overline{A}$ with the differential flux. When also applied to on/off analyses, this expression leads to the commonly-used formula for calculating differential flux (e.g. Aharonian et al., 1999; Acciari et al., 2008)

$$\frac{d\Phi}{dE} = \frac{1}{t_{\mathrm{live}} \Delta E} \left(\sum_i^{N_{\mathrm{on}}} 1/A_{\mathrm{on},i} - \alpha \sum_i^{N_{\mathrm{off}}} 1/A_{\mathrm{off},i} \right) \tag{81}$$

where N_{on} and N_{off} are the number of on and off events observed, each event has estimated effective area $A_{\mathrm{on},i}$ or $A_{\mathrm{off},i}$, and α is the ratio of expected background counts in the on region to the off region.

For the TBM, the flux can instead be estimated with

$$\frac{d\Phi}{dE} = \frac{N_{\mathrm{on}} - \mu_{\mathrm{B}}}{t_{\mathrm{live}} \Delta E} \frac{1}{N_{\mathrm{on}}} \sum_i^{N_{\mathrm{on}}} 1/A_{\mathrm{on},i} \tag{82}$$

5 VERITAS Analysis and Results

This section will present our analysis of the GC data and results concerning both astrophysical sources and dark matter.

5.1 The Galactic Center Ridge

The Sgr A* observations are reduced with VEGAS version 2.5.8, using *disp* and energy BDTs for event reconstruction, effective area tables corresponding to these reconstruction methods, and gamma/hadron separation cuts optimized for LZA data. Details on the analysis methods are found in Section 4. Of the total 177.8 hr exposure time, 154.3 hr of live time remain after quality cuts and deadtime correction. An energy threshold of 2 TeV is adopted.

We apply the template background method (TBM; Section 4.4.4) to the Sgr A* data. 2D maps of on counts, background counts, and significances are shown in Figure 71, summed over energy. Circular on regions of radius 0.13° are used. Exclusion regions include circular regions of radius 0.3° around bright stars, regions of radius 0.4° around the gamma-ray sources J1745–290, SNR G0.9+0.1, and HESS J1746–285, a region of radius 0.6° around the extended gamma-ray source HESS J1745–303 (Aharonian et al., 2006, 2008; H.E.S.S. Collaboration et al., 2018a) centered at Galactic longitude and latitude $(\ell, b) = (-1.36°, -0.56°)$, and the region $|b| < 0.3°$ covering emission along the Galactic plane.

We next perform a ring background method (RBM; Section 4.4.2) analysis for comparison with the TBM. The resulting significance map is shown in Figure 72. The on region radius is 0.13°, while the background region rings have inner radius 0.6° and outer radius 0.8°. Linear zenith angle corrections are applied to the acceptance maps of individual runs, before calculating α. The significances are similar to those of the TBM—the central source J1745–290 is detected at a significance of 40.1 standard deviations (σ) with the TBM versus 39.9σ with the RBM.

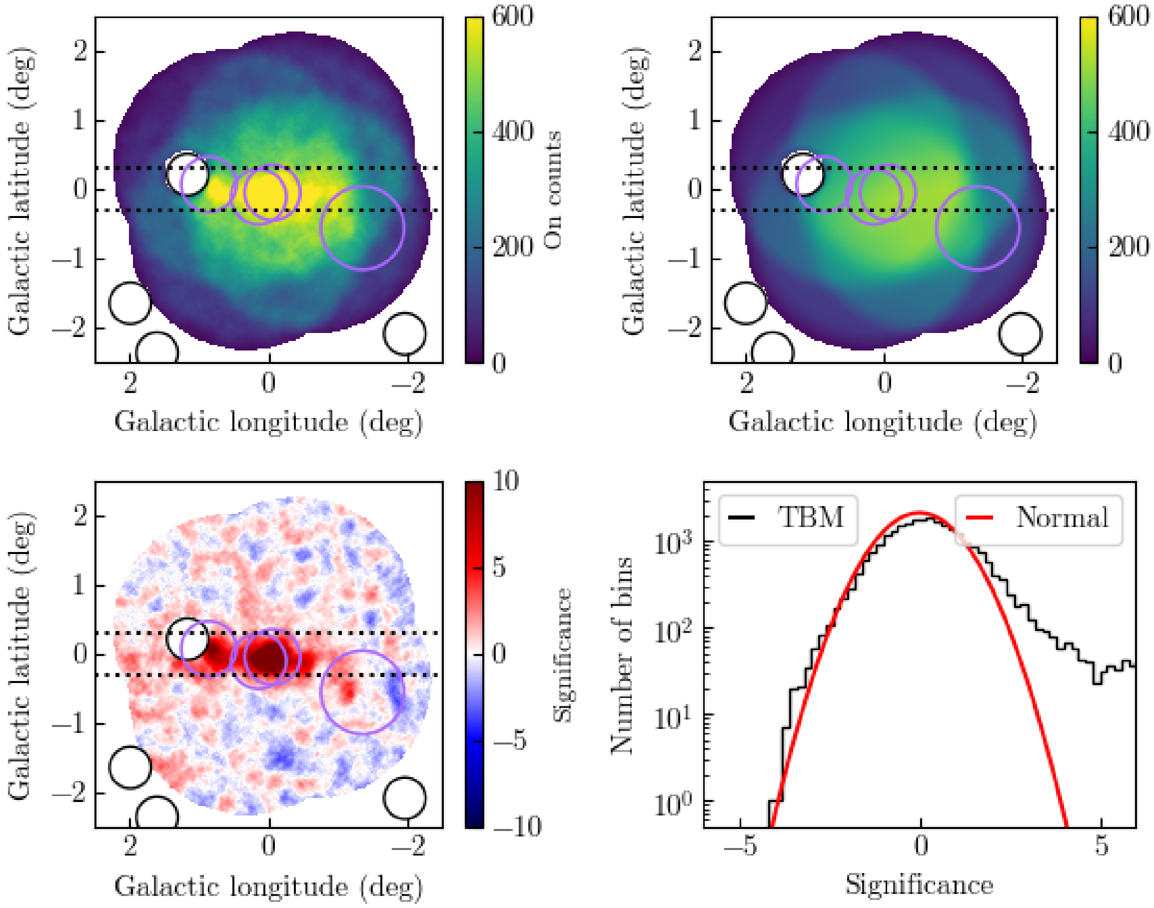

Figure 71: Application of the TBM to the Sgr A* data set. Maps are shown of correlated on counts (top left), mean background counts (top right), and significance (bottom left). The color scales of the count maps are truncated at 600 counts and the color scale of the significance map is limited to $\pm 10\sigma$, to increase the visibility of structure. Exclusion regions around bright stars (black), gamma-ray sources (purple), and the GC ridge (dotted lines) are indicated. A histogram of significances is also shown (bottom right). The red curve is the normal distribution multiplied by the number of bins where significances are evaluated, not including the bins that are in exclusion regions.

5.1.1 Source Analysis

Detailed analysis of the astrophysical sources was carried out with the RBM and reflected region methods using a subset of the data collected between 2010 April and 2018 June containing 125 hr of live time. That work, refining the analysis of Buchovecky (2019), has been presented in Adams et al. (2021). A sky map highlighting the sources studied is shown in Figure 73. Table 6 contains the fit parameters to each source's differential energy

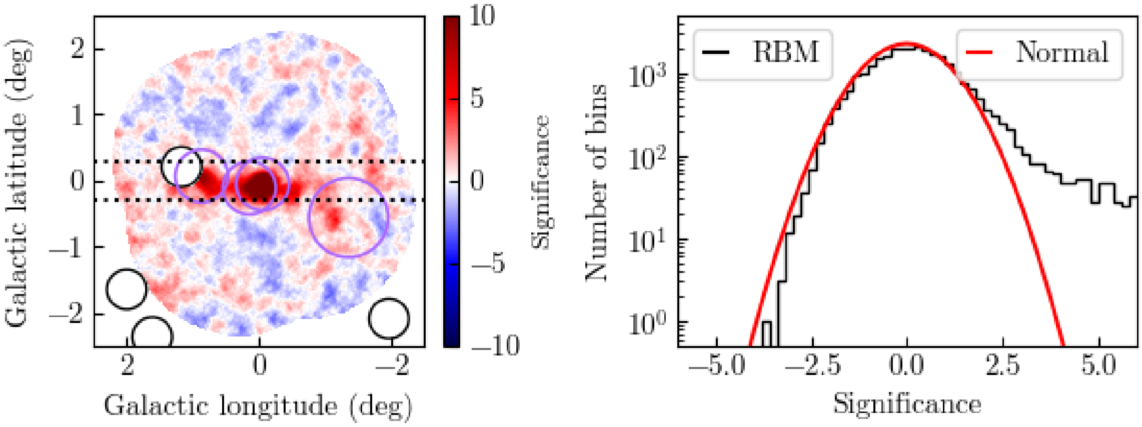

Figure 72: Sgr A* RBM significance map (left) and histogram (right). The color scale of the significance map is limited to $\pm 10\sigma$. Exclusion regions around bright stars (black), gamma-ray sources (purple), and the GC ridge (dotted lines) are indicated. The red curve is the normal distribution multiplied by the number of bins where significances are evaluated.

spectrum. We summarize the results here.

Source	Φ_0 (10^{-14} TeV^{-1} cm^{-2} s^{-1})	Γ	$E_{\rm cut}$ (TeV)
J1745–290	$12.7^{+2.2}_{-2.3}$	$2.12^{+0.22}_{-0.17}$	$10^{+4.0}_{-2.0}$
GC ridge	3.44 ± 0.62	2.19 ± 0.20	
G0.9+0.1	1.51 ± 0.30	2.00 ± 0.28	
J1746–285	1.51 ± 0.22	1.83 ± 0.22	

Table 6: Fit parameters to the differential energy spectra of sources in the GC region with significant detections. Fits are either power laws of the form $d\Phi/dE = \Phi_0(E/E_0)^{-\Gamma}$ or exponentially cutoff power laws given by Equation 83. $E_0 = 5.3$ TeV, chosen to reduce correlations between parameters. Uncertainties reflect 68% confidence intervals on the fit parameter values.

We detect J1745–290 with a significance of 37.5σ at a position $(\ell, b) = (-0.07°, -0.047°)$, consistent with previous VERITAS analyses (Archer et al., 2014, 2016). The source is spatially coincident with the radio source Sgr A* (Reid & Brunthaler, 2004), as well as PWN G359.95–0.04 (Wang et al., 2006). Its spectral energy distribution is measured between 1.9 TeV and 39.8 TeV and is shown in Figure 74, along with gamma-ray measurements from other experiments. We find that the spectrum dN/dE is inconsistent with a single power

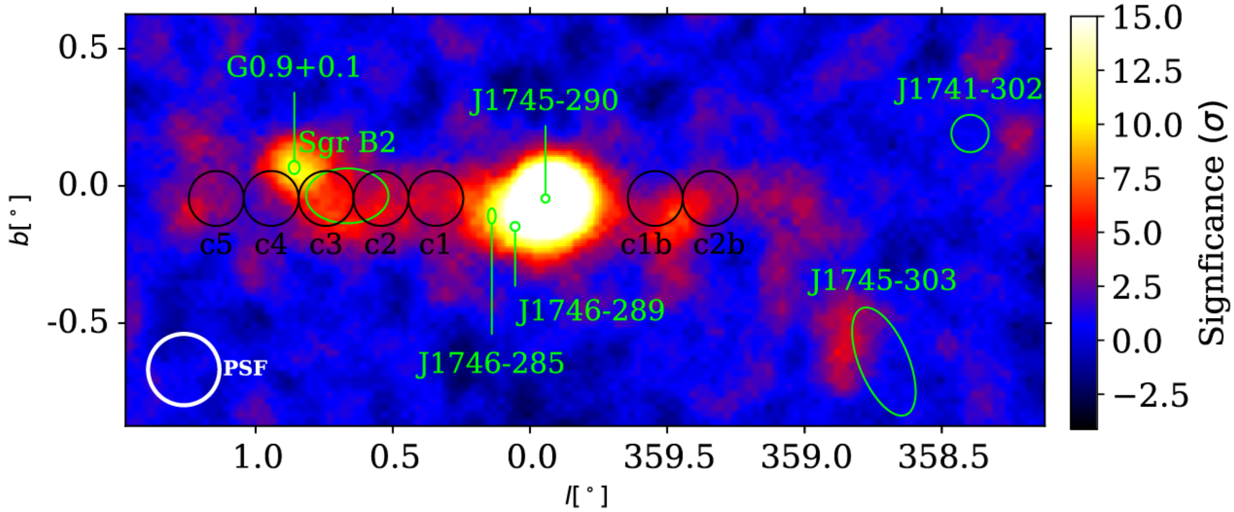

Figure 73: RBM significance map of gamma rays with energies above 2 TeV, using data taken between 2010 and 2018, zoomed in around the GC ridge. Source positions are indicated (green), including the seven regions used to measure the diffuse emission from the GC ridge (black). The VERITAS LZA PSF is also shown (white). Figure adapted from Adams et al. (2021).

law, but can be described with an exponentially cutoff power law of the form

$$\frac{d\Phi}{dE} = \Phi_0 \left(\frac{E}{E_0}\right)^{-\Gamma} e^{-E/E_{\text{cut}}} \tag{83}$$

with $\Phi_0 = 12.7^{+2.2}_{-2.3} \times 10^{-14}$ TeV^{-1} cm^{-2} s^{-1}, $\Gamma = 2.12^{+0.22}_{-0.17}$, and $E_{\text{cut}} = 10^{+4.0}_{-2.0}$ TeV, where the limits represent 68% confidence intervals. E_0 is fixed to 5.3 TeV, to minimize covariance between parameters. Alternatively, a smoothly broken power law with a break energy of ∼7 TeV also provides an adequate fit to the data. No evidence of significant variability in the integrated flux above 2 TeV and 10 TeV is found on day-to-year timescales.

J1745–290's TeV emission may be due to a number of processes involving high-energy hadronic or leptonic cosmic rays, with the cutoff representing a maximum energy of an acceleration mechanism or photon-photon absorption (e.g. Atoyan & Dermer, 2004; Aharonian & Neronov, 2005; Ballantyne et al., 2011; Chernyakova et al., 2011; Kusunose & Takahara, 2012; Fatuzzo & Melia, 2012; Linden et al., 2012; Guo et al., 2013), as reviewed by van Eldik (2015). Proposed sources include the supermassive black hole Sgr A* (Aharonian &

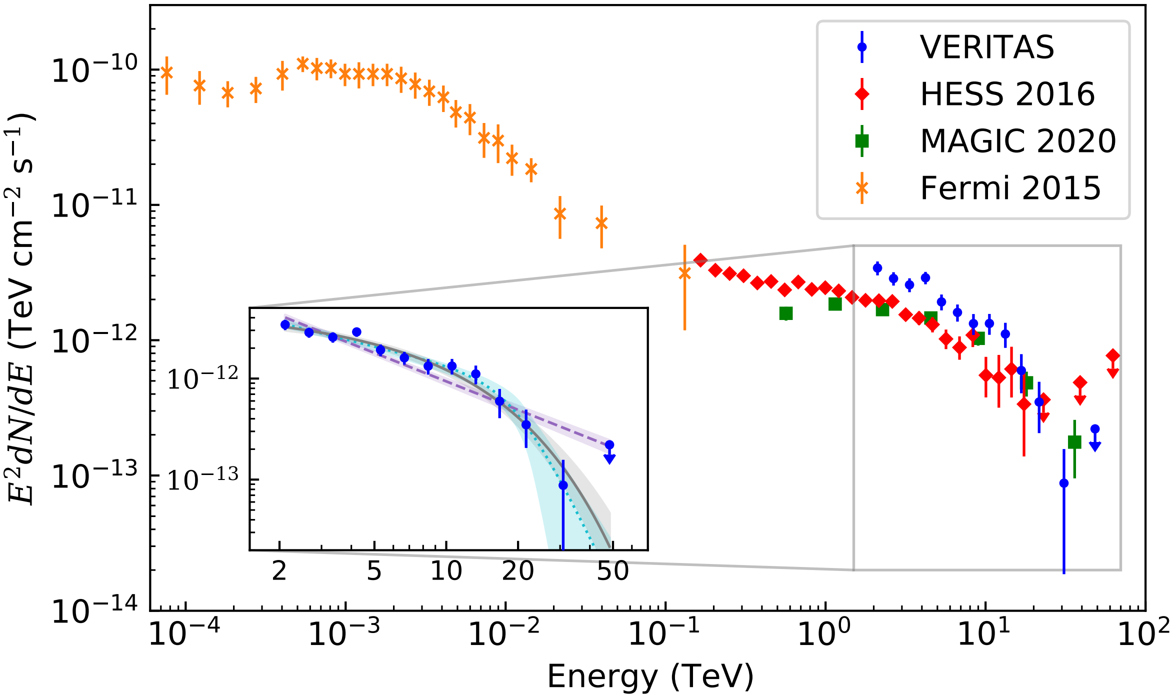

Figure 74: Spectral energy distribution of central source J1745–290. In addition to our measurement (blue), the results of H.E.S.S. (HESS Collaboration et al., 2016), MAGIC (MAGIC Collaboration et al., 2020), and *Fermi* (Malyshev et al., 2015) are shown. Error bars represent 1σ uncertainties, while data points with downward arrows indicate 95% confidence level upper limits. The VERITAS spectrum shows evidence of a cutoff around 10 TeV, consistent with other measurements. The elevated flux relative to other measurements may be due to contributions from diffuse emission or systematic uncertainties. The inset figure shows fits to the VERITAS data with an exponentially cutoff power law (gray solid line), broken power law (cyan dotted line), and power law (purple dashed line). Shaded regions represent the 1σ confidence band on the model fits. Figure from Adams et al. (2021).

Neronov, 2005) or its winds (Atoyan & Dermer, 2004; Kusunose & Takahara, 2012), PWN G359.95–0.04 (Wang et al., 2006; Hinton & Aharonian, 2007), unresolved pulsars (Hooper & Linden, 2011; Bednarek & Sobczak, 2013), or dark matter (Belikov et al., 2012). Sources highly variable at other wavelengths may still be compatible with J1745–290 if the TeV emission region is extended, damping out variability on shorter timescales. Determining the source of J1745–290 may be an important component of understanding the GeV GC excess (especially for pulsar models with TeV halos), as well as the diffuse TeV emission in the region.

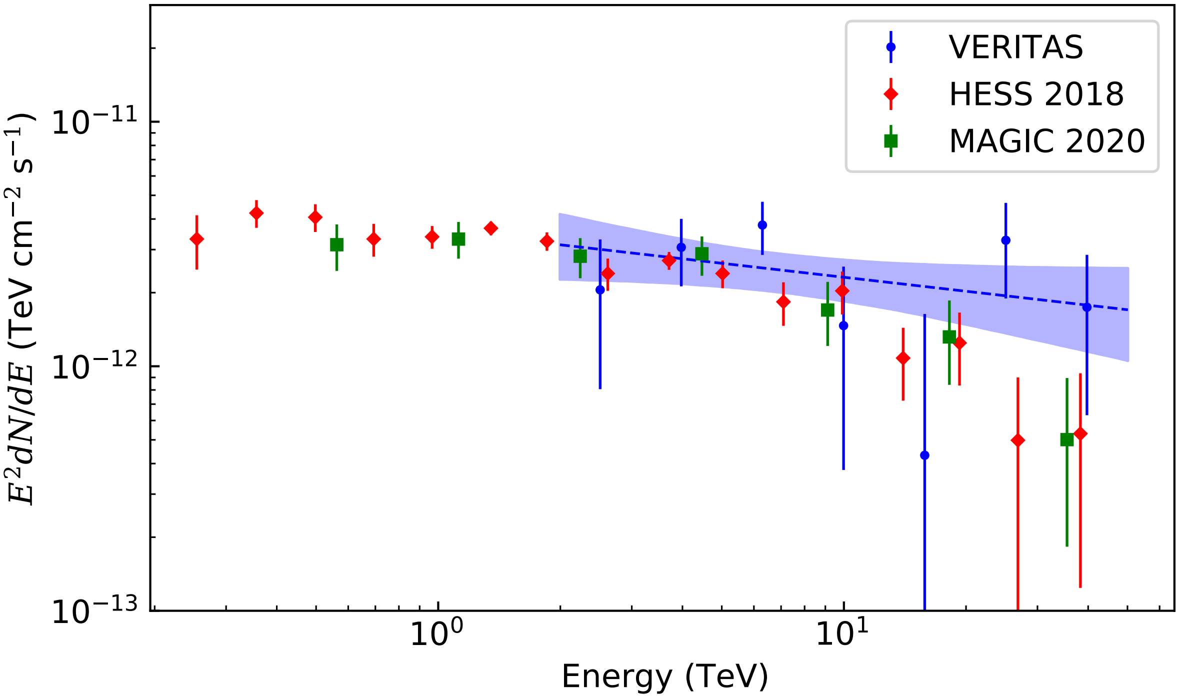

Figure 75: Spectral energy distribution of the GC ridge. The VERITAS data are shown (blue), along with the best-fit power law (blue dashed line) and 1σ confidence band on the fit (blue shaded region) is shown. In addition to our measurement, the results of H.E.S.S. (HESS Collaboration et al., 2016), MAGIC (MAGIC Collaboration et al., 2020), and *Fermi* (Malyshev et al., 2015) are shown. Error bars represent 1σ uncertainties. The VERITAS spectrum shows no evidence of a cutoff, consistent with other measurements. Figure from Adams et al. (2021).

We detect diffuse emission from the "GC ridge" with a significance of 9.5σ, using the seven circular regions of HESS Collaboration et al. (2016), shown in Figure 73. The significance map suggests spatial extension between $-1^\circ < \ell < 1.3^\circ$ and $|b| < 0.3^\circ$, corresponding to hundreds of parsecs assuming a distance from Earth of $\sim$8 kpc. We report the first VERITAS measurement of the diffuse ridge emission spectrum, shown in Figure 75. The spectrum is consistent with a power law ($d\Phi/dE \propto E^{-\Gamma}$) with index $\Gamma = 2.19 \pm 0.20$ up to 40 TeV, without evidence of a cutoff.

HESS Collaboration et al. (2016) put forward that this hard and extended emission may be explained by proton-proton interactions with a hard CR proton spectrum extending above

1 PeV. Supporting this interpretation, they point out the spatial correlation of the emission with molecular gas in the CMZ and the difficulty of pure leptonic models in producing such high-energy gamma-ray emission over the spatial extent of the CMZ. If this interpretation is correct, this would be the first evidence of a source that emits CRs up to knee/PeV energies, or "PeVatron." Using the model of Kelner et al. (2006), we find that a power-law proton spectrum with $\Gamma = 2.3$ provides the best fit to our gamma-ray spectrum. Keeping the power-law index fixed, we derive a 95% confidence level lower limit on an exponential cutoff in the proton spectrum of 0.08 PeV. HESS Collaboration et al. (2016) find a proton spectral index of $\Gamma \sim 2.4$ and 95% confidence level lower limit on the cutoff of 0.4 PeV.

The PeVatron itself was initially suggested to be Sgr A* (HESS Collaboration et al., 2016). Alternative sources of the high-energy CRs in the region include past activity from Sgr A* (Fujita et al., 2017), stellar winds from compact stellar clusters (Crocker et al., 2011), millisecond pulsars (Guépin et al., 2018), and a combination of pulsars and dark matter (Lacroix et al., 2016). Additionally, Gaggero et al. (2017) find that certain models of particle propagation alone can explain much (but not all) of the TeV emission, though this is disputed by Aharonian et al. (2020).

H.E.S.S. Collaboration et al. (2018b) and MAGIC Collaboration et al. (2020) both mention that a 3D model of the gas distribution is needed to accurately model the diffuse emission. MAGIC Collaboration et al. (2020) illustrate the effects of using a 3D rather than 2D model, using the CS 1-0 emission map of Tsuboi et al. (1999) and the theoretical mapping between line-of-sight velocity and line-of-sight distance of Sawada et al. (2004), combined with a spherically-symmetric power-law distribution for the cosmic-ray density. The 3D gas map of (Ferrière et al., 2007) has also been used in analyses of the diffuse emission (e.g. Gaggero et al., 2017).

We detect the composite SNR G0.9+0.1 with 8σ significance and measure its spectrum. The spectrum is consistent with a power law with $\Gamma = 2.00 \pm 0.28$ and a flux of $(1.51 \pm 0.30) \times 10^{-14}$ TeV^{-1} cm^{-2} s^{-1} at 5.3 TeV. G0.9+0.1 is the only TeV source in the region with a reasonably firm identification—a PWN and surrounding SNR (Helfand & Becker, 1987; Aharonian et al., 2005; Camilo et al., 2009; van Eldik, 2015). While inverse Compton scattering of relativistic electrons has been suggested as the source of emission (Aharonian et al., 2005), a more recent model fit to X-ray data finds that the TeV emission is underpredicted (Holler et al., 2012). We also note that a cutoff in the spectrum has yet to be seen.

We measure the spectrum of the source HESS J1746–285 at the position given by (H.E.S.S. Collaboration et al., 2018b) to be consistent with a power law with $\Gamma = 1.83 \pm 0.22$ and a flux of $(1.51 \pm 0.22) \times 10^{-14}$ TeV^{-1} cm^{-2} s^{-1} at 5.3 TeV. MAGIC Collaboration et al. (2020) associate the source with the radio arc while H.E.S.S. Collaboration et al. (2018a) provide several potential associations. Potential counterparts include the Galactic radio arc (Yusef-Zadeh et al., 1984, 2004), G0.13–0.11 (Wang et al., 2002), and 4FGL J1746.4-2852 (Abdollahi et al., 2020).

5.2 The Galactic Center Halo

To search for a dark matter signal in the GC halo, we use the TBM results, excluding the events falling within the exclusion regions described in Section 5.1. The TBM significance map with all exclusion regions applied is shown in Figure 76. The significance distribution is consistent with the normal distribution, showing no evidence of an excess.

We next consider a larger source region in order to search for a dark matter signal. We use multiple ring-shaped spatial regions of interest to exploit the dark matter halo's spatial profile, as was done in similar analyses performed by the H.E.S.S. collaboration (Abdallah et al., 2016, 2018; Abdalla et al., 2022). 15 regions are defined, with inner radii, θ, between 0.5° and 1.9° and thickness 0.1° centered at $(\ell, b) = (0°, 0°)$. A map of these regions, superimposed on the total live time accumulated at different points on the sky, is shown in Figure 77. For each region and each energy bin we calculate a set of $\{N_{\text{on}}, \mu_{\text{B}}, \sigma_{\text{B}}\}$, for use in the likelihood function given by Equation 74. The full likelihood function is the product

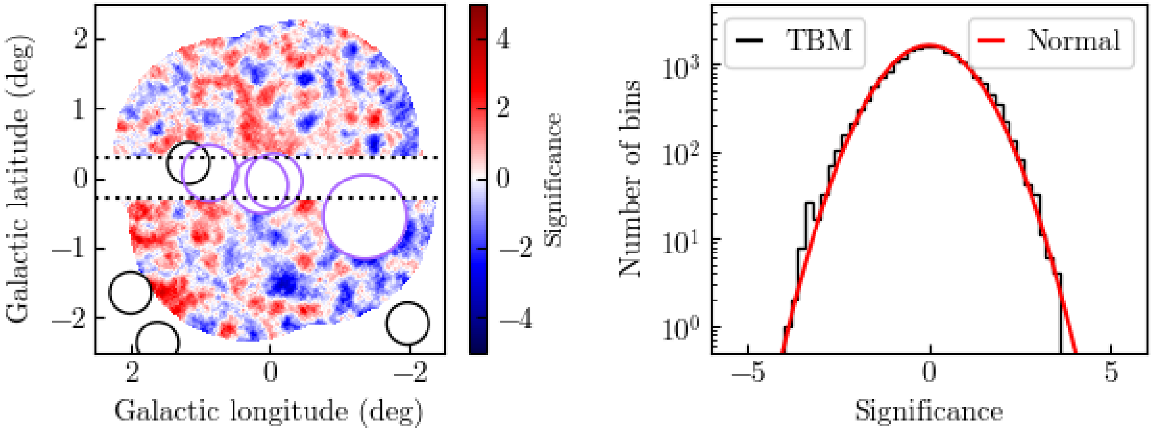

Figure 76: TBM significance map (left) and histogram (right), with known gamma-ray sources excluded. Exclusion regions around bright stars (black), gamma-ray sources (purple), and the GC ridge (dotted line) are indicated. The red curve is the normal distribution multiplied by the number of bins where significances are evaluated.

of likelihoods in each region of interest and each energy bin. The number of events in each region, summed over energies, is given in Table 7.

Effective areas are calculated separately for each region of interest and energy bin. Several effective areas are plotted in Figure 78. Since the effective areas average over V5 and V6 data, the values fall between those typical of either epoch. In the innermost region $0.5° < \theta < 0.6°$, where the dark matter signal is expected to be strongest, the effective area above 10 TeV is $\sim 2 \times 10^5$ m^2.

While the spatial distribution of events in the Sgr A* data is well-modeled, evidenced by the normally-distributed significances in the significance map, we find that the energy distribution of the events differs from the templates at high energies. This reflects differences in the differential event rates observed in the Sgr A* and the Sgr A* Off data, as illustrated in Figure 79. The event rate in the Sgr A* observations exceeds what is predicted by the templates above ∼10 TeV and is smaller at lower energies. We investigate differences in the data set properties that could potentially cause this discrepancy, but do not find the origin. Effective areas are approximately equal between data sets, after binning by epoch. The difference in rates also persists after restricting the data to small ranges of zenith angles,

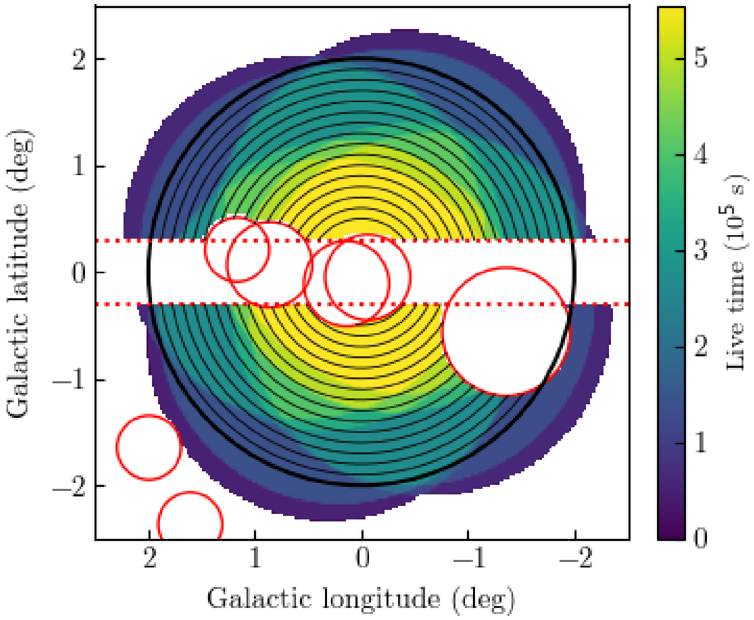

Figure 77: Map of total live time, with the ring-shaped regions of interest used for the dark matter search superimposed (black lines). The 2° radius circle bounding the total region of interest is emphasized. Exclusion regions around bright stars and gamma-ray sources are shown (red circles), as are the bounds around the Galactic plane (dotted red lines). Excluded pixels and those with zero live time are colored white.

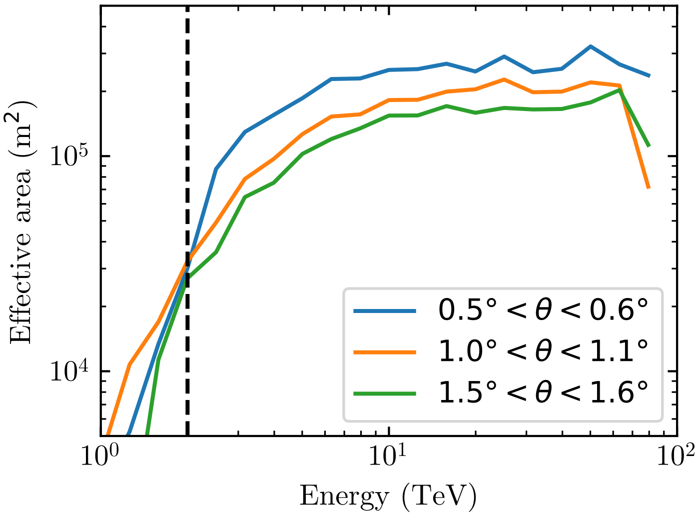

Figure 78: Effective area versus energy for different regions of interest used in the dark matter analysis, with inner radii 0.5° (blue), 1.0° (orange), and 1.5° (green). The energy threshold of 2 TeV is indicated (dashed vertical line).

Inner θ (°)	N_{on}	μ_{B}
0.5	1408	1301.4
0.6	2103	1994.5
0.7	2365	2289.3
0.8	2584	2517.1
0.9	2782	2757.7
1.0	3029	2871.2
1.1	2824	2831.6
1.2	2710	2707.8
1.3	2581	2549.0
1.4	2353	2397.4
1.5	2362	2376.5
1.6	2159	2210.2
1.7	2155	2135.6
1.8	2050	2025.7
1.9	1745	1826.1

Table 7: Number of gamma-like events and TBM prediction in each spatial region, identified by the regions' inner radii.

azimuth angles, angular offsets in the camera plane, and year of observation. Increasing the sizes of the exclusion regions also does not eliminate the difference. The discrepancy in the spectra has no noticeable spatial dependence, inconsistent with a signal expected from dark matter. Furthermore, we observe a similar effect in the differential event rates of the data passing CR-like cuts, also shown in Figure 79. This suggests that the different energy distributions result from a systematic effect affecting either the acceptance or energy reconstruction, rather than an extended source of gamma-ray emission. We proceed by modifying our template spectra to match the spectra of the gamma-like Sgr A* data.

With the modified templates, no significant excess is observed. We therefore calculate upper limits on the dark matter annihilation cross section.

The expected number of signal counts $N_{\mathrm{S},i}$ in a given region of interest $\Delta\Omega_i$ and energy bin $E_i \pm \Delta E_i/2$ can then be determined for a given dark matter mass, annihilation channel, thermally averaged cross section, and J-factor by combining Equations 4 and 78, yielding

$$N_{\mathrm{S},i} = \frac{1}{4\pi} \frac{\langle \sigma_{\mathrm{ann}} v \rangle}{2m_{\mathrm{DM}}^2} \left(\int_{E_i - \Delta E_i/2}^{E_i + \Delta E_i/2} dE' \frac{dN}{dE'} \overline{A}_i \right) \left(\int_{\Delta\Omega_i} d\Omega J t_{\mathrm{live}} \right) \tag{84}$$

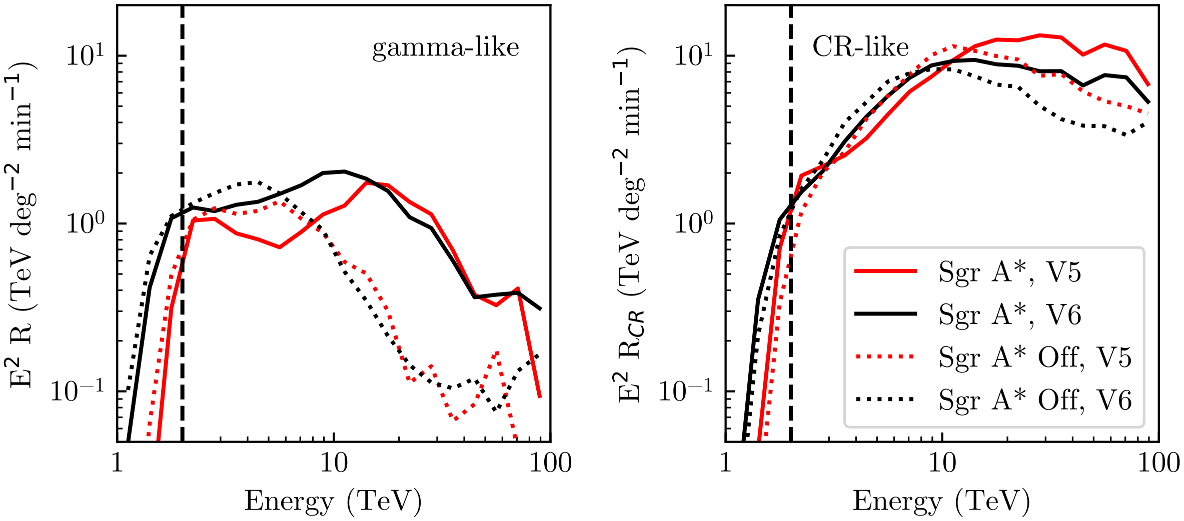

Figure 79: Differential background event rates observed in the Sgr A* (solid lines) and Sgr A* Off data (dotted lines), averaged over epochs V5 (red) and V6 (black). Differential rates are shown for gamma-like events (left) and CR-like events (right), according to gamma/hadron separation cuts. The rates are multiplied by E^2 to highlight features. The energy threshold of 2 TeV is indicated (dashed vertical line). Above ∼10 TeV, the Sgr A* rates exceed those of Sgr A* Off. The gamma-like Sgr A* Off differential rates correspond to those used by the templates.

where the energy integral is carried out over reconstructed energy, the effective area $\overline{A}_i$ has been averaged over all the events in region of interest i using Equation 80, and t_{live} is the live time map. The integral over solid angle represents a 2D integral over region of interest i. The energy resolution of our event reconstruction is incorporated by convolving $dN/dE\overline{A}_i$ with a Gaussian function with standard deviation $0.19E$ before calculating $N_{\text{S},i}$. The effective area is included in the convolution to account for gamma-ray acceptance.

We derive 95% confidence level upper limits on $\langle\sigma_{\text{ann}}v\rangle$ using the profile likelihood method. We increase $\langle\sigma_{\text{ann}}v\rangle$ in logarithmic steps of 0.001, calculating the value of $N_{\text{S},i}$ and finding the value of $N_{\text{B},i}$ that maximizes the likelihood at each step until $-2\ln\lambda$ exceeds 3.84. Limits assuming an Einasto profile and annihilation into three representative channels $\tau^+\tau^-$, $b\bar{b}$, and W^+W^- are shown in Figures 80, 81, and 82, respectively. The different dependences on dark matter mass between channels is due to the channels' differing gamma-ray

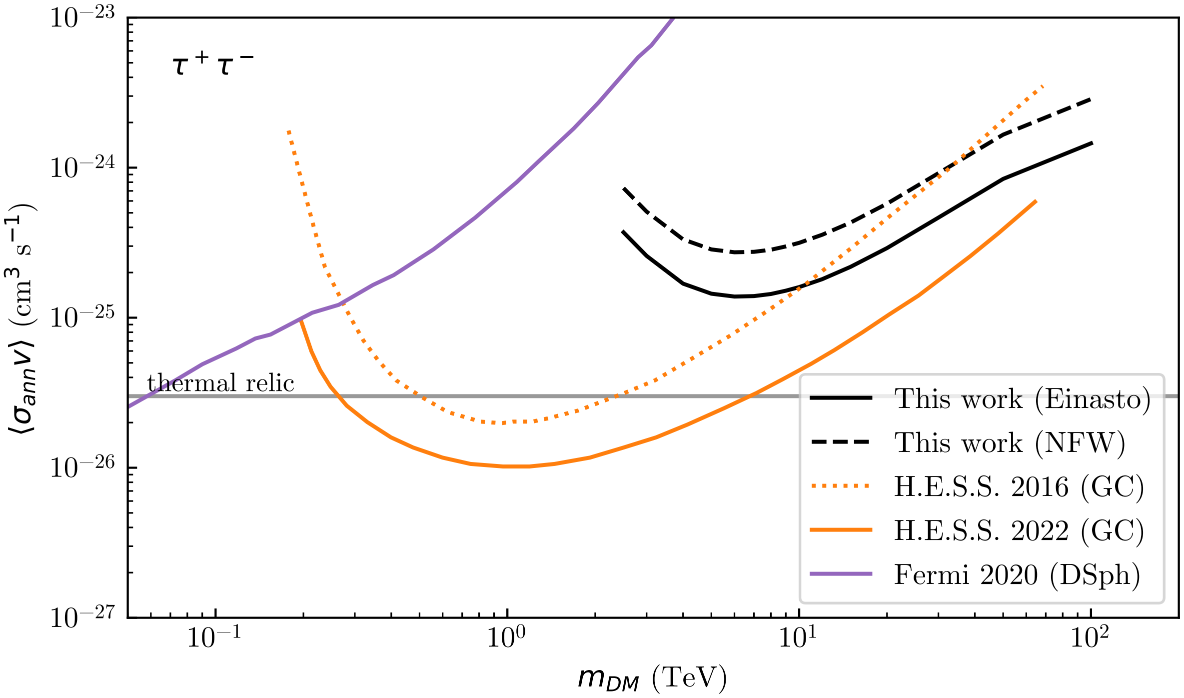

Figure 80: 95% confidence level upper limits on $\langle\sigma_{\mathrm{ann}}v\rangle$, assuming an Einasto profile (black solid line) or NFW profile (black dashed line) and annihilation into $\tau^+\tau^-$. Constraints from H.E.S.S. observations of the GC (orange; Abdallah et al., 2016; Abdalla et al., 2022) and *Fermi* observations of DSphs (purple; Hoof et al., 2020) are also shown.

spectra. In the $\tau^+\tau^-$ plot we also show limits assuming an NFW profile. The NFW limits are weaker than for the Einasto profile since, while the NFW profile is more sharply peaked, its density is on average lower in our dark matter search region. Limits derived assuming a Burkert profile are $\sim 10^3$ times weaker than either, due to the small J-factor resulting from the cored dark matter density profile, as well as the small difference in J-factors between the search region and Sgr A* Off field.

Our strongest constraints are in the $\tau^+\tau^-$ channel, where we obtain a 95% confidence level upper limit $\langle\sigma_{\mathrm{ann}}v\rangle < 1.38 \times 10^{-25}$ cm^3 s^{-1} at $m_{\mathrm{DM}} = 6$ TeV for the Einasto profile. This represents the strongest dark matter limit from VERITAS. This result, with the slightly stronger H.E.S.S. GC measurement (Abdalla et al., 2022), also represent the strongest limits from any measurement to date for the dark matter masses between ∼2 TeV and 100 TeV.

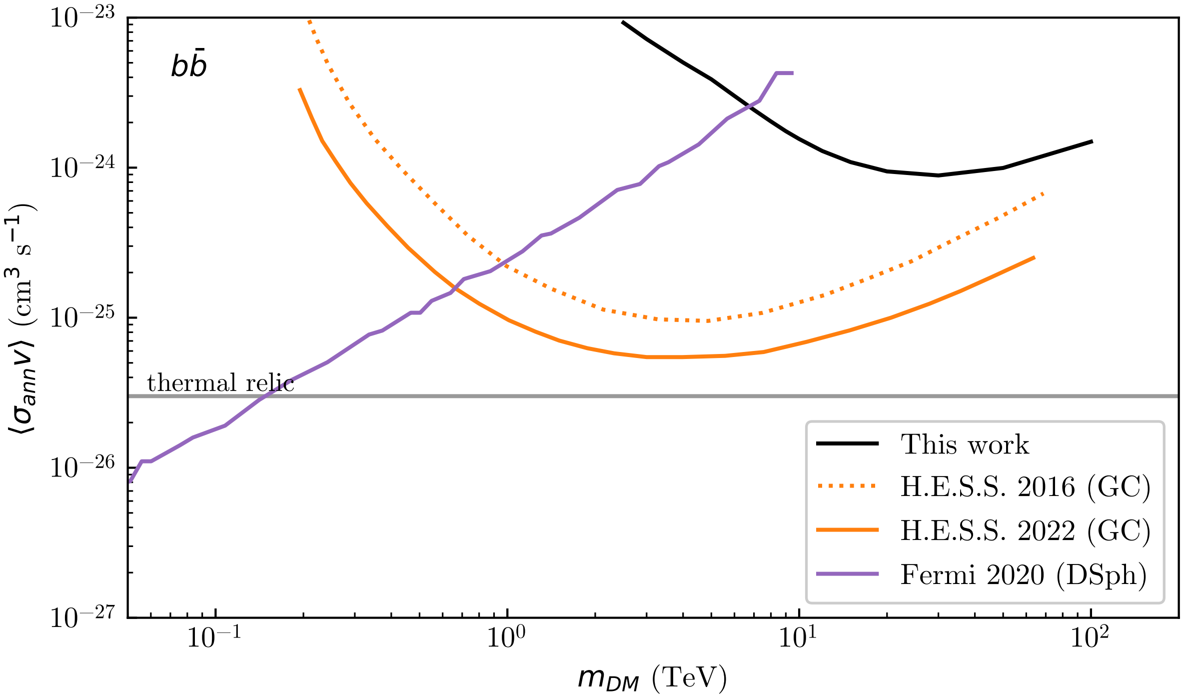

Figure 81: 95% confidence level upper limits on $\langle\sigma_{\mathrm{ann}}v\rangle$, assuming an Einasto profile and annihilation into $b\bar{b}$ (black solid line). Constraints from H.E.S.S. observations of the GC (orange; Abdallah et al., 2016; Abdalla et al., 2022) and *Fermi* observations of DSphs (purple; Hoof et al., 2020) are also shown.

Our limit approaches that of Abdalla et al. (2022) despite the difference in live time (154.3 hr versus 546 hr) due to the effective area increase at LZA, resulting in a similar product of effective area and live time, $\sim 2 \times 10^{11}$ m^2 s above $\sim$10 TeV near the GC.

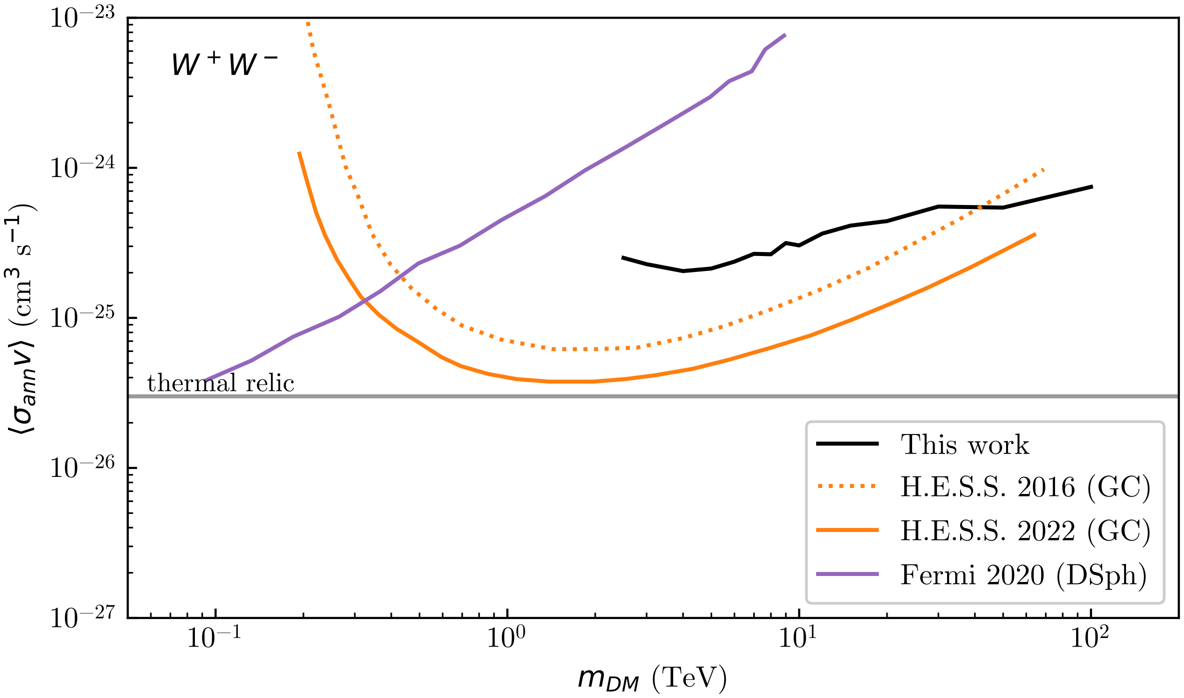

Figure 82: 95% confidence level upper limits on $\langle\sigma_{\mathrm{ann}}v\rangle$, assuming an Einasto profile and annhilation into W^+W^-. Constraints from H.E.S.S. observations of the GC (orange; Abdallah et al., 2016; Abdalla et al., 2022) and *Fermi* observations of DSphs (purple; Hoof et al., 2020) are also shown.

6 Summary

We have presented two searches for dark matter: one, ongoing, with cosmic-ray antimatter to be carried out with the GAPS experiment, and the other, completed, with gamma rays from the Galactic Center halo detected by VERITAS.

We have developed software and hardware for the GAPS TOF system. With atmospheric muon measurements, we have demonstrated the ability of the GAPS TOF design to achieve the specified resolutions in time, position, and energy.

Within VERITAS, we have developed analysis pipelines that reduce systematics from the time-dependent instrument throughput and from the effects of observing at large zenith angles. We have also developed two background estimation methods for the analysis of highly-extended sources: the matched run method and template background method. With these new analysis methods, we were able to place limits on the gamma-ray flux from the Galactic Center halo, while also measuring the source positions and spectra of the astrophysical sources in the Galactic Center region. The halo measurements translate into among the strongest limits by any experiment on the thermally-averaged annihilation cross section for dark matter with masses between 2 and 100 TeV.

References

Aartsen, M. G., Ackermann, M., Adams, J., et al. 2017, European Physical Journal C, 77, 146, doi: 10.1140/epjc/s10052-017-4689-9

Abazajian, K. N. 2011, Journal of Cosmology and Astroparticle Physics, 2011, 010, doi: 10.1088/1475-7516/2011/03/010

Abazajian, K. N., & Kaplinghat, M. 2012, Phys. Rev. D, 86, 083511, doi: 10.1103/PhysRevD.86.083511

Abdalla, H., Aharonian, F., Benkhali, F. A., et al. 2022, Phys. Rev. Lett., 129, 111101, doi: 10.1103/PhysRevLett.129.111101

Abdallah, H., Abramowski, A., Aharonian, F., et al. 2016, Phys. Rev. Lett., 117, 111301, doi: 10.1103/PhysRevLett.117.111301

—. 2018, Phys. Rev. Lett., 120, 201101, doi: 10.1103/PhysRevLett.120.201101

Abdo, A. A., Ackermann, M., Ajello, M., et al. 2010, Journal of Cosmology and Astroparticle Physics, 2010, 014, doi: 10.1088/1475-7516/2010/04/014

Abdollahi, S., Acero, F., Ackermann, M., et al. 2020, ApJ Supplement, 247, 33, doi: 10.3847/1538-4365/ab6bcb

Abe, K., Fuke, H., Haino, S., et al. 2008, Physics Letters B, 670, 103, doi: 10.1016/j.physletb.2008.10.053

—. 2012, Phys. Rev. Lett., 108, 051102, doi: 10.1103/PhysRevLett.108.051102

Abeysekara, A. 2019, in International Cosmic Ray Conference, Vol. 36, 36th International Cosmic Ray Conference (ICRC2019), 616. https://arxiv.org/abs/1908.05369

Abeysekara, A. U., Alfaro, R., Alvarez, C., et al. 2013, Astroparticle Physics, 50, 26, doi: 10.1016/j.astropartphys.2013.08.002

Abramowski, A., Acero, F., Aharonian, F., et al. 2011, Phys. Rev. Lett., 106, 161301, doi: 10.1103/PhysRevLett.106.161301

—. 2012, A&A, 548, A38, doi: 10.1051/0004-6361/201219919

Acciari, V. A., Beilicke, M., Blaylock, G., et al. 2008, ApJ, 679, 1427, doi: 10.1086/587736

Acciari, V. A., Ansoldi, S., Antonelli, L. A., et al. 2022, Physics of the Dark Universe, 35, 100912, doi: 10.1016/j.dark.2021.100912

Acerbi, F., & Gundacker, S. 2019, Nuclear Instruments and Methods in Physics Research A, 926, 16, doi: 10.1016/j.nima.2018.11.118

Acharya, S., Adam, J., Adamová, D., et al. 2018, Phys. Rev. C, 97, 024615, doi: 10.1103/PhysRevC.97.024615

Acharyya, A., Adam, R., Adams, C., et al. 2021, Journal of Cosmology and Astroparticle Physics, 2021, 057, doi: 10.1088/1475-7516/2021/01/057

Ackermann, M., Ajello, M., Allafort, A., et al. 2012, Phys. Rev. Lett., 108, 011103, doi: 10.1103/PhysRevLett.108.011103

Ackermann, M., Albert, A., Atwood, W. B., et al. 2014, ApJ, 793, 64, doi: 10.1088/0004-637X/793/1/64

Ackermann, M., Ajello, M., Albert, A., et al. 2017, ApJ, 840, 43, doi: 10.3847/1538-4357/aa6cab

Adams, C. B., Benbow, W., Brill, A., et al. 2021, ApJ, 913, 115, doi: 10.3847/1538-4357/abf926

—. 2022, A&A, 658, A83, doi: 10.1051/0004-6361/202142275

Adriani, O., Barbarino, G. C., Bazilevskaya, G. A., et al. 2009, Nature, 458, 607, doi: 10.1038/nature07942

Adriani, O., Bazilevskaya, G. A., Barbarino, G. C., et al. 2013, Soviet Journal of Experimental and Theoretical Physics Letters, 96, 621, doi: `10.1134/S002136401222002X`

Agostinelli, S., Allison, J., Amako, K., et al. 2003, Nuclear Instruments and Methods in Physics Research A, 506, 250, doi: `10.1016/S0168-9002(03)01368-8`

Aguilar, M., Alberti, G., Alpat, B., et al. 2013, Phys. Rev. Lett., 110, 141102, doi: `10.1103/PhysRevLett.110.141102`

Aguilar, M., Ali Cavasonza, L., Alpat, B., et al. 2016, Phys. Rev. Lett., 117, 091103, doi: `10.1103/PhysRevLett.117.091103`

Aguilar, M., Ali Cavasonza, L., Ambrosi, G., et al. 2019, Phys. Rev. Lett., 122, 041102, doi: `10.1103/PhysRevLett.122.041102`

Aharonian, F., & Neronov, A. 2005, ApJ, 619, 306, doi: `10.1086/426426`

Aharonian, F., Peron, G., Yang, R., Casanova, S., & Zanin, R. 2020, Phys. Rev. D, 101, 083018, doi: `10.1103/PhysRevD.101.083018`

Aharonian, F., Akhperjanian, A. G., Aye, K. M., et al. 2004, A&A, 425, L13, doi: `10.1051/0004-6361:200400055`

—. 2005, A&A, 432, L25, doi: `10.1051/0004-6361:200500022`

Aharonian, F., Akhperjanian, A. G., Bazer-Bachi, A. R., et al. 2006, ApJ, 636, 777, doi: `10.1086/498013`

Aharonian, F., Akhperjanian, A. G., Barres de Almeida, U., et al. 2008, A&A, 483, 509, doi: `10.1051/0004-6361:20079230`

Aharonian, F. A., Hofmann, W., Konopelko, A. K., & Völk, H. J. 1997, Astroparticle Physics, 6, 343, doi: `10.1016/S0927-6505(96)00069-2`

Aharonian, F. A., Akhperjanian, A. G., Barrio, J. A., et al. 1999, A&A, 342, 69. `https://arxiv.org/abs/astro-ph/9808296`

Ajello, M., Albert, A., Atwood, W. B., et al. 2016, ApJ, 819, 44, doi: `10.3847/0004-637X/819/1/44`

Akerlof, C. W., Cawley, M. F., Chantell, M., et al. 1991, ApJ Letters, 377, L97, doi: `10.1086/186125`

Albert, A., André, M., Anghinolfi, M., et al. 2020, Physics Letters B, 805, 135439, doi: `10.1016/j.physletb.2020.135439`

Alcock, C., Allsman, R. A., Alves, D. R., et al. 2000, ApJ, 542, 281, doi: `10.1086/309512`

Aleksić, J., Antonelli, L. A., Antoranz, P., et al. 2010, A&A, 524, A77, doi: `10.1051/0004-6361/201014747`

Aleksić, J., Alvarez, E. A., Antonelli, L. A., et al. 2012, Astroparticle Physics, 35, 435, doi: `10.1016/j.astropartphys.2011.11.007`

Aleksić, J., Ansoldi, S., Antonelli, L. A., et al. 2016, Astroparticle Physics, 72, 61, doi: `10.1016/j.astropartphys.2015.04.004`

Aliu, E., Archambault, S., Arlen, T., et al. 2012, ApJ, 754, 77, doi: `10.1088/0004-637X/754/1/77`

Allison, J., Amako, K., Apostolakis, J., et al. 2006, IEEE Transactions on Nuclear Science, 53, 270, doi: `10.1109/TNS.2006.869826`

—. 2016, Nuclear Instruments and Methods in Physics Research A, 835, 186, doi: `10.1016/j.nima.2016.06.125`

Anderson, R. L. 1942, The Annals of Mathematical Statistics, 13, 1. `http://www.jstor.org/stable/2236157`

Antcheva, I., Ballintijn, M., Bellenot, B., et al. 2009, Computer Physics Communications, 180, 2499, doi: `10.1016/j.cpc.2009.08.005`

Aramaki, T., Boggs, S. E., von Doetinchem, P., et al. 2014, Astroparticle Physics, 59, 12, doi: `10.1016/j.astropartphys.2014.03.011`

Aramaki, T., Hailey, C. J., Boggs, S. E., et al. 2016a, Astroparticle Physics, 74, 6, doi: `10.1016/j.astropartphys.2015.09.001`

Aramaki, T., Boggs, S., Bufalino, S., et al. 2016b, Physics Reports, 618, 1, doi: `10.1016/j.physrep.2016.01.002`

Arcadi, G., Dutra, M., Ghosh, P., et al. 2018, European Physical Journal C, 78, 203, doi: `10.1140/epjc/s10052-018-5662-y`

Archambault, S., Archer, A., Benbow, W., et al. 2017, Phys. Rev. D, 95, 082001, doi: `10.1103/PhysRevD.95.082001`

Archer, A., Barnacka, A., Beilicke, M., et al. 2014, ApJ, 790, 149, doi: `10.1088/0004-637X/790/2/149`

Archer, A., Benbow, W., Bird, R., et al. 2016, ApJ, 821, 129, doi: `10.3847/0004-637X/821/2/129`

Arkani-Hamed, N., Finkbeiner, D. P., Slatyer, T. R., & Weiner, N. 2009, Phys. Rev. D, 79, 015014, doi: `10.1103/PhysRevD.79.015014`

Arrenberg, S., Baer, H., Barger, V., et al. 2013, arXiv e-prints, arXiv:1310.8621. `https://arxiv.org/abs/1310.8621`

Atoyan, A., & Dermer, C. D. 2004, ApJ Letters, 617, L123, doi: `10.1086/427390`

Atwood, W. B., Abdo, A. A., Ackermann, M., et al. 2009, ApJ, 697, 1071, doi: `10.1088/0004-637X/697/2/1071`

Audren, B., Lesgourgues, J., Mangano, G., Serpico, P. D., & Tram, T. 2014, Journal of Cosmology and Astroparticle Physics, 2014, 028, doi: `10.1088/1475-7516/2014/12/028`

Axford, W. I., Leer, E., & Skadron, G. 1977, in International Cosmic Ray Conference, Vol. 15, 15th International Cosmic Ray Conference, 132

Baade, W., & Zwicky, F. 1934, Proceedings of the National Academy of Science, 20, 259, doi: `10.1073/pnas.20.5.259`

Baer, H., Choi, K.-Y., Kim, J. E., & Roszkowski, L. 2015, Physics Reports, 555, 1, doi: `10.1016/j.physrep.2014.10.002`

Bahcall, J. N., Flynn, C., & Gould, A. 1992, ApJ, 389, 234, doi: `10.1086/171201`

Baker, S., & Cousins, R. D. 1984, Nuclear Instruments and Methods in Physics Research, 221, 437, doi: `10.1016/0167-5087(84)90016-4`

Ballantyne, D. R., Schumann, M., & Ford, B. 2011, MNRAS, 410, 1521, doi: `10.1111/j.1365-2966.2010.17533.x`

Bally, J., Stark, A. A., Wilson, R. W., & Henkel, C. 1988, ApJ, 324, 223, doi: `10.1086/165891`

Barrau, A., Boudoul, G., Donato, F., et al. 2003, A&A, 398, 403, doi: `10.1051/0004-6361:20021588`

—. 2002, A&A, 388, 676, doi: `10.1051/0004-6361:20020313`

Bartels, R., Krishnamurthy, S., & Weniger, C. 2016, Phys. Rev. Lett., 116, 051102, doi: `10.1103/PhysRevLett.116.051102`

Beacom, J. F., Bell, N. F., & Mack, G. D. 2007, Phys. Rev. Lett., 99, 231301, doi: `10.1103/PhysRevLett.99.231301`

Becker Tjus, J., & Merten, L. 2020, Physics Reports, 872, 1, doi: `10.1016/j.physrep.2020.05.002`

Becklin, E. E., Gatley, I., & Werner, M. W. 1982, ApJ, 258, 135, doi: `10.1086/160060`

Bednarek, W., & Sobczak, T. 2013, MNRAS, 435, L14, doi: `10.1093/mnrasl/slt084`

Belikov, A. V., Zaharijas, G., & Silk, J. 2012, Phys. Rev. D, 86, 083516, doi: `10.1103/PhysRevD.86.083516`

Bell, A. R. 1978a, MNRAS, 182, 147, doi: `10.1093/mnras/182.2.147`

—. 1978b, MNRAS, 182, 443, doi: `10.1093/mnras/182.3.443`

—. 2004, MNRAS, 353, 550, doi: `10.1111/j.1365-2966.2004.08097.x`

Bengtsson, H.-U., Salati, P., & Silk, J. 1990, Nuclear Physics B, 346, 129, doi: `10.1016/0550-3213(90)90241-5`

Benito, M., Cuoco, A., & Iocco, F. 2019, Journal of Cosmology and Astroparticle Physics, 2019, 033, doi: `10.1088/1475-7516/2019/03/033`

Berge, D., Funk, S., & Hinton, J. 2007, A&A, 466, 1219, doi: `10.1051/0004-6361:20066674`

Bergström, L., Bringmann, T., Cholis, I., Hooper, D., & Weniger, C. 2013, Phys. Rev. Lett., 111, 171101, doi: `10.1103/PhysRevLett.111.171101`

Bergström, L., Bringmann, T., & Edsjö, J. 2011, Phys. Rev. D, 83, 045024, doi: `10.1103/PhysRevD.83.045024`

Bergström, L., Edsjö, J., & Gondolo, P. 1998, Phys. Rev. D, 58, 103519, doi: `10.1103/PhysRevD.58.103519`

Bergström, L., Edsjö, J., & Ullio, P. 2001, Phys. Rev. Lett., 87, 251301, doi: `10.1103/PhysRevLett.87.251301`

Bertone, G., Cerdeño, D. G., Fornasa, M., et al. 2012, Phys. Rev. D, 85, 055014, doi: `10.1103/PhysRevD.85.055014`

Bertone, G., & Hooper, D. 2018, Reviews of Modern Physics, 90, 045002, doi: `10.1103/RevModPhys.90.045002`

Bertone, G., Hooper, D., & Silk, J. 2005, Physics Reports, 405, 279, doi: `10.1016/j.physrep.2004.08.031`

Bichsel, H. 1988, Reviews of Modern Physics, 60, 663, doi: `10.1103/RevModPhys.60.663`

Billard, J., Figueroa-Feliciano, E., & Strigari, L. 2014, Phys. Rev. D, 89, 023524, doi: `10.1103/PhysRevD.89.023524`

Binney, J., Gerhard, O. E., Stark, A. A., Bally, J., & Uchida, K. I. 1991, MNRAS, 252, 210, doi: `10.1093/mnras/252.2.210`

Birks, J. B. 1964, The Theory and Practice of Scintillation Counting (Pergamon), doi: `https://doi.org/10.1016/B978-0-08-010472-0.50008-2`

Blackett, P. 1947, in International Cosmic Ray Conference, Vol. 1, 1st International Cosmic Ray Conference (ICRC1), 36–37

Blandford, R. D., & Ostriker, J. P. 1978, ApJ Letters, 221, L29, doi: `10.1086/182658`

Blasi, P. 2009, Phys. Rev. Lett., 103, 051104, doi: `10.1103/PhysRevLett.103.051104`

—. 2013, A&A Reviews, 21, 70, doi: `10.1007/s00159-013-0070-7`

Bleicher, M., Zabrodin, E., Spieles, C., et al. 1999, Journal of Physics G Nuclear Physics, 25, 1859, doi: `10.1088/0954-3899/25/9/308`

Blennow, M., Fernandez-Martinez, E., Olivares-Del Campo, A., et al. 2019, European Physical Journal C, 79, 555, doi: `10.1140/epjc/s10052-019-7060-5`

Boddy, K. K., Lisanti, M., McDermott, S. D., et al. 2022, arXiv e-prints, arXiv:2203.06380. https://arxiv.org/abs/2203.06380

Boehle, A., Ghez, A. M., Schödel, R., et al. 2016, ApJ, 830, 17, doi: 10.3847/0004-637X/830/1/17

Bonnivard, V., Hütten, M., Nezri, E., et al. 2016, Computer Physics Communications, 200, 336, doi: 10.1016/j.cpc.2015.11.012

Boschini, M. J., Della Torre, S., Gervasi, M., La Vacca, G., & Rancoita, P. G. 2018, Advances in Space Research, 62, 2859, doi: 10.1016/j.asr.2017.04.017

Boschini, M. J., Della Torre, S., Gervasi, M., et al. 2020, ApJ Supplement, 250, 27, doi: 10.3847/1538-4365/aba901

Bottaro, S., Buttazzo, D., Costa, M., et al. 2022, European Physical Journal C, 82, 31, doi: 10.1140/epjc/s10052-021-09917-9

Bottino, A., Donato, F., Fornengo, N., & Salati, P. 1998, Phys. Rev. D, 58, 123503, doi: 10.1103/PhysRevD.58.123503

Boudaud, M., Génolini, Y., Derome, L., et al. 2020, Physical Review Research, 2, 023022, doi: 10.1103/PhysRevResearch.2.023022

Bovy, J., & Rix, H.-W. 2013, ApJ, 779, 115, doi: 10.1088/0004-637X/779/2/115

Boyarsky, A., Ruchayskiy, O., Iakubovskyi, D., & Franse, J. 2014, Phys. Rev. Lett., 113, 251301, doi: 10.1103/PhysRevLett.113.251301

Bradač, M., Allen, S. W., Treu, T., et al. 2008, ApJ, 687, 959, doi: 10.1086/591246

Bringmann, T., Edsjö, J., Gondolo, P., Ullio, P., & Bergström, L. 2018, Journal of Cosmology and Astroparticle Physics, 2018, 033, doi: 10.1088/1475-7516/2018/07/033

Bringmann, T., & Weniger, C. 2012, Physics of the Dark Universe, 1, 194, doi: `10.1016/j.dark.2012.10.005`

Brun, R., & Rademakers, F. 1997, Nuclear Instruments and Methods in Physics Research A, 389, 81, doi: `10.1016/S0168-9002(97)00048-X`

Bryant, A., & Krabbe, A. 2021, New Astronomy Review, 93, 101630, doi: `10.1016/j.newar.2021.101630`

Buchovecky, M. 2019, PhD thesis, University of California, Los Angeles

Buckley, J. H., Akerlof, C. W., Carter-Lewis, D. A., et al. 1998, A&A, 329, 639

Bulbul, E., Markevitch, M., Foster, A., et al. 2014, ApJ, 789, 13, doi: `10.1088/0004-637X/789/1/13`

Burkert, A. 1995, ApJ Letters, 447, L25, doi: `10.1086/309560`

Caballero-Lopez, R. A., & Moraal, H. 2004, Journal of Geophysical Research (Space Physics), 109, A01101, doi: `10.1029/2003JA010098`

Camilo, F., Ransom, S. M., Gaensler, B. M., & Lorimer, D. R. 2009, ApJ Letters, 700, L34, doi: `10.1088/0004-637X/700/1/L34`

Carlson, E., & Profumo, S. 2014, Phys. Rev. D, 90, 023015, doi: `10.1103/PhysRevD.90.023015`

Carr, B., & Kühnel, F. 2020, Annual Review of Nuclear and Particle Science, 70, 355, doi: `10.1146/annurev-nucl-050520-125911`

Carr, B., Kühnel, F., & Sandstad, M. 2016, Phys. Rev. D, 94, 083504, doi: `10.1103/PhysRevD.94.083504`

Casandjian, J.-M., & Grenier, I. 2009, arXiv e-prints, arXiv:0912.3478. `https://arxiv.org/abs/0912.3478`

Cassel, S. 2010, Journal of Physics G Nuclear Physics, 37, 105009, doi: `10.1088/0954-3899/37/10/105009`

Cattaneo, P. W., De Gerone, M., Gatti, F., et al. 2014, IEEE Transactions on Nuclear Science, 61, 2657, doi: `10.1109/TNS.2014.2347576`

Čerenkov, P. A. 1937, Physical Review, 52, 378, doi: `10.1103/PhysRev.52.378`

Chabrier, G., Segretain, L., & M'era, D. 1996, ApJ Letters, 468, L21, doi: `10.1086/310229`

Chan, M. H., Cui, L., Liu, J., & Leung, C. S. 2019, ApJ, 872, 177, doi: `10.3847/1538-4357/aafe0b`

Charbonnier, A., Combet, C., & Maurin, D. 2012, Computer Physics Communications, 183, 656, doi: `10.1016/j.cpc.2011.10.017`

Chardonnet, P., Orloff, J., & Salati, P. 1997, Physics Letters B, 409, 313, doi: `10.1016/S0370-2693(97)00870-8`

Cheng, H.-C., Feng, J. L., & Matchev, K. T. 2002, Phys. Rev. Lett., 89, 211301, doi: `10.1103/PhysRevLett.89.211301`

Cherenkov Telescope Array Consortium, Acharya, B. S., Agudo, I., et al. 2019, Science with the Cherenkov Telescope Array, doi: `10.1142/10986`

Chernyakova, M., Malyshev, D., Aharonian, F. A., Crocker, R. M., & Jones, D. I. 2011, ApJ, 726, 60, doi: `10.1088/0004-637X/726/2/60`

Cholis, I., Evoli, C., Calore, F., et al. 2015, Journal of Cosmology and Astroparticle Physics, 2015, 005, doi: `10.1088/1475-7516/2015/12/005`

Cholis, I., Linden, T., & Hooper, D. 2019, Phys. Rev. D, 99, 103026, doi: `10.1103/PhysRevD.99.103026`

—. 2020, Phys. Rev. D, 102, 103019, doi: `10.1103/PhysRevD.102.103019`

Cirelli, M. 2012, Pramana, 79, 1021, doi: `10.1007/s12043-012-0419-x`

Cirelli, M., Corcella, G., Hektor, A., et al. 2011, Journal of Cosmology and Astroparticle Physics, 2011, 051, doi: `10.1088/1475-7516/2011/03/051`

Clowe, D., Bradač, M., Gonzalez, A. H., et al. 2006, ApJ Letters, 648, L109, doi: `10.1086/508162`

Clowe, D., Gonzalez, A., & Markevitch, M. 2004, ApJ, 604, 596, doi: `10.1086/381970`

Cogan, P. 2008, in International Cosmic Ray Conference, Vol. 3, 30th International Cosmic Ray Conference, 1385–1388. `https://arxiv.org/abs/0709.4233`

Corsi, F., Marzocca, C., Perrotta, A., et al. 2006, in 2006 IEEE Nuclear Science Symposium Conference Record, Vol. 2, 1276–1280, doi: `10.1109/NSSMIC.2006.356076`

Cousins, R. D. 2010. `https://www.physics.ucla.edu/~cousins/stats/cousins_saturated.pdf`

Cousins, R. D., Linnemann, J. T., & Tucker, J. 2008, Nuclear Instruments and Methods in Physics Research A, 595, 480, doi: `10.1016/j.nima.2008.07.086`

Cowan, G., Cranmer, K., Gross, E., & Vitells, O. 2011, European Physical Journal C, 71, 1554, doi: `10.1140/epjc/s10052-011-1554-0`

Craun, R. L., & Smith, D. L. 1970, Nuclear Instruments and Methods, 80, 239, doi: `10.1016/0029-554X(70)90768-8`

Cristofari, P. 2021, Universe, 7, 324, doi: `10.3390/universe7090324`

Crocker, R. M., Jones, D. I., Aharonian, F., et al. 2011, MNRAS, 413, 763, doi: `10.1111/j.1365-2966.2010.18170.x`

Cudell, J. R., Ezhela, V. V., Gauron, P., et al. 2002, Phys. Rev. Lett., 89, 201801, doi: `10.1103/PhysRevLett.89.201801`

Cui, M.-Y., Yuan, Q., Tsai, Y.-L. S., & Fan, Y.-Z. 2017, Phys. Rev. Lett., 118, 191101, doi: `10.1103/PhysRevLett.118.191101`

Cuoco, A., Heisig, J., Klamt, L., Korsmeier, M., & Krämer, M. 2019, Phys. Rev. D, 99, 103014, doi: `10.1103/PhysRevD.99.103014`

Cuoco, A., Heisig, J., Korsmeier, M., & Krämer, M. 2018, Journal of Cosmology and Astroparticle Physics, 2018, 004, doi: `10.1088/1475-7516/2018/04/004`

Cuoco, A., Krämer, M., & Korsmeier, M. 2017, Phys. Rev. Lett., 118, 191102, doi: `10.1103/PhysRevLett.118.191102`

Da Vela, P., Stamerra, A., Neronov, A., et al. 2018, Astroparticle Physics, 98, 1, doi: `10.1016/j.astropartphys.2018.01.002`

Dahmen, G., Huttemeister, S., Wilson, T. L., & Mauersberger, R. 1998, A&A, 331, 959. `https://arxiv.org/abs/astro-ph/9711117`

Daniel, M. K. 2008a, in International Cosmic Ray Conference, Vol. 3, 30th International Cosmic Ray Conference, 1325–1328. `https://arxiv.org/abs/0709.4006`

Daniel, M. K. 2008b, in International Cosmic Ray Conference, Vol. 3, 30th International Cosmic Ray Conference, 1329–1332

Daum, A., Hermann, G., Heß, M., et al. 1997, Astroparticle Physics, 8, 1, doi: `10.1016/S0927-6505(97)00031-5`

Davies, J. M., & Cotton, E. S. 1957, Solar Energy, 1, 16, doi: `10.1016/0038-092X(57)90116-0`

de la Calle Pérez, I., Bond, I. H., Boyle, P. J., et al. 2003, ApJ, 599, 909, doi: `10.1086/379544`

de Salas, P. F., & Widmark, A. 2021, Reports on Progress in Physics, 84, 104901, doi: `10.1088/1361-6633/ac24e7`

Desorgher, L., Flückiger, E. O., & Gurtner, M. 2006, in 36th COSPAR Scientific Assembly, Vol. 36, 2361

Devin, J. 2018, PhD thesis, Université Montpellier. `https://tel.archives-ouvertes.fr/tel-02078545`

di Mauro, M., Donato, F., Goudelis, A., & Serpico, P. D. 2014, Phys. Rev. D, 90, 085017, doi: `10.1103/PhysRevD.90.085017`

di Sciascio, G., & LHAASO Collaboration. 2016, Nuclear and Particle Physics Proceedings, 279-281, 166, doi: `10.1016/j.nuclphysbps.2016.10.024`

Dickinson, H., & Conrad, J. 2013, Astroparticle Physics, 41, 17, doi: `10.1016/j.astropartphys.2012.10.004`

Diemand, J., Kuhlen, M., & Madau, P. 2007, ApJ, 657, 262, doi: `10.1086/510736`

Dietz-Laursonn, E. 2016, arXiv e-prints, arXiv:1612.05162. `https://arxiv.org/abs/1612.05162`

Donato, F., Fornengo, N., & Maurin, D. 2008, Phys. Rev. D, 78, 043506, doi: `10.1103/PhysRevD.78.043506`

Donato, F., Fornengo, N., Maurin, D., Salati, P., & Taillet, R. 2004, Phys. Rev. D, 69, 063501, doi: `10.1103/PhysRevD.69.063501`

Donato, F., Fornengo, N., & Salati, P. 2000, Phys. Rev. D, 62, 043003, doi: `10.1103/PhysRevD.62.043003`

Donato, F., Korsmeier, M., & Di Mauro, M. 2017, Phys. Rev. D, 96, 043007, doi: `10.1103/PhysRevD.96.043007`

Donato, F., Maurin, D., Salati, P., et al. 2001, ApJ, 563, 172, doi: `10.1086/323684`

Duperray, R., Baret, B., Maurin, D., et al. 2005, Phys. Rev. D, 71, 083013, doi: `10.1103/PhysRevD.71.083013`

Egorov, A. E., & Pierpaoli, E. 2013, Phys. Rev. D, 88, 023504, doi: `10.1103/PhysRevD.88.023504`

Einasto, J. 1965, Trudy Astrofizicheskogo Instituta Alma-Ata, 5, 87

El Aisati, C., Garcia-Cely, C., Hambye, T., & Vanderheyden, L. 2017, Journal of Cosmology and Astroparticle Physics, 2017, 021, doi: `10.1088/1475-7516/2017/10/021`

Ellis, J., Hagelin, J. S., Nanopoulos, D. V., Olive, K., & Srednicki, M. 1984, Nuclear Physics B, 238, 453, doi: `10.1016/0550-3213(84)90461-9`

Evans, N. W., Ferrer, F., & Sarkar, S. 2004, Phys. Rev. D, 69, 123501, doi: `10.1103/PhysRevD.69.123501`

Evans, N. W., Sanders, J. L., & Geringer-Sameth, A. 2016, Phys. Rev. D, 93, 103512, doi: `10.1103/PhysRevD.93.103512`

Fatuzzo, M., & Melia, F. 2012, ApJ Letters, 757, L16, doi: `10.1088/2041-8205/757/1/L16`

Fegan, D. J. 1996, Space Science Reviews, 75, 137, doi: `10.1007/BF00195031`

Feldman, G. J., & Cousins, R. D. 1998, Phys. Rev. D, 57, 3873, doi: `10.1103/PhysRevD.57.3873`

Feng, J. L. 2010, Ann. Rev. Astron. Astrophys., 48, 495, doi: `10.1146/annurev-astro-082708-101659`

Feng, J. L., & Kumar, J. 2008, Phys. Rev. Lett., 101, 231301, doi: `10.1103/PhysRevLett.101.231301`

Fermi, E. 1949, Physical Review, 75, 1169, doi: `10.1103/PhysRev.75.1169`

—. 1954, ApJ, 119, 1, doi: `10.1086/145789`

Fernandes, M. V., Horns, D., Kosack, K., Raue, M., & Rowell, G. 2014, A&A, 568, A117, doi: `10.1051/0004-6361/201323156`

Ferrière, K., Gillard, W., & Jean, P. 2007, A&A, 467, 611, doi: `10.1051/0004-6361:20066992`

Finkbeiner, D. P., & Weiner, N. 2016, Phys. Rev. D, 94, 083002, doi: `10.1103/PhysRevD.94.083002`

Fisk, L. A. 1976, ApJ, 206, 333, doi: `10.1086/154387`

Flinders, A., & VERITAS Collaboration. 2015, in International Cosmic Ray Conference, Vol. 34, 34th International Cosmic Ray Conference (ICRC2015), 726. `https://arxiv.org/abs/1509.04224`

Fornengo, N., Maccione, L., & Vittino, A. 2013, Journal of Cosmology and Astroparticle Physics, 2013, 031, doi: `10.1088/1475-7516/2013/09/031`

Freese, K., Frieman, J., & Gould, A. 1988, Phys. Rev. D, 37, 3388, doi: `10.1103/PhysRevD.37.3388`

Fujita, Y., Murase, K., & Kimura, S. S. 2017, Journal of Cosmology and Astroparticle Physics, 2017, 037, doi: `10.1088/1475-7516/2017/04/037`

Fuke, H., Okazaki, S., Ogawa, H., & Miyazaki, Y. 2017, Journal of Astronomical Instrumentation, 6, 1740006, doi: `10.1142/S2251171717400062`

Fuke, H., Maeno, T., Abe, K., et al. 2005, Phys. Rev. Lett., 95, 081101, doi: `10.1103/PhysRevLett.95.081101`

Fuke, H., Ong, R. A., Aramaki, T., et al. 2014, Advances in Space Research, 53, 1432, doi: `10.1016/j.asr.2013.06.026`

Fukugita, M., Hogan, C. J., & Peebles, P. J. E. 1998, ApJ, 503, 518, doi: `10.1086/306025`

Gabici, S., Evoli, C., Gaggero, D., et al. 2019, International Journal of Modern Physics D, 28, 1930022, doi: `10.1142/S0218271819300222`

Gabici, S., Gaggero, D., & Zandanel, F. 2016, arXiv e-prints, arXiv:1610.07638. `https://arxiv.org/abs/1610.07638`

Gaggero, D., Grasso, D., Marinelli, A., Taoso, M., & Urbano, A. 2017, Phys. Rev. Lett., 119, 031101, doi: `10.1103/PhysRevLett.119.031101`

Gaggero, D., Taoso, M., Urbano, A., Valli, M., & Ullio, P. 2015, Journal of Cosmology and Astroparticle Physics, 2015, 056, doi: `10.1088/1475-7516/2015/12/056`

Gaisser, T. K. 1990, Cosmic Rays and Particle Physics (Cambridge University Press)

Galbraith, W., & Jelley, J. V. 1953, Nature, 171, 349, doi: `10.1038/171349a0`

Gao, L., Navarro, J. F., Cole, S., et al. 2008, MNRAS, 387, 536, doi: `10.1111/j.1365-2966.2008.13277.x`

Gaskins, J. M. 2016, Contemporary Physics, 57, 496, doi: `10.1080/00107514.2016.1175160`

Genzel, R., Eisenhauer, F., & Gillessen, S. 2010, Reviews of Modern Physics, 82, 3121, doi: `10.1103/RevModPhys.82.3121`

Genzel, R., & Townes, C. H. 1987, Ann. Rev. Astron. Astrophys., 25, 377, doi: `10.1146/annurev.aa.25.090187.002113`

Geringer-Sameth, A., Koushiappas, S. M., & Walker, M. 2015, ApJ, 801, 74, doi: `10.1088/0004-637X/801/2/74`

Ghassemi, A., Kobayashi, K., & Sato, K. 2018, Hamamatsu Photonics KK, Tech. Rep., Jan

Ghez, A. M., Salim, S., Weinberg, N. N., et al. 2008, ApJ, 689, 1044, doi: `10.1086/592738`

Ginzburg, V. L. 1953, Uspekhi Fizicheskikh Nauk, 51, 343

—. 1956, Il Nuovo Cimento, 3, 38, doi: `10.1007/BF02745509`

Gleeson, L. J., & Axford, W. I. 1968, ApJ, 154, 1011, doi: `10.1086/149822`

Gola, A., Piemonte, C., & Tarolli, A. 2013, IEEE Transactions on Nuclear Science, 60, 1296, doi: `10.1109/TNS.2013.2252196`

Goldman, I., & Nussinov, S. 1989, Phys. Rev. D, 40, 3221, doi: `10.1103/PhysRevD.40.3221`

Gómez-Vargas, G. A., Sánchez-Conde, M. A., Huh, J.-H., et al. 2013, Journal of Cosmology and Astroparticle Physics, 2013, 029, doi: `10.1088/1475-7516/2013/10/029`

Gondolo, P., Edsjö, J., Ullio, P., et al. 2004, Journal of Cosmology and Astroparticle Physics, 2004, 008, doi: `10.1088/1475-7516/2004/07/008`

Gondolo, P., & Gelmini, G. 1991, Nuclear Physics B, 360, 145, doi: `10.1016/0550-3213(91)90438-4`

Goodenough, L., & Hooper, D. 2009, arXiv e-prints, arXiv:0910.2998. `https://arxiv.org/abs/0910.2998`

Goodman, J., Ibe, M., Rajaraman, A., et al. 2010, Phys. Rev. D, 82, 116010, doi: `10.1103/PhysRevD.82.116010`

Goodman, M. W., & Witten, E. 1985, Phys. Rev. D, 31, 3059, doi: `10.1103/PhysRevD.31.3059`

Górski, K. M., Hivon, E., Banday, A. J., et al. 2005, ApJ, 622, 759, doi: `10.1086/427976`

Graff, D. S., & Freese, K. 1996, ApJ Letters, 467, L65, doi: `10.1086/310195`

Gravity Collaboration, Abuter, R., Amorim, A., et al. 2019, A&A, 625, L10, doi: `10.1051/0004-6361/201935656`

Greisen, K. 1960, Annual Review of Nuclear and Particle Science, 10, 63, doi: `10.1146/annurev.ns.10.120160.000431`

—. 1966, Phys. Rev. Lett., 16, 748, doi: `10.1103/PhysRevLett.16.748`

Griest, K., Kamionkowski, M., & Turner, M. S. 1990, Phys. Rev. D, 41, 3565, doi: `10.1103/PhysRevD.41.3565`

Griest, K., & Seckel, D. 1991, Phys. Rev. D, 43, 3191, doi: `10.1103/PhysRevD.43.3191`

Griffiths, D. J. 2008, Introduction to Elementary Particles; 2nd rev. version, Physics textbook (New York, NY: Wiley). `https://cds.cern.ch/record/111880`

Grindlay, J. E. 1971, PhD thesis, Harvard University, Massachusetts

Groom, D. E., Mokhov, N. V., & Striganov, S. I. 2001, Atomic Data and Nuclear Data Tables, 78, 183, doi: `10.1006/adnd.2001.0861`

Guan, M., Chu, M.-C., Cao, J., Luk, K.-B., & Yang, C. 2015, arXiv e-prints, arXiv:1509.06176. `https://arxiv.org/abs/1509.06176`

Guenduez, M., Becker Tjus, J., Ferrière, K., & Dettmar, R. J. 2020, A&A, 644, A71, doi: `10.1051/0004-6361/201936081`

Guépin, C., Rinchiuso, L., Kotera, K., et al. 2018, Journal of Cosmology and Astroparticle Physics, 2018, 042, doi: `10.1088/1475-7516/2018/07/042`

Gunn, J. E., Lee, B. W., Lerche, I., Schramm, D. N., & Steigman, G. 1978, ApJ, 223, 1015, doi: `10.1086/156335`

Guo, Y.-Q., Yuan, Q., Liu, C., & Li, A.-F. 2013, Journal of Physics G Nuclear Physics, 40, 065201, doi: `10.1088/0954-3899/40/6/065201`

Hailey, C. J., Aramaki, T., Craig, W. W., et al. 2006, Journal of Cosmology and Astroparticle Physics, 2006, 007, doi: `10.1088/1475-7516/2006/01/007`

Hanna, D. 2008, in International Cosmic Ray Conference, Vol. 3, 30th International Cosmic Ray Conference, 1417–1420. `https://arxiv.org/abs/0709.4479`

Hanna, D., McCann, A., McCutcheon, M., & Nikkinen, L. 2010, Nuclear Instruments and Methods in Physics Research A, 612, 278, doi: `10.1016/j.nima.2009.10.107`

Hartwig, Z. S., & Gumplinger, P. 2014, Nuclear Instruments and Methods in Physics Research A, 737, 155, doi: `10.1016/j.nima.2013.11.027`

Harvey, D., Massey, R., Kitching, T., Taylor, A., & Tittley, E. 2015, Science, 347, 1462, doi: `10.1126/science.1261381`

Hayakawa, S., Ito, K., & Terashima, Y. 1958, Progress of Theoretical Physics Supplement, 6, 1, doi: `10.1143/PTPS.6.1`

Hays, E. 2008, in International Cosmic Ray Conference, Vol. 3, 30th International Cosmic Ray Conference, 1543–1546. `https://arxiv.org/abs/0710.2288`

Heck, D., Knapp, J., Capdevielle, J. N., Schatz, G., & Thouw, T. 1998, CORSIKA: a Monte Carlo code to simulate extensive air showers.

Heisig, J., Korsmeier, M., & Winkler, M. W. 2020, Physical Review Research, 2, 043017, doi: `10.1103/PhysRevResearch.2.043017`

Helfand, D. J., & Becker, R. H. 1987, ApJ, 314, 203, doi: `10.1086/165050`

Henshaw, J. D., Barnes, A. T., Battersby, C., et al. 2022, arXiv e-prints, arXiv:2203.11223. `https://arxiv.org/abs/2203.11223`

Hess, V. F. 1912, Physikalische Zeitschrift, 13, 1084

HESS Collaboration, Abramowski, A., Aharonian, F., et al. 2016, Nature, 531, 476, doi: `10.1038/nature17147`

H.E.S.S. Collaboration, Abdalla, H., Abramowski, A., et al. 2018a, A&A, 612, A1, doi: `10.1051/0004-6361/201732098`

—. 2018b, A&A, 612, A9, doi: `10.1051/0004-6361/201730824`

Hillas, A. M. 1985, in International Cosmic Ray Conference, Vol. 19, 19th International Cosmic Ray Conference, 445

Hillas, A. M. 1996, Space Science Reviews, 75, 17, doi: `10.1007/BF00195021`

Hinshaw, G., Larson, D., Komatsu, E., et al. 2013, ApJ Supplement, 208, 19, doi: `10.1088/0067-0049/208/2/19`

Hintjens, P. 2013, ZeroMQ: messaging for many applications (" O'Reilly Media, Inc.")

Hinton, J. A., & Aharonian, F. A. 2007, ApJ, 657, 302, doi: `10.1086/510283`

Hinton, J. A., & HESS Collaboration. 2004, New Astron. Rev., 48, 331, doi: `10.1016/j.newar.2003.12.004`

Hisano, J., Matsumoto, S., & Nojiri, M. M. 2004, Phys. Rev. Lett., 92, 031303, doi: `10.1103/PhysRevLett.92.031303`

Hisano, J., Matsumoto, S., Nojiri, M. M., & Saito, O. 2005, Phys. Rev. D, 71, 063528, doi: `10.1103/PhysRevD.71.063528`

Hoecker, A., Speckmayer, P., Stelzer, J., et al. 2007, arXiv e-prints, physics/0703039. `https://arxiv.org/abs/physics/0703039`

Hofmann, W., Jung, I., Konopelko, A., et al. 1999, Astroparticle Physics, 12, 135, doi: `10.1016/S0927-6505(99)00084-5`

Holder, J., Atkins, R. W., Badran, H. M., et al. 2006, Astroparticle Physics, 25, 391, doi: `10.1016/j.astropartphys.2006.04.002`

Holler, M., Schöck, F. M., Eger, P., et al. 2012, A&A, 539, A24, doi: `10.1051/0004-6361/201118121`

Hona, B., & VERITAS Collaboration. 2022, in International Cosmic Ray Conference, Vol. 37, 37th International Cosmic Ray Conference (ICRC2021), 729. `https://arxiv.org/abs/2108.07663`

Hoof, S., Geringer-Sameth, A., & Trotta, R. 2020, Journal of Cosmology and Astroparticle Physics, 2020, 012, doi: `10.1088/1475-7516/2020/02/012`

Hooper, D., Cholis, I., Linden, T., & Fang, K. 2017, Phys. Rev. D, 96, 103013, doi: `10.1103/PhysRevD.96.103013`

Hooper, D., & Goodenough, L. 2011, Physics Letters B, 697, 412, doi: `10.1016/j.physletb.2011.02.029`

Hooper, D., & Linden, T. 2011, Phys. Rev. D, 84, 123005, doi: `10.1103/PhysRevD.84.123005`

—. 2018, Phys. Rev. D, 98, 043005, doi: `10.1103/PhysRevD.98.043005`

—. 2022, Phys. Rev. D, 105, 103013, doi: `10.1103/PhysRevD.105.103013`

Hörandel, J. R. 2004, Astroparticle Physics, 21, 241, doi: `10.1016/j.astropartphys.2004.01.004`

Hütten, M., Combet, C., & Maurin, D. 2019, Computer Physics Communications, 235, 336, doi: `10.1016/j.cpc.2018.10.001`

IceCube Collaboration, Aartsen, M. G., Ackermann, M., et al. 2017, arXiv e-prints, arXiv:1705.08103. `https://arxiv.org/abs/1705.08103`

Iocco, F., & Benito, M. 2017, Physics of the Dark Universe, 15, 90, doi: `10.1016/j.dark.2016.12.004`

Jackson, J. D. 1998, Classical Electrodynamics, 3rd Edition (New York, NY: Wiley)

Janecek, M., & Moses, W. W. 2008, IEEE Transactions on Nuclear Science, 55, 2432, doi: `10.1109/TNS.2008.2001408`

Jean, P., Knödlseder, J., Lonjou, V., et al. 2003, A&A, 407, L55, doi: `10.1051/0004-6361:20031056`

Jones, P. A., Burton, M. G., Cunningham, M. R., Tothill, N. F. H., & Walsh, A. J. 2013, MNRAS, 433, 221, doi: `10.1093/mnras/stt717`

Jones, P. A., Burton, M. G., Cunningham, M. R., et al. 2012, MNRAS, 419, 2961, doi: `10.1111/j.1365-2966.2011.19941.x`

Jungman, G., Kamionkowski, M., & Griest, K. 1996, Physics Reports, 267, 195, doi: `10.1016/0370-1573(95)00058-5`

Kachelrieß, M., Ostapchenko, S., & Tjemsland, J. 2020, Journal of Cosmology and Astroparticle Physics, 2020, 048, doi: `10.1088/1475-7516/2020/08/048`

Kachelrieß, M., & Semikoz, D. V. 2019, Progress in Particle and Nuclear Physics, 109, 103710, doi: `10.1016/j.ppnp.2019.07.002`

Kadota, K., Sekiguchi, T., & Tashiro, H. 2016, arXiv e-prints, arXiv:1602.04009. `https://arxiv.org/abs/1602.04009`

Kahlhoefer, F. 2017, International Journal of Modern Physics A, 32, 1730006, doi: `10.1142/S0217751X1730006X`

Kaifu, N., Kato, T., & Iguchi, T. 1972, Nature Physical Science, 238, 105, doi: `10.1038/physci238105a0`

Kamionkowski, M., Koushiappas, S. M., & Kuhlen, M. 2010, Phys. Rev. D, 81, 043532, doi: `10.1103/PhysRevD.81.043532`

Kelley-Hoskins, N. 2019, PhD thesis, Humboldt University of Berlin. `https://veritas.sao.arizona.edu/the-science-of-veritas/publications/theses-dissertations/524-kelleyhoskinsthesis`

Kelner, S. R., Aharonian, F. A., & Bugayov, V. V. 2006, Phys. Rev. D, 74, 034018, doi: `10.1103/PhysRevD.74.034018`

Kertzman, M. P., & Sembroski, G. H. 1994, Nuclear Instruments and Methods in Physics Research A, 343, 629, doi: `10.1016/0168-9002(94)90247-X`

Kieda, D. B. 2013, in International Cosmic Ray Conference, Vol. 33, 33rd International Cosmic Ray Conference (ICRC2013). `https://arxiv.org/abs/1308.4849`

Kim, J. E., & Carosi, G. 2010, Reviews of Modern Physics, 82, 557, doi: `10.1103/RevModPhys.82.557`

Klanner, R. 2019, Nuclear Instruments and Methods in Physics Research A, 926, 36, doi: `10.1016/j.nima.2018.11.083`

Knödlseder, J., Jean, P., Lonjou, V., et al. 2005, A&A, 441, 513, doi: `10.1051/0004-6361:20042063`

Knödlseder, J., Tibaldo, L., Tiziani, D., et al. 2019, A&A, 632, A102, doi: `10.1051/0004-6361/201936010`

Knoll, G. F. 2010, Radiation Detection and Measurement (Wiley). `https://books.google.com/books?id=4vTJ7UDel5IC`

Kolb, E. W., & Turner, M. S. 1990, The Early Universe, Frontiers in physics (Boulder, CO: Westview Press), doi: `10.1201/9780429492860`

Kölbig, K. S., & Schorr, B. 1984, Computer Physics Communications, 31, 97, doi: `10.1016/0010-4655(84)90085-7`

Konopelko, A., Aharonian, F., Hemberger, M., et al. 1999, Journal of Physics G Nuclear Physics, 25, 1989, doi: `10.1088/0954-3899/25/9/316`

Konopelko, A. K. 1995, in Towards a Major Atmospheric Cherenkov Detector IV, 373

Korsmeier, M., Donato, F., & Fornengo, N. 2018, Phys. Rev. D, 97, 103011, doi: `10.1103/PhysRevD.97.103011`

Kosack, K., Badran, H. M., Bond, I. H., et al. 2004, ApJ Letters, 608, L97, doi: `10.1086/422469`

Kozai, M., Fuke, H., Yamada, M., et al. 2019, Nuclear Instruments and Methods in Physics Research A, 947, 162695, doi: `10.1016/j.nima.2019.162695`

Krawczynski, H., Carter-Lewis, D. A., Duke, C., et al. 2006, Astroparticle Physics, 25, 380, doi: `10.1016/j.astropartphys.2006.03.011`

Krennrich, F., Blaylock, G., Bradbury, S. M., et al. 2007, in Journal of Physics Conference Series, Vol. 60, Journal of Physics Conference Series, 34–39, doi: `10.1088/1742-6596/60/1/006`

Krieger, N., Ott, J., Beuther, H., et al. 2017, ApJ, 850, 77, doi: `10.3847/1538-4357/aa951c`

Krimigis, S. M., Decker, R. B., Roelof, E. C., et al. 2013, Science, 341, 144, doi: `10.1126/science.1235721`

—. 2019, Nature Astronomy, 3, 997, doi: `10.1038/s41550-019-0927-4`

Kruijssen, J. M. D., Dale, J. E., & Longmore, S. N. 2015, MNRAS, 447, 1059, doi: `10.1093/mnras/stu2526`

Krymskii, G. F. 1977, Soviet Physics Doklady, 22, 327

Kuhlen, M., Vogelsberger, M., & Angulo, R. 2012, Physics of the Dark Universe, 1, 50, doi: `10.1016/j.dark.2012.10.002`

Kumar, J., & Marfatia, D. 2013, Phys. Rev. D, 88, 014035, doi: `10.1103/PhysRevD.88.014035`

Kusunose, M., & Takahara, F. 2012, ApJ, 748, 34, doi: `10.1088/0004-637X/748/1/34`

Lacroix, T., Silk, J., Moulin, E., & BÅ‘hm, C. 2016, Phys. Rev. D, 94, 123008, doi: `10.1103/PhysRevD.94.123008`

Lagage, P. O., & Cesarsky, C. J. 1983, A&A, 125, 249

Landau, L. D. 1944, J. Phys., 8, 201. `https://cds.cern.ch/record/216256`

Langer, W. D., Velusamy, T., Morris, M. R., Goldsmith, P. F., & Pineda, J. L. 2017, A&A, 599, A136, doi: `10.1051/0004-6361/201629497`

Large, M. I., Quigley, M. J. S., & Haslam, C. G. T. 1962, MNRAS, 124, 405, doi: `10.1093/mnras/124.5.405`

Leane, R. K., Linden, T., Mukhopadhyay, P., & Toro, N. 2021, Phys. Rev. D, 103, 075030, doi: `10.1103/PhysRevD.103.075030`

Leane, R. K., Slatyer, T. R., Beacom, J. F., & Ng, K. C. Y. 2018, Phys. Rev. D, 98, 023016, doi: `10.1103/PhysRevD.98.023016`

Leane, R. K., Shin, S., Yang, L., et al. 2022, arXiv e-prints, arXiv:2203.06859. `https://arxiv.org/abs/2203.06859`

Lee, B. W., & Weinberg, S. 1977, Phys. Rev. Lett., 39, 165, doi: `10.1103/PhysRevLett.39.165`

Lee, S. K., Lisanti, M., Safdi, B. R., Slatyer, T. R., & Xue, W. 2016, Phys. Rev. Lett., 116, 051103, doi: `10.1103/PhysRevLett.116.051103`

Lessard, R. W., Buckley, J. H., Connaughton, V., & Le Bohec, S. 2001, Astroparticle Physics, 15, 1, doi: `10.1016/S0927-6505(00)00133-X`

Leventhal, M., MacCallum, C. J., & Stang, P. D. 1978, ApJ Letters, 225, L11, doi: `10.1086/182782`

Li, T. P., & Ma, Y. Q. 1983, ApJ, 272, 317, doi: `10.1086/161295`

Linden, T., Lovegrove, E., & Profumo, S. 2012, ApJ, 753, 41, doi: `10.1088/0004-637X/753/1/41`

Lindsey, J. K. 1998, Parametric Statistical Inference (Oxford University Press)

Longair, M. S. 2011, High Energy Astrophysics (Cambridge University Press)

Ludlow, A. D., Bose, S., Angulo, R. E., et al. 2016, MNRAS, 460, 1214, doi: `10.1093/mnras/stw1046`

Lyons, L. 2013, arXiv e-prints, arXiv:1310.1284. `https://arxiv.org/abs/1310.1284`

MacGibbon, J. H. 1987, Nature, 329, 308, doi: `10.1038/329308a0`

Macias, O., Gordon, C., Crocker, R. M., et al. 2018, Nature Astronomy, 2, 387, doi: `10.1038/s41550-018-0414-3`

MAGIC Collaboration, Acciari, V. A., Ansoldi, S., et al. 2020, A&A, 642, A190, doi: `10.1051/0004-6361/201936896`

Maier, G. 2008, in International Cosmic Ray Conference, Vol. 3, 30th International Cosmic Ray Conference, 1413–1416. `https://arxiv.org/abs/0709.4195`

Maier, G., & Holder, J. 2017, in International Cosmic Ray Conference, Vol. 301, 35th International Cosmic Ray Conference (ICRC2017), 747. `https://arxiv.org/abs/1708.04048`

Maier, G., & Knapp, J. 2007, Astroparticle Physics, 28, 72, doi: `10.1016/j.astropartphys.2007.04.009`

Malyshev, D., Chernyakova, M., Neronov, A., & Walter, R. 2015, A&A, 582, A11, doi: `10.1051/0004-6361/201526120`

Massey, R., Kitching, T., & Richard, J. 2010, Reports on Progress in Physics, 73, 086901, doi: `10.1088/0034-4885/73/8/086901`

Maurin, D., Donato, F., Taillet, R., & Salati, P. 2001, ApJ, 555, 585, doi: `10.1086/321496`

Mayer, M. 2014, PhD thesis, Potsdam University

Mazziotta, M. N., Costanza, F., Cuoco, A., et al. 2018, Phys. Rev. D, 98, 022006, doi: `10.1103/PhysRevD.98.022006`

Meekins, J. F., Fritz, G., Chubb, T. A., & Friedman, H. 1971, Nature, 231, 107, doi: `10.1038/231107a0`

Mertsch, P., & Sarkar, S. 2014, Phys. Rev. D, 90, 061301, doi: `10.1103/PhysRevD.90.061301`

Milgrom, M. 1983, ApJ, 270, 365, doi: `10.1086/161130`

Mills, E. A. C. 2017, arXiv e-prints, arXiv:1705.05332. `https://arxiv.org/abs/1705.05332`

Mognet, S. A. I., Aramaki, T., Bando, N., et al. 2014, Nuclear Instruments and Methods in Physics Research A, 735, 24, doi: `10.1016/j.nima.2013.08.030`

Mohanty, G., Biller, S., Carter-Lewis, D. A., et al. 1998, Astroparticle Physics, 9, 15, doi: `10.1016/S0927-6505(98)00005-X`

Mohrmann, L., Specovius, A., Tiziani, D., et al. 2019, A&A, 632, A72, doi: `10.1051/0004-6361/201936452`

Molinari, S., Bally, J., Noriega-Crespo, A., et al. 2011, ApJ Letters, 735, L33, doi: `10.1088/2041-8205/735/2/L33`

Monroe, J., & Fisher, P. 2007, Phys. Rev. D, 76, 033007, doi: `10.1103/PhysRevD.76.033007`

Monroy-Rodríguez, M. A., & Allen, C. 2014, ApJ, 790, 159, doi: `10.1088/0004-637X/790/2/159`

Moore, B., Ghigna, S., Governato, F., et al. 1999, ApJ Letters, 524, L19, doi: `10.1086/312287`

Mori, K., Hailey, C. J., Baltz, E. A., et al. 2002, ApJ, 566, 604, doi: `10.1086/338057`

Morris, M., & Serabyn, E. 1996, Ann. Rev. Astron. Astrophys., 34, 645, doi: `10.1146/annurev.astro.34.1.645`

Munini, R., Vannuccini, E., Boezio, M., et al. 2021, Astroparticle Physics, 133, 102640, doi: `10.1016/j.astropartphys.2021.102640`

Murgia, S. 2020, Annual Review of Nuclear and Particle Science, 70, 455, doi: `10.1146/annurev-nucl-101916-123029`

Navarro, J. F., Frenk, C. S., & White, S. D. M. 1996, ApJ, 462, 563, doi: `10.1086/177173`

—. 1997, ApJ, 490, 493, doi: `10.1086/304888`

Navarro, J. F., Ludlow, A., Springel, V., et al. 2010, MNRAS, 402, 21, doi: `10.1111/j.1365-2966.2009.15878.x`

Nesti, F., & Salucci, P. 2013, Journal of Cosmology and Astroparticle Physics, 2013, 016, doi: `10.1088/1475-7516/2013/07/016`

Niggemann, T., Dietz-Laursonn, E., Hebbeker, T., et al. 2015, Nuclear Instruments and Methods in Physics Research A, 787, 344, doi: `10.1016/j.nima.2015.01.067`

Ogawara, R., & Ishikawa, M. 2016, Review of Scientific Instruments, 87, 075114, doi: `10.1063/1.4959186`

O'Hare, C. A. J. 2021, Phys. Rev. Lett., 127, 251802, doi: 10.1103/PhysRevLett.127.251802

Oka, T., & Geballe, T. R. 2020, ApJ, 902, 9, doi: 10.3847/1538-4357/abb1b5

Oka, T., Hasegawa, T., Hayashi, M., Handa, T., & Sakamoto, S. 1998, ApJ, 493, 730, doi: 10.1086/305133

Okazaki, S., Fuke, H., Ogawa, H., et al. 2018, Applied Thermal Engineering, 141, 20, doi: https://doi.org/10.1016/j.applthermaleng.2018.05.116

Ong, R. A. 1998, Physics Reports, 305, 93, doi: 10.1016/S0370-1573(98)00026-X

Oort, J. H. 1932, Bulletin of the Astronomical Institutes of the Netherlands, 6, 249

Ostapchenko, S. 2011, Phys. Rev. D, 83, 014018, doi: 10.1103/PhysRevD.83.014018

Otte, A. N., Garcia, D., Nguyen, T., & Purushotham, D. 2017, Nuclear Instruments and Methods in Physics Research A, 846, 106, doi: 10.1016/j.nima.2016.09.053

Otte, A. N., Meagher, K., Nguyen, T., et al. 2015, Nuclear Instruments and Methods in Physics Research A, 787, 85, doi: 10.1016/j.nima.2014.11.026

Papini, P., Grimani, C., & Stephens, S. A. 1996, Nuovo Cimento C Geophysics Space Physics C, 19, 367, doi: 10.1007/BF02509295

Parker, E. N. 1965, P&SS, 13, 9, doi: 10.1016/0032-0633(65)90131-5

Particle Data Group, Zyla, P. A., Barnett, R. M., et al. 2020, Progress of Theoretical and Experimental Physics, 2020, doi: 10.1093/ptep/ptaa104

Pato, M., Iocco, F., & Bertone, G. 2015, Journal of Cosmology and Astroparticle Physics, 12, 001, doi: 10.1088/1475-7516/2015/12/001

Peccei, R. D. 2008, The Strong CP Problem and Axions, ed. Kuster, Markus, Raffelt, Georg, & Beltrán, Berta (Berlin, Heidelberg: Springer Berlin Heidelberg), 3–17, doi: `10.1007/978-3-540-73518-2_1`

Peccei, R. D., & Quinn, H. R. 1977a, Phys. Rev. Lett., 38, 1440, doi: `10.1103/PhysRevLett.38.1440`

—. 1977b, Phys. Rev. D, 16, 1791, doi: `10.1103/PhysRevD.16.1791`

Perez, K., Aramaki, T., Hailey, C. J., et al. 2018, Nuclear Instruments and Methods in Physics Research A, 905, 12, doi: `10.1016/j.nima.2018.07.024`

Perkins, J. S., Maier, G., & The VERITAS Collaboration. 2009, arXiv e-prints, arXiv:0912.3841. `https://arxiv.org/abs/0912.3841`

Perko, J. S. 1987, A&A, 184, 119

Peters, B. 1961, Il Nuovo Cimento, 22, 800, doi: `10.1007/BF02783106`

Petrović, J., Serpico, P. D., & Zaharijaš, G. 2014, Journal of Cosmology and Astroparticle Physics, 2014, 052, doi: `10.1088/1475-7516/2014/10/052`

Pieri, L., Lavalle, J., Bertone, G., & Branchini, E. 2011, Phys. Rev. D, 83, 023518, doi: `10.1103/PhysRevD.83.023518`

Planck Collaboration, Aghanim, N., Akrami, Y., et al. 2020, A&A, 641, A6, doi: `10.1051/0004-6361/201833910`

Potgieter, M. S. 2013, Living Reviews in Solar Physics, 10, 3, doi: `10.12942/lrsp-2013-3`

Prandini, E., Pedaletti, G., Da Vela, P., et al. 2015, in International Cosmic Ray Conference, Vol. 34, 34th International Cosmic Ray Conference (ICRC2015), 251. `https://arxiv.org/abs/1509.02391`

Purcell, W. R., Cheng, L. X., Dixon, D. D., et al. 1997, ApJ, 491, 725, doi: `10.1086/304994`

Read, J. I. 2014, Journal of Physics G Nuclear Physics, 41, 063101, doi: `10.1088/0954-3899/41/6/063101`

Reeves, H., Audouze, J., Fowler, W. A., & Schramm, D. N. 1973, ApJ, 179, 909, doi: `10.1086/151928`

Reid, M. J., & Brunthaler, A. 2004, ApJ, 616, 872, doi: `10.1086/424960`

Renker, D., & Lorenz, E. 2009, Journal of Instrumentation, 4, P04004, doi: `10.1088/1748-0221/4/04/p04004`

Ritt, S., Dinapoli, R., & Hartmann, U. 2010, Nuclear Instruments and Methods in Physics Research A, 623, 486, doi: `10.1016/j.nima.2010.03.045`

Roberts, M. S. 1966, ApJ, 144, 639, doi: `10.1086/148645`

Rogers, F., Xiao, M., Perez, K. M., et al. 2019, Journal of Instrumentation, 14, P10009, doi: `10.1088/1748-0221/14/10/P10009`

Rogers, F., Aramaki, T., Boezio, M., et al. 2022, arXiv e-prints, arXiv:2206.12991. `https://arxiv.org/abs/2206.12991`

Rolke, W. A., López, A. M., & Conrad, J. 2005, Nuclear Instruments and Methods in Physics Research A, 551, 493, doi: `10.1016/j.nima.2005.05.068`

Rosado, J., & Hidalgo, S. 2015, Journal of Instrumentation, 10, P10031, doi: `10.1088/1748-0221/10/10/P10031`

Roszkowski, L., Sessolo, E. M., & Trojanowski, S. 2018, Reports on Progress in Physics, 81, 066201, doi: `10.1088/1361-6633/aab913`

Rowell, G. P. 2003, A&A, 410, 389, doi: `10.1051/0004-6361:20031194`

Rubin, V. C., & Ford, Jr., W. K. 1970, ApJ, 159, 379, doi: `10.1086/150317`

Rubin, V. C., Ford, Jr., W. K., & Thonnard, N. 1980, ApJ, 238, 471, doi: `10.1086/158003`

Rybicki, G. B., & Lightman, A. P. 1985, Radiative Processes in Astrophysics (Wiley)

Saffold, N., Aramaki, T., Bird, R., et al. 2021a, Astroparticle Physics, 130, 102580, doi: `10.1016/j.astropartphys.2021.102580`

Saffold, N., Rogers, F., Xiao, M., et al. 2021b, Nuclear Instruments and Methods in Physics Research A, 997, 165015, doi: `10.1016/j.nima.2020.165015`

Sawada, T., Hasegawa, T., Handa, T., & Cohen, R. J. 2004, MNRAS, 349, 1167, doi: `10.1111/j.1365-2966.2004.07603.x`

Schumann, M. 2019, Journal of Physics G Nuclear Physics, 46, 103003, doi: `10.1088/1361-6471/ab2ea5`

Schwarzschild, A., & Zupančič, Č. 1963, Physical Review, 129, 854, doi: `10.1103/PhysRev.129.854`

Scoville, N. Z. 1972, ApJ Letters, 175, L127, doi: `10.1086/181000`

Senchyshyn, V., Lebedev, V., Adadurov, A., Budagov, J., & Chirikov-Zorin, I. 2006, Nuclear Instruments and Methods in Physics Research A, 566, 286, doi: `10.1016/j.nima.2006.06.037`

Senturk, G. D. 2011, in International Cosmic Ray Conference, Vol. 9, International Cosmic Ray Conference, 127, doi: `10.7529/ICRC2011/V09/0925`

Serpico, P. D. 2012, Astroparticle Physics, 39, 2, doi: `10.1016/j.astropartphys.2011.08.007`

Servant, G., & Tait, T. M. P. 2003, Nuclear Physics B, 650, 391, doi: `10.1016/S0550-3213(02)01012-X`

Shukla, P., & Sankrith, S. 2016, arXiv e-prints, arXiv:1606.06907. `https://arxiv.org/abs/1606.06907`

Silk, J., & Srednicki, M. 1984, Phys. Rev. Lett., 53, 624, doi: `10.1103/PhysRevLett.53.624`

Simpson, J. A. 1983, Annual Review of Nuclear and Particle Science, 33, 323, doi: `10.1146/annurev.ns.33.120183.001543`

Slatyer, T. R. 2021, arXiv e-prints, arXiv:2109.02696. `https://arxiv.org/abs/2109.02696`

Smart, D. F., & Shea, M. A. 2005, Advances in Space Research, 36, 2012, doi: `10.1016/j.asr.2004.09.015`

Smirnov, J., & Beacom, J. F. 2019, Phys. Rev. D, 100, 043029, doi: `10.1103/PhysRevD.100.043029`

Sofue, Y. 2020, Galaxies, 8, 37, doi: `10.3390/galaxies8020037`

Sommerfeld, A. 1931, Annalen der Physik, 403, 257, doi: `10.1002/andp.19314030302`

Sommers, P., & Elbert, J. W. 1987, Journal of Physics G Nuclear Physics, 13, 553, doi: `10.1088/0305-4616/13/4/019`

Speckmayer, P., Höcker, A., Stelzer, J., & Voss, H. 2010, in Journal of Physics Conference Series, Vol. 219, Journal of Physics Conference Series, 032057, doi: `10.1088/1742-6596/219/3/032057`

Spengler, G. 2015, Astroparticle Physics, 67, 70, doi: `10.1016/j.astropartphys.2015.02.002`

Srednicki, M., Watkins, R., & Olive, K. A. 1988, Nuclear Physics B, 310, 693, doi: `10.1016/0550-3213(88)90099-5`

Stecker, F. W. 1978, ApJ, 223, 1032, doi: `10.1086/156336`

Stecker, F. W., Rudaz, S., & Walsh, T. F. 1985, Phys. Rev. Lett., 55, 2622, doi: `10.1103/PhysRevLett.55.2622`

Steigman, G. 1976, Ann. Rev. Astron. Astrophys., 14, 339, doi: `10.1146/annurev.aa.14.090176.002011`

Steigman, G., Dasgupta, B., & Beacom, J. F. 2012, Phys. Rev. D, 86, 023506, doi: `10.1103/PhysRevD.86.023506`

Steigman, G., & Turner, M. S. 1985, Nuclear Physics B, 253, 375, doi: `10.1016/0550-3213(85)90537-1`

Stone, E. C., Cummings, A. C., Heikkila, B. C., & Lal, N. 2019, Nature Astronomy, 3, 1013, doi: `10.1038/s41550-019-0928-3`

Stone, E. C., Cummings, A. C., McDonald, F. B., et al. 2013, Science, 341, 150, doi: `10.1126/science.1236408`

Storm, E., Jeltema, T. E., Profumo, S., & Rudnick, L. 2013, ApJ, 768, 106, doi: `10.1088/0004-637X/768/2/106`

Stricker-Shaver, D., Ritt, S., & Pichler, B. J. 2014, IEEE Transactions on Nuclear Science, 61, 3607, doi: `10.1109/TNS.2014.2366071`

Strigari, L. E. 2009, New Journal of Physics, 11, 105011, doi: `10.1088/1367-2630/11/10/105011`

Strong, A. W., Moskalenko, I. V., & Ptuskin, V. S. 2007, Annual Review of Nuclear and Particle Science, 57, 285, doi: `10.1146/annurev.nucl.57.090506.123011`

Su, M., Slatyer, T. R., & Finkbeiner, D. P. 2010, ApJ, 724, 1044, doi: `10.1088/0004-637X/724/2/1044`

Tan, L. C., & Ng, L. K. 1982, Phys. Rev. D, 26, 1179, doi: `10.1103/PhysRevD.26.1179`

Tatischeff, V., & Gabici, S. 2018, Annual Review of Nuclear and Particle Science, 68, 377, doi: `10.1146/annurev-nucl-101917-021151`

Tegmark, M., Strauss, M. A., Blanton, M. R., et al. 2004, Phys. Rev. D, 69, 103501, doi: `10.1103/PhysRevD.69.103501`

Ting, S. 2016, in Press Conference at CERN, Vol. 8

Tisserand, P., Le Guillou, L., Afonso, C., et al. 2007, A&A, 469, 387, doi: `10.1051/0004-6361:20066017`

Tremaine, S., & Gunn, J. E. 1979, Phys. Rev. Lett., 42, 407, doi: `10.1103/PhysRevLett.42.407`

Tsuboi, M., Handa, T., & Ukita, N. 1999, ApJ Supplement, 120, 1, doi: `10.1086/313165`

Tsuchiya, K., Enomoto, R., Ksenofontov, L. T., et al. 2004, ApJ Letters, 606, L115, doi: `10.1086/421292`

Tulin, S., & Yu, H.-B. 2018, Physics Reports, 730, 1, doi: `10.1016/j.physrep.2017.11.004`

Usoskin, I. G., Alanko-Huotari, K., Kovaltsov, G. A., & Mursula, K. 2005, Journal of Geophysical Research (Space Physics), 110, A12108, doi: `10.1029/2005JA011250`

van Eldik, C. 2015, Astroparticle Physics, 71, 45, doi: `10.1016/j.astropartphys.2015.05.002`

Vergados, J. D., & Ejiri, H. 2008, Nuclear Physics B, 804, 144, doi: `10.1016/j.nuclphysb.2008.06.004`

Virtanen, P., Gommers, R., Oliphant, T. E., et al. 2020, Nature Methods, 17, 261, doi: `10.1038/s41592-019-0686-2`

Vogelsberger, M., Helmi, A., Springel, V., et al. 2009, MNRAS, 395, 797, doi: `10.1111/j.1365-2966.2009.14630.x` von Doetinchem, P. 2009, PhD thesis, RWTH Aachen University

von Doetinchem, P., Aramaki, T., Bando, N., et al. 2014, Astroparticle Physics, 54, 93, doi: 10.1016/j.astropartphys.2013.11.009

von Doetinchem, P., Perez, K., Aramaki, T., et al. 2020, Journal of Cosmology and Astroparticle Physics, 2020, 035, doi: 10.1088/1475-7516/2020/08/035

von Harling, B., & Petraki, K. 2014, Journal of Cosmology and Astroparticle Physics, 2014, 033, doi: 10.1088/1475-7516/2014/12/033

Vovk, I., Strzys, M., & Fruck, C. 2018, A&A, 619, A7, doi: 10.1051/0004-6361/201833139

Wang, J., Bose, S., Frenk, C. S., et al. 2020, Nature, 585, 39, doi: 10.1038/s41586-020-2642-9

Wang, Q. D., Lu, F., & Lang, C. C. 2002, ApJ, 581, 1148, doi: 10.1086/344401

Wang, Q. D., Lu, F. J., & Gotthelf, E. V. 2006, MNRAS, 367, 937, doi: 10.1111/j.1365-2966.2006.09998.x

Webber, W. R., Lee, M. A., & Gupta, M. 1992, ApJ, 390, 96, doi: 10.1086/171262

Weekes, T. C. 1976, Nuovo Cimento B Serie, 35, 95, doi: 10.1007/BF02726286

—. 1988, Physics Reports, 160, 1, doi: 10.1016/0370-1573(88)90177-9

—. 1996, Space Science Reviews, 75, 1, doi: 10.1007/BF00195020

Weekes, T. C., Cawley, M. F., Fegan, D. J., et al. 1989, ApJ, 342, 379, doi: 10.1086/167599

Weekes, T. C., Akerlof, C., Biller, S., et al. 1997, in International Cosmic Ray Conference, Vol. 5, International Cosmic Ray Conference, 173. https://arxiv.org/abs/astro-ph/9706143

Weekes, T. C., Badran, H., Biller, S. D., et al. 2002, Astroparticle Physics, 17, 221, doi: `10.1016/S0927-6505(01)00152-9`

Weiner, O. M. 2017, PhD thesis, Columbia University, New York

White, S. D. M., Frenk, C. S., & Davis, M. 1983, ApJ Letters, 274, L1, doi: `10.1086/184139`

Wilks, S. S. 1938, The annals of mathematical statistics, 9, 60

Wilson, T. L., & Mauersberger, R. 1994, A&A, 282, L41

Woolf, N. J. 1967, ApJ, 148, 287, doi: `10.1086/149148`

Yüksel, H., Kistler, M. D., & Stanev, T. 2009, Phys. Rev. Lett., 103, 051101, doi: `10.1103/PhysRevLett.103.051101`

Yusef-Zadeh, F., Arendt, R. G., Wardle, M., et al. 2022, ApJ Letters, 925, L18, doi: `10.3847/2041-8213/ac4802`

Yusef-Zadeh, F., Hewitt, J. W., & Cotton, W. 2004, ApJ Supplement, 155, 421, doi: `10.1086/425257`

Yusef-Zadeh, F., Morris, M., & Chance, D. 1984, Nature, 310, 557, doi: `10.1038/310557a0`

Yusef-Zadeh, F., Hewitt, J. W., Wardle, M., et al. 2013, ApJ, 762, 33, doi: `10.1088/0004-637X/762/1/33`

Zatsepin, G. T., & Kuz'min, V. A. 1966, Soviet Journal of Experimental and Theoretical Physics Letters, 4, 78

Zitzer, B., & VERITAS Collaboration. 2013, in International Cosmic Ray Conference, Vol. 33, 33rd International Cosmic Ray Conference (ICRC2013), 3076. `https://arxiv.org/abs/1307.8360`

Zitzer, B., & VERITAS Collaboration. 2017, in International Cosmic Ray Conference, Vol. 301, 35th International Cosmic Ray Conference (ICRC2017), 769. `https://arxiv.org/abs/1708.07444`

Zwicky, F. 1933, Helvetica Physica Acta, 6, 110

—. 1937, ApJ, 86, 217, doi: `10.1086/143864`